Investigations on bio and natural gas conditioning and separation via gas hydrate formation under the use of surface active materials (promoters)

Dissertation

zur Erlangung des akademischen Grades eines

Doktors der Naturwissenschaften

— Dr. rer. nat. —

vorgelegt von

Florian Filarsky

an der

Universität Duisburg-Essen

Fakultät der Chemie

in Essen

DOI: 10.17185/duepublico/70583
URN: urn:nbn:de:hbz:464-20191023-122022-3

Die vorliegende Arbeit mit dem Titel: „Investigations on bio and natural gas conditioning and separation via gas hydrate formation under the use of surface active materials (promoters)“ wurde im Zeitraum vom Juli 2016 bis Juni 2019 im Arbeitskreis von Prof. Dr. Schmuck am Institut für Supramolekulare Chemie der Universität Duisburg-Essen sowie im Arbeitskreis von Prof. Dr.-Ing. Schultz am Institut für Lacke und Oberflächenchemie (ILOC) der Hochschule Niederrhein durchgeführt.

Tag der Disputation: 23.09.2019

Gutachter: Prof. Dr. Thomas Schrader
Prof. Dr.-Ing. Heyko Jürgen Schultz
Vorsitzender: Prof. Dr.-Ing. Stephan Barcikowski

Eidesstattliche Erklärung

Ich versichere hiermit an Eides statt, dass ich die vorgelegte Dissertation mit dem Titel: „Investigations on bio and natural gas conditioning and separation via gas hydrate formation under the use of surface active materials (promoters)“ selbstständig, ohne fremde Hilfe und ohne die Benutzung anderer als die in der Arbeit angegebenen Hilfsmittel angefertigt habe. Alle Stellen, die wörtlich oder sinngemäß aus veröffentlichten und nicht veröffentlichten Quellen entnommen wurden, sind als solche in der Arbeit kenntlich gemacht. Die vorliegende Arbeit hat in dieser oder ähnlicher Form oder auch auszugsweise im Rahmen einer anderen Prüfung noch nicht vorgelegen.

Essen, 05.06.2019

_____

Florian Filarsky

Danksagung

Zunächst einmal möchte ich mich besonders bei Prof. Dr.-Ing. Heyko Jürgen Schultz für die vergangenen drei Jahre bedanken, die ich Teil seiner Arbeitsgruppe sein durfte. Es war eine äußerst interessante und lehrreiche Zeit, in welcher ich viele neue Erfahrungen sammeln und mich individuell weiterentwickeln konnte. Stets wurde ich ermutigt mit Neugier und innovativen Gedanken, neuartige und pragmatische Lösungsansätze zu verfolgen, um dadurch den Stand der Wissenschaft und Technik voranzutreiben.

Weiterhin möchte ich mich bei Prof. Dr. Carsten Schmuck für die Möglichkeit zur, und seine Unterstützung im Laufe der Promotion bedanken. Der rege wissenschaftliche Austausch, vor allem im persönlichen Gespräch, lieferte stets neue Impulse und Denkansätze, welche maßgeblich zum Gelingen des Forschungsvorhabens beigetragen haben.

Prof. Dr. Thomas Schrader danke ich für sein kurzfristiges Aushelfen als Erstgutachter für diese Arbeit.

Ein weiterer Dank gebührt allen Kollegen und Mitarbeitern der Hochschule Niederrhein, welche mich während meiner Arbeit begleitet und unterstützt haben. Hierbei möchte ich mich vor allem bei Dr. Bartholomäus Luczak, Dr. Alexander Stefan, Björn Lewandowski und Joscha Prießen für die freundschaftliche Motivation und den ausgiebigen wissenschaftlichen Disput bedanken.

Ein großes Dankeschön geht an die zahlreichen Studierenden, die ich im Laufe Ihrer Abschlussarbeiten betreuen durfte und die mich persönlich haben wachsen lassen. Ich wünsche M. Hagelstein, T. Hommen, N. Patzner, J. Wieser, F. Barths, N. Theunißen, G. Lee, A. Breuer, G. Karadag, L. Gobbers und R. Winterott alles erdenklich Gute auf Ihrem weiteren Lebensweg.

Laura Wörmeyer, Timo Ufermann und nochmals Dr. Bartholomäus Luzcak danke ich für Ihre Zeit und Bereitschaft, als private Reviewer diese Arbeit Korrektur zu lesen, um ihr den nötigen Feinschliff zu verleihen.

Zu guter Letzt gebührt mein außerordentlicher Dank Familie und Freunden, die mich bis hier hin auf meinem Lebensweg begleitet, unterstützt und geprägt haben und somit immer Teil meines Wirkens sein werden.

Vielen Dank

Abstract

Gas hydrates are solid crystalline inclusions of guest molecules in water. In nature, due to high pressures and low temperatures, they can be found in deep sea or permafrost areas where water molecules form cage-like structures in which stabilizing guest molecules are centered inside. The guest molecules are e.g. lower hydrocarbons or carbon dioxide. Former research was mainly focused on the exploitation of natural gas hydrate deposits and the prevention of gas hydrate formation in gas pipelines. Along with the growing knowledge on gas hydrate properties, new applications are conceivable. Nowadays, efficient gas storages, desalination units, gas separation processes etc. are thinkable. In the coming decades, the relevance of *natural and biogas* will rise due to the decline of conservative fossil fuels like crude oil. Currently, both gases need to be conditioned with a high cost and energy effort.

The presented thesis follows the attempt to solve these problems by developing an energy saving gas hydrate separation process. Therefore, the gas hydrate formation behavior in presence of diverse kinetic and thermodynamic promoter mixtures is extensively investigated under different conditions and the separation efficiency evaluated. Surface active substances are tested and a promoting coating for reactors and particles is designed. A multitude of reactor designs is developed, operated and optimized with regard to an improved, targeted gas hydrate formation. Furthermore, first-time feasibility studies are performed proving a successful development of a promoting coating, a combined biogas production with subsequent gas hydrate separation, and a gas hydrate absorption process. Additionally an Excel-Tool© is developed for the prediction of gas hydrate equilibria. Supported by simulations, the promising results of this thesis result in economic considerations revealing the vast energy and cost saving potential of a gas hydrate separation process applicable for bio and natural gas conditioning. Further, a pilot plant is designed to allow further research with an industrial and commercial focus in the future.

Contents

1 Introduction

Gas hydrates are inclusion-like compounds consisting of water molecules, which act as host molecules, and small gas molecules, acting as guest molecules. Under extreme conditions, namely high pressure and low temperature found for example in deep-sea and permafrost areas, water molecules arrange around the gas molecules in a crystalline framework. First found by Priestley in 1778 and designated as “hydrate of gas” by Sir Humphrey Davy in 1811, gas hydrates are known to cause problems in gas pipelines where operating conditions allow the possibility of spontaneous gas hydrate formation and agglomeration at internals as valves, leading to so-called gas hydrate plugs [1,2]. Furthermore, natural gas hydrate deposits show a vast potential as a future energy resource since the estimated amount exceeds all other remaining fossil resources by a factor of two [3,4]. Therefore, gas hydrate research gains more and more attention since the 1960s. Nowadays, several application areas have been identified for a targeted gas hydrate formation: gas storage and transport, gas separation, desalination, phase change materials, biotechnology, food engineering and even electricity supply, whereby this thesis is going to focus on the first ones, storage and separation.

The problem which needs to be overcome for all gas hydrate technologies is the slow, crystallization-like formation process only occurring under extreme conditions, and additionally, regarding gas separation, a low selectivity. The main approach focuses on the use of kinetic and thermodynamic promoters.

Kinetic promoters accelerate the hydrate growth by facilitating the gas solubility, usually by forming a foam or a mushy hydrate plug with a reduced surface tension. Therefore, the most common kinetic promoters are surfactants. Amino acids, polymers, starch, saccharide, nanoparticles, hydrogels should be mentioned here inter alia. However, kinetics can be enhanced by choosing an appropriate reactor design. Usually stirred reactor systems are used in the field of gas hydrate research, although to a small extent fixed bed, bubble column or spray reactors are utilized as well.

Thermodynamic promoters shift the equilibrium of gas hydrate formation to moderate conditions as these substances are able to form hydrate structures by themselves. In doing so, thermodynamic promoters significantly dictate the type of gas hydrate structure formed and occupy the corresponding large cages themselves, which cannot be filled by other guest molecules anymore.

The presented thesis contributes to the solution of the named problem by investigating the potential of the innovative and pioneering gas hydrate separation with a holistic multi-pronged approach which combines fundamental research on promoters and reactor designs, simulations

and engineering science considerations. After providing an insight into theoretical basics in chapter two and explanation of the used experimental set-ups in chapter three, chapter four deals with an extensive promoter screening of surfactants, crown and acyclic ethers, amino acids, aprotic solvents and fatty acids in different concentrations. Subsequently the development of a promoting coating made from different silanes is outlined in chapter five before several technical promotion methods are investigated. Different stirrer setups, the influence of the rotation frequency and a packed bed as well as a spray reactor design are examined in chapter six. Following this, chapter seven deals with the purification of biogas and chapter eight with the separation of natural gas by gas hydrate separation in presence of different thermodynamic promoters and synergetic additives. Additionally, an Excel©-Tool is developed for the prediction of gas hydrate equilibria with a competitive accuracy in chapter nine. This thesis concludes in chapter ten with economic considerations based on the preceding findings to answer the question: Is the gas hydrate separation process a promising alternative for established processes in the field of bio and natural gas conditioning? As an outcome from this question, a pilot plant, which can be continuously operated in a laboratory, is designed and installation costs are estimated to allow further gas hydrate separation experiments with a clear industrial and commercial orientation in chapter 11. At the end, a summary of results, a conclusion and an outlook are given.

2 Theory

This chapter contains a general theoretical background for all the performed experiments. It starts by answering the question “What are gas hydrates?”, proceeds with the molecular structure and formation mechanism of gas hydrates, explains the terms “Promoter” and “Inhibitor”, continues with information about bio and natural gas conditioning and closes with possible applications for targeted gas hydrate formation. It is stated here that every chapter, dealing with conducted experiments during this PhD-project, starts with a separate theoretical section, to give the reader a detailed background at the required point.

2.1 Gas hydrates

Clathrates are “inclusion compounds in which the guest molecule is in a cage formed by the host molecule or by a lattice of molecules” [5]. If the host molecules are solely water molecules, the compound counts towards “pure clathrates” and is also called hydrate. Natural hydrates occur in every region of the world, where high pressures and low temperatures can be found, for example in the deep sea, permafrost areas and even in inland seas or water lakes. Thereby van der Waals interactions stabilized cavities are filled with, e.g. small hydrocarbons or carbon dioxide [6]. They are known for their vast potential as energy source as there is approximately twice the amount of all other fossil fuels deposited in natural gas hydrates [3,4]. Simultaneously, natural methane hydrate deposits are regarded as an upcoming danger in the course of the climate change. Due to the steady temperature rise in the sea, pessimistic estimations sketch a scenario in which methane, from no longer thermodynamic stable hydrate deposits, is released and subsequently promotes the greenhouse effect because methane is an even stronger greenhouse gas than carbon dioxide. This, in turn, leads to a faster temperature increase in the sea, destabilizing further methane hydrate reservoirs, and so on [3].

Gas hydrate research began with their accidental creation by Priestley in 1778, while bubbling sulfur dioxide through water at 273.15 K [1]. However, the obtained crystals were not named hydrates until 1811 when Sir Humphrey Davy wrote about “hydrate of gas” [2]. During the following 120 years, gas hydrates drew only little attention to a few researchers like Villard. In the 1930s, when natural gas pipelines were laid into colder climate regions, methane hydrates became an issue attracting attention. First natural gas hydrate deposits were found in the 1960s and since, then gas hydrates gained more and more prominence, not only with regard to flow assurance or natural gas hydrate exploitation, but also to possible applications [7–12].

2.2 Molecular structure

Common natural hydrate structures belong to three different crystal structures, sI, sII and sH even though there are more known structures in the present. The major difference to ice is that ice forms as a pure component, while gas hydrates are only stable with an additional guest molecule. It should be mentioned that it is possible to transform structure sII neon hydrates by applying a vacuum at extremely low temperatures to form the sixteenth known ice structure, which is eventually an empty sII structure [13]. Depending on the guest molecule size, different cage structures are formed. The cages built by the water molecules have quadratic, pentagonal and hexagonal faces. All structures have in common that they have a small cage consisting of 12 pentagonal faces forming a dodecahedron. The larger cages have added hexagonal faces and structure sH is special in view of a third cage formed by three quadratic, six pentagonal and three hexagonal faces. A multitude of these cages in a certain ratio form the structures. An overview is given in Figure 2-1 in addition to common guest molecules.

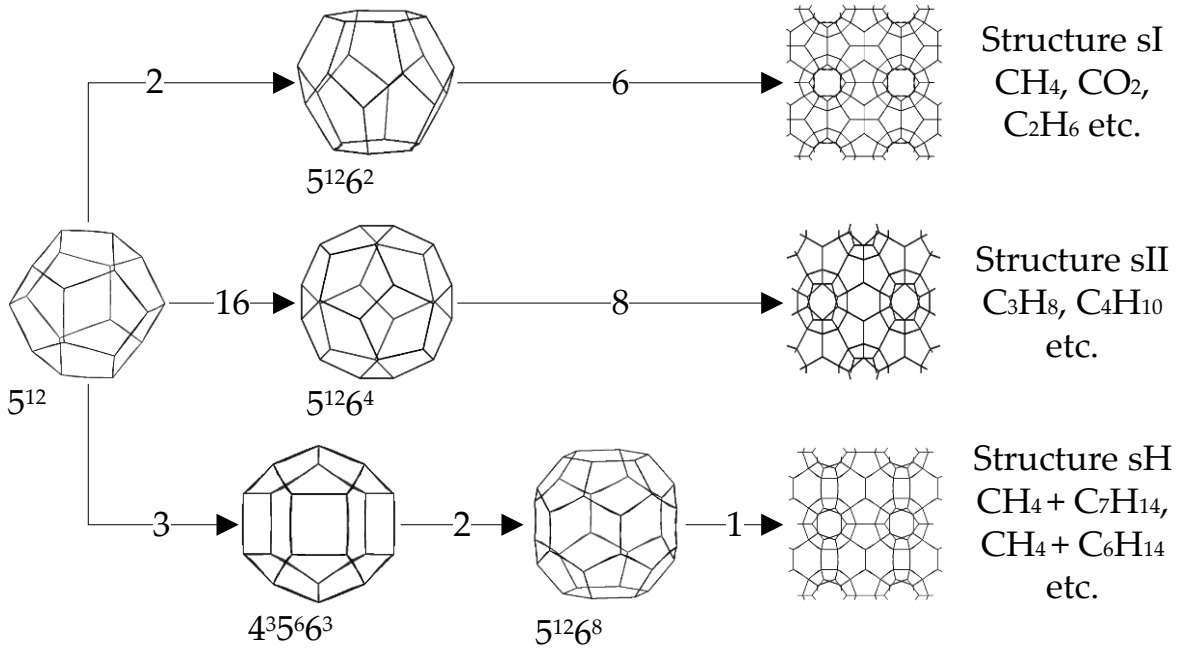

Figure 2-1 Gas hydrate structures

The numbers on the arrows represent the respective amount of cages in the corresponding structure. The number of water molecules per unit cell is also of importance. The formula for an unit cell is given by $2(5^{12}) \cdot 6(5^{12}6^2) \cdot 46\, H_2O$ for sI, $16(5^{12}) \cdot 8(5^{12}6^4) \cdot 136\, H_2O$ for sII and $3(5^{12}) \cdot 2(4^35^66^3) \cdot 1(5^{12}6^4) \cdot 34\, H_2O$ for sH [6]. If all cages in structure sI or sII are occupied, each guest molecule would bind 5.75 or 5.67 water molecules respectively. As there is always the possibility of empty cages due to steric barriers, a good rule of thumb is the Villard's rule as approximation for the hydration number. Villard stated that gas hydrates can be expressed by the formula $n_{Gas} \cdot 6\, H_2O$ which is solely and roughly true for small guests occupying both cages of structure sI or sII [6].

2.3 Gas hydrate formation

Generally the hydrate formation is an exothermic, crystallization-like process, however still incompletely explainable. It can be divided into two steps, the nucleation and the growth. The following section deals with both topics.

2.3.1 Nucleation

Nucleation is a stochastic process, especially occurring at low driving forces, and apparatus-dependent. The process can be influenced by several parameters like apparatus geometry, water contaminants and history or degree of agitation. By using optimized operating conditions the nucleation becomes less stochastic. Today the following theories exist to explain the nucleation:
The labile cluster theory (see Figure 2-2) states that in the hydrate formation region pure water exists with transient, labile pentagonal or hexagonal ring structures. If a guest molecule is dissolved in the liquid, clusters form immediately and irreversibly. In an equilibrium step, these labile cluster agglomerate by sharing faces until a critical value is reached. Then the nucleation is completed and growth starts [14].

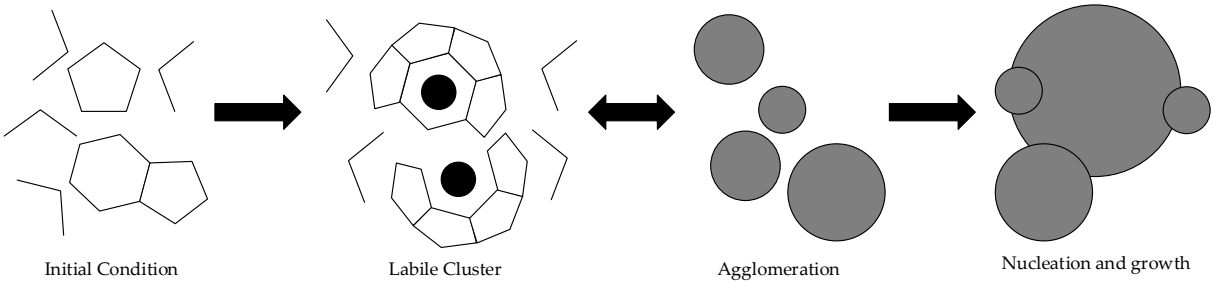

Figure 2-2 Scheme explaining the labile cluster theory according to [15,16]

An extension of the labile cluster theory is the nucleation at the interface hypothesis, developed by Long and Kvamme, which describes a heterogeneous nucleation right at the interface. The guest molecules are adsorbed on the aqueous surface where water molecules form first partial and then complete cages. Again, if a critical size is achieved, nucleation is finished and growth proceeds [15,16].
According to molecular simulations, the third hypothesis is the local structuring. Free energy calculations showed that labile clusters are thermodynamically unfavorable. Furthermore, it was found that guest molecules arrange in hydrate-like configurations restraining the water molecule movement. Therefore, the water molecules start to order in a local arrangement around the guest molecules until a critical nucleus is attained [17,18].
A combination of these theories can be found in the so-called “Blob”-Theory, presented in Figure 2-3.

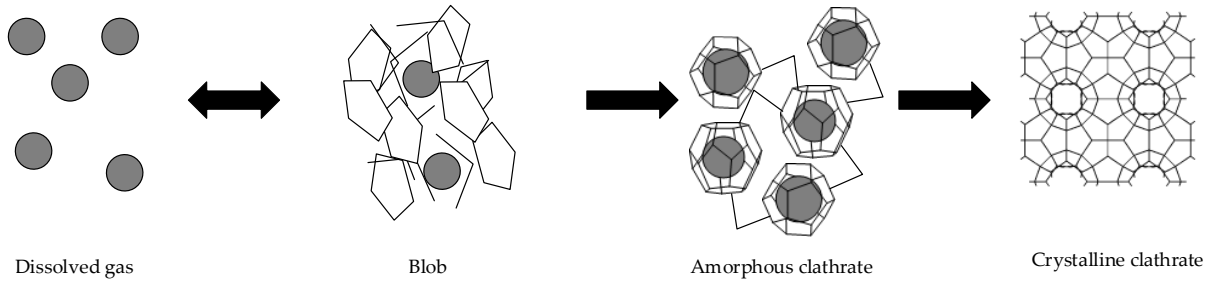

Figure 2-3 Reaction scheme for the Blob-Theory according to [19]

Dissolved guest molecules stay in an equilibrium state with a blob. This blob is able to form in two irreversible steps, at first an amorphous blob and the crystalline hydrate afterwards [19]. Latest studies confirm this mechanism, however the possibility exists that the amorphous state can be skipped under some circumstances, resulting in the multi-pathway theory [20].

2.3.2 Growth

Hydrate growth is mainly influenced by kinetic, heat and mass transfer restrictions. Today, approximately 27 different approaches exist to model the hydrate growth, which can be retraced to the following three works. An overview is given by Yin et al. [21]. Vysniauskas and Bishnoi described the hydrate formation as a three-step reaction [22]. Englezos and Kalogerakis used a crystallization and mass transfer processes for their studies [23]. Skovborg's and Rasmussen's model states that the entire hydrate formation is mainly limited by the mass transfer of the gas through the liquid film at the gas–liquid interphase. In addition, Skovborg used the dataset provided by Englezos to calculate the mass transfer coefficients k_L for methane (4.0476 x 10-5 m/s) and ethane (5.457 x 10-5 m/s) hydrate formation [24]. Mathematically, the following relation describes the change of the molar amount of the guest molecule over time $\frac{dn_i}{dt}$ which is proportional to the mass transfer coefficients k_L, the gas-liquid exchange area $A_{(g-l)}$ and the difference between the molar fraction at the interface x_i^{Int} and in the bulk x_i^b. (See Eq. 2-1) This approach leaves heat transfer restrictions unconsidered.

$$\frac{dn_i}{dt} = k_L A_{(g-l)}\left(x_i^{Int} - x_i^b\right)\left[\frac{mol}{s}\right] \qquad \text{Eq. 2-1}$$

If the gas uptake over time is recorded, hydrate formation shows the following course. (see Figure 2-4) Until no induction occurred, the cumulated gas uptake is nearly zero, only absorption can be recognized. As soon as the nucleation arises, the hydrate growth starts, along with a rapid increase in the gas uptake. Afterwards the gas uptake slows down significantly, as most of the water is transformed into gas hydrates. Then hydrate formation becomes a diffusion-limited process, until no free water is left.

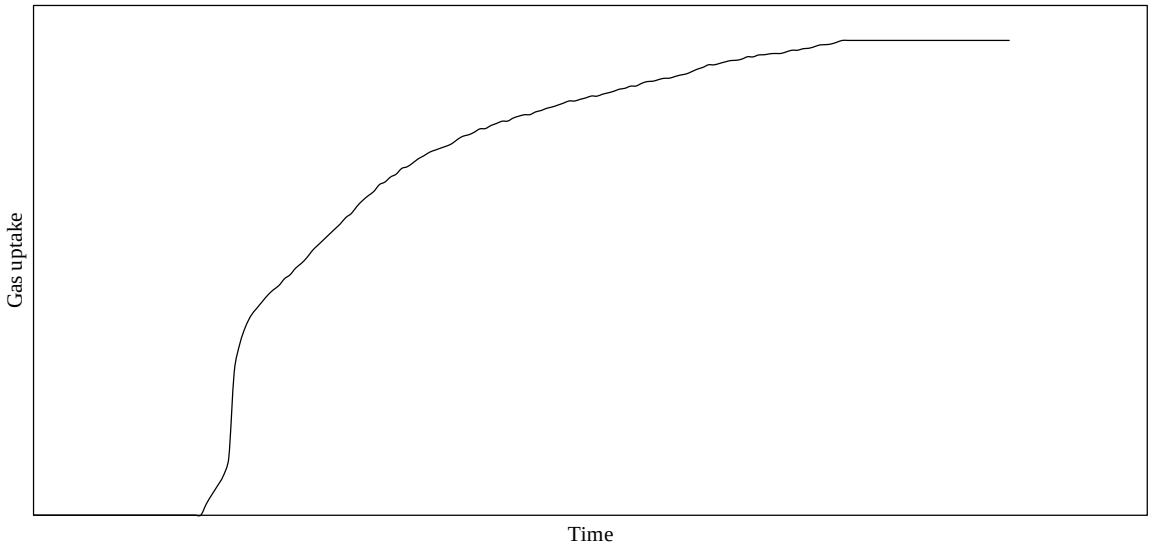

Figure 2-4 Schematic diagram of the cumulative gas uptake vs. time during gas hydrate formation

In literature, the gas uptake is normalized as mmol gas per mol water. Therefore, the following equation describes the water conversion.

$$C = \frac{n_{Gas}}{n_{Water}} * Hydration\ number\ [\%] \qquad \text{Eq. 2-2}$$

Dependent on the guest molecules and hydrate structure which is formed, the hydration number varies. Structure sI has a hydration number of 5.75 and structure sII 5.67, leaving empty cages unconsidered. Literature provides hydration numbers for different gas hydrates which were obtained from experiments. For example, for methane hydrate Tulk et al. registered a value of 6.10 [25]. Kumar et al. found 7.03 for carbon dioxide hydrate [26].

2.4 Promoter

Promoters are substances which influence the hydrate kinetics or thermodynamic equilibrium in a positive way with regard to a desired hydrate formation. They are divided into kinetic and thermodynamic promoters.

2.4.1 Kinetic promoters

Kinetic promoters accelerate the hydrate formation especially the growth. The most common class of molecules are surfactants. They are amphiphilic, consisting of a hydrophobic and hydrophilic part and are classified based on the charge of the hydrophilic head as anionic, nonionic or cationic respectively. Since surfactants lower the surface tension and facilitate the gas solubility, they have special relevance in this field. Furthermore, the addition of surfactants

influences the morphology of gas hydrates, which is why they play an important role as antiagglomerants in the field of flow-assurance [27]. An overview can be obtained from Kumar et al. [28]. Most notably, sodium dodecyl sulfate (SDS) is known as an outstanding kinetic promoter for methane and carbon dioxide hydrates simultaneously [28]. Further possibilities to promote hydrate formation are the use of silica nanoparticles or active carbon [29]. Veluswamy et al. showed that amino acids are also capable of promoting methane hydrate formation [30]. Some polymers, even ones which are meant to be inhibitors, enhance the kinetics as well [31–33]. It should be pointed out, that starch molecules can also act as promoters [34–36]. Therefore, research is still proceeding to find new promoters and far away from completion.

2.4.2 Thermodynamic promoters

Thermodynamic promoters shift the hydrate formation conditions from extreme to moderate. The most common thermodynamic promoter is tetrahydrofuran (THF). The effect is based on the property of THF to form large cages of the sII hydrate structures. While building large cages, small ones occur as well and nearby gas molecules are able to occupy these. Hence, a mixture of water and THF in presence of methane forms mixed sII hydrates which are stable at similar conditions like THF hydrates. A comparison between both equilibrium trends is shown in Figure 2-5.

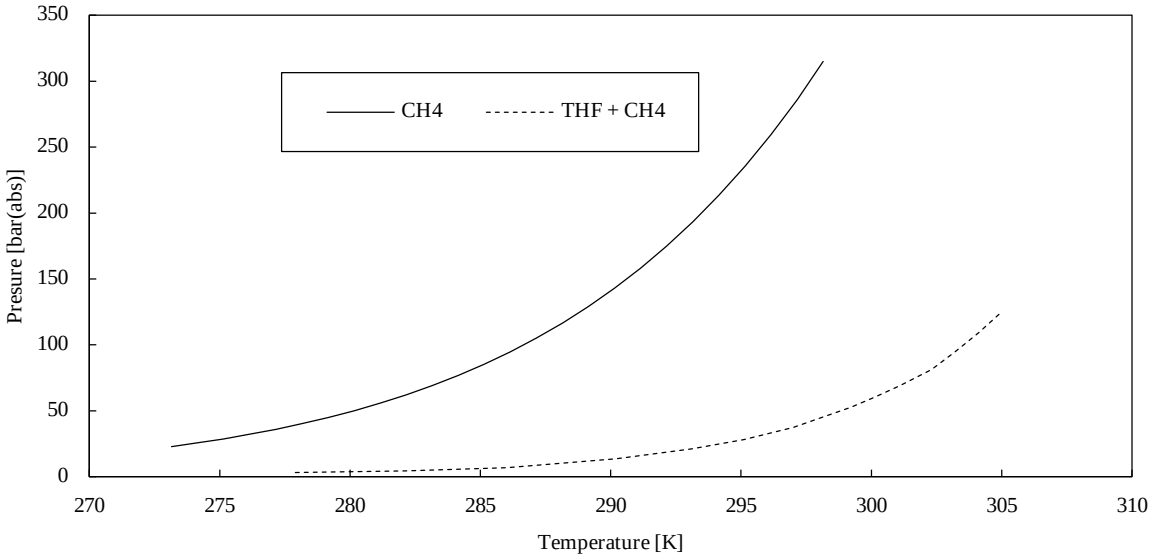

Figure 2-5 Comparison of the P-T-equilibrium of pure methane hydrates [6] and THF + methane mixed hydrates [37]

Another substance class which represents good promoters includes tetra butyl pnictogen salts like tetrabutylammonium bromide (TBAB) or tetrabutylphosphonium bromide (TBPB). They are able to form semiclathrates and their promoting effect is similar to THF with the difference that these compounds form further clathrate structures which differ from the natural appearing ones. Semiclathrates differ from gas hydrates as they act as host and guest simultaneously. Anions

replace some water molecules in the clathrate framework leading to broken cages enclosing the large cations [38].

2.5 Inhibitors

Inhibitors are the opposite of promoters and used to prevent undesired hydrate formation in technical systems like gas pipelines where dehydration or trace heating is not an economically feasible approach. They are divided into thermodynamic and low-dosage hydrate inhibitors (LDHI). This section gives a short overview considering both classes.

2.5.1 Thermodynamic inhibitors

In water, solute thermodynamic inhibitors shift the gas hydrate equilibrium conditions towards more extreme ones, namely lower temperatures and higher pressures. This effect is similar to the operating principle of antifreeze agents used in car radiators. The most commonly used substances are alcohols, glycols and salts [27]. Due to its effectiveness, low cost, and easy availability, methanol is an inhibitor used in large quantities [39]. However, its use has an quantitative limitation and can additionally lead to corrosion problems [39]. Ethanol is often used in South America, as it is a waste product which accrues from the sugar industry, but has the disadvantage that above a concentration of 5.6 mol% ethanol can form binary hydrates with methane counteracting its intended purpose [27]. In case of the glycols, ethylene, diethylene and triethylene glycol are the common ones because of the advantage that they can be recovered from the process [27,39]. Among those, ethylene glycol has an outstanding position due to its low costs, low viscosity, and lower solubility in liquid hydrocarbons [40]. Besides alcohols and glycols, salts such as sodium chloride, calcium chloride, potassium formate, and sodium acetate act as inhibitors in the gas industry. These salts are commonly used while drilling to prevent hydrate formation, sometimes in addition to glycols [27]. However, THI can cause several operational issues, which is why research in this field is still under development. A detailed list of these operational issues and further information can be obtained from Kelland [27].

2.5.2 Low-dosage hydrate inhibitors

Low-dosage inhibitors provide clear advantages, mainly affecting economic parameters, in contrast to THIs. For example they can be used in low concentrations (0.1-1.0 wt%), are less volatile in comparison to methanol and provide a lower toxicity. There are two classes of LDHIs, kinetic hydrate inhibitors (KHI) and anti-agglomerants (AA). Kinetic hydrate inhibitors delay the gas hydrate nucleation and/or crystal growth while not influencing the thermodynamic hydrate

formation conditions [40]. Their mode of action is based on their uptake on the hydrate surface preventing the formation and growth of hydrate crystals. Thereby, the aim is to prevent hydrate formation during the residence time of the process stream in the hydrate formation regime. Primary, low molecular weight polymers, like polyethylene or polyvinyl chains with attached polar groups are used [39]. AAs should neither prevent hydrate formation nor slow down the kinetics. The idea behind their usage is to impede the agglomeration of hydrate particles to form a hydrate plug. Thereby, a non-sticky slurry is formed in a liquid hydrocarbon phase of the process stream, which is also the requirement for their application in the industry. Frequently used AAs are surfactants or quaternary ammonium and phosphonium salts [27,39].

2.6 Bio and natural gas conditioning

Figure 2-6 shows the energy production of the U.S. according to the "Annual Energy Outlook 2017". It is visible that within the next decades the importance of dry natural gas and renewable energy sources are expected to raise and are assumed to become the main energy sources. Hence bio and natural gas conditioning to enable these energy sources will be a major topic as well.

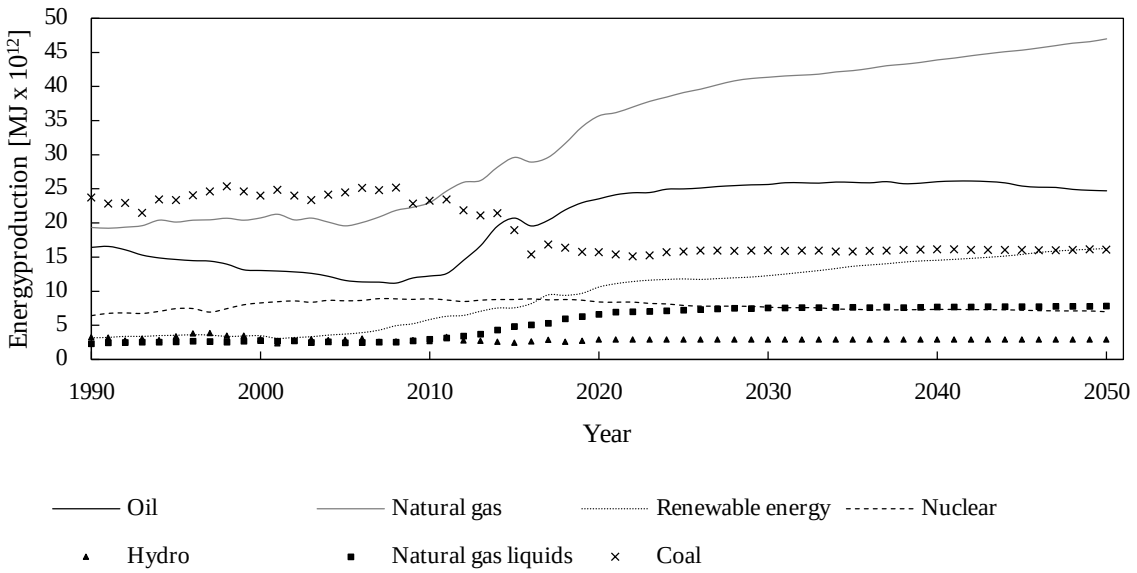

Figure 2-6 Energy production of the U.S. according to the "Annual Energy Outlook 2017" [41]

Table 2-1 shows typical bio and natural gas compositions. Both consist mainly of methane. While for the purification of biogas carbon dioxide is the major contaminant, natural gas requires the removal of heavy hydrocarbons like ethane and propane as other components like nitrogen, hydrogen sulfide, ammonia and chlorine appear only in small amounts.

Table 2-1 Typical bio and natural gas compositions [42]

Content	Dimension	Biogas from anaerobic digestion	Natural gas
Lower calorific value	MJ/kg	12.3	48
Methane	Vol-%	60 – 70	85 – 92
Heavy hydrocarbons	Vol-%	0	9
Hydrogen	Vol-%	0	-
Carbon dioxide	Vol-%	35 – 40	0.2 – 1.5
Nitrogen	Vol-%	0.2	0.3 – 1.0
Oxygen	Vol-%	-	-
Hydrogen sulfide	ppm	0 – 4000	1.1 – 5.9
Ammonia	ppm	100	-
Chlorine as Cl^-	ppm	0 – 5	-

The process to purify natural gas is outlined in Figure 2-7.

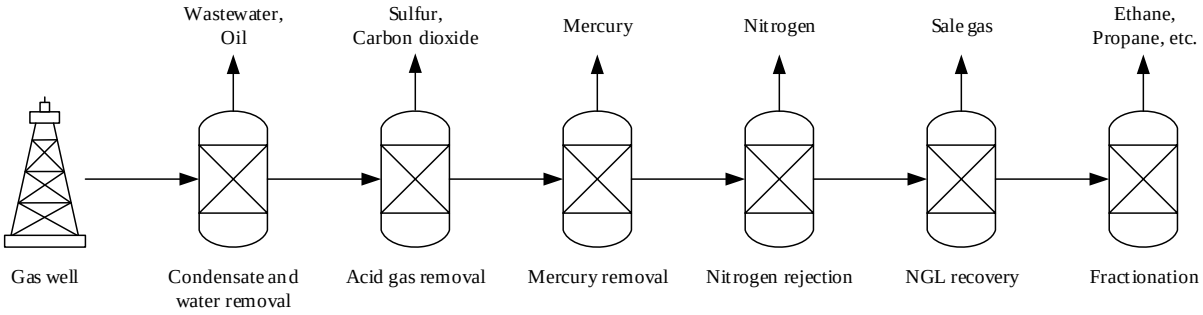

Figure 2-7 Flow-diagram showing natural gas treatment

At first, natural gas from the well is separated from crude oil and water via a low-temperature separation which is installed at or near the wellhead. To remove residual water vapor, a glycol absorption is used. Afterwards, amine absorption removes acid gas components like hydrogen sulfide and carbon dioxide. Elemental sulfur can be recovered from the amine treatment with a downstream “Claus”-process. The sweetened gas is freed from mercury with the help of a mole sieve or activated carbon before nitrogen is taken away by absorption or adsorption. The natural gas obtained in this way only consists of hydrocarbons and negligible impurities. To obtain saleable natural gas and acquire higher chained hydrocarbons, cryogenic fractionation is implemented [40,43]. As cryogenic fractionation is the most energy consuming step in the natural gas treatment process, this work focuses on the natural gas fractionation by gas hydrate separation.

Biogas treatment to obtain saleable gas is similar to the natural gas treatment with the difference that less components have to be removed. First, raw biogas is acquired from a fermentation process or rather anaerobic digestion. Water must be removed which can for example be achieved

by glycol absorption. Afterwards, hydrogen sulfide is adsorbed on activated carbon or chemisorbed on iron. To reduce the carbon dioxide fraction, amine or water absorption can be used. Now, the product gas has a mole fraction higher than 0.96 of methane and is saleable after compression [44,45]. Figure 2-8 sketches this process.

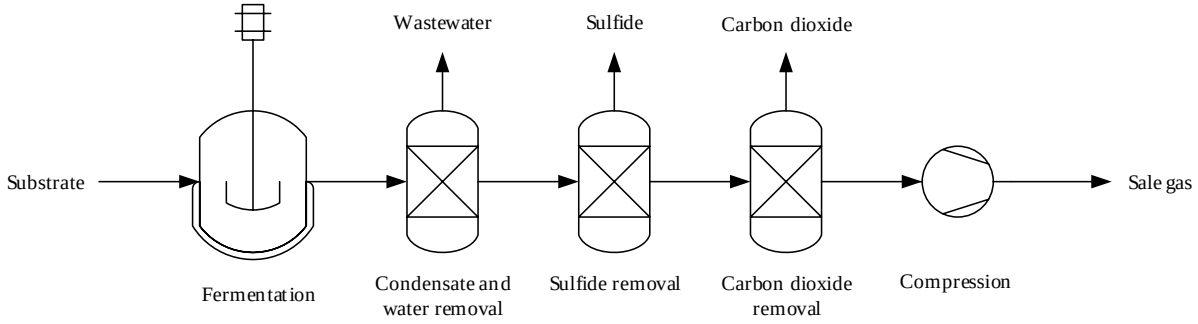

Figure 2-8 Flow-diagram showing the biogas treatment

2.7 Gas hydrate applications

Due to the increasing knowledge towards hydrate properties, several applications are imaginable like water desalination, CO2 capture and sequestration, food industry processes, refrigeration, gas separation, gas storage as well as transportation. As this work concentrates on gas separation and storage, both technologies are further explained in this section.

2.7.1 Gas separation

The idea for separating gases by hydrate formation was first proposed by Nikitin who performed experiments with a radon-dihydrogen sulfide-sulfur dioxide system in 1936 [46]. Due to affinity differences of varying gas species to occupy gas hydrate cages, a mixture of these gases can be separated as some components tend to enrich either in the hydrate or in the gas phase. The process is sketched in Figure 2-9.

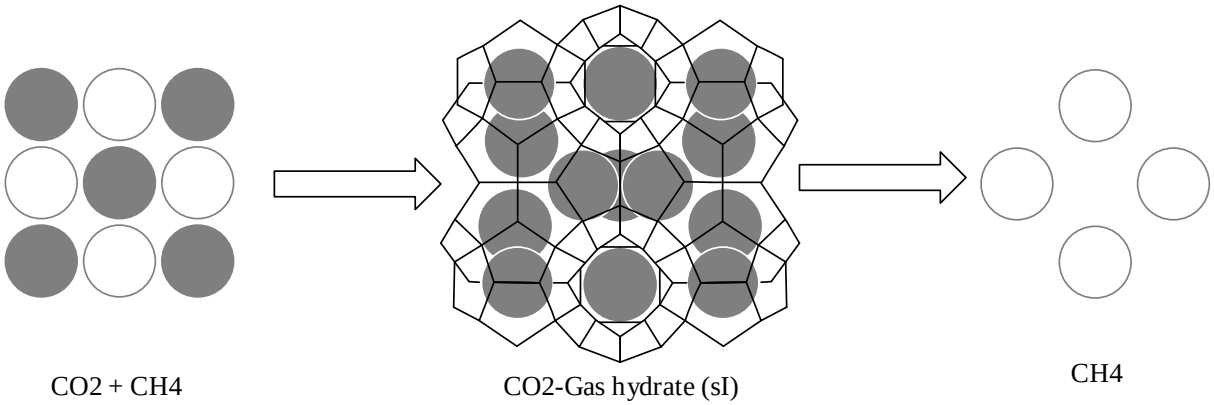

Figure 2-9 Schematic gas hydrate separation process

Later, the hydrate phase can be dissociated by depressurization and/or heating thereby releasing the stored gas if necessary. As this thesis focuses on biogas and natural gas conditioning, exemplary studies dealing with the separation of methane and carbon dioxide via pure gas hydrate formation are referenced here [47–52].

Over time, many studies were conducted dealing with gas hydrate separation of different gas mixtures in presence of different promoters with varying experimental conditions. An overview which systems and thermodynamic promoters were investigated is given in Table 2-2.

Table 2-2 Matrix showing gas hydrate separation investigations in presence of different thermodynamic promoters. A – without promoter, B – cyclopentane, C - 1,3-dioxolane, D - 2-methyl tetrahydrofuran, E – tetrabutylammonium bromide, F – tetrabutylammonium fluoride, H – tetrabutylammonium nitrate, I – tetrabutylphosphonium bromide, J – tetrabutylphosphonium chloride, K - tetrahydrofuran

Gas	CO_2	CH_4	H_2S	N_2	C_2H_6	SO_2	CHF_3	H_2
CO_2		A, B, C, D, E, I, K	E	A, E, H, I, J, K		E		A, B, E, F, H, K
CH_4	A, B, C, D, E, I, K		E	E	A, K			B, E
H_2S	E	E						E
N_2	A, E, H, I, J, K	E					A	
C_2H_6		A, K						
SO_2	E							
CHF_3				A				
H_2	A, B, E, F, H, K	B, E	E					

It is visible that research concentrates on the purification of fuel, flue and biogas which is presumably due to an increased environmental awareness and industrial interest. Therefore, the most used promoters are tetrabutylammonium bromide and tetrahydrofuran. An extensive overview can be obtained from Eslamimanseh et al. [53].

2.7.2 Gas storage

Already back in 1942, Banesh claimed a patent on storage and transport of natural gas in form of gas hydrates [54]. Gas hydrate storages have the advantage of a lower storage space and an energy density equivalent to a highly compressed gas, but with less density in comparison to liquefied natural gas [6] as 1 m^3 of methane hydrate can store up to 170 Nm^3 of methane [55]. A comparison of the storage capacity in Nm^3/m^3 of different gas storage technologies is given in Figure 2-10.

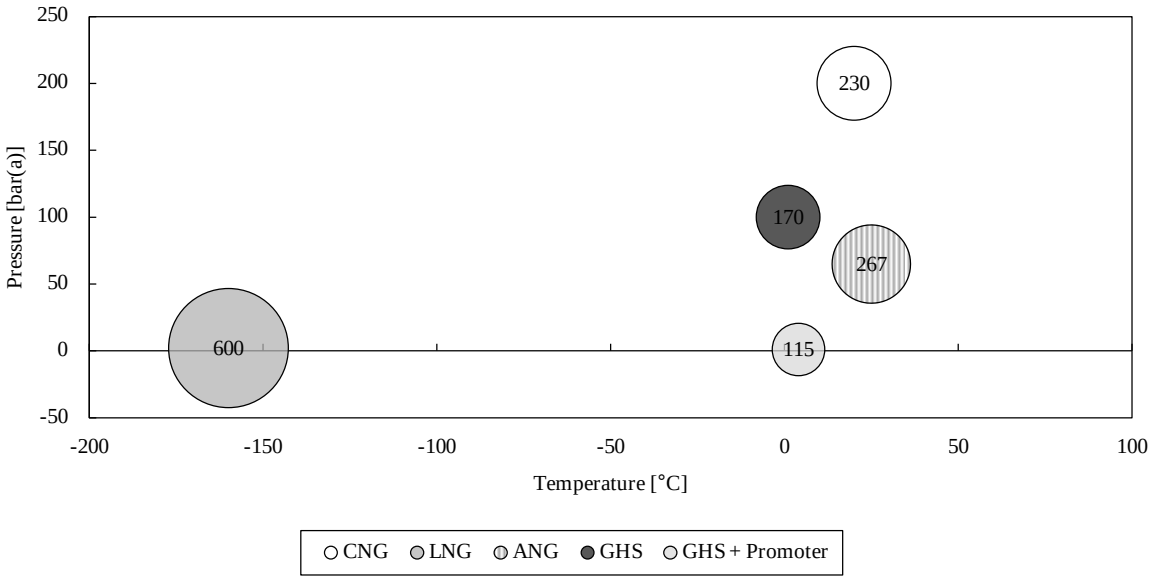

Figure 2-10 Different gas storage technologies and operating conditions, bubble size represents the storage capacity in Nm^3/m^3: CNG – compressed natural gas, LNG – liquefied natural gas, ANG – adsorbed natural gas, GHS - gas hydrate storage adapted from [56]

With regard to safety aspects, solidified natural gas in form of gas hydrates has a lower pressure and is less flammable than the other options. In the 1990s, Gudmundsson suggested several times the possibility to ship hydrated natural gas rather than in liquefied form [57–59]. Therefore, the Mitsui Shipbuilding in cooperation with the Japanese Maritime Research Institute performed field tests with hydrated gas in pellet form [60–62]. According to Veluswamy et al., Japan possesses the largest expertise in the area of gas hydrate storage technology as from 2003 to 2008 gradually three test facility were put into operation. The first plant had a capacity of 0.6 t per day and the last one produced 5 t per day of hydrate pellets [56]. In 2012, the Korea Institute of Industrial Technology followed with a pilot plant producing 1 t per day using an especially designed double helix hydrate reactor [56].

Concerning the costs of storage and transport of natural gas in form of gas hydrate pellets, different reports with varying outcome are available. While Gudmundsson and Borehang, Javanmardi et al. and other researchers estimated a superior performance of solidified natural gas, Najebi et al., Khalilpour and Karimi or Rehder et al. could not confirm these findings [63–68]. However, the studies focused partly on certain world regions with strongly differing framework conditions and considered the formation of sI methane hydrate in conventional stirred tank reactors without any thermodynamic promoters. Recently, Kumar et al. proved the usage of seawater for rapid methane storage in sII hydrates promoted by THF which could improve the economic efficiency of solidified natural gas significantly [69]. An extensive review dealing with the whole topic is given by Veluswamy et al. [56].

3 Simulation of gas hydrate equilibrium

Whether for research or industrial purpose, in the field of gas hydrates it is of high importance to have accurate knowledge about the phase equilibrium in presence of different guest molecules. However, experiments are costly and time consuming and commercially available software is expensive. This chapter describes the development of a Visual Basic© and Microsoft Excel© based software tool to determine hydrate equilibrium with an appropriate accuracy. Thereby, it focuses on the guest molecules used during this work, namely methane, ethane, propane, carbon dioxide and THF.

In the early years of gas hydrate research, methods like the K-value or the gravity chart method were used to predict gas hydrate formation at specific conditions [70,71]. In 1972, Parrish and Prausnitz developed a thermodynamic model to predict the phase equilibrium of single and mixed hydrates based on a combination of the Kihara potential and the van der Waals & Platteeuw model [72]. Afterwards, many, similar thermodynamic models followed, however differing in some aspects. For example, the calculation of the vapor liquid equilibrium can be based on the Henry's law, SRK-EoS, PSRK-EoS or CPA-EoS. Furthermore, a necessary Langmuir constant can be calculated based on an empirical approach or by calculating the Kihara potential [10,73–78]. Newer approaches model the gas hydrate equilibrium via neural networks [79,80]. As thermodynamic modelling of gas hydrate equilibrium is a complex topic, the developed program will be explained in detail here.

3.1 Thermodynamics of vapor-liquid equilibrium

The thermodynamic equilibrium is given if the fugacity f of one component i is equal in all present phases ($\alpha, \beta, \gamma \ldots$). This concept is known as the iso-fugacity criterion [81].

$$f_i^{\alpha} = f_i^{\beta} = f_i^{\gamma} \ldots \qquad \text{Eq. 3-1}$$

Thereby, the relation between fugacity f and pressure P is given by the fugacity coefficient φ. For an ideal gas the fugacity coefficient φ is equal to one [81].

$$\varphi \equiv \frac{f}{P} \qquad \text{Eq. 3-2}$$

To calculate the fugacity coefficient of a pure component by using a pressure-explicit EoS the following equation is used [81].

$$\ln \varphi = \frac{1}{RT}\int_{v}^{\infty}\left(P - \frac{RT}{v}\right)dv - \ln Z + Z - 1 \qquad \text{Eq. 3-3}$$

As the Peng-Robinson-Stryjek-Vera-EoS has the advantage, in comparison to the Peng-Robinson-EoS, that vapor pressure of polar components at low temperatures can be calculated appropriately, it is used in this work. The EoS has initially the known form of the Peng-Robinson-EoS [82].

$$P = \frac{RT}{v - b} - \frac{a(T)}{v(v + b) + b(v - b)} \qquad \text{Eq. 3-4}$$

The intrinsic volume of a real gas is given by the constant b [82].

$$b = 0.077796 * \frac{RT_c}{P_c} \qquad \text{Eq. 3-5}$$

The constant a(T) considers that a real gas cannot have an internal pressure equal to zero due to a change of the internal energy on isothermal expansion. It is described by [82]:

$$a(T) = \alpha_i(T) * 0.457235 * \frac{R^2 T_c^2}{P_c} \qquad \text{Eq. 3-6}$$

Stryjek and Vera modified the $\alpha_i(T)$-term [82].

$$\alpha_i(T) = \left[1 + \kappa_i\left(1 - \sqrt{\frac{T}{T_{c_i}}}\right)\right]^2 \qquad \text{Eq. 3-7}$$

κ_i is a dimensionless constant which consists of a substance characteristic constant κ_{l_i}, obtained from experimental data and a constant κ_{0_i} which depends on the acentric factor ω_i [82].

$$\kappa_i = \kappa_{0_i} + \kappa_{1_i}\left(1 + \sqrt{\frac{T}{T_{c_i}}}\right)\left(0{,}7 - \frac{T}{T_{c_i}}\right)$$
$$\text{with } \kappa_{0_i} = 0{,}378893 + 1{,}4897153\ \omega_i - 0{,}17131848\ \omega_i^2 + 0{,}0196554\ \omega_i^3 \qquad \text{Eq. 3-8}$$

To solve Eq. 3-3 the compressibility factor Z needs to be calculated. Hence, the EoS is transformed into a cubic equation which has the form of Eq. 3-9. An analytical solution can be obtained by using the Cardano's formula [81].

$$Z^3 + (B - 1)Z^2 + (A - 2B - 3B^2)Z - AB + B^2 + B^3 = 0$$
$$\text{with } A = \frac{a(T)P}{(RT)^2} \text{ and } B = \frac{bP}{RT} \qquad \text{Eq. 3-9}$$

Now it is possible to calculate the fugacity coefficient of a pure component and determine the equilibrium conditions in case of the vapor–liquid-equilibrium. However, in case of gas hydrates

at least two components are present, water and a gas hydrate forming guest. Therefore, to describe mixtures, the partial fugacity coefficient is needed. By derivation the following equation is obtained [81].

$$\left(\frac{\partial n \ln \varphi}{\partial n_i}\right)_{T,P,n_j \neq n_i} = \ln \varphi_i = \frac{1}{RT}\int_V^\infty \left[\left(\frac{\partial P}{\partial n_i}\right)_{T,V,n_{j\neq i}} - \frac{RT}{V}\right] dV - \ln Z \qquad \text{Eq. 3-10}$$

Furthermore, mixtures affect the van der Waals parameter a and b. The van der Waals co-volume b of a mixture can be corrected by a simple linear mixing rule [81].

$$b = \sum_i b_i x_i \qquad \text{Eq. 3-11}$$

The classic mixing rules for the attractive parameter a fail because they only represent nonpolar or slightly polar substances, which is why g^E-mixing rules were introduced. Here the first order modified Huron-Vidal mixing rule (MHV1) was used [81].

$$\frac{a}{bRT} = \sum_i x_i \frac{a_i}{b_i RT} + \frac{1}{C}\left(\frac{g^E}{RT} + \sum_i x_i \ln\left(\frac{b}{b_i}\right)\right) \qquad \text{Eq. 3-12}$$

$$\text{with } C = -0.53$$

The excess Gibbs free energy g^E can be obtained by using the non-random-two-liquid approach [83].

$$\frac{g^E}{RT} = \sum_i x_i \left(\frac{\sum_j \tau_{ji} G_{ji} x_j}{\sum_j G_{ji} x_j}\right) \qquad \text{Eq. 3-13}$$

$$\text{with } \tau_{ji} = \frac{(g_{ji} - g_{ii})}{RT} \text{ and } G_{ji} = \exp(-\alpha_{ji}\tau_{ji})$$

$(g_{ji} - g_{ii})$ describes the interaction between two different components and α_{ji} is a non-randomness parameter. The interaction $(g_{ji} - g_{ii})$ is fitted to experimental data and temperature dependency is taken into account by [83]:

$$(g_{ji} - g_{ii}) = g'_{ij} + g''_{ij} T + \frac{g'''_{ij}}{T} \qquad \text{Eq. 3-14}$$

g'_{ij}, g''_{ij} and g'''_{ij} are the fit parameters [83]. However, this approach is pressure independent. Therefore, because gas hydrates form within extreme conditions (high pressures), a pressure dependent fourth term with another fit parameter g''''_{ij} was added in this work.

$$(g_{ji} - g_{ii}) = g'_{ij} + g''_{ij} T + \frac{g'''_{ij}}{T} + g''''_{ij} P \qquad \text{Eq. 3-15}$$

Considering

$$g^E = \sum_i \left(x_i g_i^E\right) = RT \sum_i \left(x_i \ln(\gamma_i)\right) \quad \text{Eq. 3-16}$$

Eq. 3-13 can also be written as [83]:

$$\ln \gamma_i = \frac{\sum_j \tau_{ji} G_{ji} x_j}{\sum_k G_{ki} x_k} + \sum_j \frac{x_j G_{ij}}{\sum_k G_{kj} x_k} \left(\tau_{ij} - \frac{\sum_n \tau_{nj} G_{nj} x_n}{\sum_k G_{kj} x_k} \right) \quad \text{Eq. 3-17}$$

Now Eq. 3-10 can be complemented with the MHV1 and the fugacity coefficient of one component in a mixture can be described as [84]:

$$\ln(\varphi_i) = \frac{b_i}{b}(Z-1) - \ln(Z-B) - \frac{1}{2\sqrt{2}} \left[\frac{a_i}{b_i RT} + \frac{\ln(\gamma_i)}{C} + \frac{1}{C} \ln\left(\frac{b}{b_i}\right) + \frac{1}{C}\left(\frac{b_i}{b} - 1\right) \right] \ln\left(\frac{Z + \left(1+\sqrt{2}\right)B}{Z + \left(1-\sqrt{2}\right)B} \right) \quad \text{Eq. 3-18}$$

3.2 Thermodynamics of gas hydrate equilibrium

The starting point of the gas hydrate equilibrium state is also the iso-fugacity criterion. The fugacity of water in the liquid f_W^L and the hydrate phase f_W^H has to be equal [85].

$$f_W^H = f_W^L \quad \text{Eq. 3-19}$$

To determine the fugacity in the hydrate phase, a hypothetical transition of an empty hydrate (β) into an occupied hydrate (H) is assumed which can be described by the following equation [85].

$$f_W^H = f_W^\beta \exp\left(\frac{-\Delta\mu_W^H}{RT}\right) \quad \text{Eq. 3-20}$$

This equation contains two unknown factors, the chemical potential difference $\Delta\mu_W^H$ and the fugacity of an empty hydrate shell f_W^β. According to the van-der-Waals-Plateeuw approach, the chemical potential difference can be described as [85]:

$$\Delta\mu_W^H(T,P) = \mu_W^\beta - \mu_W^H = -RT \sum_m \nu_m \ln\left(1 - \sum_l \Theta_{ml}\right) \quad \text{Eq. 3-21}$$

Here ν_m is the amount of cages of type m per unit cell in the corresponding structure. Θ_{ml}, the occupancy of a type m cage with the guest component l, is represented by a Langmuir absorption approach [85].

$$\Theta_{ml}(T,P) = \frac{C_{ml}(T)\, f_l(T,P)}{1 + \sum_l C_{ml}(T)\, f_l(T,P)} \quad \text{Eq. 3-22}$$

f_l is the fugacity of the component l and C_{ml} a Langmuir absorption constant which describes the tendency of this component l to occupy the hydrate cage m. The Langmuir absorption constant C_{ml} results from the stabilizing interactions between the guest and the water molecules. Therefore, the Lennard Jones-Devonshire-cell-theory can be used which leads to the following equation [85]:

$$C_{ml}(T) = \frac{4\pi}{kT}\int_0^{R-a} \exp\left(\frac{-\omega(r)}{kT}\right) r^2\, dr \quad \text{Eq. 3-23}$$

Here, R is the free cavity radius, r the distance between the guest and a cage center, a the radius of a spherical core and k the Boltzmann constant. $\omega(r)$ represents the cell potential as a function of the distance of the guest from cavity center. This, can be expressed through the Kihara potential [85]:

$$\omega(r) = 2z\epsilon\left[\frac{\sigma^{12}}{R^{11}r}\left(\delta^{10} + \frac{a}{R}\delta^{11}\right) - \frac{\sigma^6}{R^5 r}\left(\delta^4 + \frac{a}{R}\delta^5\right)\right] \quad \text{Eq. 3-24}$$

z is a cage type specific coordination number, ϵ an energy parameter and σ the distance between the cores at 0 potential energy. With N taking values of 10, 11, 4 and 5, δ is given by [85]:

$$\delta^N = \frac{1}{N}\left[\left(1 - \frac{r}{R} - \frac{a}{R}\right)^{-N} - \left(1 + \frac{r}{R} - \frac{a}{R}\right)^{-N}\right] \quad \text{Eq. 3-25}$$

There are approaches where the parameters ϵ, σ and a are fitted to experimental data and the Kihara potential and Langmuir constants are calculated during each iteration. Due to the time-consuming and complex simulations resulting from this method, it was decided to use the approximation suggested by Parrish and Prausnitz [72].

$$C_{ml} = \frac{A_{ml}}{T}\exp\left(\frac{B_{ml}}{T}\right) \quad \text{Eq. 3-26}$$

A_{ml} and B_{ml} depend on the component, structure and cage type. To calculate the chemical potential difference $\Delta\mu_W^H$, the fugacity of the hypothetical empty hydrate shell f_W^β must be determined. Therefore, the equation Eq. 3-27 is used [85]:

$$f_W^\beta = P_W^{sat,\beta}\, \varphi_W^{sat,\beta} \exp\left(\frac{V_W^\beta\left(P - P_W^{sat,\beta}\right)}{RT}\right) \quad \text{Eq. 3-27}$$

$P_W^{sat,\beta}$ and $\varphi_W^{sat,\beta}$ represent the saturation pressure and fugacity coefficient of the empty hydrate shell, respectively. As the vapor pressure in the empty hydrate shell is very low, the fugacity coefficient $\varphi_W^{sat,\beta}$ is equal to one. According to Klauda and Sandler, the volume of the empty hydrate shell is given by empirical correlations for structure sI and sII [85]:

$$V_W^{\beta,I} = (11{,}835 + 2{,}217 \cdot 10^{-5} \cdot T + 2{,}242 \cdot 10^{-6} \cdot T^2)^3 \frac{10^{-30} N_A}{N_W^{\beta}} - 8{,}006 \cdot 10^{-9} \cdot P + 5{,}448 \cdot 10^{-12} \cdot P^2 \quad \text{Eq. 3-28}$$

$$V_W^{\beta,II} = (17{,}13 + 2{,}429 \cdot 10^{-4} \cdot T + 2{,}013 \cdot 10^{-6} \cdot T^2 + 1{,}009 \cdot 10^{-9} \cdot T^3)^3 \frac{10^{-30} N_A}{N_W^{\beta}} - 8{,}006 \cdot 10^{-9} \cdot P + 5{,}448 \cdot 10^{-12} \cdot P^2 \quad \text{Eq. 3-29}$$

N_A is the Avogadro's number and N_W^{β} the amount of water molecules in the unit cell. The saturation pressure $P_W^{sat,\beta}$ is described by an approach suggested by Růržička and Majer where the parameters A^{β}, B^{β}, C^{β} and D^{β} are fitted to experimental data [86]:

$$P_W^{sat,\beta} = A^{\beta} \ln(T) + \frac{B^{\beta}}{T} + C^{\beta} + D^{\beta} T \quad \text{Eq. 3-30}$$

In addition, in mixed hydrates, these parameters are corrected by using a simple mixing rule.

$$X_{mix}^{\beta} = \sum_l z_l X_l^{\beta} \text{ with } X_l^{\beta} \equiv \left(A^{\beta}, B^{\beta}, C^{\beta} \text{ or } D^{\beta}\right) \quad \text{Eq. 3-31}$$

z_l is equal to the fraction of the component l in the occupied hydrate and can be calculated with:

$$z_l = \frac{\sum_m \upsilon_m \Theta_{ml}}{\sum_l \sum_m \upsilon_m \Theta_{ml}} \quad \text{Eq. 3-32}$$

3.3 Algorithm

The implemented algorithm is shown in Figure 3-1.

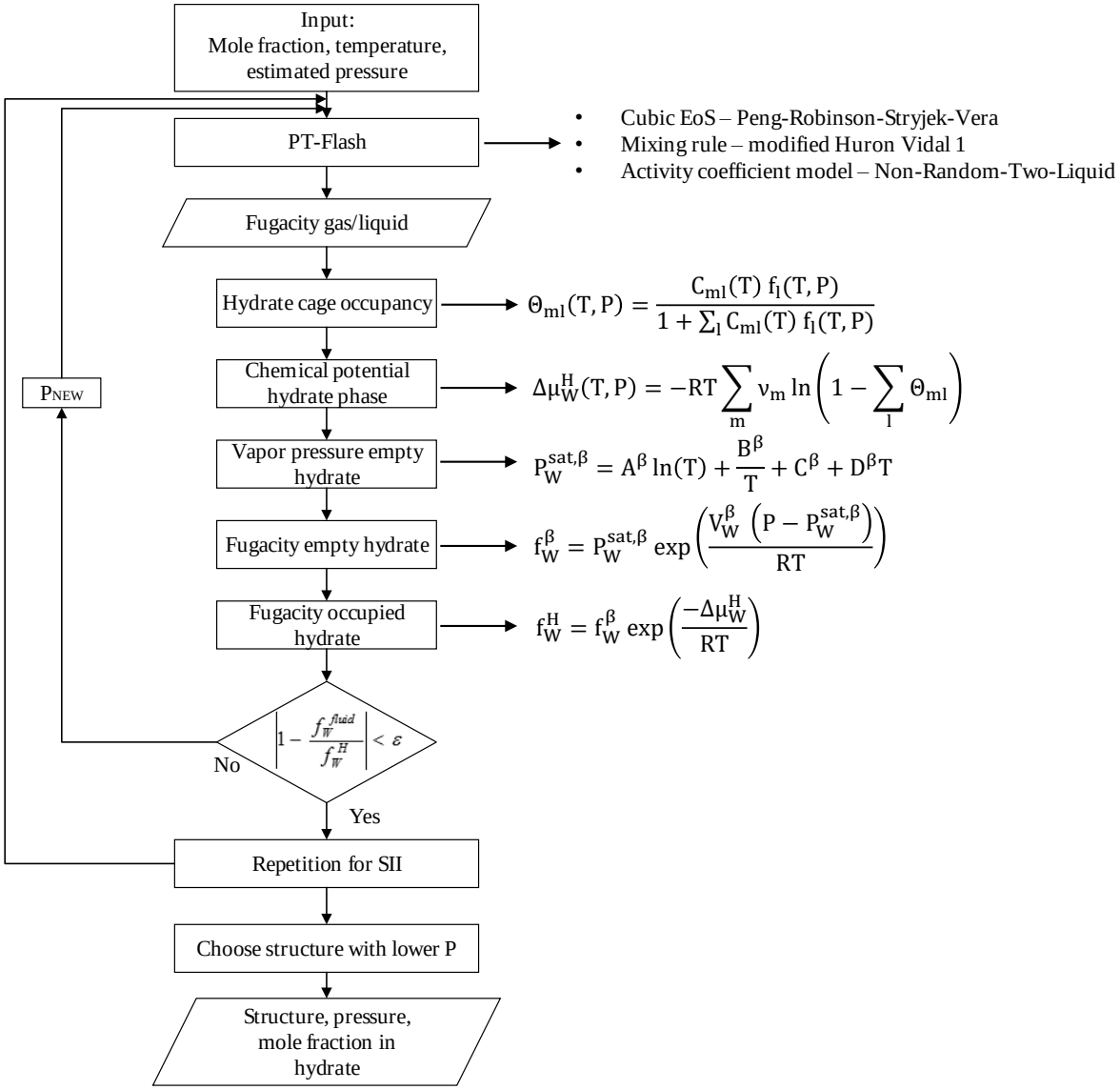

Figure 3-1 Implemented algorithm to simulate gas hydrate equilibrium

The algorithm works as follows:

1. The user enters the amount of substance for each guest component, the equilibrium temperature and an estimated pressure.
2. A PT-Flash is performed to calculate the fugacity of each component in the vapor and liquid phase. This step is trivial and will not be explained in detail here. A detailed guide is available in Feuerriegel for example [87]. As it was explained in chapter 3.1 the Peng-Robinson-Stryjek-Vera-EoS, the first order modified Huron-Vidal mixing rule and the non-random-two-liquid activity coefficient model were used. Necessary parameters can be found in the appendix 14.4.

3. The hydrate cage occupancy (Eq. 3-22) is calculated using the fugacity in the liquid for each component and the empirical approach from Parrish and Prausnitz (Eq. 3-26) with constants from Munck et al. [72,88]. In case of THF, new constants were obtained by solving equations Eq. 3-23, Eq. 3-24 and Eq. 3-25 numerically. Hereby, the free radius *R* was taken from Strobel et al. and Kihara parameters from Kang et al. [89,90]. Afterwards, the parameters were obtained by fitting Eq. 3-26 to the Langmuir constants in dependency of the temperature. Used A_{ml} and B_{ml} parameters are listed in the appendix 14.4.
4. The chemical potential difference is calculated using Eq. 3-21.
5. The next step serves to compute the vapor pressure of a hypothetical empty hydrate shell by using Eq. 3-30, Eq. 3-31 and Eq. 3-32. Fitted parameters can be found in the appendix 14.4.
6. The fugacity of the hypothetical empty hydrate shell is obtained from Eq. 3-27 and, depending on the hydrate structure, Eq. 3-28 or Eq. 3-29.
7. The fugacity of the occupied hydrate is determined (Eq. 3-20).
8. If the difference between the fugacity of water in the liquid and in the hydrate phase is low enough to meet the criterion $\varepsilon < 10^{-4}$, the algorithm repeats the calculations for a structure SII hydrate. Otherwise a new pressure is predicted using the Newton-Raphson-method and the algorithm follows a loop until the criterion is met [91].
9. After determining both equilibrium pressures, for structure sI and sII, the lower pressure corresponds to the thermodynamically favored structure and the user obtains the structure, equilibrium pressure and composition of the hydrate phase.

By making appropriate changes in the algorithm, the developed program is also able to calculate equilibrium temperatures originating from a given pressure and construct equilibrium trends for set conditions which means pressure and temperature are set by the user.

3.4 Results and discussion

To investigate the performance of the developed simulation program, exemplary simulation results are compared to experimental results with the help of the percent absolute average pressure deviation (% AAD). The % AAD is defined as [85]:

$$\%\ \mathrm{AAD} = \frac{100}{n}\sum_{i=1}^{n}\frac{\left|p_i^{exp} - p_i^{sim}\right|}{p_i^{exp}} \qquad \text{Eq. 3-33}$$

Figure 3-2 shows PT-trends obtained from the simulations in comparison to experimental data [92].

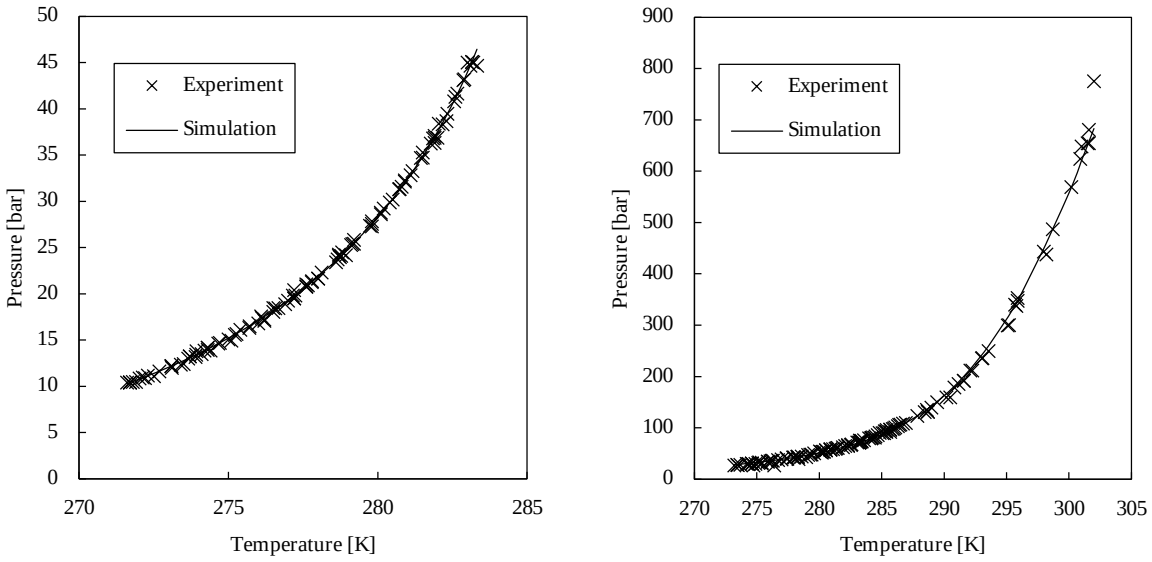

Figure 3-2 PT-trends obtained from simulations compared with experimental data [92] (Left: CO_2, Right: CH_4)

It is shown, that both curves, for pure carbon dioxide and methane hydrate, represent the experimental data, visually extremely well. This result is approved by comparing the % AAD to previous works which was done in Figure 3-3.

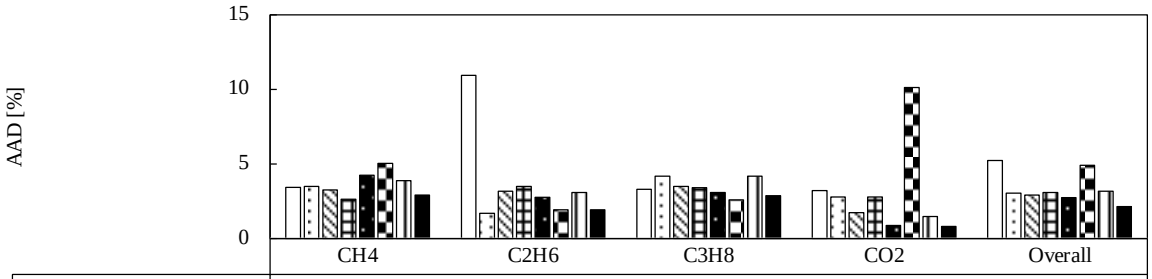

	CH4	C2H6	C3H8	CO2	Overall
Sloan	3.44	10.94	3.32	3.22	5.23
Martìn & Peters	3.50	1.70	4.20	2.80	3.05
Klauda & Sandler	3.26	3.19	3.50	1.75	2.93
Bandyopadhyay & Klauda	2.65	3.51	3.41	2.79	3.09
Zhang et al.	4.25	2.77	3.09	0.89	2.75
Hsieh et al.	5.04	1.93	2.61	10.12	4.93
Dehaghani & Karami	3.90	3.10	4.20	1.50	3.18
This work	2.93	1.95	2.89	0.82	2.15

Figure 3-3 % AAD of the simulation results of pure gas hydrates in comparison to other works [75,76,84,85,93–95]

The wide range of references cover the period from 1998 to 2018 and therefore allow a realistic assessment of the simulation results. It is visible that the model, used in this work, is most suitable to represent the PT-equilibrium of carbon dioxide hydrates. The other components are simulated with an appropriate accuracy and overall the best performance was achieved with the here presented model. In sum an average % AAD of 2.15 was achieved.

Figure 3-4 shows likewise that the predicted PT-trend of mixed methane-propane hydrates represents the experimental data qualitatively well.

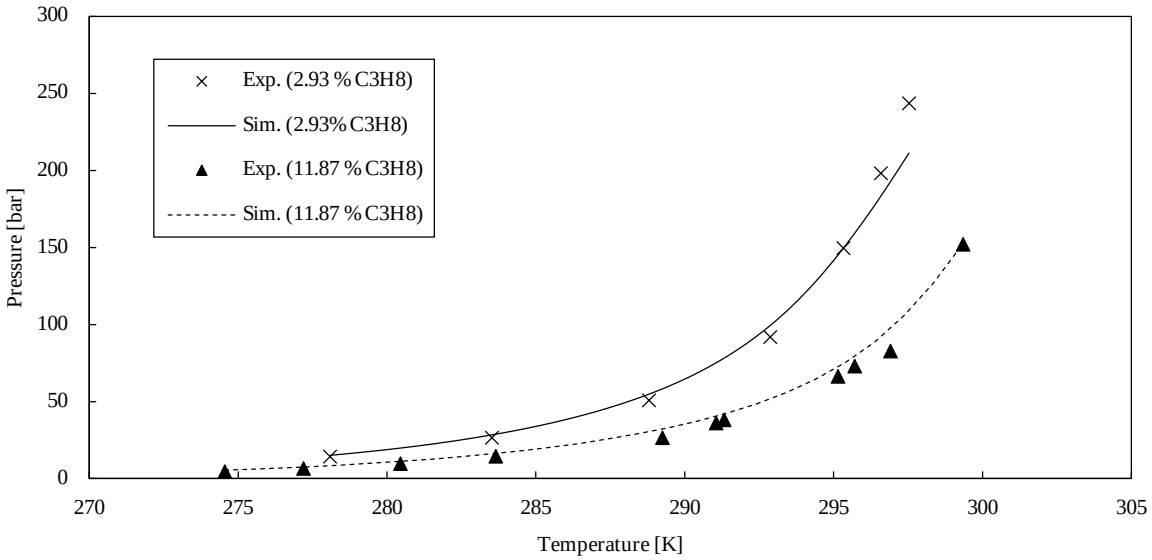

Figure 3-4 PT-trends obtained from simulations compared with experimental data for mixed hydrates from methane and propane [155]

The % AAD for different mixed hydrates in comparison to previous works are presented in Figure 3-5.

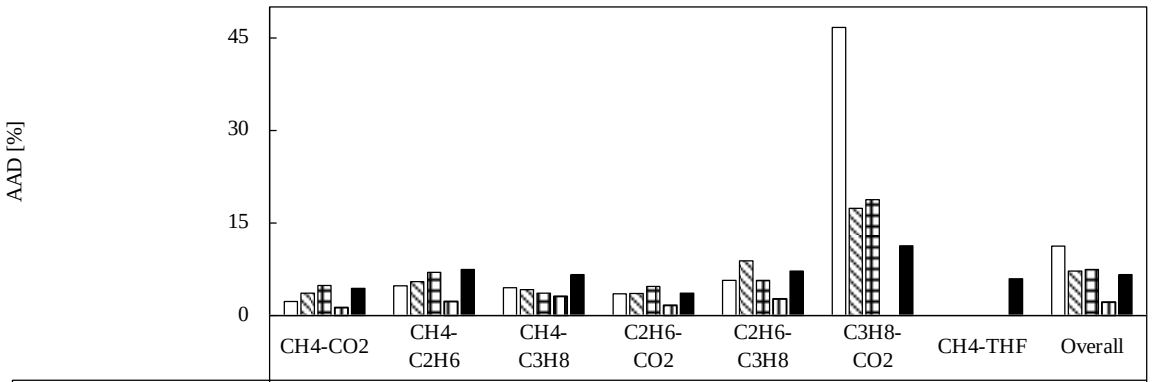

	CH4-CO2	CH4-C2H6	CH4-C3H8	C2H6-CO2	C2H6-C3H8	C3H8-CO2	CH4-THF	Overall
Sloan	2.29	4.86	4.55	3.56	5.72	46.70		11.28
Klauda & Sandler	3.66	5.50	4.23	3.60	8.86	17.40		7.21
Bandyopadhyay & Klauda	4.91	7.03	3.62	4.74	5.74	18.80		7.47
Dehaghani & Karami	1.32	2.30	3.11	1.66	2.70			2.22
This work	4.41	7.50	6.67	3.62	7.21	11.32	5.99	6.67

Figure 3-5 % AAD of the simulation of mixed hydrates results in comparison to other works [75,84,85,93]

The model developed by Dehaghani and Karami is overall the best to describe the PT-equilibrium of mixed hydrates. The difference to the here developed algorithm is that it uses the UNIQUAC activity coefficient model and additionally not uses the Parrish and Prausnitz approximation (Eq. 3-26) or the roundabout approach with a hypothetical empty hydrate shell. Instead, equality of the chemical potential difference in the hydrate and the liquid phase is set as the criterion for the phase equilibrium [84]. Obviously, this leads to better results in case of mixed hydrates but not of pure hydrates. This shows that the two used approximation equations (Eq. 3-26 and Eq. 3-30) represent a source of error which should be changed or improved in future works. However, the

tool designed in this work, showed the second-best performance in comparison to former studies. In addition, it can describe mixed hydrates with THF with an accuracy of 5.99 % AAD. In comparison to Strobel et al., who achieved an accuracy of 2.9 % AAD with regard to THF + methane hydrates, it is still worse, but the here named reference focused especially on mixed hydrates from THF which was not the aim of the model illustrated here [89].

4 Experimental setups

The following chapter deals with the used experimental setups in detail. Besides of a brief description and schematic figures, the accuracy of measurement is declared. Some experiments needed special changes in the setup and are explained in the section for the experimental series itself.

4.1 Parr high pressure autoclave system

High pressure experiments were performed in a stirred autoclave type “4568”, manufactured by Parr Instruments. The reactor has two observation windows and can be filled with anything after detachment from its tongue-and-groove flange. Its operating window ranges between 0 to 200 bar(g) and -10 to +150 °C. The reactor can be tempered by using a thermostat type “Presto A40” manufactured by Julabo, which can directly control the reactor temperature via a Juchheim Pt100-temperature sensor. The cooling performance is 0.9 kW, the heating performance 2.7 kW. The pressure was measured with a “4848B Rosemount” sensor and controlled by using a control valve. Additionally, the system is equipped with a torque measurement delivered by Parr Instruments and the flow into the reactor can be measured by using a “mini cori-flow” coriolis mass flow system manufactured by Bronkhorst. To compress gas, a two-stage compressor station can be used consisting of a compressor type “DLE 2-5-2-GG” and “DLE 30-GG-H2” manufactured by Maximator. For stirring a self-priming paddle shaped gas entry stirrer and a pitched blade stirrer were available. Whereas the paddle stirrer can only stir the liquid phase, the pitched blade stirrer can freely be positioned along the stirrer shaft. Data logging was done with a PC and either with the software “Labview” or “Specview”. The accuracy of the measurements can be obtained from Table 4-1 and a P&ID is shown in Figure 4-1.

Table 4-1 Accuracy of measurements for the high pressure Parr reactor 4568

Parameter	Device	Accuracy
Mass flow $\dot{m}$ [g/h]	Bronkhorst mini cori-flow	$\leq$ 1.12 % of measured value g/h
Mass m [g]	Sartorius LE1003s	$\pm$ 0.001 g
Pressure p [bar(g)]	Emerson Rosemount 2088	0.1 % of calibrated value ($\pm$ 0.18 bar)
Temperature T [°C]	Juchheim PT100	$\pm$ 0.1 + 0.0017 * ϑ K
Torque M [Ncm]	Parr DR-2500	$\pm$ 0.1 Ncm

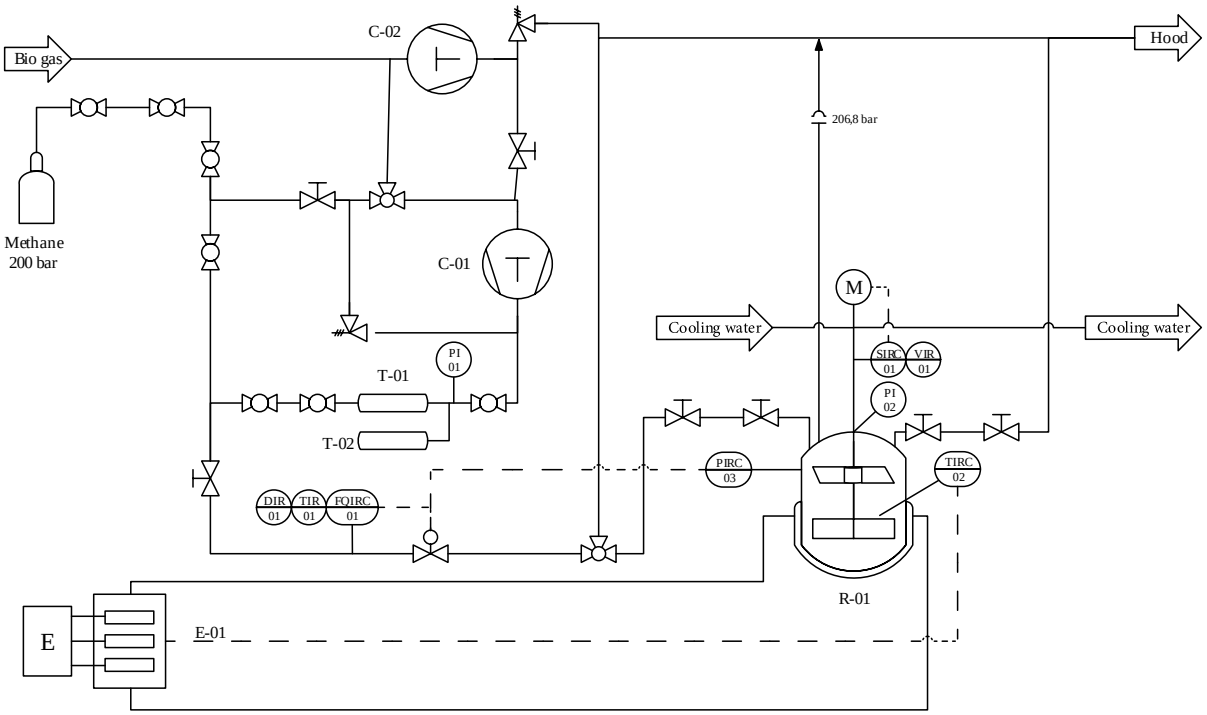

Short sign	C-01	C-02	E-01	R-01	T-01	T-02
Name	Compressor	Compressor	Thermostat	Autoclave	Vessel	Vessel
Technical data			2.7 kW	0.6 L	0.5 L	0.5 L
Permitted pressure [bar(g)]			1.7	200	200	200
Permitted temperature [°C]	100	100	250	150	150	150
Material				T316	316L	316L

Figure 4-1 P&ID for the high pressure Parr reactor 4568 system

4.2 Büchi low pressure system

The Büchi reactor system consists of a 0.5 L glass reactor manufactured by Büchi AG type ”ecoclave 1”. It is equipped with a controllable Heidolph stirrer motor type “RZR2102”, a “mini cori-flow” coriolis mass flow system manufactured by Bronkhorst and a thermostat “Presto A40” by Julabo. The stirrer setup consists of a self-priming paddle shaped gas entry stirrer in the liquid phase and a pitched blade stirrer in the gas phase. Temperature and pressure were measured and controlled by a process control system “deltaV” delivered by Emerson. In addition, the system is connected to a 0.7 L Amar reactor which was used as deposit for gases and their mixtures. The accuracy of the measurements can be obtained from Table 4-2. A process and instrument diagram can be obtained from Figure 4-2.

Table 4-2 Accuracy of measurements for the low pressure Büchi reactor system

Parameter	Device	Accuracy
Mass flow $\dot{m}$ [g/h]	Bronkhorst mini cori-flow	$\leq$ 1.12 % of measured value g/h
Mass m [g]	Sartorius LE1003s	$\pm$ 0.001 g
Pressure p [bar(g)]	Siemens SITRANS P200	0.25 % characteristic curve ($\pm$ 0.04 bar)
Temperature T [°C]	Julabo PT100	$\pm 0.15 + 0.002 * \vartheta$ K

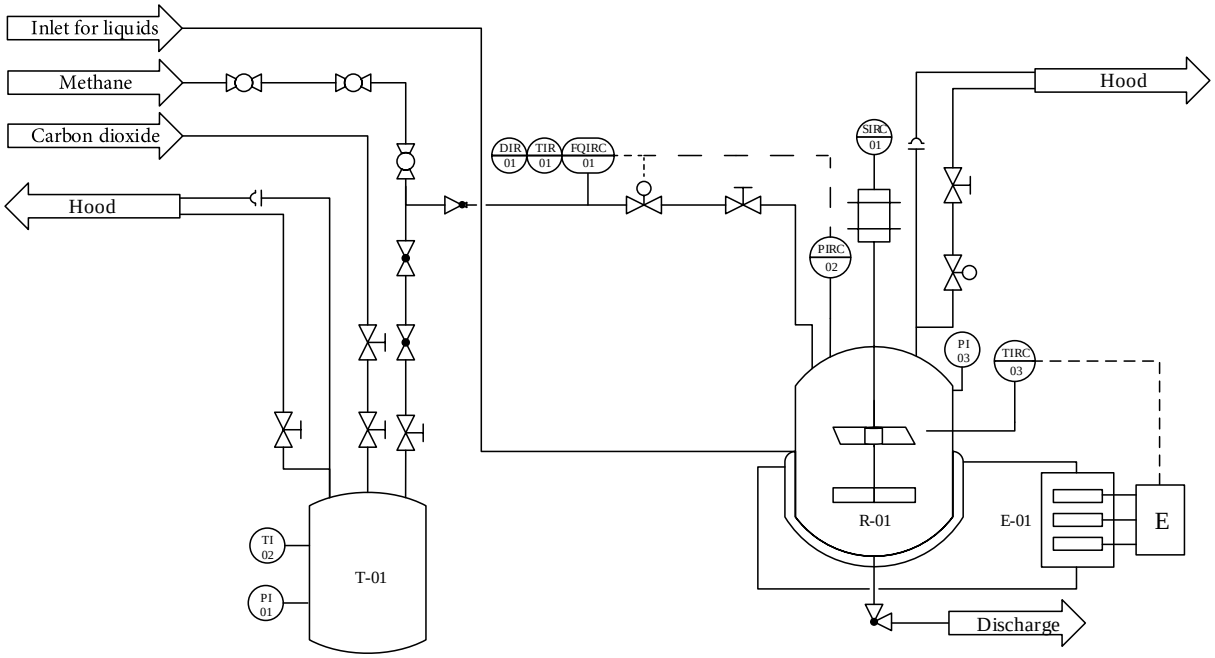

Short sign	E-01	R-01	T-01
Name	Thermostat	Autoclave	Deposit
Technical data	2.7 kW	0.5 L	0.7 L
Permitted pressure [bar(g)]	1.7	12	100
Permitted temperature [°C]	250	150	250
Material	316L	Glass	316L

Figure 4-2 P&ID for the low pressure Büchi reactor system

5 Promoter screenings

Due to the slow kinetics of hydrate formation and to enable gas hydrate applications, it is necessary to find a promoter which enhances the kinetics of hydrate formation. This chapter describes all performed experiments with regard to this topic. Different surfactants, crown and acyclic ethers, amino acids, aprotic solvents and fatty acids with varying concentrations were tested regarding their promoting or inhibiting effects on methane hydrate formation. Experiments were performed in stirred autoclaves either at high pressure in the Parr reactor system or low pressure in the Büchi reactor system in presence of THF as thermodynamic promoter.

5.1 Influences of surfactants

Surfactants have been focused several times as kinetic promoters. An exemplary overview is given in the work of Kumar et al. [28]. Due to a reduced surface tension, the gas transport into the liquid phase is enhanced and further the gas hydrate formation. At the same time, the promoting effect differs from surfactant to surfactant and from gas to gas compound.

5.1.1 SDS, HDA and lecithin

The following experimental series investigates the performance of sodium dodecyl sulfate (SDS) and hexadecylamine (HDA) in comparison to lecithin as a renewable and biodegradable raw material on the mixed hydrate formation of THF and methane.
Sodium dodecyl sulfate is an anionic surfactant consisting of a sulfate group and a C_{12}-chain. (See Figure 5-1)

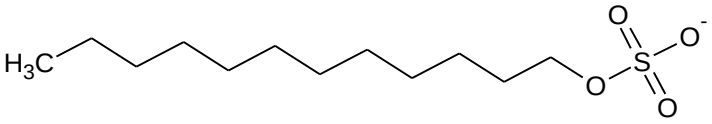

Figure 5-1 Structure of the dodecylsulfate anion

Hexadecylamine is a nonionic surfactant consisting of an amine-group and a C_{16}-chain. (See Figure 5-2)

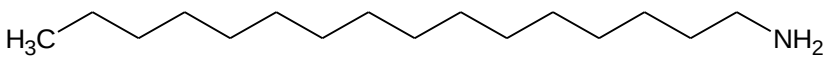

Figure 5-2 Structure of hexadecylamine

Lecithins are mixtures of glycerophospholipids including phosphatidylcholine, phosphatidylethanolamine, phosphatidylinositol and phosphatidic acid. The used lecithin is based on soybeans and therefore consists of at least 30 % of phosphatidylcholine. The structure is given in Figure 5-3.

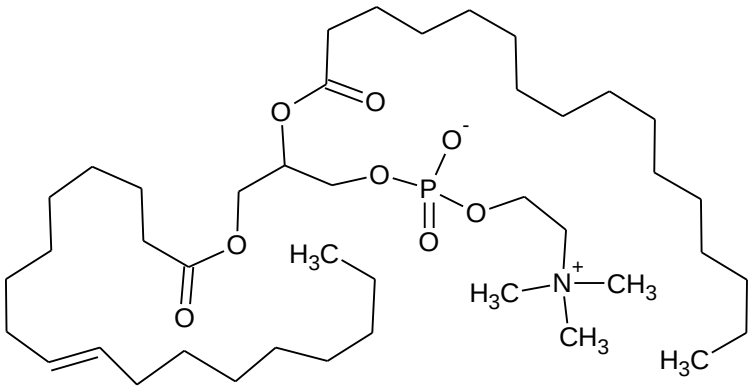

Figure 5-3 Structure of phosphatidylcholine

In this experimental series the induction, growth and formation time of methane-THF hydrates were determined in presence of each substance in concentrations of 0.5, 1.0 and 3.0 wt%. In addition, the system without promoter was measured as a reference.

Experimental procedure

The experimental series was performed in the Büchi reactor system (see chapter 4.2). Millipore water was degassed 15 min under vacuum, 250 mL of the hydrate forming mixture (5.56 mol% THF + water + surfactant) were weighed out and filled into the reactor which was closed afterwards. The stirrer was turned on and operated at a rotation frequency of 300 rpm. The reactor was cooled down to a temperature of 2.5 °C ± 0.5 °C. Before the measurement started, the reactor was purged 3 times to a pressure of 4 bar(g) and drained to a pressure of 0.5 bar(g), filled with methane to an operating pressure of 8 bar(g) and the gas counter was reset. The measurement started and it was waited until gas hydrates formation occurred. Due to the gas hydrate formation, a heat agglomeration inside the reactor occurred. The time at the start of the gas hydrate formation and at the highest reached temperature were recorded. Hence, the temperature trends were used to evaluate the induction and growth time. In addition, the final gas uptake was calculated by dividing the gas counter values by the molar mass of methane and the molar amount of the used water. The tests ended ten minutes after the temperature maximum was reached. Five repetitive measurements were performed to investigate promoting effects. An exemplary experimental trend is given in Figure 5-4.

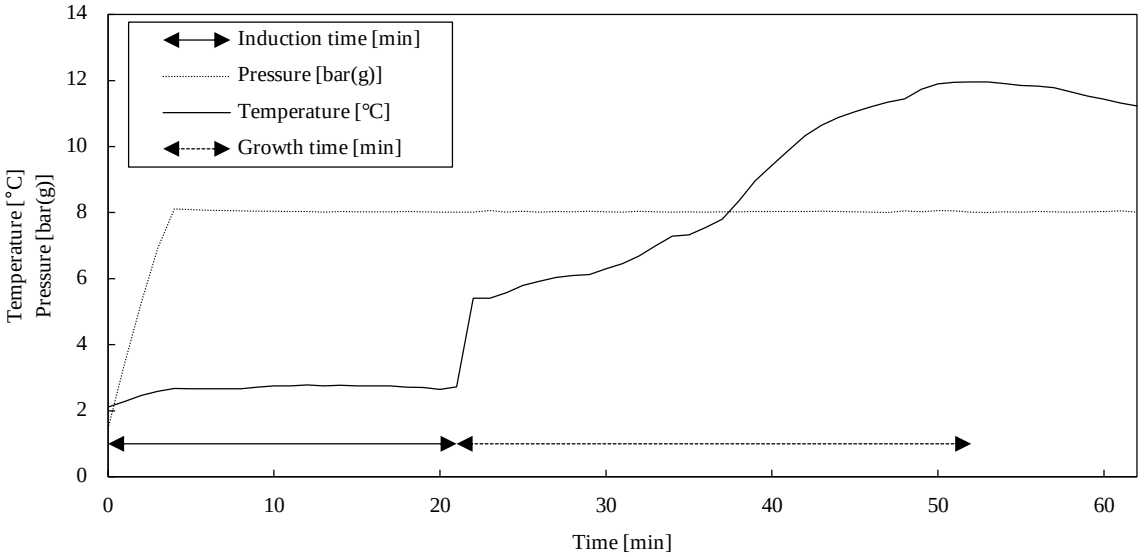

Figure 5-4 Representative experimental trend for the experimental series of chapter 5.1.1

Results and discussion

The results of the experimental series are shown in Figure 5-5. Therein, the hydrate induction and growth time for methane-THF hydrate in presence and absence of SDS, HDA and Lecithin in concentrations of 0.5, 1.0 and 3.0 wt% is plotted.

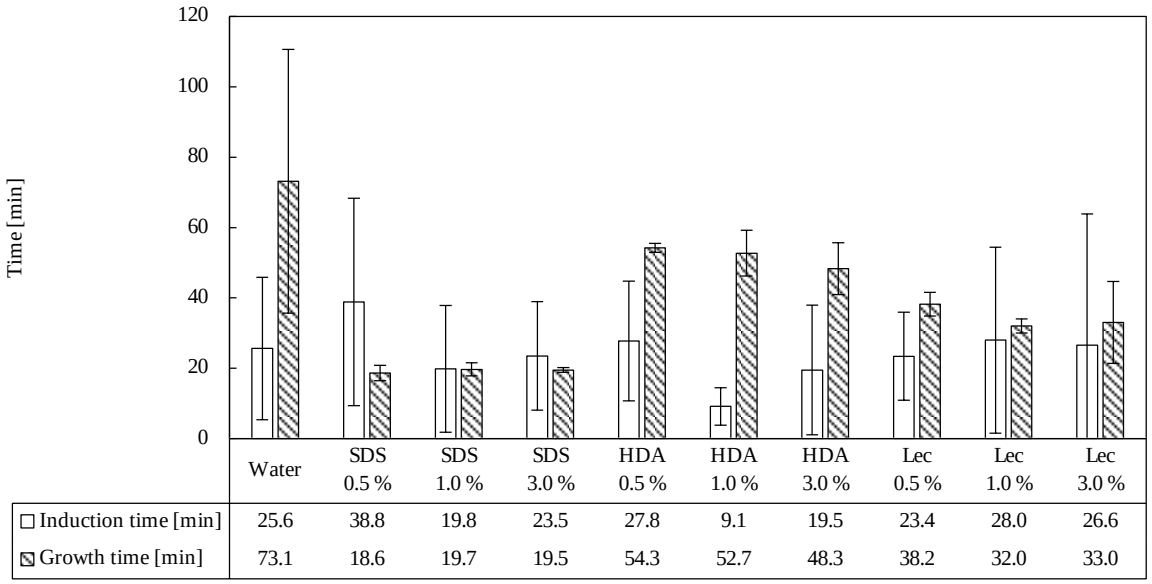

	Water	SDS 0.5 %	SDS 1.0 %	SDS 3.0 %	HDA 0.5 %	HDA 1.0 %	HDA 3.0 %	Lec 0.5 %	Lec 1.0 %	Lec 3.0 %
Induction time [min]	25.6	38.8	19.8	23.5	27.8	9.1	19.5	23.4	28.0	26.6
Growth time [min]	73.1	18.6	19.7	19.5	54.3	52.7	48.3	38.2	32.0	33.0

Figure 5-5 Average induction time [min] and growth time [min] with standard deviation of five measurements for methane-THF hydrate formation in presence of SDS, HDA and lecithin in different concentrations [wt%]

Starting with the induction time, it is conceivable that the standard deviation is continuously wide-spread proving again that nucleation is stochastic. All values are in the same range in comparison to the pure water tests. SDS 0.5 wt% shows the longest and HDA 1.0 wt% the shortest induction time. By comparing the growth times, it is visible that all substances act as promoters,

accelerating the hydrate growth. A ranking in view of the suitability can be compiled in the following order: SDS > lecithin > HDA.

Figure 5-6 shows the average final gas uptake of the here conducted experiments.

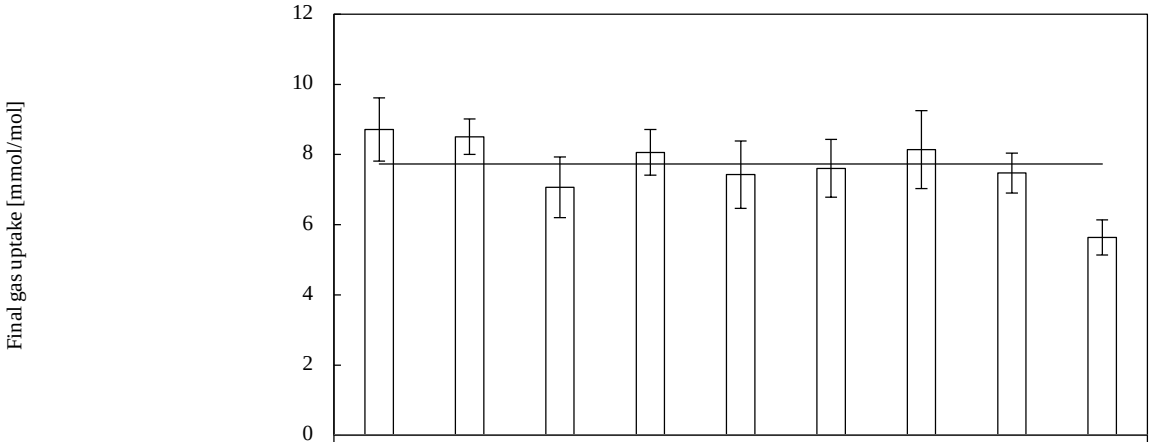

	SDS 0.5 %	SDS 1.0 %	SDS 3.0 %	HDA 0.5 %	HDA 1.0 %	HDA 3.0 %	Lec 0.5 %	Lec 1.0 %	Lec 3.0 %
Final gas uptake [mmol/mol]	8.72	8.51	7.07	8.06	7.43	7.61	8.14	7.47	5.64
Water [mmol/mol]	7.73	7.73	7.73	7.73	7.73	7.73	7.73	7.73	7.73

Figure 5-6 Average final gas uptake [mmol/mol] with standard deviation of five measurements for methane-THF hydrate formation in presence of SDS, HDA and lecithin in different concentrations [wt%]

It is shown, that all substances reached similar final gas uptakes expect SDS in all concentrations and lecithin with 3.0 wt%. Both low SDS concentrations raised the final gas uptake whereas SDS and lecithin with 3.0 wt% had an inhibiting effect. This is consistent with the work of Kang et al. who observed an inhibiting effect with an excess amount of SDS [96]. Due to the outstanding growth times and final gas uptakes, SDS shows the best promoting effects in a concentration of 1.0 wt%. That SDS is especially a good promoter for methane hydrate formation, has been investigated by several works before and was proven here again [28]. For example Morajevi et al. showed that SDS in concentration of 500 ppm had the best promoting effect and in addition they found a minimum for the induction time approximately at 450 ppm which is the critical micelle concentration [97]. This correlation is interesting because Di Profio et al. discovered that at hydrate formation conditions no micelles are formed [98]. This was confirmed by Alberti et al. with the help of MD simulations [99]. All substances were used in concentrations above the CMC and the best promoting effects were achieved in a concentration of 0.5 wt%.

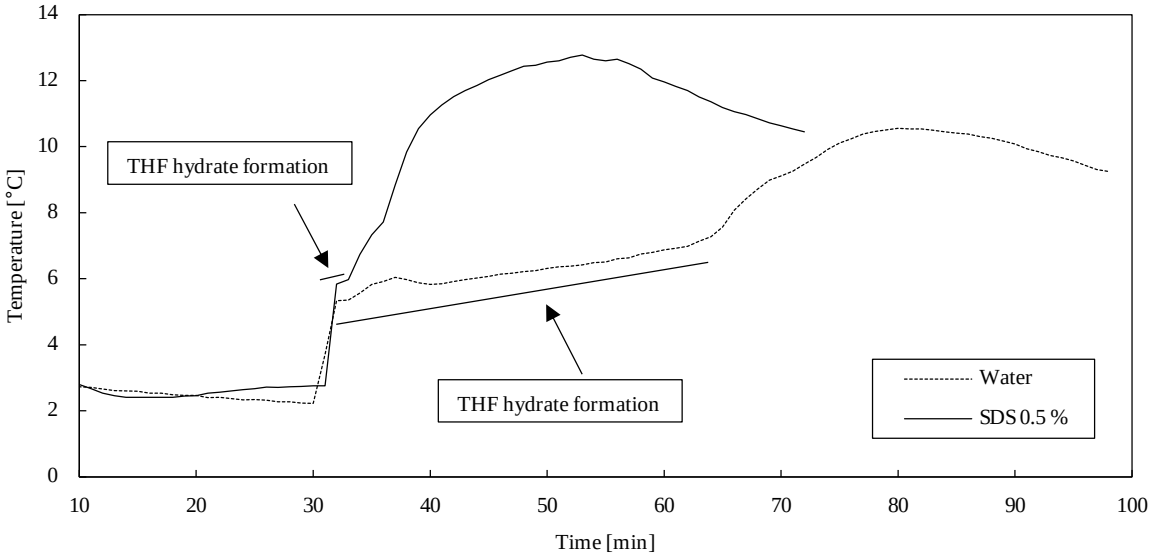

Figure 5-7 Comparison of temperature trends [°C] for a representative water and SDS 0.5 % test

Figure 5-7 exemplary shows a comparison between a representative water and SDS 0.5 % test to point out the effect of a two stage hydrate formation process. During the experiments it was observed, that THF hydrates form, followed by the filling of small hydrate cages with methane, indicated by a second significant raise in the temperature. The time between both events is clearly reduced by the promoters leading to smaller growth times.

This experimental series has shown once more, that surfactants promote the induction and the growth time due to their lowering effect on the surface tension. The outstanding outcome of this work is that even with lecithin, a renewable and biodegradable raw material, a respectable promoting effect can be achieved. Therefore, with regard to environmentally friendly process requirements, renewable surfactants appear as a good alternative for promoting hydrate formation although further substances should be tested to achieve nearly the same or even a better kinetically promotion than SDS.

5.1.2 SDS, Tween80, Triton X-100 and PFOA

This chapter follows thematically chapter 5.1 and investigates again the influences of different surfactants on the hydrate formation. Since surfactants decrease the surface tension and enhance the transport of gas molecules into the liquid phase, it should be possible to increase the promoting effect - compared to SDS - even more by using fluorosurfactants. Furthermore, García-Aguilar et al. showed that nonionic surfactants with high HLB (**h**ydrophilic-**l**ipophilic **b**alance) numbers increase the methane solubility [100]. Therefore, a second approach aims to use nonionic surfactants with high HLB numbers to facilitate methane hydrate formation.

The concept of the HLB number goes back to Griffin who introduced the HLB number as the ratio between the lipophilic molar mass M_l and the molecules overall molar mass M. This leads to the following equation:

$$HLB = 20 * \left(1 - \frac{M_l}{M}\right) \qquad \text{Eq. 5-1}$$

The number 20 is a freely chosen scaling factor. A HLB number of 1 describes a lipophilic substance whereas a value of 20 represents a hydrophilic compound [101].

In this experimental series, SDS was used as a benchmark and the investigated system focuses on mixed methane-THF hydrate formation. (See chapter 5.1) The following substances were examined.

Tween 80, also known as Polysorbate 80, is a nonionic surfactant and emulsifier used in foods, cosmetics and medicine. The critical micelle concentration of Tween 80 in pure water is reported as 0.012 mM [102]. Its HLB number is 15. A promoting effect was confirmed for carbon dioxide hydrate and cylcopentane-carbon dioxide-hydrate formation [103–105]. Figure 5-8 shows its structure.

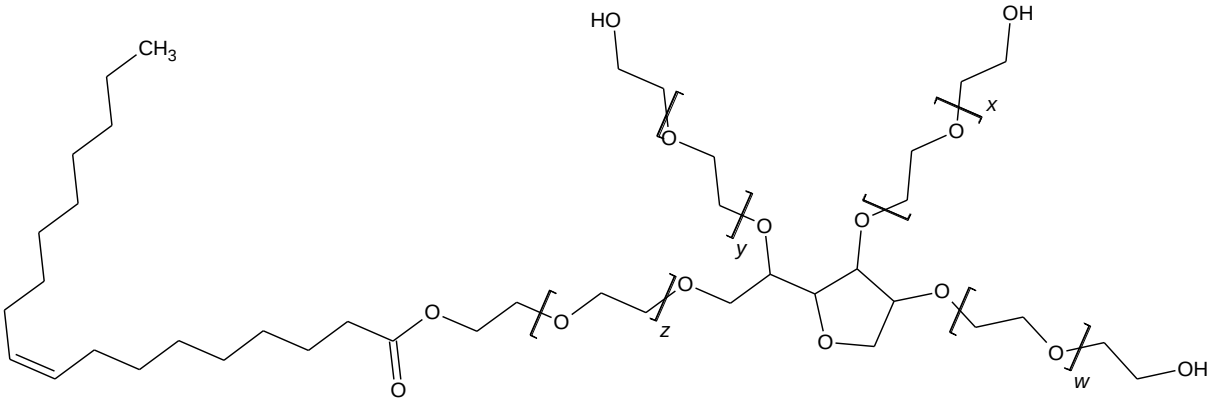

Figure 5-8 Structure of Tween 80 (w + x + y + z = 16)

Triton X-100 is a nonionic surfactant and a commonly used detergent in laboratories. The critical micelle concentration of Triton X-100 in pure water is reported as 0.22 mM [106]. Its HLB number is 13.5. Ethane hydrate formation is promoted by this surfactant [107]. Figure 5-9 shows its structure.

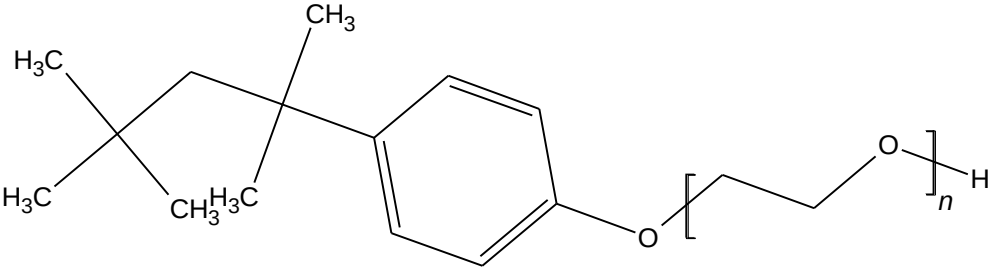

Figure 5-9 Structure of Triton X-100 (n = 8 – 9)

Perfluorooctanic acid (PFOA) is a synthetic perfluorinated carboxylic acid and fluorosurfactant. It is used in industrial applications as a surfactant in the emulsion polymerization of fluoropolymers and in the manufacturing process of polytetrafluoroethylene which is commercially known as Teflon. According to Yu et al. the CMC has a value of 3.8 mM and a HLB number of 17.8 [108]. Its structure is shown in Figure 5-10.

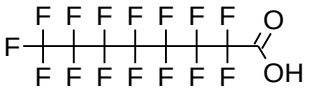

Figure 5-10 Structure of PFOA

In this experimental series, the induction time and the gas uptake of a water-methane-THF hydrate was measured in presence of each substance in the CMC. In addition, the system without promoter was measured.

Experimental procedure

The experimental series was performed in the Büchi reactor system (see chapter 4.2). Millipore water was degased 15 min under vacuum and 250 mL of the hydrate forming mixture (5.6 mol% THF + water + surfactant in the CMC) was weighed out and filled into the reactor which was closed afterwards. The reactor was purged 3 times to a pressure of 5 bar(g) and drained to a pressure of 0.5 bar(g). Subsequently, while stirring, cooling began until an operating temperature of 6 °C was reached. The stirrer rotation frequency was set to 900 rpm. In order to start the measurement, the reactor was filled with methane to an operating pressure of 8 bar(g) and the gas counter was reset. During the measurement, temperature and gas flow were recorded to determine the induction time and the gas uptake. The test ended 110 min after the start. The whole process was automated by using the “delta V” process control system. Five repetitive measurements were performed to investigate promoting effects. An exemplary experimental trend is given in Figure 5-11.

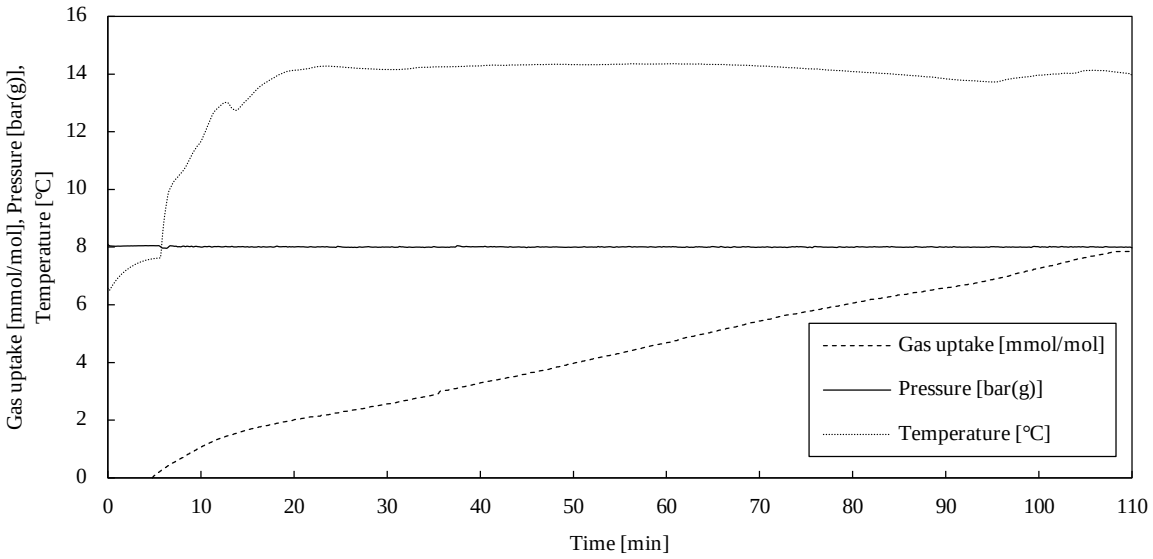

Figure 5-11 Representative experimental trend for the experimental series of chapter 5.1.2

The measurement started as the experimental pressure of 8 bar(g) was reached and held constant. After approx. five minutes the temperature rises significantly indicating the onset of the gas hydrate formation and therefore the induction time. Due to heat accumulation in the reactor and progressing gas hydrate formation, the temperature reaches a maximum temperature of 14 °C which cannot be compensated by the thermostat. However, gas uptake is recorded and after 110 minutes the experiment ended.

Results and discussion

Figure 5-12 shows again that nucleation is a stochastic process and visualized by large error bars. With regard to the effectiveness to promote the gas hydrate induction, SDS showed the best results followed by Tween 80. Triton X-100 and PFOA have a similar performance but in comparison to the other it is worse.

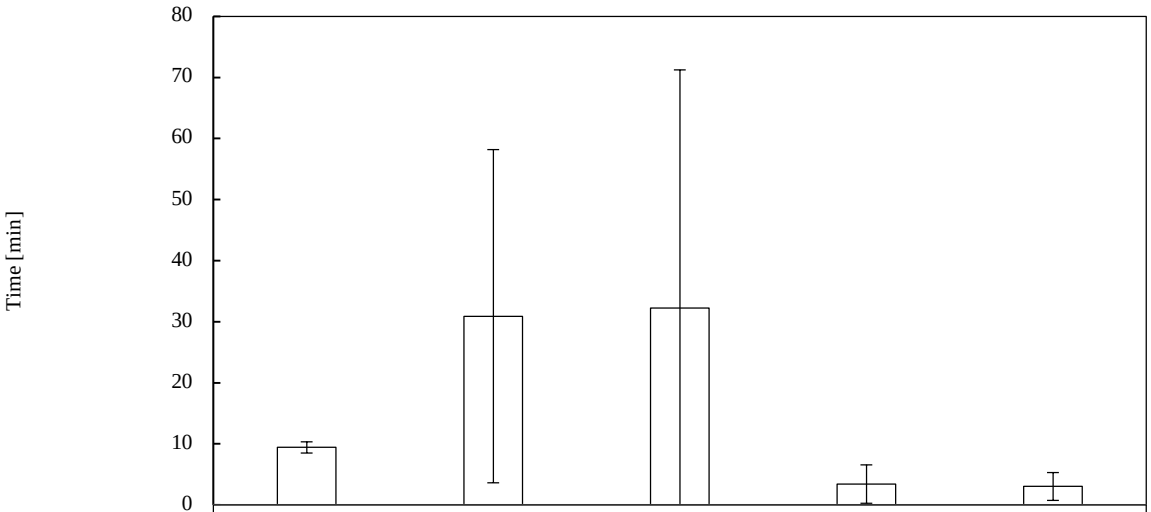

Figure 5-12 Average induction times [min] with standard deviation for methane-THF hydrate formation in presence of different surfactants

Figure 5-13 presents the averaged gas uptake in mmol gas per mol water in the first 80 minutes after induction. The trends show that in the first 10 minutes PFOA and Triton X-100 displayed the best performance. Most of all, this is caused by their effect to reduce the surface tension even stronger than SDS or Tween 80. Especially, PFOA reduces the surface tension to 15.2 mN/m which is weaker than SDS does with 38 mN/m [109]. The trends of Tween 80 and Triton X-100 are primarily traced back to the enhanced solubility of methane due to their high HLB numbers. After 15 minutes the trends are changing and SDS becomes the best promoter while Triton X-100 and PFOA follow in second place. Tween 80 is the worst promoter of the tested substances. The superior performance of SDS in comparison to Tween 80 was found during carbon dioxide hydrate formation as well [104,105]. The excellent effect of SDS is either explainable by the lowering of the surface tension or the HLB number. Therefore, morphological and steric reasons are considered to be responsible for this phenomenon as the hydrate formation becomes a diffusion-limited process during plug formation. This hypothesis is supported by a recent molecular dynamic study which stated that SDS molecules adsorb on the gas hydrate surface with their hydrophobic tails by anchoring into the open cages of the growing gas hydrate while the polar head groups protrude uncovered into the liquid phase. Thereby, adsorbed SDS molecules alter the hydrate morphology leading to an increased porosity, improving the mass transfer of methane significantly and enhancing the hydrate growth kinetics [110].

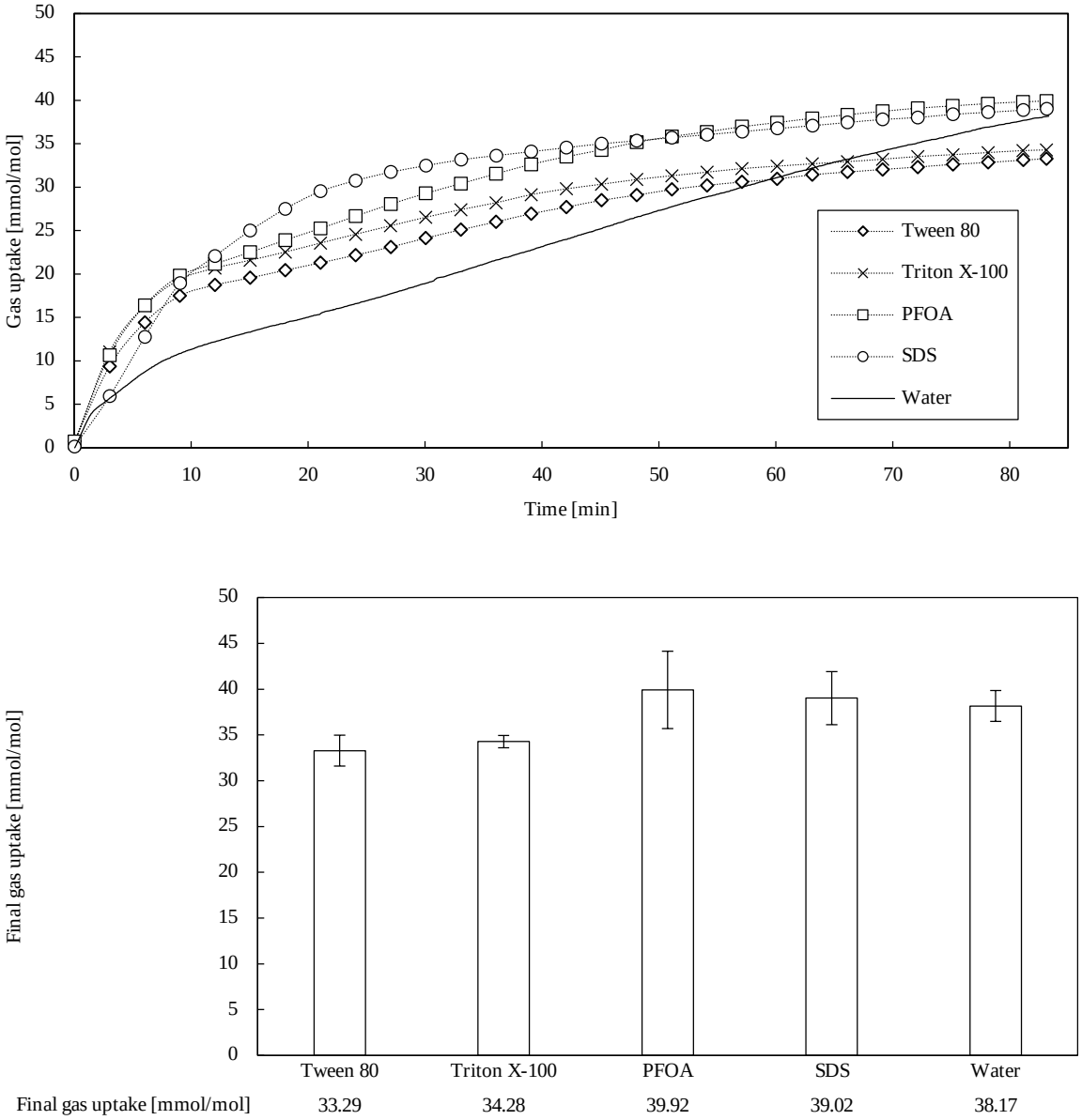

Figure 5-13 Average gas uptake [mmol/mol] during methane-THF hydrate formation for five repetitive measurements with standard deviation in presence of different surfactants in the CMC

This experimental series has shown that lowering the surface tension and increasing HLB numbers lead to a massive facilitation of hydrate formation at the beginning. The induction times were stochastic and especially high for Triton X-100 and PFOA. The highest gas uptake is achieved by using PFOA, though comparable to SDS. However, Tween 80 and Triton X-100 showed an inhibiting performance on the final gas uptake.

5.2 Influences of phase transfer catalysts and aprotic solvents

A phase-transfer catalyst or PTC is a catalyst that facilitates the migration of a reactant from one phase into another phase where the reaction occurs. Therefore, phase-transfer catalysis is a special form of heterogeneous catalysis and normally used for reactions were an ionic surfactant is soluble in the aqueous phase but insoluble in the organic phase. The PTC links the two phases enabling a faster reaction at the interphase. PTC is also employed in liquid/solid and liquid/gas reactions. Typical PTCs are quaternary ammonium salts, crown ethers and phosphonium compounds [111–114].

In difference to protic solvents like methanol, ethanol or water, aprotic solvents possess no positive polarized hydrogen atom and are not able to form hydrogen bonds. In addition, they have high dipole moments and permittivity which can be useful in view of the solubility of substances [115]. This experimental series was performed to determine the influences of both substance classes on gas hydrate formation. The following chemicals were used:

15-crown-5 is a crown ether and a cyclic pentamer of ethylene oxide that forms complexes with various cations. It is used as PTC and its structure is shown in Figure 5-14 [116].

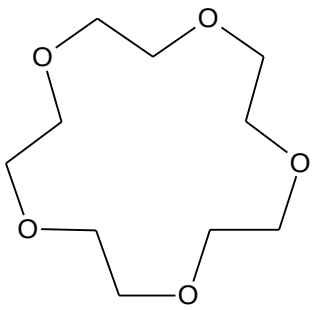

Figure 5-14 Structure of 15-Crown-5

Propylene carbonate (PC) is a carbonate ester derived from propylene glycol and an aprotic solvent with a high molecular dipole moment. It is used in lithium batteries as electrolyte component as well as in some adhesives, paint strippers, and in cosmetics. Further it is used as a solvent for the removal of carbon dioxide from natural and synthesis gas in absence of hydrogen sulfide [117,118]. The structure is displayed in Figure 5-15.

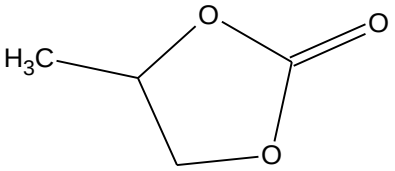

Figure 5-15 Structure of propylene carbonate

In this experimental series the induction time, gas uptake and equilibrium temperature of water-methane hydrate formation was measured under transient conditions in presence of PC in a concentration of 2 mol% - following Xia et al. who investigated the aprotic solvent dimethyl

sulfoxide [119] - and 15-crown-5 in concentrations of 0.1, 0.2 and 0.5 mol%. In addition, the system was measured without any additive.

Experimental procedure

The experimental series were performed in the Parr reactor system (see chapter 4.1). Millipore water was degassed 15 min under vacuum and 250 mL of the hydrate forming mixture (water + additive) was weighed out and filled into the reactor which was closed afterwards. The reactor was purged three times to a pressure of 5 bar(g) and drained to a pressure of 0.5 bar(g). Subsequently, cooling began until an operating temperature of 4 °C was reached. To start the measurement, the reactor was filled with methane to an operating pressure of 100 bar(g) and the gas counter was reset. Afterwards, the stirrer was turned on and set to a rotation frequency of 900 rpm. During the measurements, temperature and gas flow were recorded to determine the induction time and the gas uptake. The test was operated with a duration of 24 hours. Three repetitive measurements were performed to investigate possible promoting effects. An exemplary experimental trend is given in Figure 5-16.

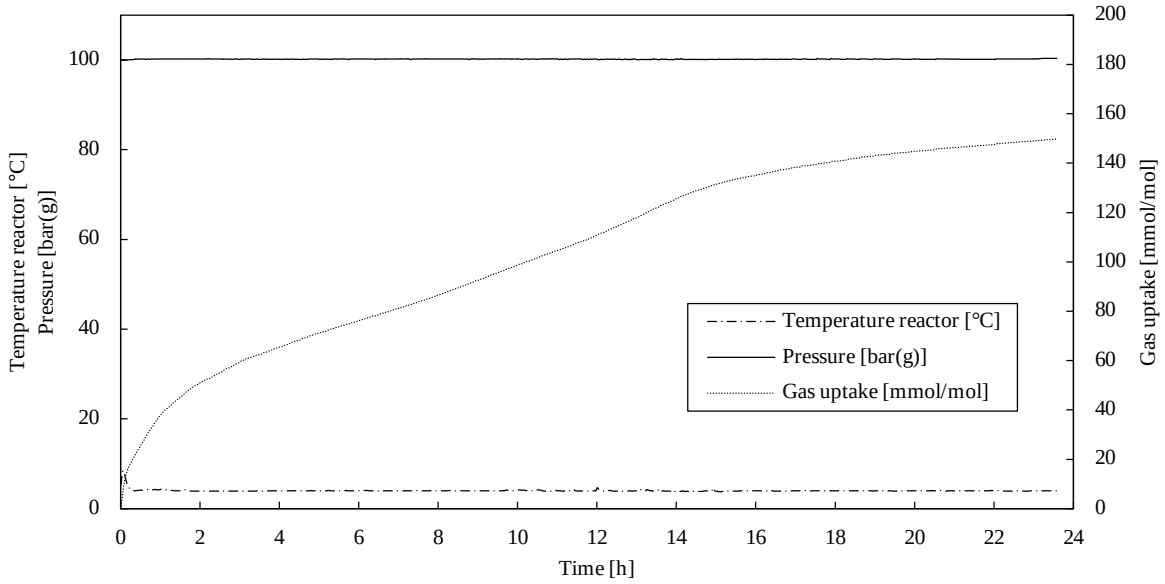

Figure 5-16 Exemplary experimental trend for experimental series of chapter 5.2

In addition, the gas hydrates were once dissociated after a measurement by heating to 20 °C in order to evaluate the equilibrium temperature and to identify thermodynamic effects. Figure 5-17 shows an exemplary experimental trend.

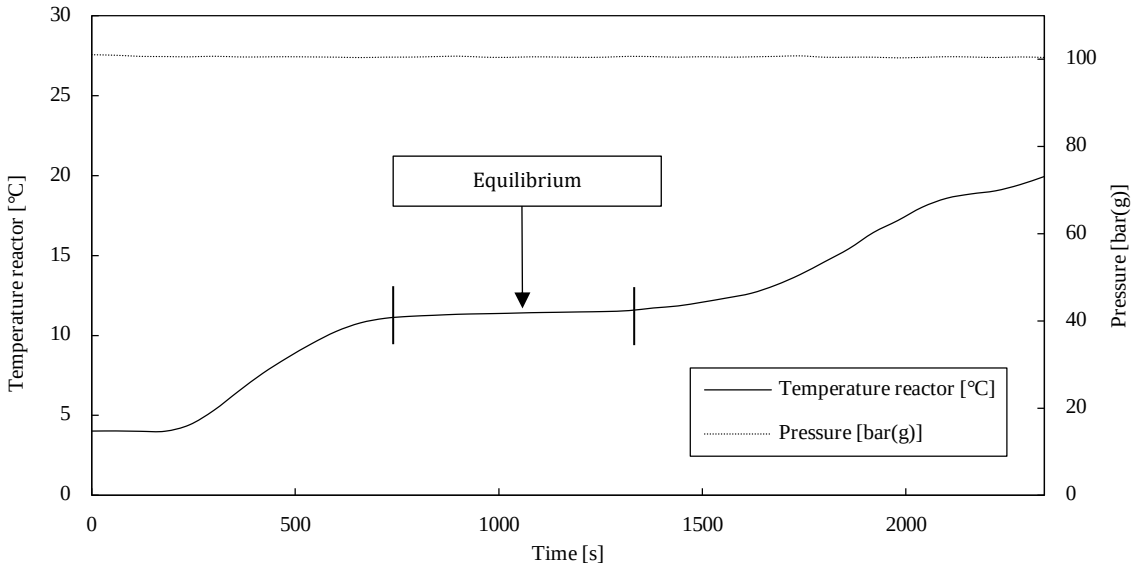

Figure 5-17 Exemplary experimental trend to determine the equilibrium temperature for experimental series of chapter 5.2

Results and discussion

Figure 5-18 shows the average induction times with standard deviation for this experimental series. Obviously in comparison to pure water, each substance has an inhibiting effect. 15-crown-5 in a concentration of 0.2 mol% showed three times absolutely no nucleation during the 24 hours of measurement. The wide-spread deviation proves the stochastic character of nucleation.

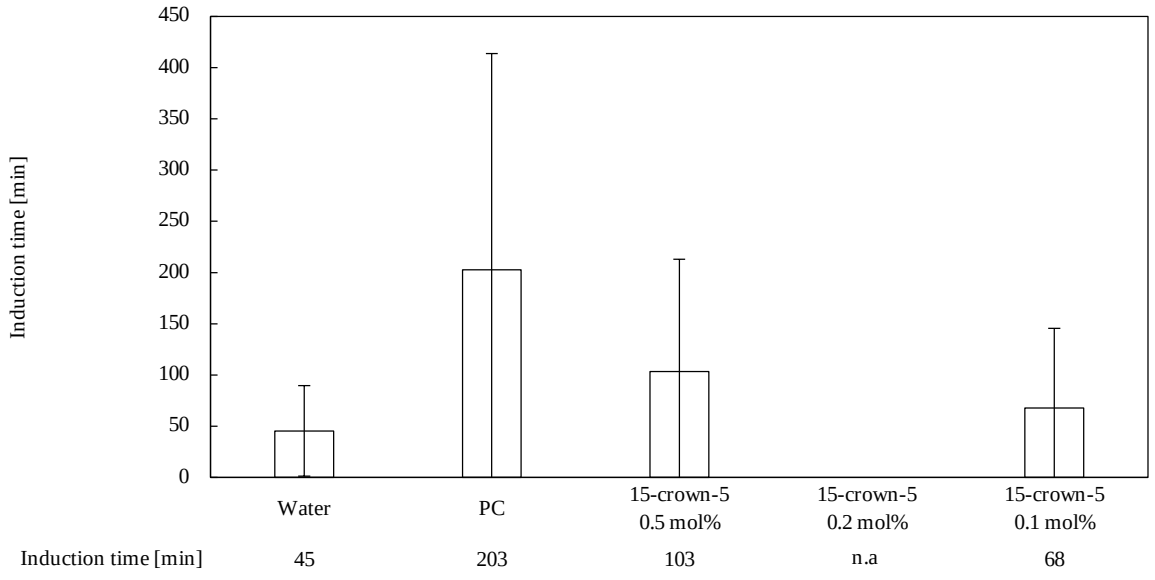

Figure 5-18 Average induction times [min] with standard deviation for methane hydrate formation in presence and absence of 15-crown-5 and PC

The average gas uptake can be obtained from Figure 5-19. In view of the kinetic effects, it is stated that especially PC exhibits a promoting effect in the first 9 hours. Beyond this point, water showed the better performance ending in the highest gas uptake. 15-crown-5 showed in both

concentrations an inhibiting effect whereas the lower concentration of 0.1 mol% had a stronger effect. As 15-crown-5 in a concentration of 0.2 mol% had no nucleation in the first 24 hours, no conclusion about the kinetics can be made.

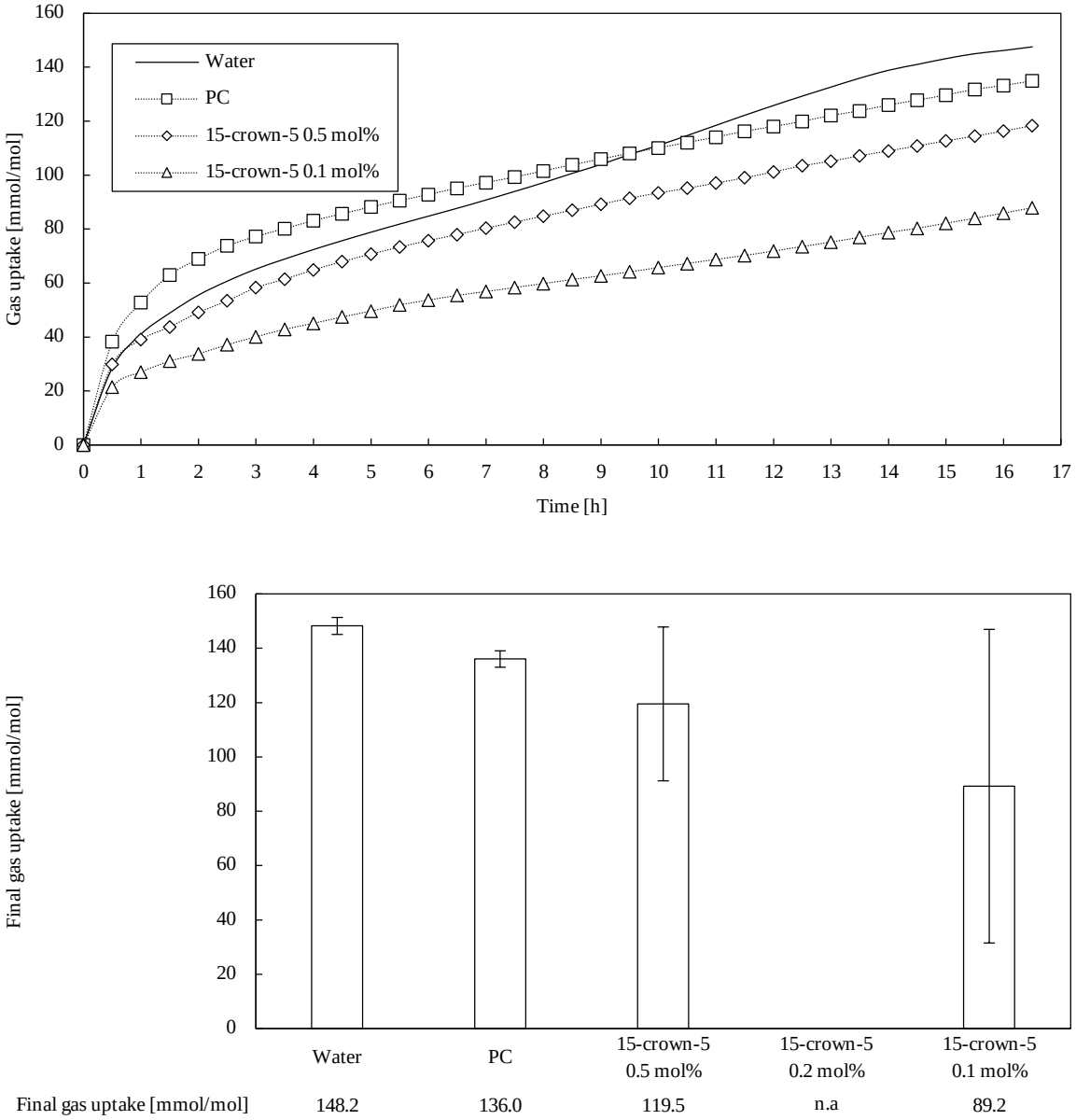

Figure 5-19 Average gas uptake [mmol/mol] during methane hydrate formation in presence and absence of 15-crown-5 and PC

Figure 5-20 displays the measured equilibrium temperatures. The results show that all substances had a slight thermodynamic inhibiting effect, PC even more than 15-Crown-5.

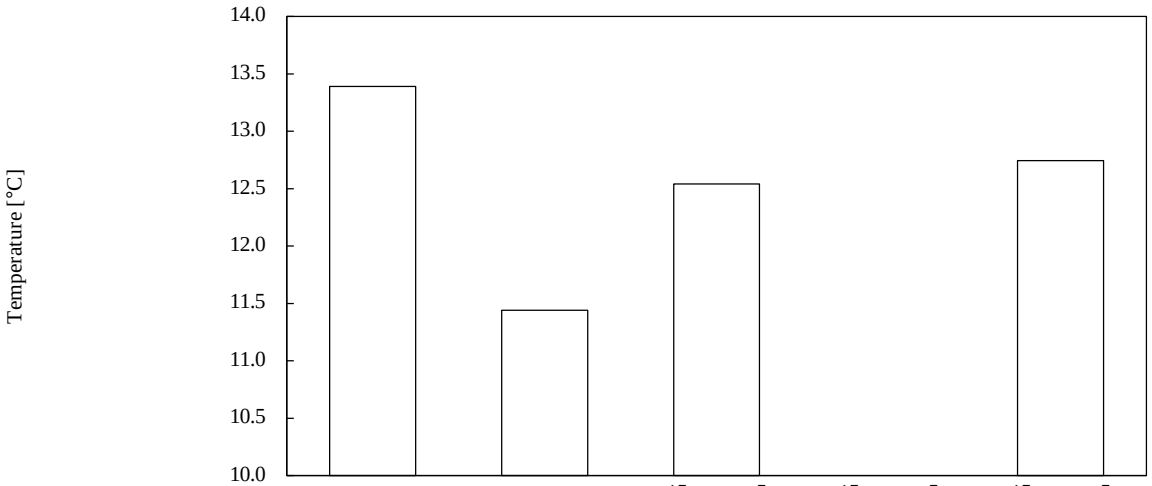

Equilibrium Temperature [°C]	13.39	11.44	12.54	n.a	12.75

Figure 5-20 Equilibrium temperatures [°C] of methane hydrates in presence and absence of 15-crown-5 and PC

The key findings are that both substances showed inhibiting effects with regard to the induction and thermodynamic equilibrium. Especially 15-crown-5 with its additional kinetically inhibiting effect demonstrated a good performance in a concentration of 0.2 mol%. This is explainable by the fact that Merkel proved that particularly ether groups have an inhibiting effect [120]. According to Nickolov et al. 15-crown-5 is able to bind up to 15 water molecules [121] and that would hinder the formation of hydrate cage structures. Furthermore, all substances had a lower gas uptake than pure water. It was found that propylene carbonate is at least suitable as a potential kinetic promoter for the first 9 - 10 hours. A possible explanation for this is that propylene carbonate, due to its high dipole character, increases the solubility of methane in water, but in the course of gas hydrate formation it seals the pores of the hydrate bulk and thus prevents further diffusion of methane into the cages. Furthermore, as PC is a carbonate ester, it is classified as a potential inhibitor [27].

5.3 Influences of crown ethers

The preceding chapter 5.2 showed an inhibiting performance of 15-crown-5 on the methane hydrate formation. Additionally, a suspicious anomaly was found while using 15-crown-5 in a concentration of 0.2 mol% as no induction occurred. Therefore, the question rose up if there is an optimal concentration of 15-crown-5 to achieve an inhibiting effect and the experimental series of this chapter was performed. Three different crown ethers were tested in different concentrations to determine their effect on methane hydrate formation in more detail. The structure of 15-crown-5 is already known from chapter 5.2. Furthermore, 12-crown-4 and 18-crown-6 were tested. The structures can be obtained from Figure 5-21.

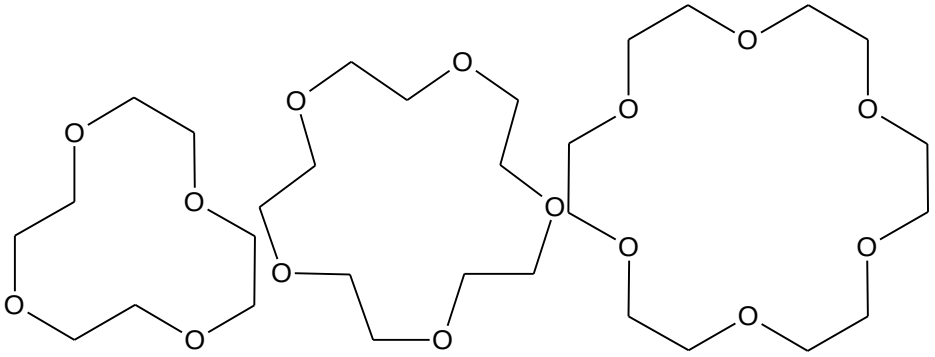

Figure 5-21 From left to right the structure of 12-crown-4, 15-crown-5 and 18-crown-6

The following concentrations were tested:

- 12-crown-4 was tested in a concentration of 0.1 mol%
- 15-crown-5 in a concentration of 0.15 mol% and 0.3 mol%
- 18-crown-6 in a concentration of 0.1 mol% and 0.5 mol%

Experimental procedure

The experiments were conducted analogously to chapter 5.2 with three repetitive measurements.

Results and discussion

Figure 5-22 shows the average induction time from three repetitive measurements with standard deviation. In nearly all cases an immediate induction occurred. Only in case of 18-crown-6 induction times are higher especially in a concentration of 0.5 mol%, resulting in an inhibiting effect. Compared to the measurements of chapter 5.2 15-crown-5 has a promoting character which contradicts the previous results.

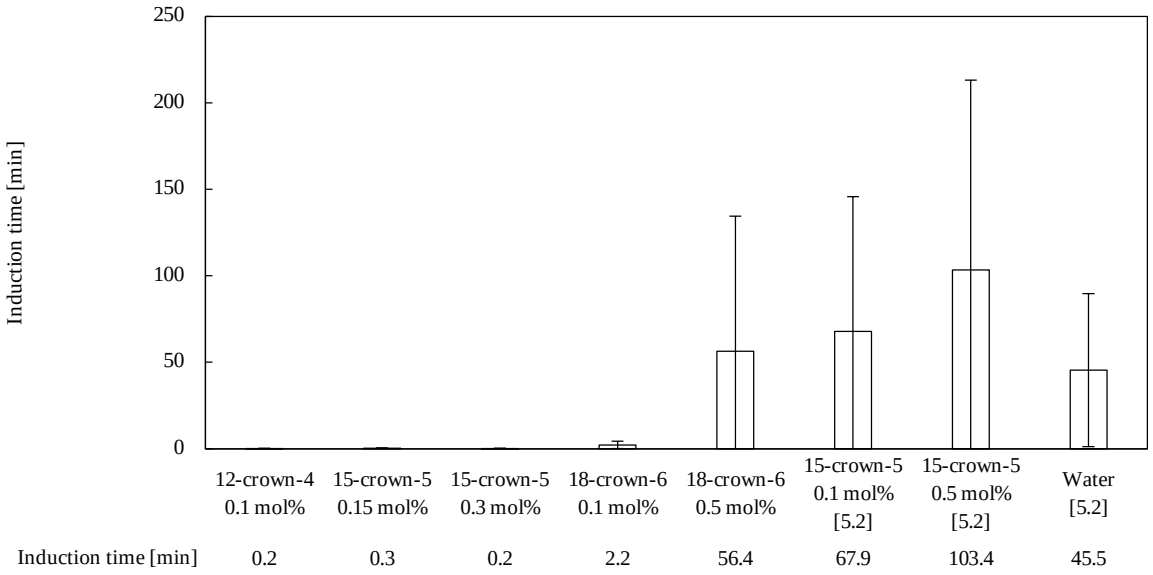

Figure 5-22 Average induction time [min] with standard deviation for methane hydrate formation in presence of different crown ethers with varying concentrations

The average gas uptake over time is presented in Figure 5-23. The obtained relations from the induction times are reflected here again. All crown ethers showed a promoting effect except of 18-Crown-6 with 0.5 mol%. The trends are optically similar and only show little differences.

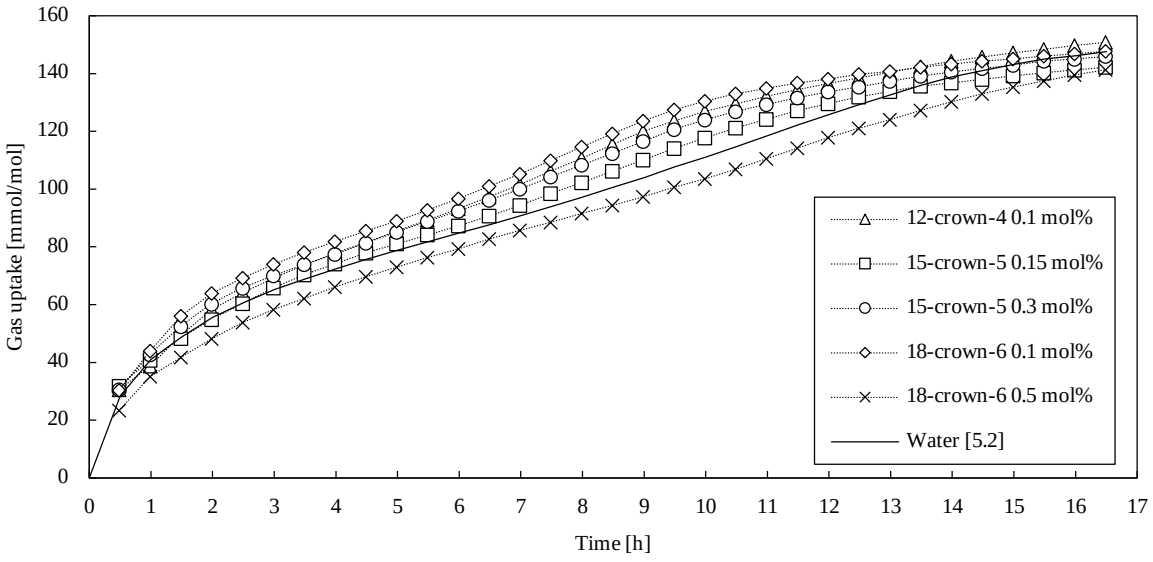

Figure 5-23 Average gas uptake [mmol/mol] over time for methane hydrate formation in presence of different crown ethers with varying concentrations

The results for the 15-Crown-5 ether in all measured concentrations including the trends from chapter 5.2 are compared in Figure 5-24. While inhibiting effects were obtained in the preceding measurements, now promoting effects occurred. No clear relation between the concentration and the kinetic of methane hydrate formation was found.

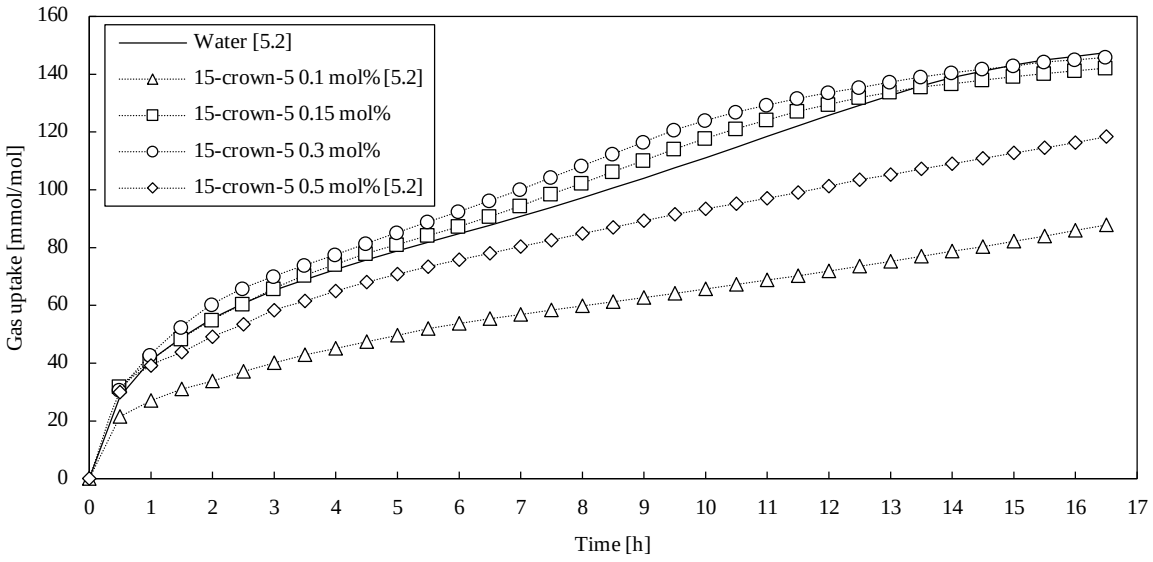

Figure 5-24 Average gas uptake [mmol/mol] over time for methane hydrate formation in presence of 15-crown-5 in different concentrations

All these findings with regard to the kinetics can also be recognized in Figure 5-25 which shows the average final gas uptake. All ethers in every concentration showed similar promoting results. No correlation between concentration or number and the final gas uptake of ether groups was obtained. The former measurements (15-crown-5 0.1 and 0.5 mol%) resulted in an inhibiting effect afflicted with large error bars.

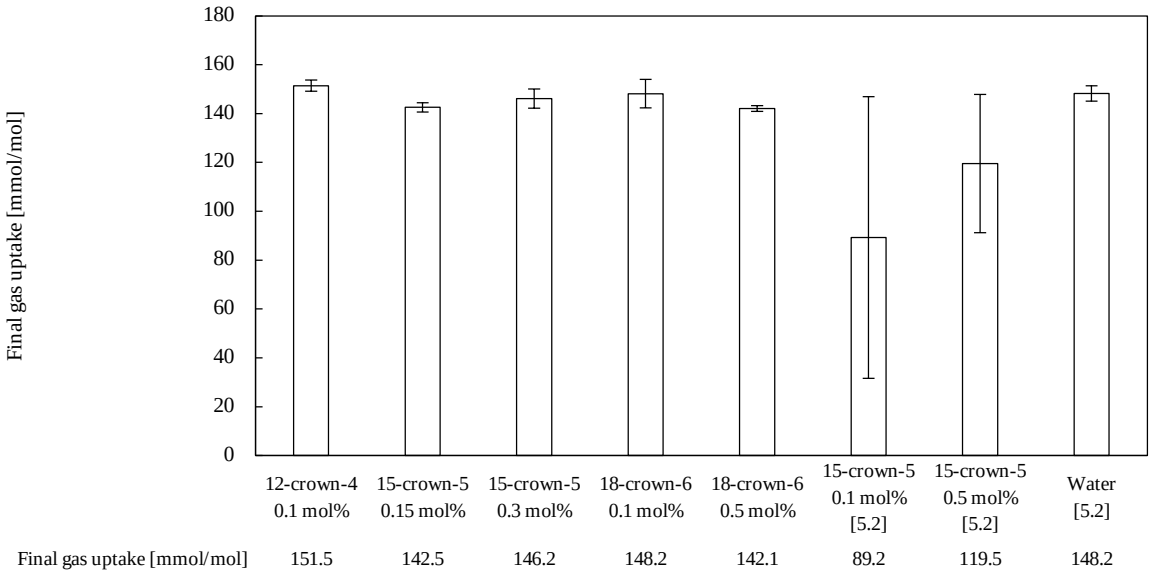

Figure 5-25 Average final gas uptake [mmol/mol] with standard deviation for methane hydrate formation in presence of different crown ethers with varying concentrations

Last, the thermodynamic effects are discussed based on Figure 5-26. The equilibrium temperatures lead to the conclusion that ether groups have a thermodynamic inhibiting effect. The work of Merkel is underlined here as reference [120]. As 18-crown-6 showed a significant

stronger thermodynamic inhibition than the other ethers, further test should be performed to find an optimal concentration for each ether.

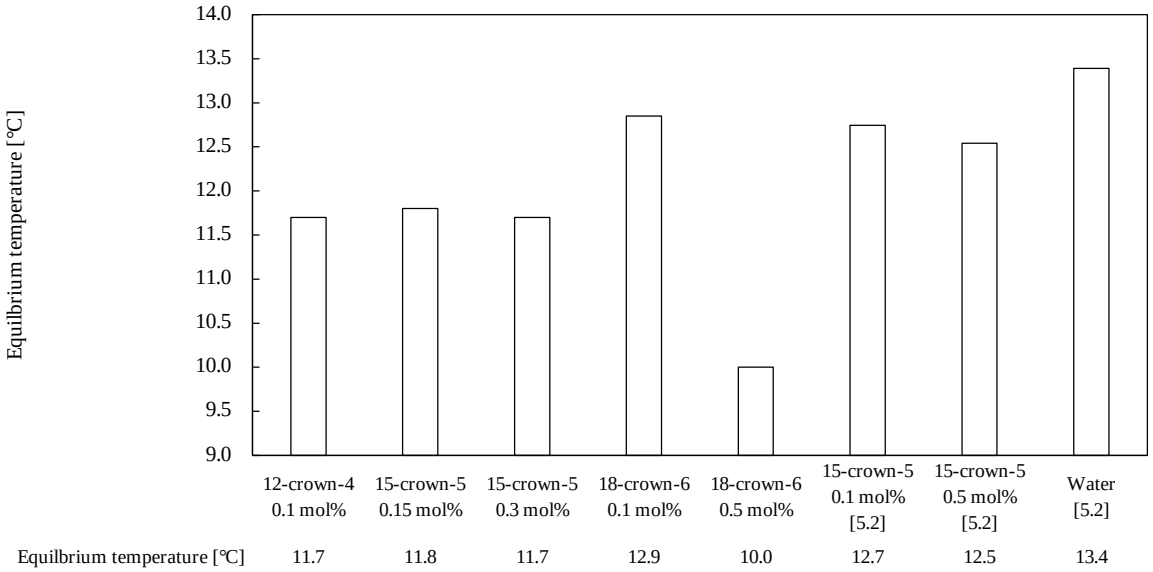

Figure 5-26 Equilibrium temperature [°C] during dissociation of methane hydrates in presence of different crown ethers with varying concentrations

Finally, it is stated that the effects on methane hydrate formation kinetic could not be clearly identified and a tendency towards promotion was found here which is in conflict with the former results. However, these effects are small and not even nearly as good to enhance gas hydrate formation as other known promoters. Furthermore, the thermodynamic inhibition would not be desired with regard to the usage in an industrial application. Therefore, the obtained results are unsatisfactory from a scientific point of view. Nevertheless, from an application oriented and economic standpoint, further investigations on crown ethers as inhibitors would make no sense, as these substances are far more expensive than methanol or ethylene glycol.

5.4 Influences of amino acids

This chapter deals with the effects of different amino acids with differing hydrophobicity on the formation of mixed methane-THF hydrates. Hydrophobic amino acids were already tested as thermodynamic inhibitors. While using glycine, L-alanine and L-valine in a concentration range of 0.1-3.0 mol% as thermodynamic inhibitors for CO_2-hydrate formation, all substances were less efficient than methanol, but have the advantage that they are environmentally friendly and nonvolatile [122]. A thermodynamic inhibiting effect caused by glycine and L-leucine (0.05-1.5 wt%) was found for THF-hydrate formation as well [123]. Roosta et al. used different amino acids in a concentration of 0.5 and 1.5 wt%. While the hydrophilic amino acids L-histidine and L-glutamine showed a promoting effect on ethane and methane-propane hydrate growth, hydrophobic amino acids, namely glycerine and L-serine acted as inhibitors for ethane, methane-propane. The methane-THF hydrate formation was inhibited in all cases [95]. Further studies proved a promoting effect on methane hydrate formation. Bhattacharjee et al. showed that L-histidine (0.1-1.0 wt%) is able to improve the hydrate formation kinetic and gas uptake significantly but not as good as SDS [124]. Veluswamy et al. tested tryptophan (0.0009-0.0264 mol%), histidine (0.035-0.116 mol%), arginine (0.031-0.103 mol%) and L-leucine (0.1-1.0 wt%) with regard to methane hydrate formation and all substances showed a promoting effect. The main influencing factors are the hydrophobicity and the side chain characteristics. Longer side chains and a hydrophobic characteristic tend to enhance the hydrate formation [30,125]. Not investigated extensively by now is the formation of mixed methane-THF hydrates in presence of amino acids which is the subject of this following chapter. The used amino acids are tabulated in Table 5-1. Concentrations of 0.1, 0.5, 1.0 and 3.0 wt% were chosen.

Table 5-1 Overview of amino acids used in experimental series of chapter 5.4

Name	Side chain polarity [126]	Hydropathy index [127]	Structure
Glycine	Nonpolar	-0.4	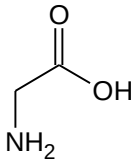
L-arginine	Basic polar	-4.5	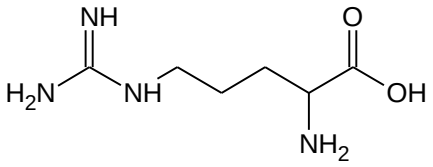
L-isoleucine	Nonpolar	4.5	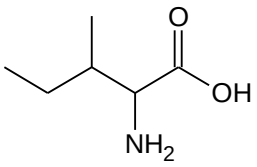
L-lysine	Basic polar	-3.9	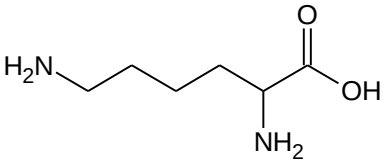

Experimental procedure

The experiments were conducted analogously to chapter 5.1.2 and five repetitive measurements were performed.

Results and discussion

Figure 5-27 shows the average induction times for all tested amino acids in their corresponding concentration.

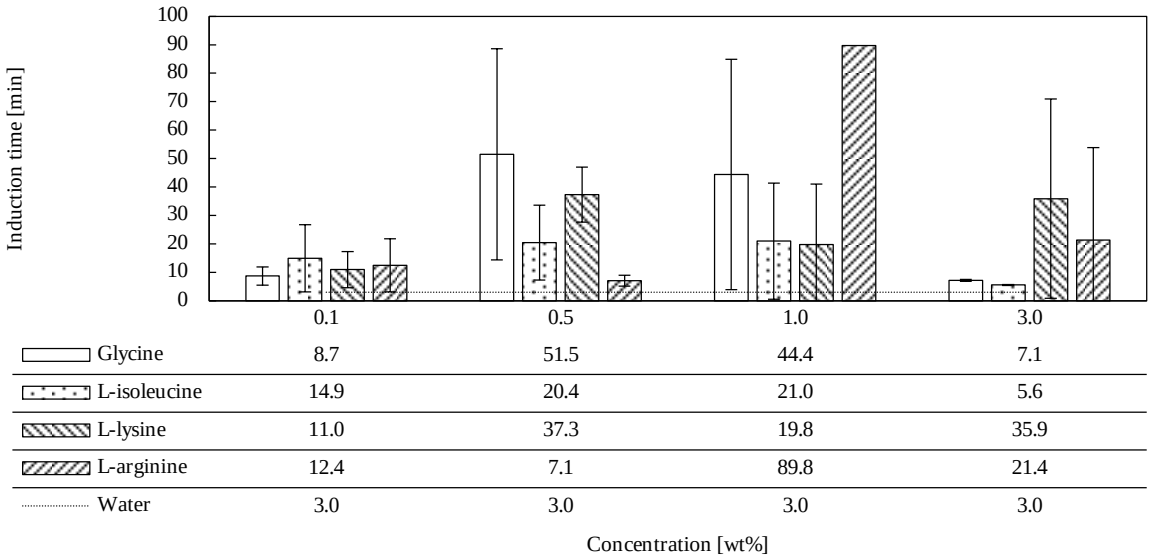

	0.1	0.5	1.0	3.0
Glycine	8.7	51.5	44.4	7.1
L-isoleucine	14.9	20.4	21.0	5.6
L-lysine	11.0	37.3	19.8	35.9
L-arginine	12.4	7.1	89.8	21.4
Water	3.0	3.0	3.0	3.0

Figure 5-27 Average induction times [min] with standard deviation for methane-THF hydrate formation in presence of different amino acids with varying concentrations

The induction times are widespread and the stochastic character of hydrate nucleation is once more demonstrated. While induction times are very low and similar in case of a concentration of 0.1 wt%, induction times become more random in case of the higher concentrations. Outstanding here is L-arginine in a concentration of 1.0 wt% as only one of five repetitive measurements started to form hydrates after 89.8 minutes hinting towards an inhibiting effect. Inhibiting effects were also found with glycine in the concentration of 0.5 and 1.0 wt%, L-lysine in the concentration of 0.5 and 3.0 wt%. L-isoleucine is not awarded with an inhibiting effect as induction times were still low and the widespread deviation allows no clear statement.

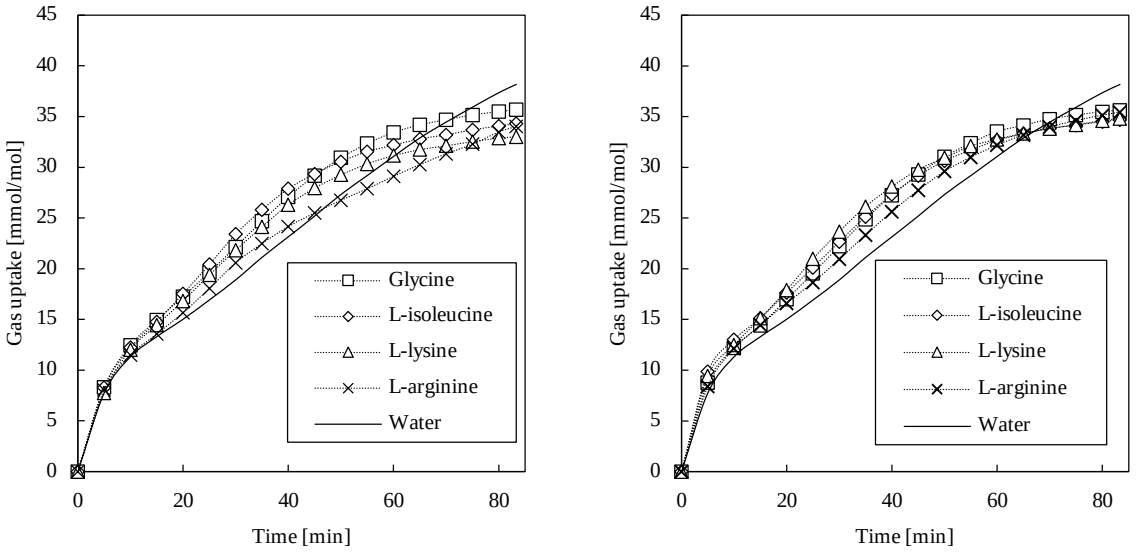

Figure 5-28 Average gas uptake [mmol/mol] over time for methane-THF hydrate formation in presence of different amino acids in a concentration of 0.1 wt% (left) and 0.5 wt% (right)

Figure 5-28 shows the gas uptake over time for different amino acids in the concentrations of 0.1 and 0.5 wt%. It can be seen, that in the first 15 minutes no difference to the pure water + THF system can be observed. Afterwards, all amino acids have a promoting effect, whereby L-arginine is the worst and L-isoleucine the best promoter. However, in a concentration of 0.1 wt% the trends fan out reaching a lower final gas uptake in comparison to the comparative probe. While using 0.5 wt%, trends are narrowed and reach a nearly equal end gas uptake which is still lower than that of pure water + THF. Therefore, in the concentrations 0.1 wt% and 0.5 wt% all amino acids enhance the kinetics but to the disadvantage of a lower gas uptake. With higher concentrations new effects occur as Figure 5-29 shows.

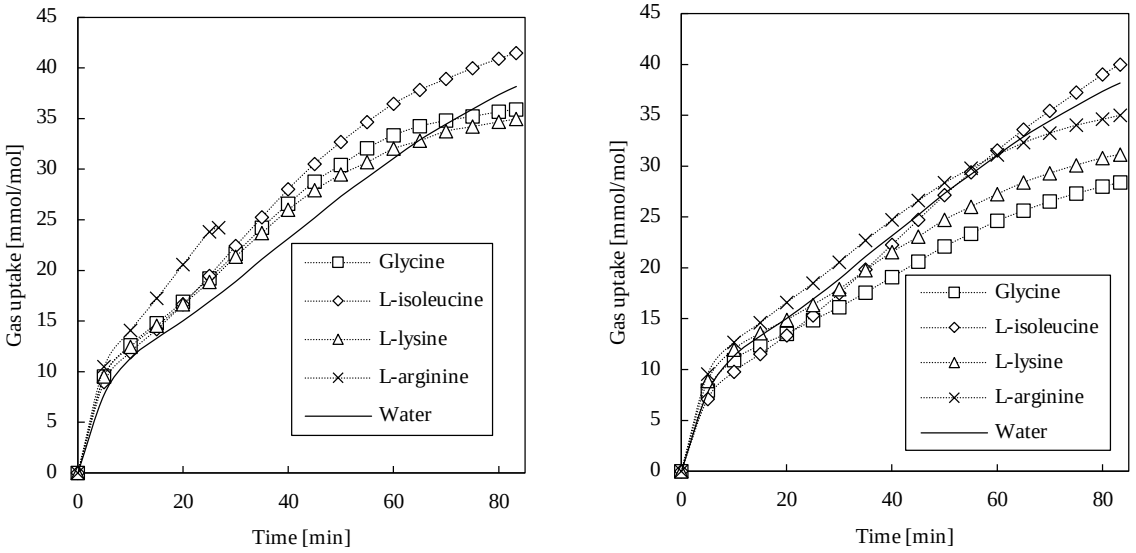

Figure 5-29 Average gas uptake [mmol/mol] over time for methane-THF hydrate formation in presence of different amino acids in a concentration of 1.0 wt% (left) and 3.0 wt% (right)

In a concentration of 1.0 wt% all amino acids have a kinetic promoting effect right from the beginning of the experiments. The trend of L-arginine stops after 30 minutes as only one attempt induced successfully but exceeded the experimental time. Glycine and L-lysine reach once more a lower end gas uptake with regard to the comparative probe. Only L-isoleucine shows a promoting effect over the whole experimental time. With regard to 3.0 wt% glycine and L-lysine have an inhibiting effect and no significant difference between the trends of L-isoleucine, L-lysine and the water measurement can be seen. The end gas uptake for L-isoleucine is slightly higher than that of water and L-lysine is classified below these two. For the greater clarity all average final gas uptake are displayed in Figure 5-30.

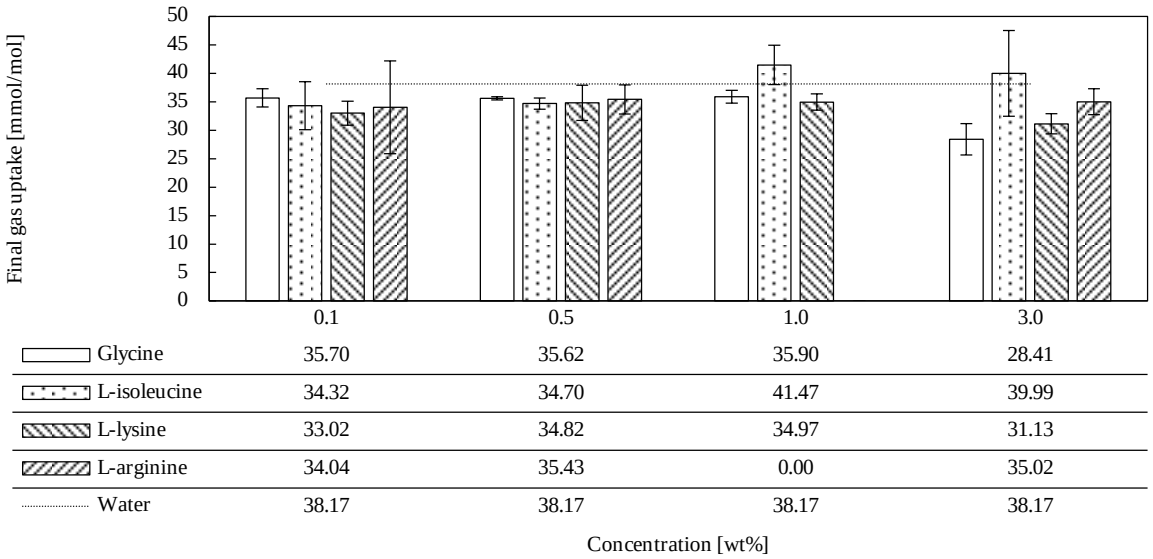

	0.1	0.5	1.0	3.0
Glycine	35.70	35.62	35.90	28.41
L-isoleucine	34.32	34.70	41.47	39.99
L-lysine	33.02	34.82	34.97	31.13
L-arginine	34.04	35.43	0.00	35.02
Water	38.17	38.17	38.17	38.17

Figure 5-30 Average final gas uptake [mmol/mol] with standard deviation for methane-THF hydrate formation in presence of different amino acids with varying concentrations

Summarizing it can be said (see Table 5-2): All amino acids showed a kinetically promotion up to a concentration of 3.0 wt% and the gas uptake was lower in comparison to water. In a concentration of 3.0 wt% the kinetic effect shifted to no effect or inhibition. Exceptions are an increased gas uptake in the case of L-isoleucine, which was achieved in concentrations ≥ 1.0 wt% and L-arginine with no effect on the kinetics with 0.1 wt% and no assessment of the gas uptake due to high induction times while using 1.0 wt%. Therefore, the conclusion is that indeed longer side chains and a hydrophobic characteristic improve the hydrate formation. However, the influences of amino acids are highly concentration dependent and further research has to be done to understand the mechanism behind their effects [19,66].

Table 5-2 Summarized results of the influences of different amino acids with varying concentrations on the methane-THF hydrate formation kinetics and gas uptake

	0.1 wt%		0.5 wt%		1.0 wt%		3.0 wt%	
	Kinetic	Uptake	Kinetic	Uptake	Kinetic	Uptake	Kinetic	Uptake
Glycine	↑	↓	↑	↓	↑	↓	↓	↓
L-isoleucine	↑	↓	↑	↓	↑	↑	–	↑
L-lysine	↑	↓	↑	↓	↑	↓	↓	↓
L-arginine	–	↓	↑	↓	↑		–	↓

5.5 Influences of fatty acids

As SDS is known as one of the kinetic promoters, it seems obvious that fatty acids in general, and especially sodium dodecanoate, could be good promoters as well. However, fatty acids were neither tested as promoters nor inhibitors for gas hydrate formation. Therefore, this chapter deals with the screening of four saturated fatty acids with raising carbon chains from C_8 to C_{14}.

The term fatty acids includes all saturated and unsaturated aliphatic carboxylic acids with a chain lengths ranging from C_6 to C_{24}. They play an important industrial role, as already back in 2000 world production was about 5.4 x 10^6 t per year and is still estimated to grow [128]. Fatty acids act as raw material for the production of soaps, esters, alcohols or amides and can be found in textiles, cosmetics, rubber, waxes, plastics etc.. Saturated fatty acids of a chain length of 14 or higher are not classified as being dangerous to water because of a low toxicity and easy biodegradability. Saturated acids up to C12 are classified as slightly water endangering [128]. Therefore, they have superior properties in comparison to SDS with regard to impacts on the environment. Fatty acids can also act as surfactants, as they consist of a hydrophilic head and a hydrophobic tail. Table 5-3 shows the fatty acids with their corresponding CMCs used in this experimental series

Table 5-3 Investigated fatty acids, CMCs obtained from [129,130], surface tension σ obtained from [131]

Name	Structure	Linear formula	CMC [mM]	σ [mN/m]
Sodium octanoate (SO)	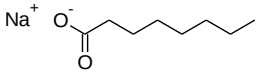	$CH_3(CH_2)_6COONa$	300	40
Sodium decanoate (SD)	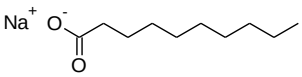	$CH_3(CH_2)_8COONa$	86	37
Sodium dodecanoate (SDD)	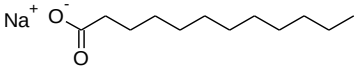	$CH_3(CH_2)_{10}COONa$	29.9	24
Sodium myristate (SM)	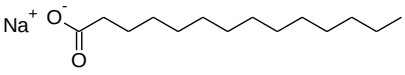	$CH_3(CH_2)_{12}COONa$	4.5	35

Experimental procedure

The experiments were conducted analogously to chapter 5.1.2. For each fatty acid five repetitive measurements were performed.

Results and discussion

The average induction times shown in Figure 5-31 have a widespread standard deviation with exception of SM which has a proportionate induction time. In comparison to water, the induction times are nearly 10 times and in the case of SD nearly 20 times higher. Therefore, all fatty acids inhibit the hydrate nucleation.

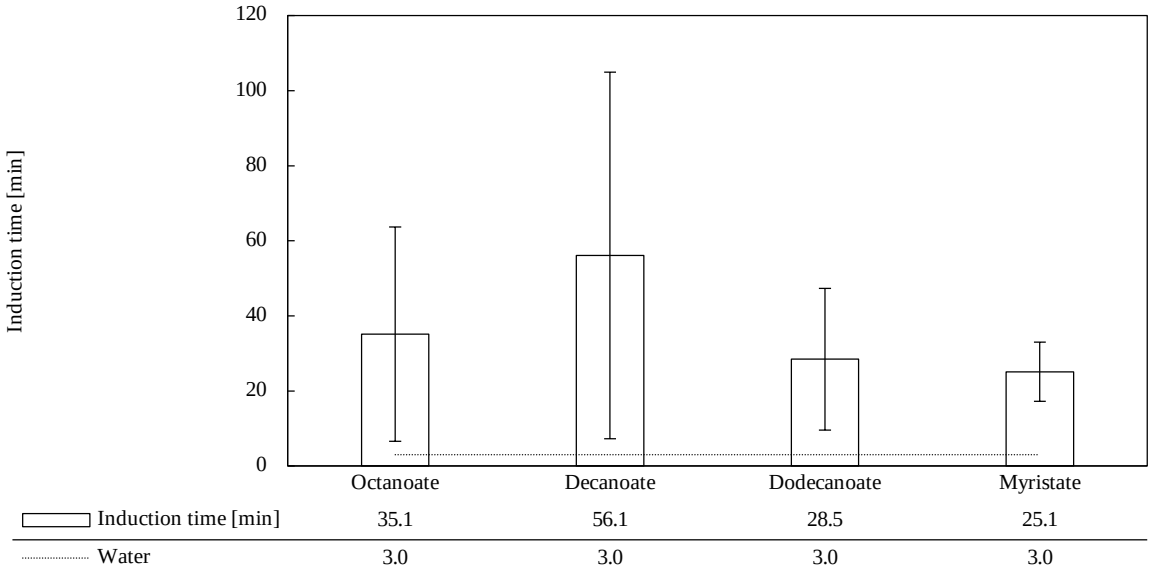

Figure 5-31 Average induction times [min] with standard deviation for methane-THF hydrate formation in presence of different fatty acids in the CMC

Figure 5-32 indicates, that all fatty acids act as kinetic promoters, at least in the first 50 minutes after hydrate induction occurred. Thus, SO shows the strongest promoted kinetics. In general this effect is once more attributed to a lowering of the surface tension, as the fatty acids act as surfactants. Afterwards, SM still has the kinetically promoting characteristic, whereas SDD behaves similar to water and SO and SD become kinetic inhibitors.

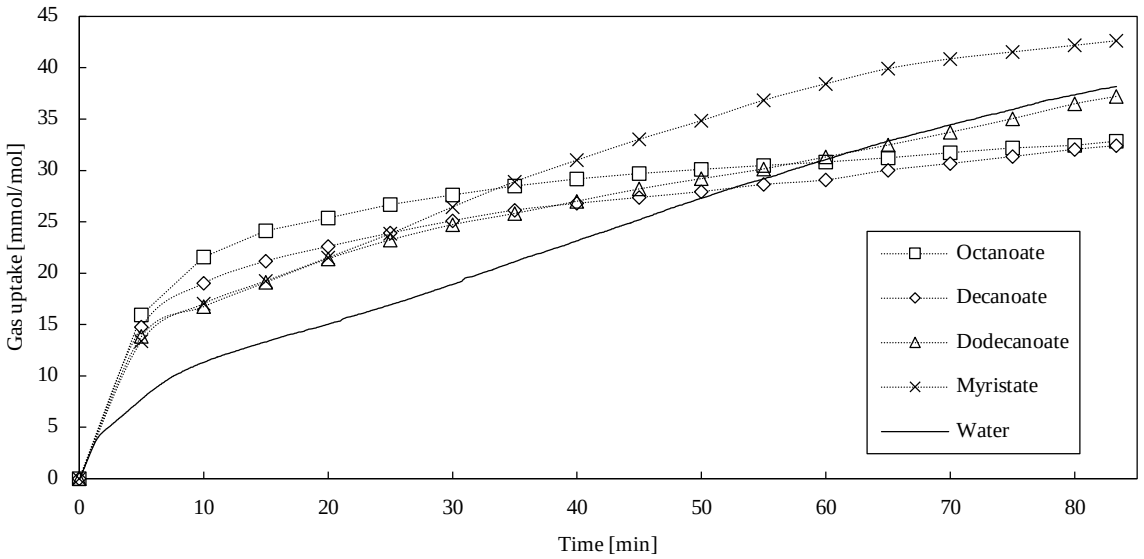

Figure 5-32 Average gas uptake [mmol/mol] over time for methane-THF hydrate formation in presence of different fatty acids in the CMC

A look at the final gas uptake presented in Figure 5-33 shows that with increasing carbon chain length, the final gas uptake rises.

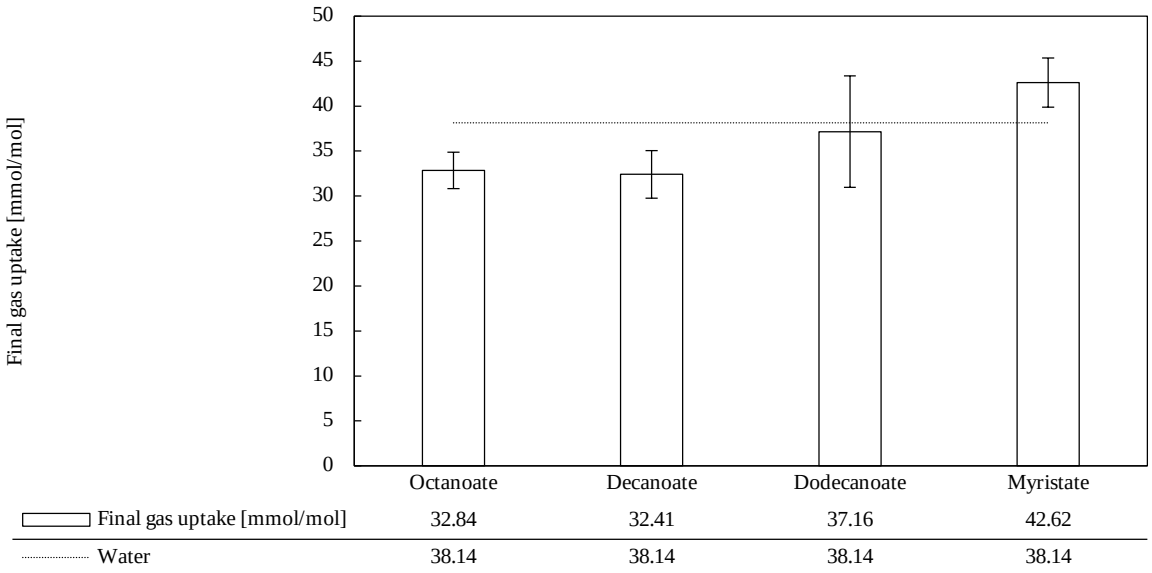

Figure 5-33 Average final gas uptake [mmol/mol] with standard deviation for methane-THF hydrate formation in presence of different fatty acids in the CMC

As no literature regarding the effects of fatty acids is available for the comparison, studies dealing with the impact of sodium alkyl sulfates with varying carbon-chain lengths are used here. Okutani et al. tested SDS, sodium tetradecyl sulfate and sodium hexadecyl sulfate and found no qualitative differences in the methane hydrate growth behavior. However, water to hydrate conversion was nearly the same for all substances. Sodium tetradecyl sulfate showed a high formation rate in low concentrations which is why it was suggested as the most favorable promoter of these three [132]. If SDS, sodium tetradecyl sulfate and sodium hexadecyl sulfate are used in the CMC, no difference

between these substances concerning the final gas uptake and kinetics were observed [133]. Dicharry et al. showed that there is no significant difference between sodium alkyl sulfates in a range of C_8 to C_{16} with regard to the total gas consumption whereas the rate of hydrate growth raised from C_{10} to the highest value for C_{14} and declined notable afterwards with higher carbon chain length [134]. This shows, that in the case of sodium alkyl sulfates, with the same carbon chain length like the fatty acids used here, no significant differences were found. In contrast, the fatty acids accelerated the hydrate formation in the first 50 minutes as well. Though they differed afterwards in their behavior as SO and SD lowered the storage capacity whereas SM had an enhancing effect. Therefore, SM is a promising alternative to SDS as a promoter for gas hydrate applications and possibly, higher fatty acids could even perform better. SDD could delineate some kind of boundary for the classification as promoter or inhibitor with regard to the final gas uptake.

5.6 Influences of glycol ethers

Glycol ethers are used in industry in pharmaceuticals, cosmetics, textiles, rubber and ceramics due to their advantageous solubility properties. Furthermore, most glycol ethers are water-soluble, biodegradable and only a few are considered toxic [135]. As the influences of crown ethers (see Chapter 5.2 and 5.3) could not be clearly identified, a study is conducted here with the corresponding acyclic ethers, i.e. tetraethylene (TEG), pentaeythlene (PEG) and hexaethylene (HEG) glycol. The universal structure of the used polyethylene glycols is given in Figure 5-34 with n = 4, 5 and 6 respectively.

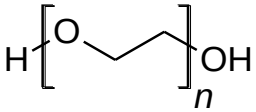

Figure 5-34 Universal structure of a polyethylene glycol

As glycols like ethylene, diethylene and triethylene glycol are used in the field of flow assurance, inhibiting effects are expected for all substances [21]. The following concentrations were tested:

- TEG was tested in a concentration of 0.1 mol%, 0.3 mol% and 0.5 mol%
- PEG was tested in a concentration of 0.1 mol%
- HEG was tested in a concentration of 0.1 mol%

Experimental procedure

The experimental series was performed in the Parr reactor system under transient conditions (see chapter 4.1). First, Milli-Q Water was degassed 15 minutes under stirring. Afterwards, the corresponding polyethylene glycol in a set concentration was added. The autoclave was filled with 250 mL of the hydrate forming mixture and tempered to 40 °C to prevent the “memory-effect”.

Thereafter, the reactor was cooled down to the experimental temperature of 4 °C and the reactor was purged three times by pressurizing to 5 bar(g) and depressurizing to 0.5 bar(g). Then, the reactor was filled with methane to the starting pressure of 150 bar(g) The measurements started with the stirrer turn on, set to 900 rpm and ended after 19 hours. As measurements were performed under transient conditions, the pressure inside the reactor dropped over time due to the progressing enclathration of gas molecules into the growing gas hydrate structure. Therefore, the pressure trend can be converted into the gas uptake by using the Peng-Robinson equation of state. Three repetitive measurements were performed for each glycol ether.

Results and discussion

All experiments showed an almost immediate induction with the exception of two experiments for TEG 0.3 mol%. The average induction times are shown in Figure 5-35.

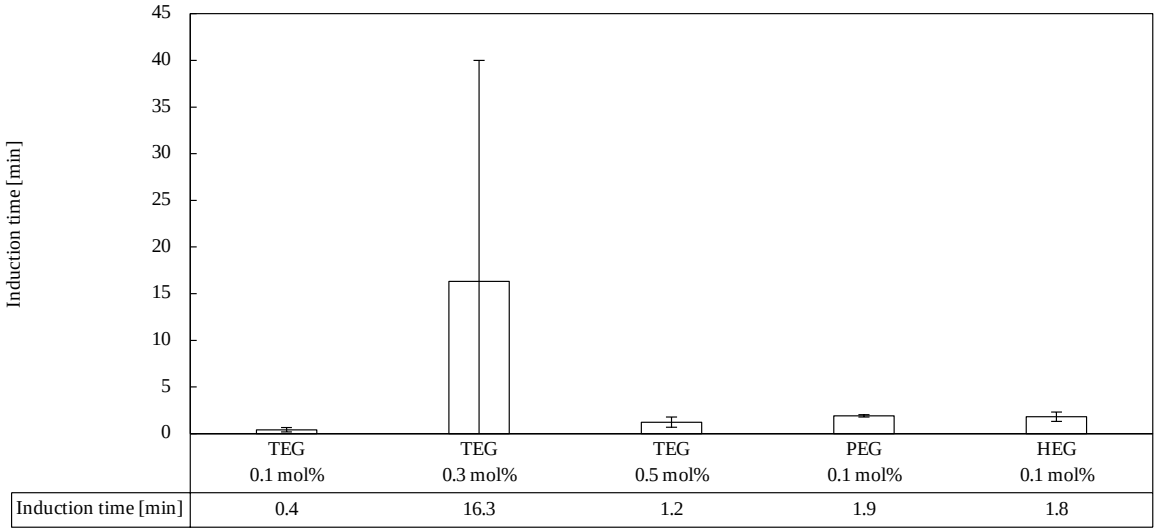

Figure 5-35 Average induction times [min] with standard deviation for methane hydrate formation in presence of different polyethylene glycols with varying concentrations

The average gas uptake trends over three repetitive measurements are given in Figure 5-36 to compare the influences on gas hydrate formation kinetics.

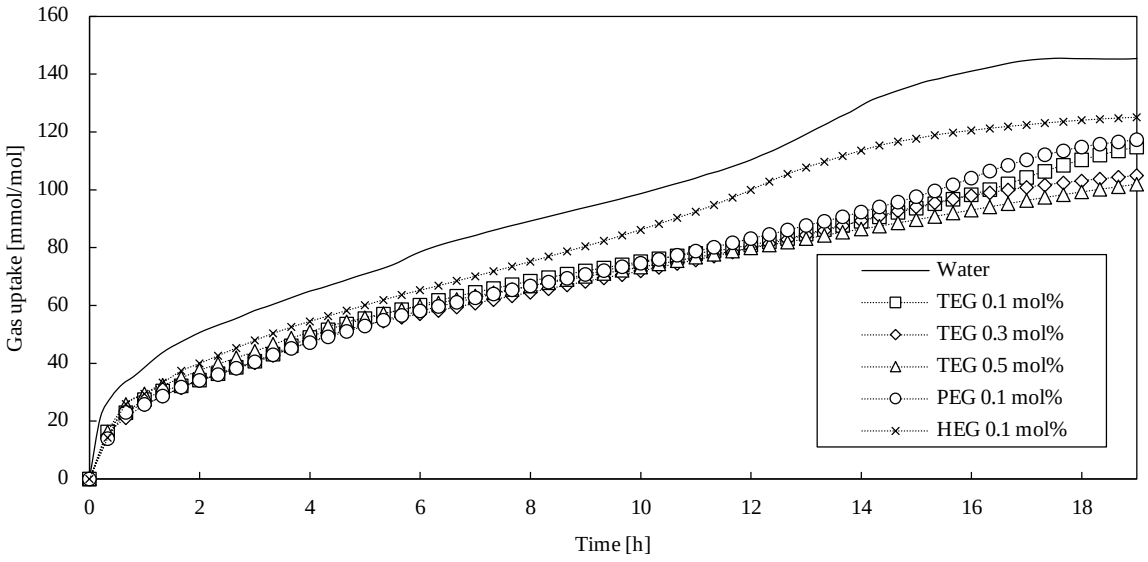

Figure 5-36 Average gas uptake [mmol/mol] over time for methane hydrate formation in presence of different polyethylene glycols with varying concentrations

It is visible that all substances show a clearly kinetically inhibiting effect in comparison to measurements without any additives. TEG in all concentrations and PEG take nearly the same course and start to divide after approximately 12 hours. HEG has a slightly higher growth speed in comparison to the other polyethylene glycols. Therefore, the kinetically inhibiting effect seems to be less pronounced than the other polyethylene glycols. With the help of Figure 5-37, which features the average final gas uptake with standard deviation, a ranking can be created.

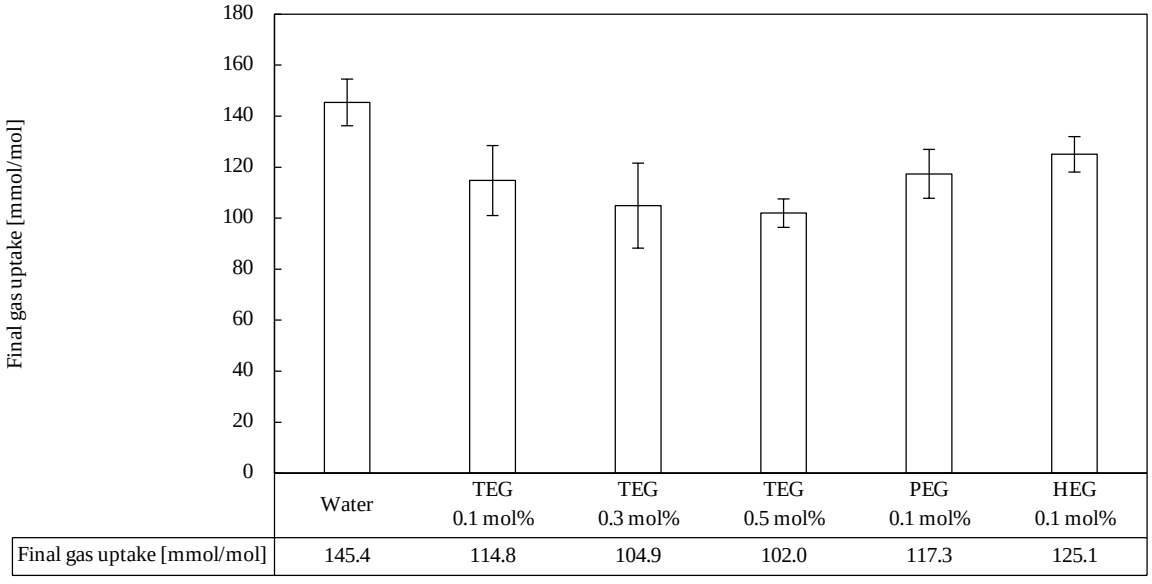

Figure 5-37 Average final gas uptake [mmol/mol] with standard deviation for methane hydrate formation in presence of different polyethylene glycols with varying concentrations

The tested polyethylene glycols can be arranged in the following order starting with the least inhibiting substance:

HEG 0.1% < PEG 0.1 mol% < TEG 0.1 mol% < TEG 0.3 mol% < TEG 0.5 mol%.

Thus, it is stated that the here found kinetically inhibiting effect increases with a smaller molecule size and particularly in higher concentrations. To conclude, the inhibiting effect of acyclic ethers was proven once more in this chapter. As higher mole fractions of a polyethylene glycol contribute more to the inhibiting effect than its amount of ether groups, it is clear why ethylene glycol as a low cost, low viscosity, and in liquid hydrocarbons low soluble inhibitor has an outstanding position [34].

6 Promoting coating

This chapter deals with the development of a surface active coating to promote gas hydrate formation and parts have been published in [136]. Former studies already considered the use of inhibiting coatings [137]. For example, Schultz et al. and Merkel developed an inhibiting surface based on polyethylenglycol [120,138]. An anti-agglomeration effect was achieved by the usage of polydimethylsiloxane [139]. To obtain promoting effects, Li and Wang modified particles with octadecyltrichlorosilane reducing the induction time of gas hydrate formation [140]. Furthermore, thermodynamic promotion was observed during gas hydrate formation in “dry water” made from water and hydrophobic nanoparticles [141]. Nguyen et al. stated that a hydrophobic surface can lead to an interfacial gas enrichment (IGE) and an increased tendency of local ordering of water thereby leading to promoted gas hydrate formation [142]. Different surface characteristics have a clear influence on the gas hydrate formation. This chapter investigates the influences of surfaces modified with silanes of varying chain length, and therefore different contact angles and hydrophobicity, on methane hydrate formation under transient and stationary operating conditions in a stirred tank reactor.

6.1 Modification procedure and evaluation of the coating characteristics

The tested silanes are triethoxysilanes with varying chain length. Additionally a superhydrophobic silane with a fluorized carbon chain is tested. The structures can be obtained from Table 6-1.

Table 6-1 Used silanes with corresponding structure for the development of a promoting coating

Name	Structure
Ethyltriethoxysilane (ES)	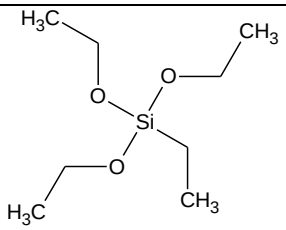
n-Octyltriethoxysilane (OS)	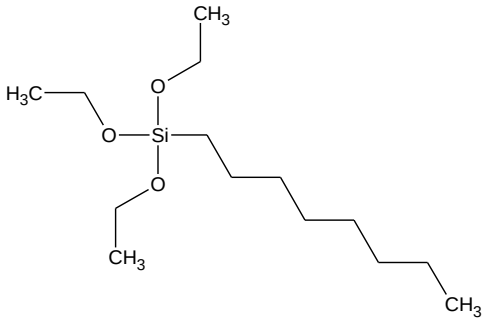
n-Dodecyltriethoxysilane (DS)	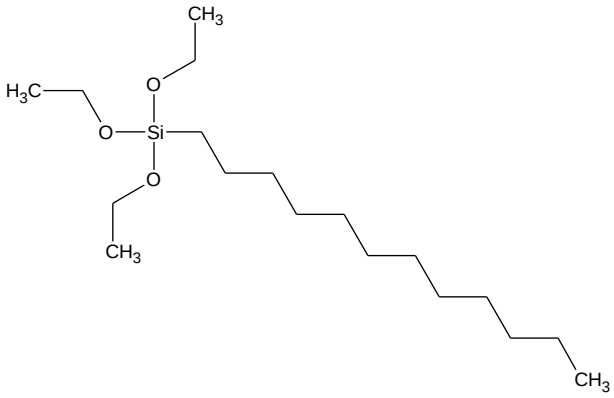
1H, 1H, 2H, 2H Perfluorooctyltriethoxy-silane (PS)	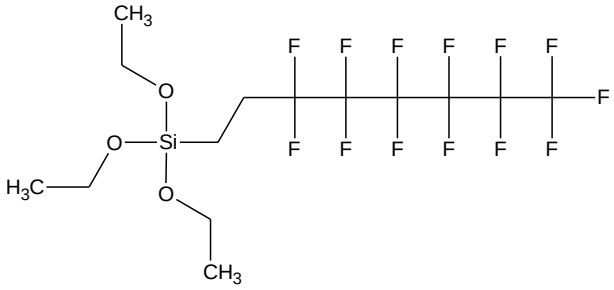

Experimental procedure

For this experimental series, object slides to determine contact angles and reactor fitting soda-lime glasses simulating a coating were modified similar to the process of Kutelova et al. and Jradi et al. [143,144]. Initially, the slides and glasses were cleaned and activated by oxidation with peroxymonosulfuric acid (POMSA) which lasted for 24 hours. Afterwards, both were washed with deionized water and dried at 70 °C followed by conditioning with ethanol and a further drying at 70 °C. Subsequently, the materials were modified by using a fresh solution of ethanol and 1 Vol-% of a corresponding silane. To specify an appropriate reaction time for the silanization, an object

slide was treated for 1, 4, 7 and 14 days with each silane. The in this way found reaction time was applied to glasses for the reactor coating. The reaction is illustrated in Figure 6-1.

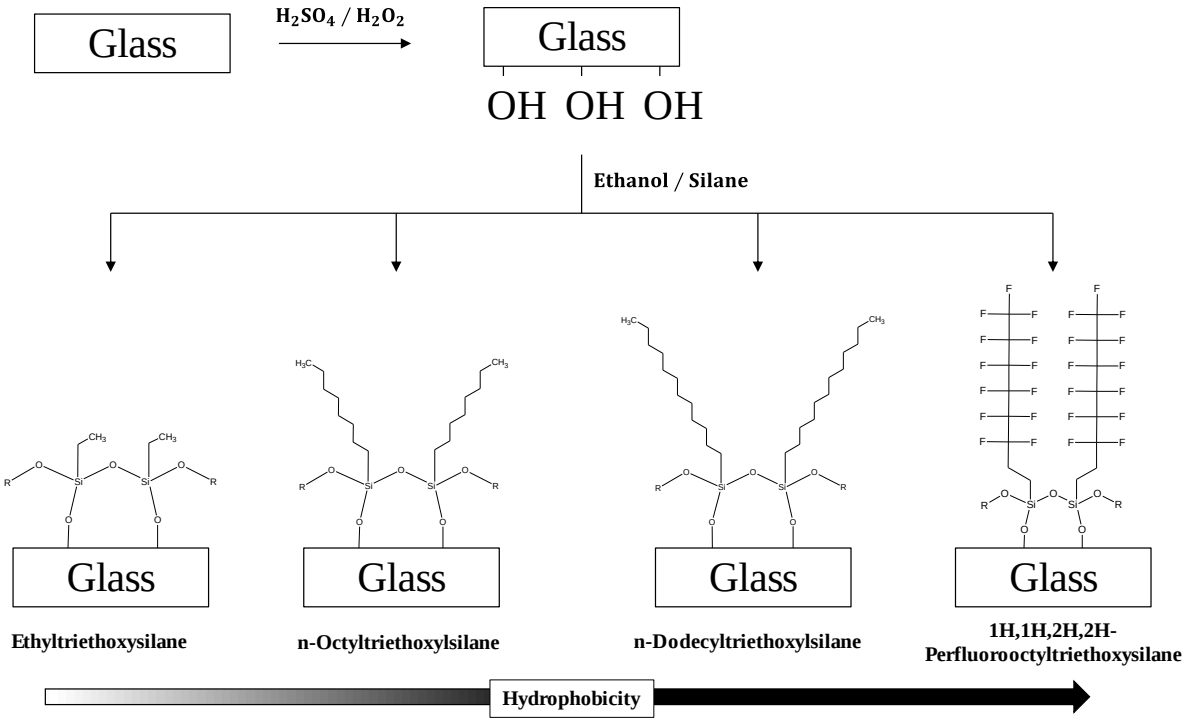

Figure 6-1 Reaction scheme for the silanization of glass

The contact angle measurements were conducted by using a device from Dataphysics type "OCA 15 plus". Three object slides were prepared for each silane and measured five times.

Results and discussion

The objective of this experimental series was to measure the contact angle of surfaces modified by silanization as a measure of their hydrophobic character and to find an appropriate reaction time for the surface treatment of the reactor fitting soda-lime glasses. Figure 6-2 shows the results.

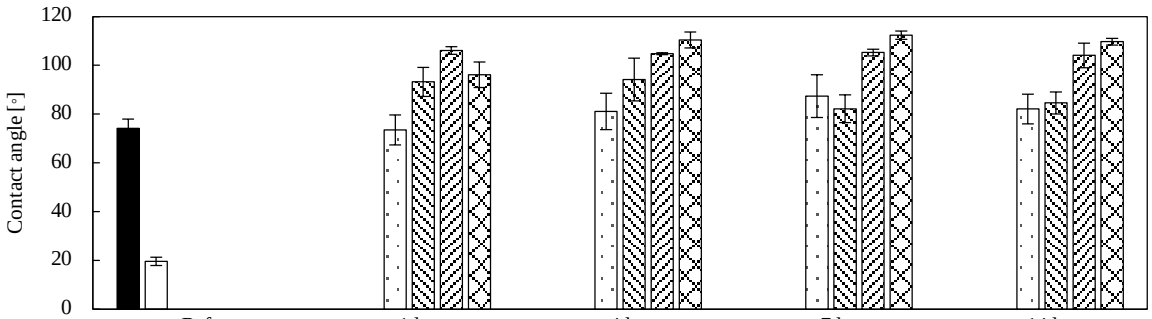

	Ref.	1d	4d	7d	14d
Steel	74.2				
Blind	19.6				
ES		73.5	81.1	87.3	82.1
OS		93.2	94.2	82.2	84.6
DS		106.1	104.7	105.3	104.1
PS		96.1	110.4	112.4	109.7

Figure 6-2 Average results from the contact angle measurements with standard deviation. Steel reference obtained from [145].

According to Chang and Hsiao, 316L steel has a contact angle of 74.2 ° and is used to characterize the surface of the Parr reactor [145]. Another reference measurement of an object slide after the treatment with POMSA and ethanol after the first conditioning process was performed to characterize a clean glass surface. The results seem realistic as, for example, a contact angle for water on an ES-surface is given in literature with a value of 80 ° and 100 ° on a DS-surface [146,147]. One can see that after a silane modification for at least four days, all object slides had higher contact angles and therefore an increased hydrophobicity in comparison to a cleaned glass or steel surface. Beyond four days, the differences between the silanized surfaces became worse that is why a reaction time of 4 days was chosen for the modified reactor fitting glasses. A detailed explanation of the mechanism exceeds the scope of this section. Potentially multi molecular layers occurred which are linked in a loose network, and/or intermixed besides of the fact that covalent bonds may form, break and reform continuously. In addition, functional groups are not absolutely orientated planar on the substrate surface [148]. The successful silanization of the reactor fitting glasses was verified optically and is shown in Figure 6-3.

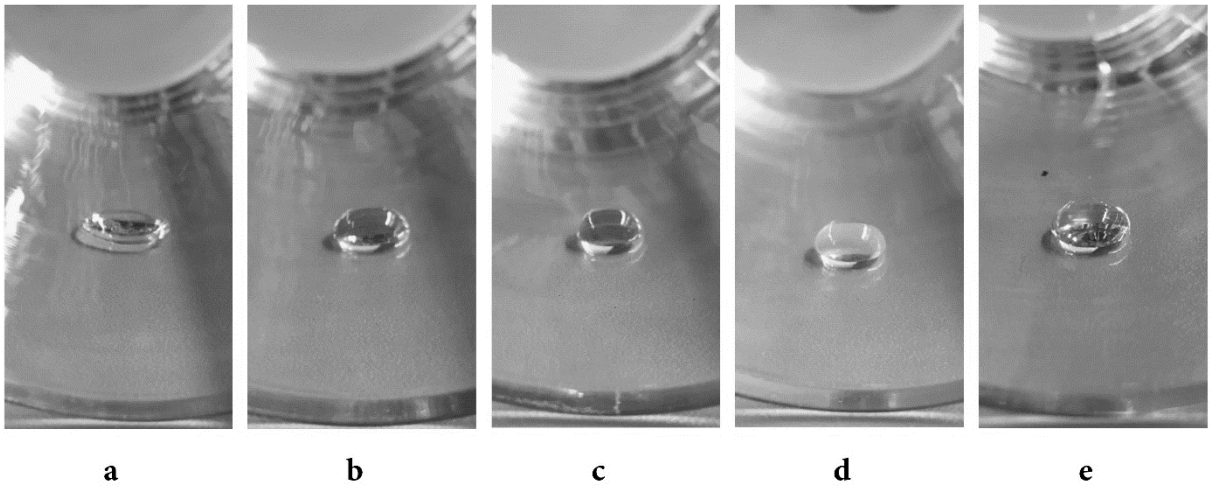

Figure 6-3 Optical verification of the successful silanization of the reactor glasses. a – unprocessed glass, b – ES, c - OS, d – DS, e – PS

6.2 Influences in presence of the promoting coating

This chapter presents the experimental series to investigate the influences of different coatings with an increasing hydrophobicity on gas hydrate formation under stationary and transient conditions.

Experimental procedure

The experimental series was performed in the Parr reactor system (see chapter 3.1). The stirrer setup included a self-priming paddle shaped gas entry stirrer in the liquid phase and a pitched blade stirrer in the gas phase. Stirring frequency was set to 900 rpm, leading to turbulent conditions at Re ≈ 10571. Under stationary conditions the following test procedure was performed: Initially, Milli Q Water was vented 15 minutes under stirring to remove oxygen. Afterwards 200 ml water were filled into the reactor which was cooled down to an experimental temperature of 4 °C. To remove air and create a pure methane atmosphere, the gas phase was purged three times by pressurizing to 5 bar(g) and depressurizing to 0.5 bar(g). Subsequently, the reactor was filled with methane to the start pressure of 100 bar(g) during stationary and to 150 bar(g) during transient tests. By reaching the experimental pressure, the stirrer was turned on, measurements started and lasted for 19 h after occurrence of gas hydrate induction. Each experiment was repeated 3 times. During steady experiments, the gas flow was measured. With regard to the non-steady trials, the pressure trend is converted into the gas uptake by using the Peng-Robinson EoS.

Results and discussion

Figure 6-4 shows the average measured induction times with standard deviation of three repetitive measurements of the steady experiments.

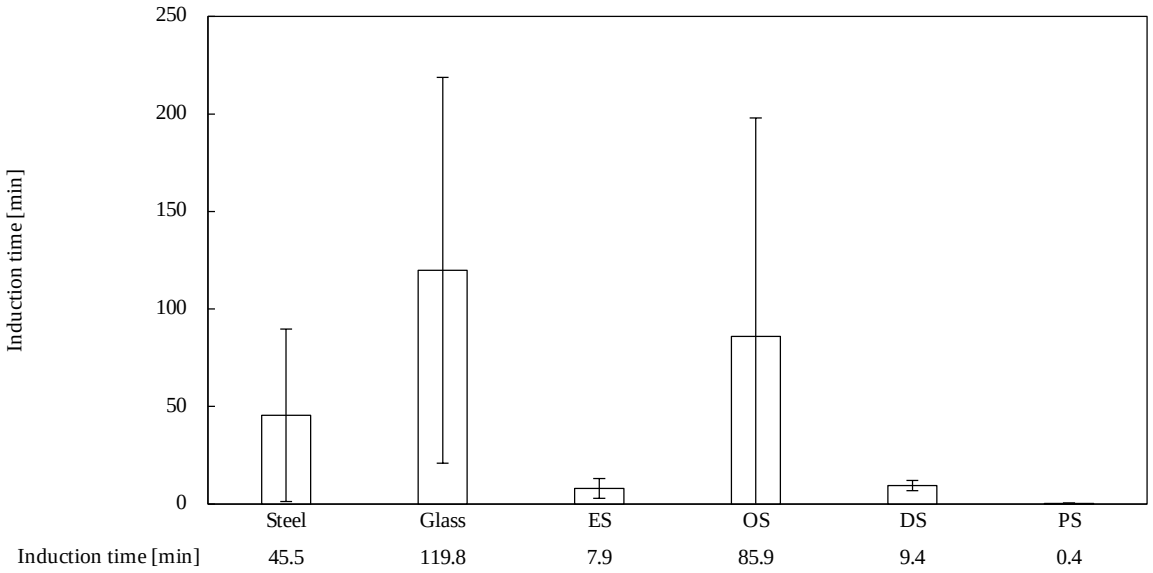

Figure 6-4 Average induction times [min] with standard deviation in presence of different coatings

As the induction is stochastic, especially the steel, glass and OS surface show widespread deviations. In comparison to pure steel, the unprocessed glass and the OS-coating inhibit the methane hydrate formation, whereas the ES-, DS and PS-coating have a significant promoting effect. Figure 6-5 shows the average gas uptake in mmol gas per mol water over time and after 19 hours with standard deviation of three repetitive measurements.

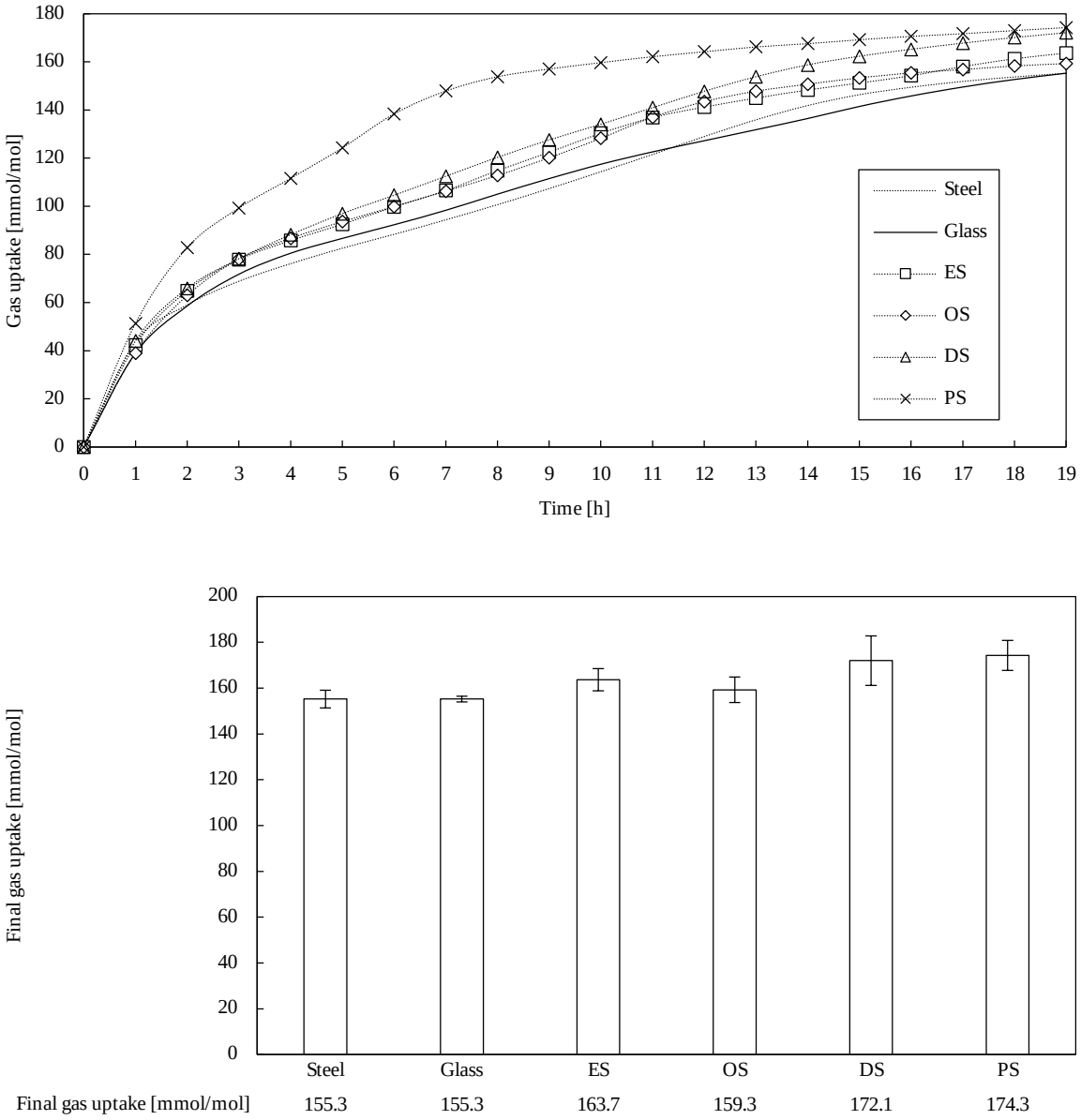

Figure 6-5 Stationary experimental trends in presence of different coatings; Averaged gas uptake [mmol/mol] with standard deviation for methane hydrate formation

By using Figure 6-5, all tested surfaces can be ranked in view of the gas hydrate formation kinetics and the final gas uptake:

$$\text{Steel} = \text{Glass} < \text{OS} < \text{ES} < \text{DS} < \text{PS}$$

All coatings have a promoting effect compared to the uncoated steel or glass surface. However, no correlation between the raising carbon chain length of the used silanes and the gas hydrate formation was obtained. The highest improvement of gas hydrate formation was achieved with the PS-coating which increased the final gas uptake by approx. 12 %. Therefore, a promoting coating should have the highest hydrophobicity possible in order to achieve the largest promoting effect. Similar results were obtained from the unprocessed glass and steel tests. Although, the contact angle and hydrophobicity of the unprocessed glass are lower. One explanation could be that both surfaces were only cleaned with deionized water and possess a rough, aged surface with

unevenness which facilitates a heterogenic nucleation in a way that there is no measurable difference in their effectiveness. In comparison to previous works where methane hydrate formation in a stirred steel reactor was investigated and a gas uptake of 125 mmol/mol was measured, a higher value of 155.3 mmol/mol was achieved due to a higher operating pressure (driving force) and an optimized stirring setup (see chapter 7.2) [149]. Figure 6-6 shows the average rate of consumption and final gas uptake with standard deviation of three repetitive measurements in case of the transient experimental series. Induction times were neither recorded nor will be discussed due to immediate nucleation events occurring with the stirrer turn-on.

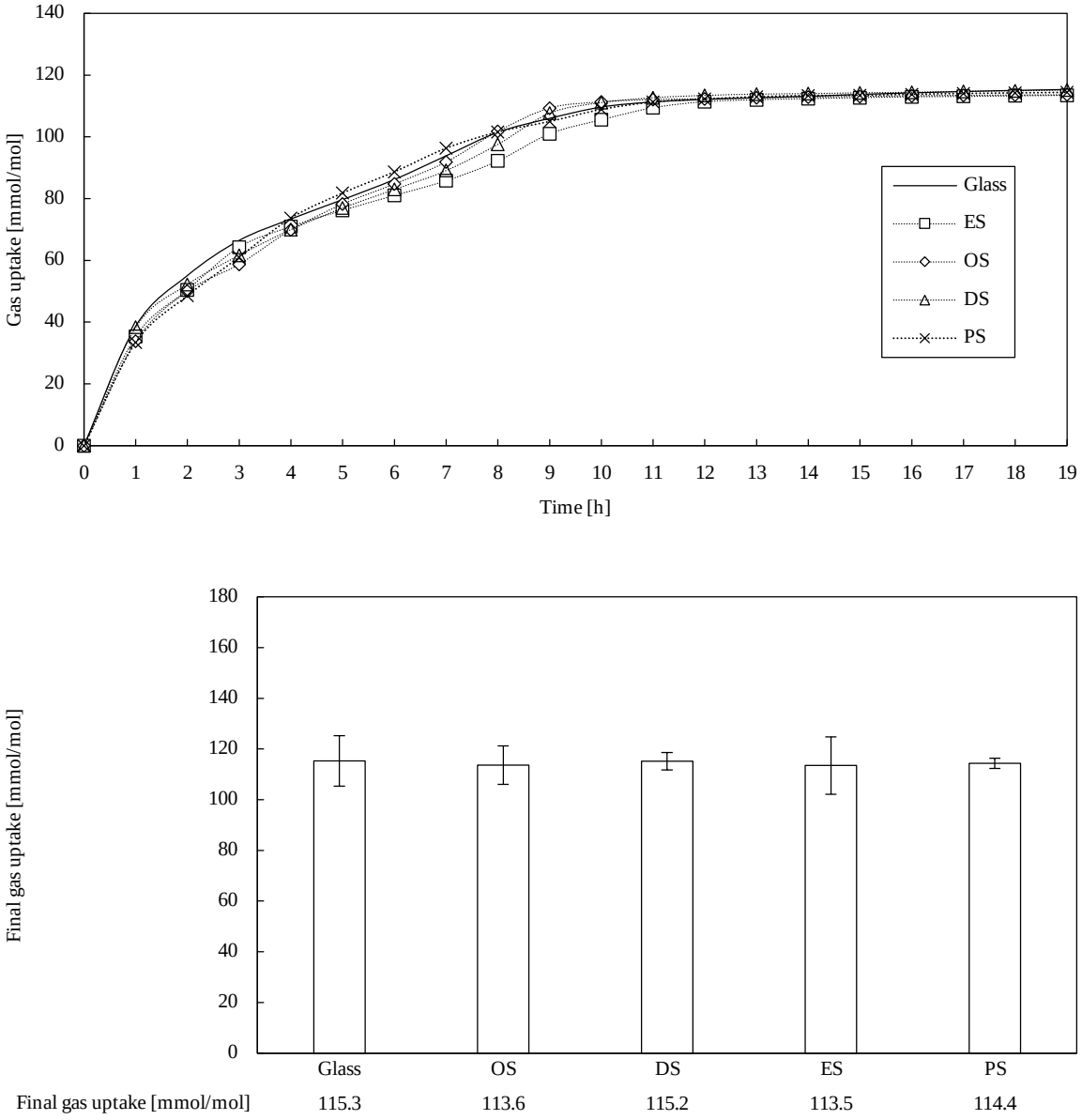

Figure 6-6 Transient experimental trends in presence of different coatings; Averaged gas uptake [mmol/mol] with standard deviation for methane hydrate formation

All coatings show the same trend and differences in the final gas uptake are within the deviation. Therefore, the promoting effect does not exist under transient conditions. This can be explained by the slightly different experimental setup. During *stationary* operation, an ascending pipe is

used to inject gas into the reactor and later right into the hydrate plug. Leaving the ascending pipe outlet, gas diffuses into the gas enriched layer mentioned by Nguyen et al. directly located at the modified glass surface, promoting methane hydrate formation [142]. Gas flows presumably from the bottom to the top of the plug along the modified glass surface. During *transient* operation, gas is stored above the hydrate plug and has to diffuse from the top into the liquid bulk for gas hydrate formation. The gas flow can be described from the top to the bottom. With progressing gas hydrate formation, a hydrate plug seals and impedes the access to the promoting surface similar to a cork. Besides, the driving pressure is becoming less and less in the course of the experiment. After this process, the initially promoting surface has no further effect. Hence, a promoting coating depends significantly on the apparatus and dimensional circumstances. Figure 6-7 outlines and sketches the findings.

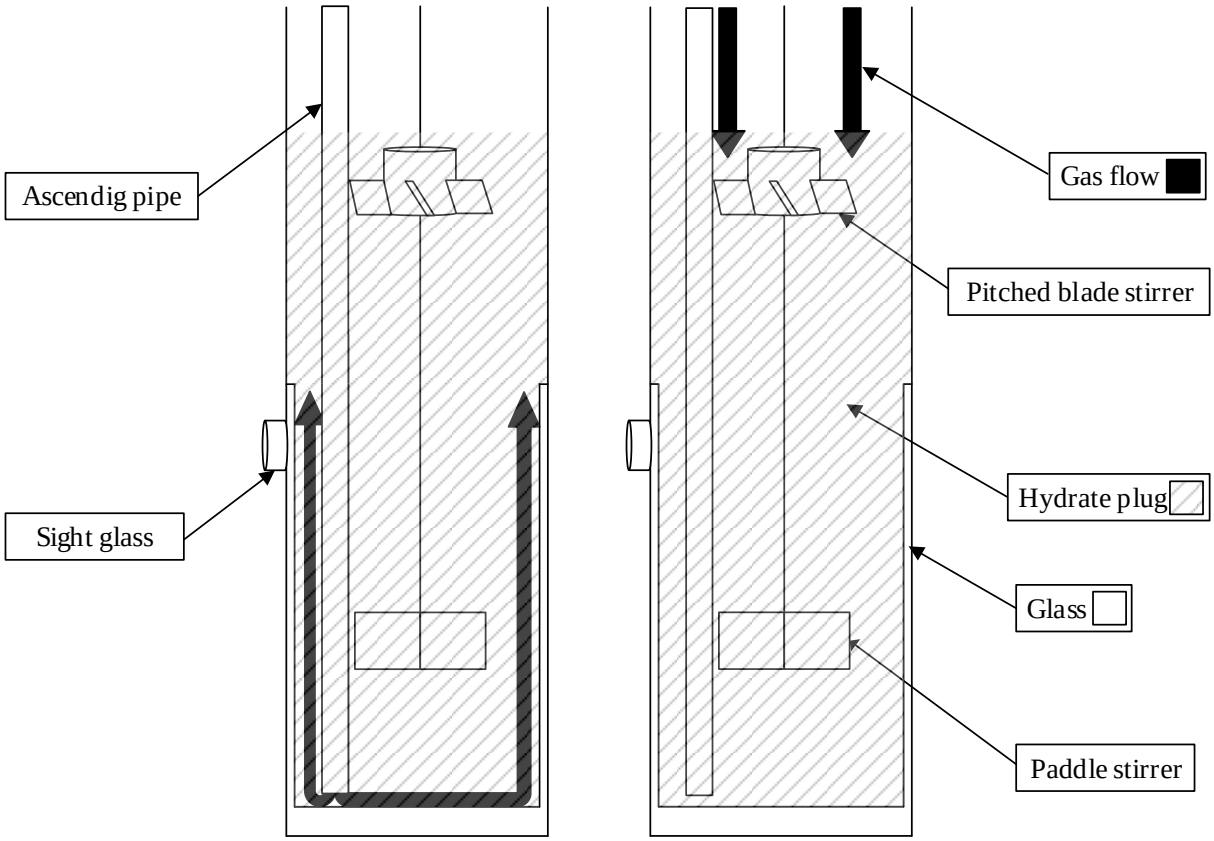

Figure 6-7 Sketch of hydrate plug and gas flow under stationary (left) and transient (right) conditions [136]

7 Technical promotion

This chapter deals with the technical possibilities to promote hydrate formation. Therefore, especially hydrate formation under stirring, spraying and in a packed bed reactor were investigated.

7.1 Influences of different stirrer setups

Mainly gas hydrate experiments were carried out in agitated autoclaves. There were also tests in bench-scale or pilot-plant-scale reactors [150]. Therefore the most used reactor design is the stirred reactor. What is known by now is that the degree of agitation influences the induction time and equilibrium state [6], although Wilson et al. recognized no significant effect in case of nucleation of THF [151]. Over the years, a few works examined the occurring phenomena at different stirring rates [152,153]. Summarizing it can be said that with higher stirring rates, gas hydrate growth is accelerated while this effect is limited to an apparatus dependent rotation frequency. Moreover, this effect can be ascribed to the influence of stirring on heat and mass transfer limitations, where higher turbulences promote interphase exchange activities. Hydrate nucleation can be accelerated by stirring as well [22,23,153–155]. Hence, stirring has a significant impact on the gas hydrate formation.

This experimental series examines the influences of different stirrer setups under turbulent flow conditions on the gas hydrate formation. Transient conditions were used during the experiments so the driving force (pressure) dropped over time due to an entrapment of methane molecules in the gas hydrate cavities. Temperature, pressure, and stirrer torque were measured continuously. Five different setups were used for stirring, shown in Figure 7-1. To investigate the effect of different flow patterns on the hydrate formation, an axial pumping pitched blade stirrer and a radial pumping paddle stirrer were used. The axial pattern is characterized by a wide area axial directed flow along the stirrer shaft and the radial pattern by two toroid vortices above and below the stirrer. The experiments were carried out with 300 rpm to secure turbulent flow conditions at a stirrer Reynolds number of 3263 for the paddle blade stirrer and 3934 for the pitched blade stirrer.

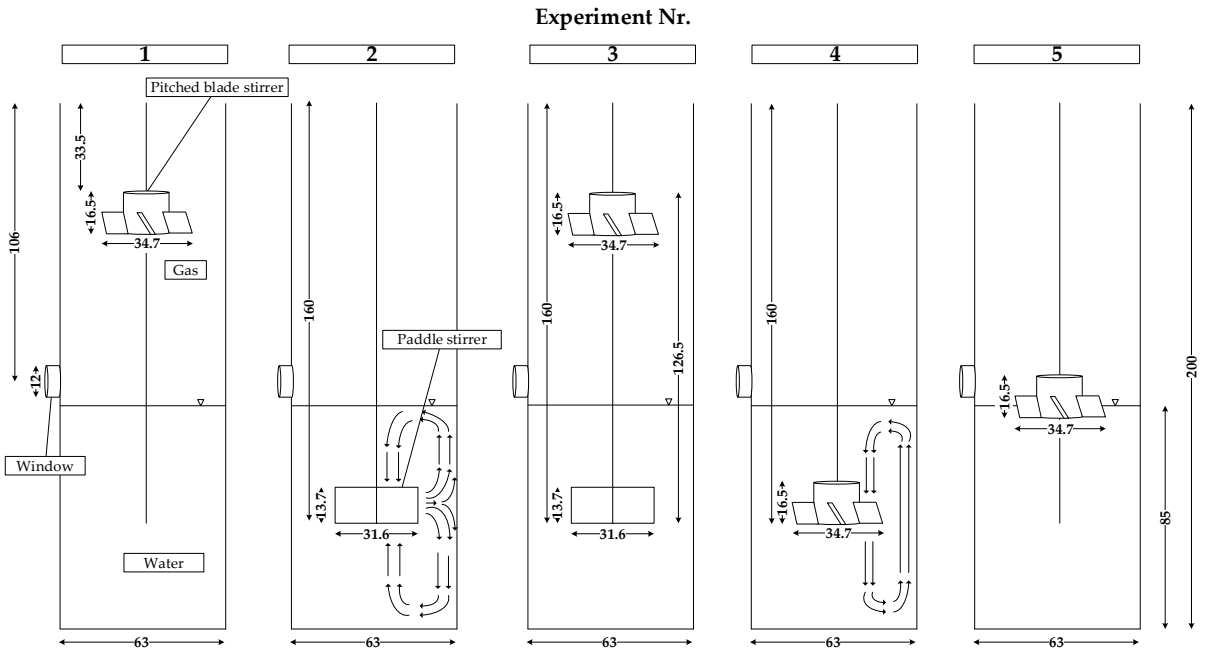

Figure 7-1 Experimental stirring configurations, length specifications in mm, 1 – pitched blade stirrer gas phase, 2 – paddle stirrer liquid phase with radial flow profile, 3 – paddle stirrer liquid phase + pitched blade stirrer gas phase, 4 - pitched blade stirrer liquid phase with axial flow profile, 5 – pitched blade stirrer gas-liquid interphase

The experiments were observed on a random basis via the glass windows. For every stirrer setup, three repetitive measurements were performed. The five different setups were used to find an optimal configuration to form gas hydrates with a reproducible final gas uptake. In addition, the pressure decrease was converted into the gas uptake by using the Peng-Robinson-EoS to make an inference on the hydrate formation mechanism.

Experimental procedure

The experimental series was performed in the Parr reactor system (see chapter 4.1). An experimental procedure had the following course of actions. First, Milli-Q Water was vented 15 minutes under stirring to eliminate the influence of oxygen on gas hydrate formation. Then 250 mL of water were filled into the reactor and heated up to 40 °C to suspend possible "memory-effects". After that, the autoclave was cooled to 4 °C which was the experimental temperature. To remove air and create a pure methane atmosphere, the gas phase was exchanged three times by pressurizing to 6.5 bar(g) and depressurizing to 0.5 bar(g). Afterwards, the reactor was filled with methane to the starting pressure of 150 bar(g). At reaching 150 bar(g), the stirrer was turned on and the measurements started. The experiments ended after 720 minutes, because during that time plugs always occurred. Three repetitive measurements were performed for each setup. Representative $p - M - T$-trends like shown in Figure 7-2 were obtained.

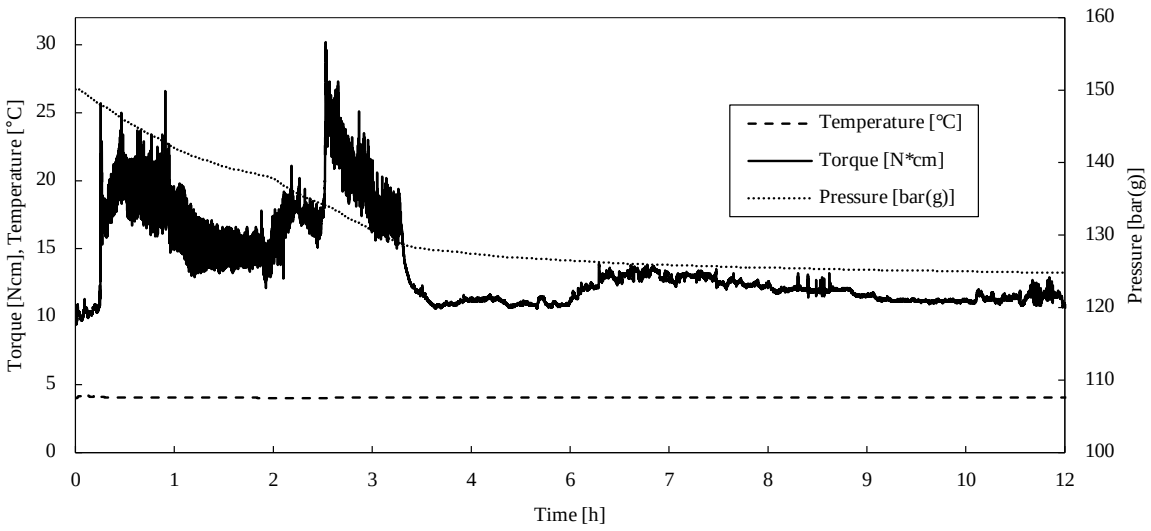

Figure 7-2 Representative experimental trend, *p-M-T*-diagram for experimental series of chapter 7.1

Results and discussion

The average gas uptake trends were calculated from the three obtained pressure trends from each experimental series, shown in Figure 7-3 in comparison to unstirred conditions. The measurements started as the stirrer was turned on, so does the timeline.

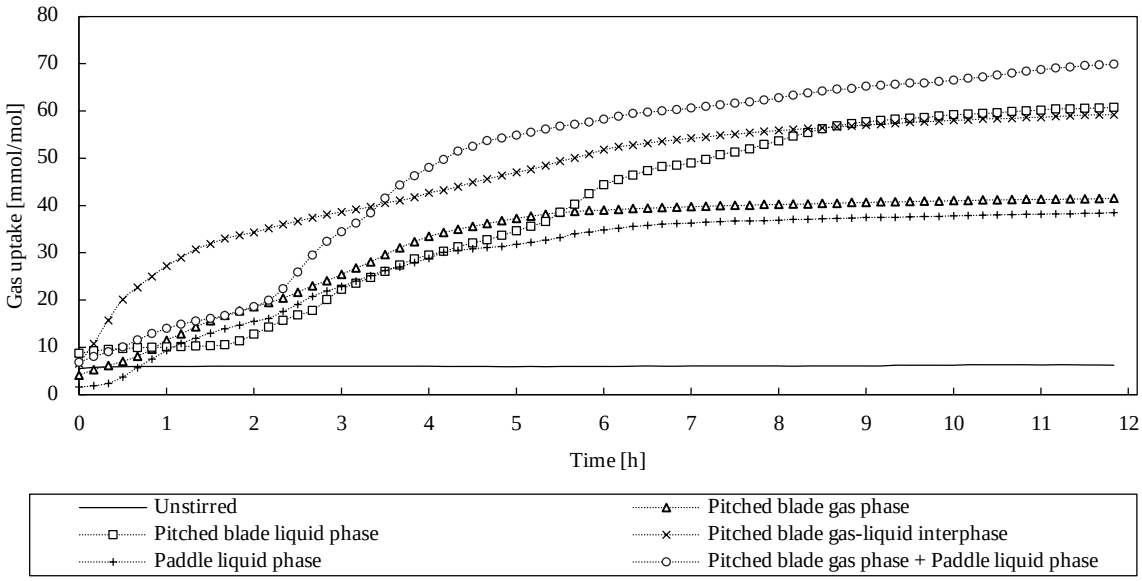

Figure 7-3 Average gas uptake [mmol/mol] for methane hydrate formation with different stirrer setups at 300 rpm

Under unstirred conditions, a small gas uptake can be seen followed by a constant average value of approximately 6 mmol/mol. Stirring of the gas-liquid interphase offers the fastest increase from the start, but slows down after 1.5 hours ending up in an average end gas uptake of 60 mmol/mol. Stirring the gas phase with a pitched blade stirrer compared to using a paddle stirrer in the liquid phase leads to similar trends. Stirring the liquid phase with a paddle stirrer shows a slightly lower average final gas uptake of 39 mmol/mol than stirring the gas phase (42 mmol/mol). The pitched

blade stirrer in the liquid phase shows a kind of plateau in the first 2 hours. After that, a strong increase ends up in an average end gas uptake of 61 mmol/mol. Combining both stirrer types by stirring the gas and the liquid phase shows the second fastest increase in the gas uptake right from the start. The gas uptake accelerates around 130 minutes, leading to the highest average final gas uptake of 71 mmol/mol. The final gas uptake results are visualized in Figure 7-4.

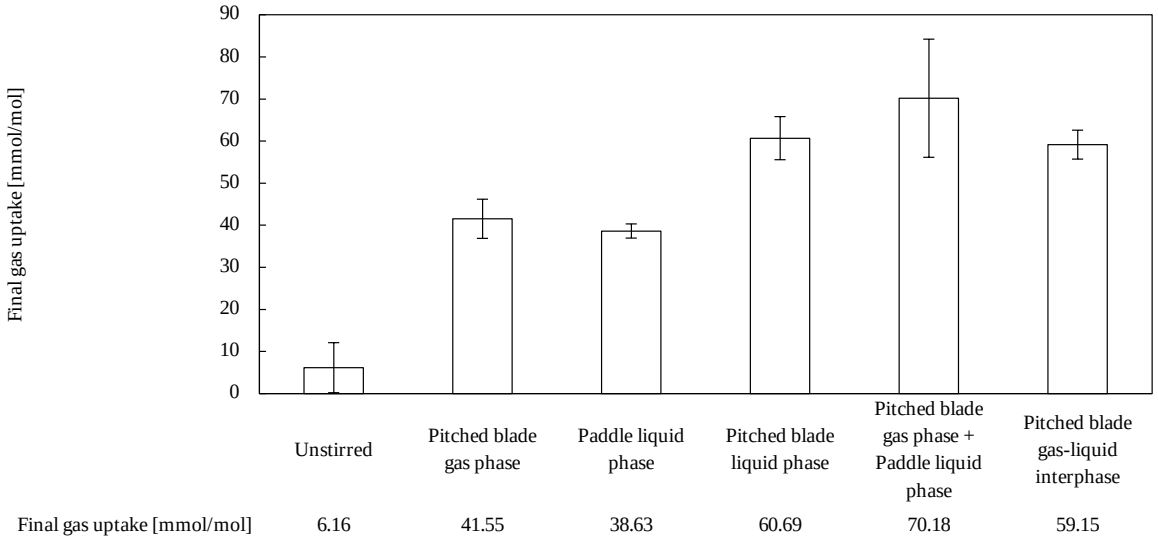

	Unstirred	Pitched blade gas phase	Paddle liquid phase	Pitched blade liquid phase	Pitched blade gas phase + Paddle liquid phase	Pitched blade gas-liquid interphase
Final gas uptake [mmol/mol]	6.16	41.55	38.63	60.69	70.18	59.15

Figure 7-4 Average final gas uptake [mmol/mol] with standard deviation for methane hydrate formation with different stirrer setups at 300 rpm

The results verify that stirring influences gas hydrate formation massively. Without stirring, it is not possible to form gas hydrates within 12 hours in the used test setup. Therefore, the nucleation of gas hydrates can be induced by stirring. Furthermore, there seems to be a relation between gas hydrate formation and stirrer position. Stirring the gas-liquid interphase leads to the fastest gas hydrate formation within the first 3 hours. The glass windows allowed the observation that by starting the stirrer, water droplets were dispersed into the gas phase. This phenomenon was additionally reconstructed in a glass beaker with similar dimensions like the reactor. Hence, the fastest way to induce gas hydrates is to create a high interphase area by scraping and swirling the water surface. This is in agreement with previous works which investigated spraying or sprinkling of liquid water in a continuous gas phase [156–161]. During the experiments it was noticed, that the first gas hydrate crystals arose at the gas-liquid interphase, followed by the formation of a gas hydrate slurry, which grows vertically along the stirrer shaft in both phases, forming a hard but porous hydrate plug enclosing the stirrer. Figure 7-5 shows the enclosed stirrer in a hydrate plug after opening the autoclave.

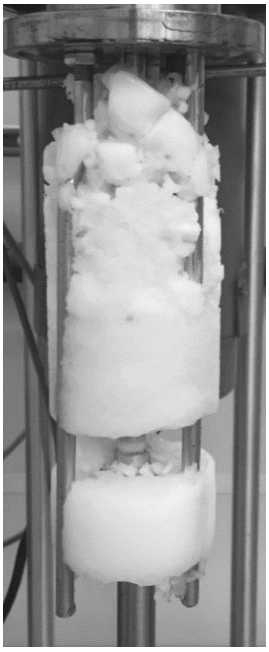

Figure 7-5 Methane hydrate plug enclosed stirrer after opening of the autoclave

This could explain why the liquid phase stirring and the gas-liquid interphase stirring reached nearly the same final gas uptake. The stirring of the gas-liquid interphase induced nuclei immediately whereas the liquid stirring offers an average gas uptake plateau around 11 mmol/mol within the first two hours and therefore no nucleation. During that time, a plug was built during the gas-liquid interphase experiments, which happened in the liquid stirring experiments at approximately eight hours. The stirrer can only affect the gas hydrate growth as long as it is not separated from the surrounding methane enclosed in the hydrate plug core and that is happening faster in the case of gas-liquid interphase stirring. From the point of hydrate plugging, the process is limited by a much slower diffusion transfer rate. That could be the reason why all gas uptake trends reach a state in which stirring has no further influence on the gas hydrate growth, while maximum gas uptake is far from being reached.

Stirring the gas phase comes along with a shorter induction time than stirring the liquid phase with an axial stirrer, resulting in a lower final gas uptake. The rapid induction is explainable by the idea of an axial pumping gas stream penetrating the interphase with methane molecules, which is more effective than reducing the phase transfer resistance on the liquid side by turbulence. The lower end gas uptake provides an indication of preferred hydrate growth into the gas phase in comparison to the liquid phase, affirming an earlier plugging.

Stirring both phases, liquid and gas, leads to the highest final gas uptake. Therefore, penetrating the interphase from both sides accelerates gas hydrate formation, having a longer lasting effect on the hydrate growth than the single stirred setups.

Additionally the stirrer shapes and therefore different flow profiles affect the gas hydrate formation. Probably the pitched blade stirrer with an axial pumping flow pattern induces the formation process later in comparison to the radial pumping paddle stirrer. In return, the pitched

blade stirrer reaches a higher average gas uptake than the paddle blade stirrer. Hence, a radial flow profile has the advantage that it lowers the induction time but also decreases the growth rate. An axial flow pattern promotes the gas hydrate growth longer than the radial flow profile but has an increased induction time. Possibly, the higher energy input in the zone between stirrer and interphase could be a reason. This hypothesis is supported by the fact that the paddle stirrer in the liquid phase showed a slightly higher torque right from the beginning than the pitched blade stirrer. There could be a critical energy dissipation necessary for the gas hydrate induction, similar to the homogenous nucleation barrier known from crystallization processes [6].

The different flow patterns can also explain the better hydrate formation by stirring only the gas phase with the axial stirrer compared to the paddle stirrer in the liquid phase. Based on the diffusional boundary theory, the mass transfer coefficients k_L can be divided into two resistances that a methane molecule has to overcome to get from the gas into the liquid phase. Each resistance can be described through the quotient of the interphase thickness and the diffusivity. As the diffusivity cannot be influenced by stirring, acceleration of hydrate formation can only be achieved by minimizing the interphase thickness either on the gas or the liquid side. The radial flow pattern leads to higher energy input indeed but is affecting the interphase thickness less than the axial stirrer in the gas phase.

In sum, the results show, that gas hydrate formation is a strongly interphase-controlled process which can be manipulated by penetrating the gas-liquid interphase. Skovborg and Rasmussen already developed a phase transfer model to describe the hydrate growth. This model is based on the diffusional boundary theory [24]. Using this approach while replacing the mole fractions with the ideal gas law leads to following equation:

$$\frac{dn}{dt} = k_L A(n^* - n) \rightarrow \int_{n_{start}}^{n} (n^* - n)\, dp = k_L A dt \rightarrow \ln\left(\frac{n^* - n_{start}}{n^* - n}\right) = k_L A\, t \qquad \text{Eq. 7-1}$$

Eq. 7-1 describes the change in the molar amount over time $\left(\frac{dn}{dt}\right)$ proportional to the mass transfer coefficients k_L, the gas-liquid exchange area A and the difference between the maximum amount of substance n^* and the consumed amount n. The starting amount of substance is labeled with n_{start} and equals to zero as no gas is consumed at the beginning. By using the measurements and assigning $\ln\left(\frac{n^*}{n^*-n}\right)$ on the ordinate and the time on the abscissa, linear regressions are created to determine the gas transmission rate in the first 300 minutes (See Figure 7-6). Like in Skovborg's work, the induction time is unaccounted for the linearization.

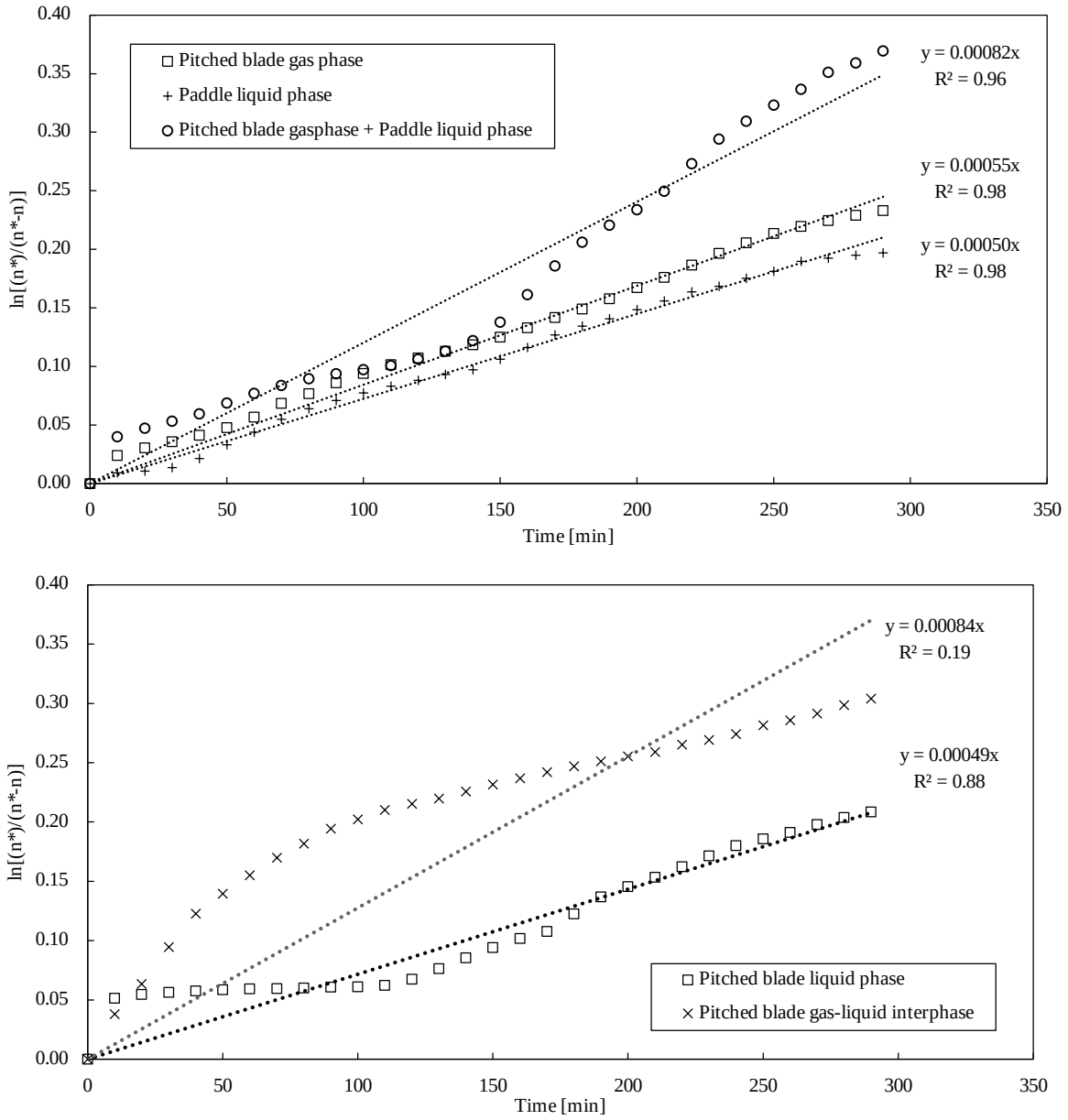

Figure 7-6 $\ln\left(\frac{n^*}{n^*-n}\right)$ vs. time for the stirring setups: paddle stirrer liquid phase, pitched blade stirrer gas phase, paddle stirrer liquid phase + pitched blade stirrer gas phase, pitched blade stirrer liquid phase, pitched blade stirrer gas-liquid interphase

Aside from the "pitched blade gas-liquid interphase" measurements, all regressions fit with a correlation coefficient ≥ 0.88. The slope can be used to evaluate the gas transmission rate $k_L A$. Table 7-1 shows the obtained results.

Table 7-1 Calculated gas transmission rates

Setup	k_LA [1/min]	Correlation coefficient
Pitched blade gas phase	0.00055	0.98
Paddle liquid phase	0.00050	0.98
Pitched blade gas phase + Paddle liquid phase	0.00082	0.96
Pitched blade liquid phase	0.00049	0.88

At this point, a comparison to the calculated mass transfer coefficients by Skovborg is not possible, due to the unknown interphase exchange area, which can only be determined by CFD modeling or e.g. optical measuring methods. For industrial applications, it is sufficient to know the gas transmission rate. Compared to the k_LA values of Herri et al. (approximately $10^{-3}\ to\ 10^{-2}\ s^{-1}$) the found values are much smaller. The reason for that is that Herri observed methane hydrate particles, and this work is focused on the methane hydrate slurry and plug formation process where smaller transfer coefficients are expected [162].

This leads to the conclusion that the gas hydrate formation rate can be controlled right from the beginning by either changing the volumetric phase exchange area or the mass transfer coefficient e.g. the interphase thickness. In this case, the process can be modeled like a mass-transport phenomenon based on the diffusional boundary theory. For stirring the gas-liquid interphase, the model does not fit, so it needs a new approach to describe the measured behavior.

This chapter showed that the gas hydrate formation follows the model of the diffusional boundary theory. Furthermore, there is an influence on gas hydrate formation depending on the flow profile of different stirrer types, coming along with a different energy input. This could be a hint for an activation energy, which is necessary to induce gas hydrate nucleation and in accordance with the classical nucleation theory [6]. It was observed that plug formation proceeded as follows:

1. Nucleation at the interphase
2. Accumulation of a hydrate slurry
3. Plug formation vertically along the stirrer shaft, preferred into the gas phase
4. Enclosing of the stirrer by a hydrate capsule → Diffusion transfer limited hydrate growth

All states are sketched in Figure 7-7.

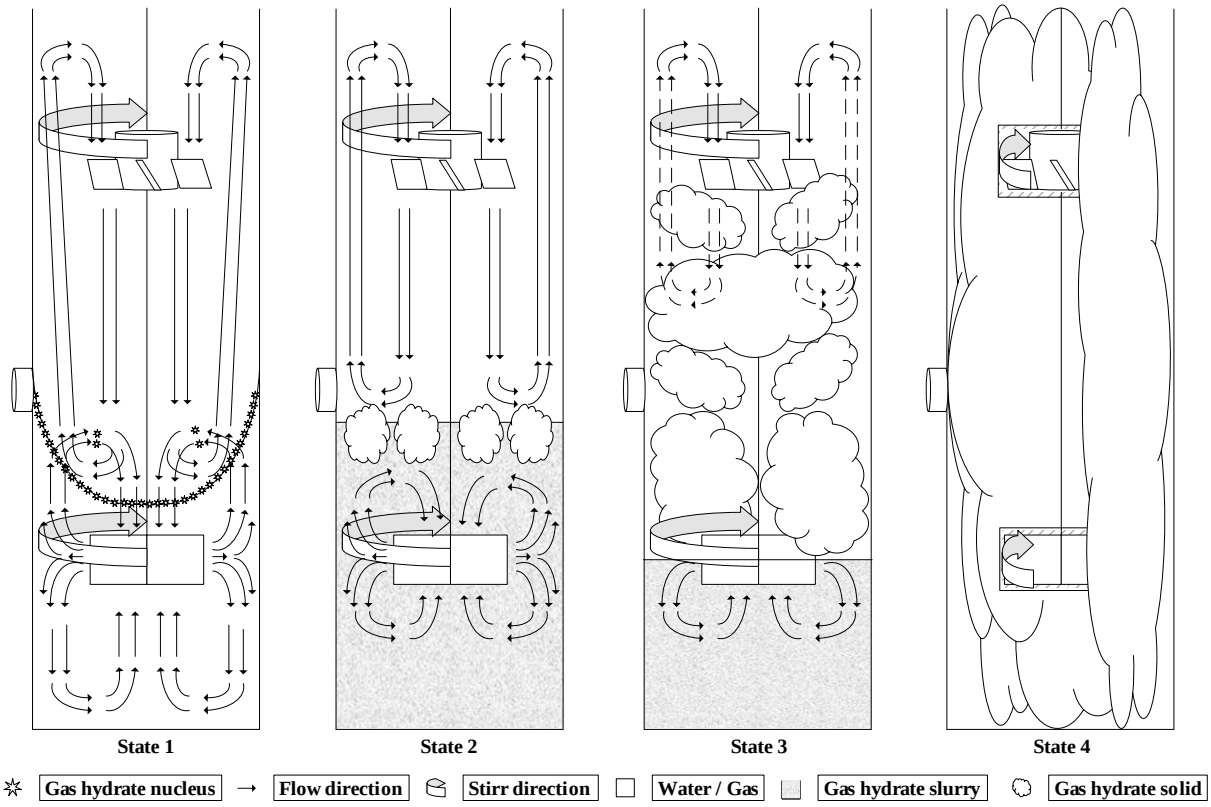

Figure 7-7 Schematic gas hydrate formation mechanism in a stirred reactor system

When intending to produce fast and reproducible gas hydrates, stirring the gas-liquid interphase is preferred. However, to reach the highest methane storage capacity, it is suggested to stir gas *and* liquid phase additionally. Ultimately, the found complex influences of the stirrer system show that it is not sufficient for a detailed mathematical description of the gas hydrate formation to do investigations with magnetic stirrer bar setups. The influence of a suitable stirring setup to secure a maximum mass and heat transport appears to be an essential factor for the optimization of gas hydrate storages.

7.2 Determination of scale-up factors for stirred hydrate gas storages

The influences of stirring on the gas hydrate formation are discussed in detail in chapter 7.1. In addition, gas hydrate formation, nucleation and growth is sped up with higher stirring rates, while higher turbulences promote interphase exchange activities and affect heat and mass transfer limitations. However, it seems that the promoting effect of agitation has an apparatus dependent limitation [22,23,152–155]. Therefore, the description of gas hydrate formation through dimensionless numbers delivers an universal approach for calculating an optimal stirrer rotation frequency. Over the years, there were only a few scale-up considerations performed [150,152,163]. Hence, the lack of knowledge, concerning the necessary scale-up examinations, impedes an industrial application of the new and innovative gas hydrate storage technology.
For the scale up of experimental setups to an industrial reactor, dimensionless numbers are used. They describe a chemical or physical problem dimensional homogeneously and reduce the physical relations between several physical variables to independent numbers [164]. Table 7-2 shows the dimensionless numbers relevant in this chapter.

Table 7-2 Relevant dimensionless numbers [164]

Name	Dimensionless number	Physical meaning	Relevance for stirring
Froude	$Fr = \frac{N^2 \cdot d}{g}$	$\frac{\text{centrifugal force}}{\text{gravity}}$	Gas absorption, waterspout
Newton	$Ne = \frac{P}{\rho \cdot N^3 \cdot d^5}$	$\frac{\text{resistance force}}{\text{inertia force}}$	Stirring power
Reynolds	$Re = \frac{\rho \cdot N \cdot d^2}{\eta}$	$\frac{\text{inertia force}}{\text{internal friction}}$	Flow conditions
Weber	$We = \frac{\rho \cdot N^2 \cdot d}{\sigma}$	$\frac{\text{inertia force}}{\text{surface force}}$	Dispersion

Furthermore, two prerequisites must be fulfilled. First, the model experiments must be carried out with the operating parameters equal to the industrial scale. Second, the characteristic lengths must be scaled up in a set ratio. For stirring processes, where the dispersion of a fluid phase is the main task, the specific volume power (P/V) is the criteria which must be constant.

$$\left(\frac{P}{V}\right)_{Model} = \left(\frac{P}{V}\right)_{Industrial\ scale} \qquad \text{Eq. 7-2}$$

This chapter investigates the influence of different rotational frequencies on the gas hydrate formation and experiments were performed in the Parr reactor system (chapter 4.1) by using

methane as guest molecule. Temperature, pressure, and stirrer torque were measured continuously. By determining dimensionless numbers, it is possible to gain a deeper understanding of the gas hydrate formation process and give some practical advice for promoting gas hydrate growth. The stirrer setup consisted of an axial pumping pitched blade stirrer in the gas phase and a radial pumping paddle gas entry stirrer in the liquid phase. Figure 7-8 shows the setup.

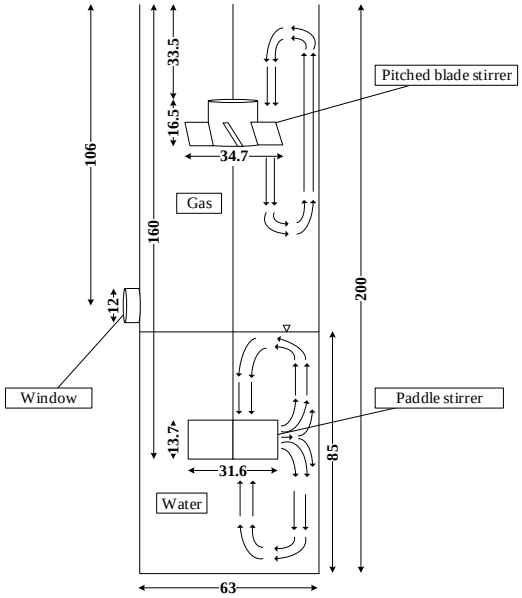

Figure 7-8 Experimental stirring configuration with characteristically flow patterns, length specifications in [mm]

An axial flow profile is characterized by a wide area axial directed flow along the stirrer shaft. A radial pattern shows typically two toroid vortices above and below the agitator. The stirrer rotation frequency was varied between 10 rpm and 1200 rpm. It is important to say that the necessary rotation frequency for gas entry of the gas entry stirrer is around 610 rpm. Pressure [bar(g)], temperature [°C], rotational frequency [min^{-1}] and stirrer torque [Ncm] were recorded continuously. The experiments were repeated three times.

Experimental procedure

The experimental series was performed in the Parr reactor system (see chapter 4.1). First, Milli-Q Water was vented 15 minutes under stirring to degas oxygen. Then the autoclave was filled with 250 mL of water and tempered to 40 °C to eliminate possible “memory-effects”. Afterwards, the reactor was cooled to 4 °C, the experimental temperature. The gas phase was purged three times by pressurizing to 6.5 bar(g) and depressurizing to 0.5 bar(g) to remove air and create a pure methane atmosphere. Then, the starting pressure of 150 bar(g) was set by filling the reactor with methane. The measurements started as the stirrer was turned on and ended after 1152 minutes. All experiments have the same experimental time span to enable a quantitative comparison of the gas hydrate formation. Figure 7-2 shows a $p - M - T$-trend obtained from the experiments. On a

random basis observations were made via the glass windows. Each rotation frequency was tested three times to test the reproducibility of the results. The final gas uptake and the average stirrer torque (øM) were calculated. In addition, dimensionless numbers required for a scale-up were determined.

Results and discussion

Figure 7-9 shows the average final gas uptake for the experimental series with standard deviation. It is apparent that with higher rotation frequency the final gas uptake increases hitting a limiting value approximately at 900 rpm. From this point a further increase of the rotation frequency has no further impact as the final gas uptake increases slightly for 1200 rpm.

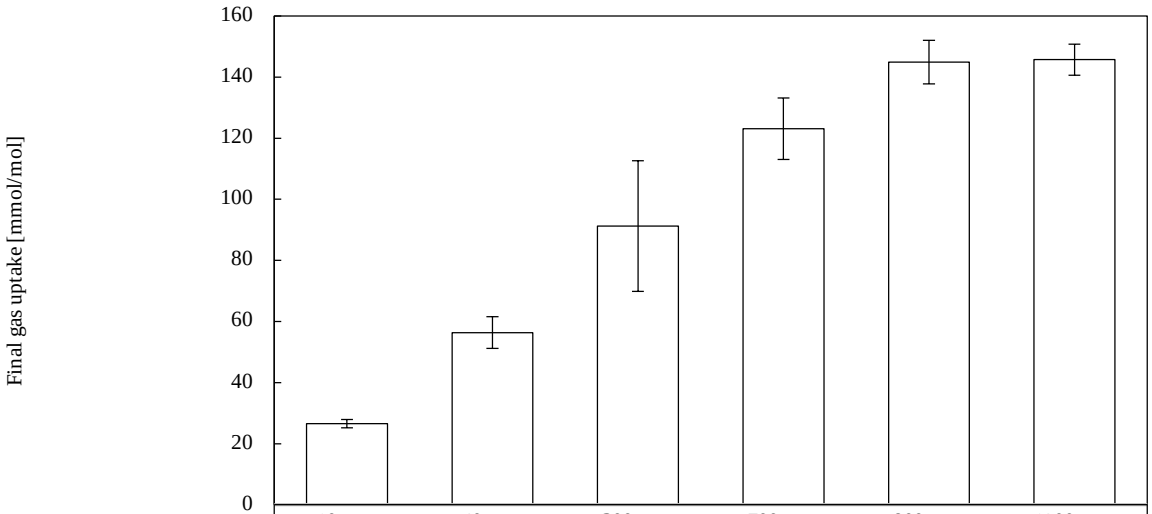

	10 rpm	40 rpm	300 rpm	700 rpm	900 rpm	1200 rpm
Final gas uptake [mmol/mol]	26.6	56.4	91.3	123.1	144.9	145.7

Figure 7-9 Average final gas uptake [mmol/mol] with standard deviation for methane hydrate formation at varying stirring frequencies

The average torque is illustrated in Figure 7-10. Except for the experimental series at 10 rpm, a decreasing trend in the average stirrer torque can be recognized. Compared to the gas uptake, there is the same result that the average torque reaches a certain limiting value.

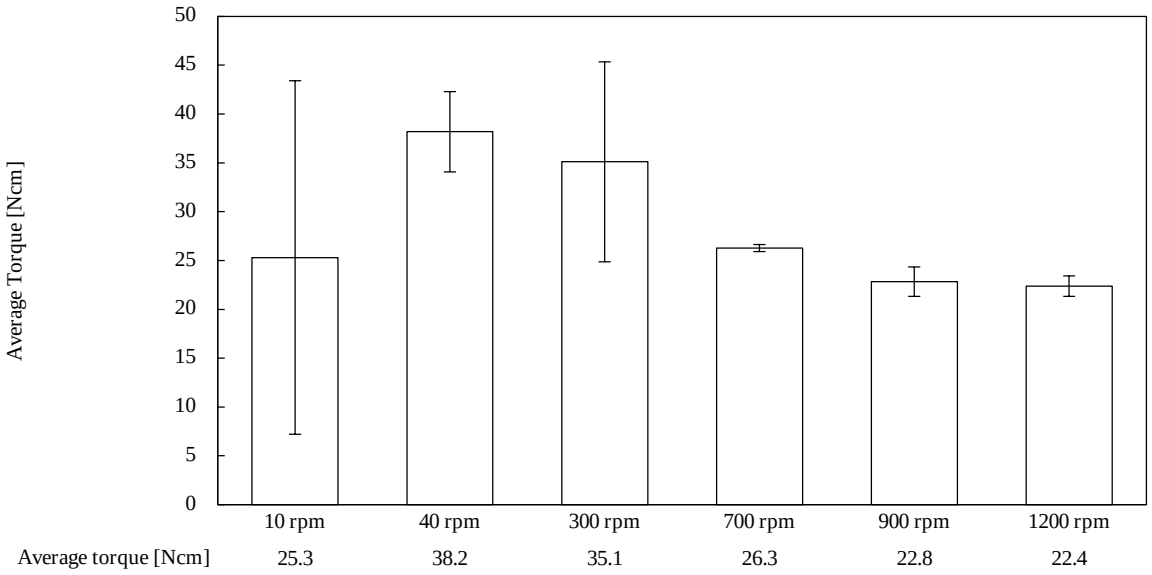

Figure 7-10 Average stirrer torque [Ncm] with standard deviation for methane hydrate formation at varying stirring frequencies

In a next step the dimensionless numbers for a scale-up are calculated. The average power input can be calculated by using the average stirrer torque.

$$P = 2 * \pi * \emptyset M * N \qquad \text{Eq. 7-3}$$

The methane flow through the gas entry stirrer is determined via an approach based on the Bernoulli equation. Δp is the pressure difference at the stirrer tip p_{outlet} and the entry into the hollow shaft p_{inlet}.

$$p_{inlet} + \frac{\rho_{CH_4}}{2} w^2 = p_{outlet} + \frac{\rho_{H_2O}}{2} w^2 \rightarrow w = \sqrt{2 * \frac{\Delta p}{\Delta \rho}} \qquad \text{Eq. 7-4}$$

$$\dot{q} = A * w = A * \sqrt{2 * \frac{\Delta p}{\Delta \rho}} \qquad \text{Eq. 7-5}$$

Table 7-3 includes further necessary material parameters for the calculations. Table 7-4 contains the calculation results.

Table 7-3 Material parameters to calculate dimensionless numbers

Parameter	Description	Value	Unit
$\dot{q}$	Gas flow	f(N)	L/h
A	Cross flow section	7.07E-06	m^2
d	Averaged stirrer diameter	3.315E-02	m
g	Gravity	9.81	m/s^2
Ø M	Average stirrer torque	Depends on experiment	Nm
N	Rotation frequency	Depends on experiment	1/min
η	Dynamic viscosity	1.56E-03	Pa*s
π	Pi	3.14	-
σ	Surface tension water	0.07942	N/m
ρ_{H_2O}	Density water	999.97	kg/m^3
ρ_{CH_4}	Density methane	134.45	kg/m^3

Table 7-4 Calculation results for the determination of dimensionless numbers for the scale-up of a stirred methane hydrate reactor

Stirring frequency [rpm]	Power [W]	Gas flow [L/h]	Fr [-]	Ne [-]	Re [-]	We [-]
10	0.27	-	$9.39 * 10^{-5}$	$1.43 * 10^{8}$	116	12
40	1.60	-	$1.50 * 10^{-3}$	$1.35 * 10^{7}$	467	185
300	11.03	-	$8.45 * 10^{-2}$	$2.20 * 10^{5}$	$3.51 * 10^{3}$	$1.04 * 10^{4}$
700	19.26	31.54	0.46	$3.03 * 10^{4}$	$8.18 * 10^{3}$	$5.68 * 10^{4}$
900	21.52	40.56	0.76	$1.59 * 10^{4}$	$1.05 * 10^{4}$	$9.39 * 10^{4}$
1200	28.12	54.08	1.35	$8.78 * 10^{3}$	$1.40 * 10^{4}$	$1.67 * 10^{5}$

The results prove that stirring influences gas hydrate formation massively. As with higher rotation frequency, the final gas uptake rises as well. However, this effect is limited with a maximum between 900 and 1200 rpm. The same observation can be achieved by drawing the Froude number versus the final gas uptake. (See Figure 7-11)

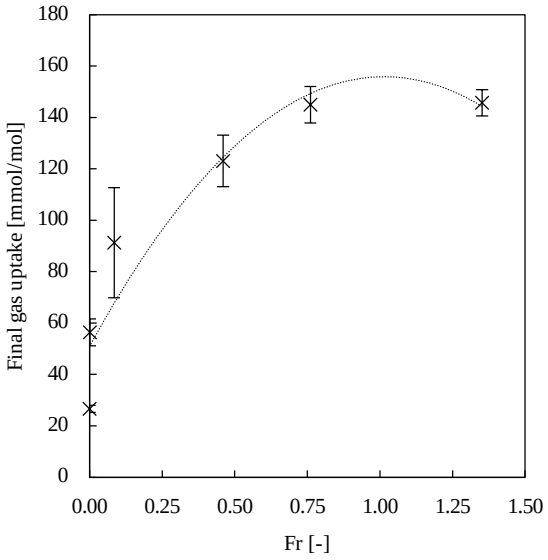

Figure 7-11 Average final gas uptake [mmol/mol] with standard deviation for methane hydrate formation vs. Froude number

With a higher Froude number, the final gas uptake rises reaching a maximum around 1.0. As the Froude number describes the ratio between the centrifugal force and gravity, it can be stated that higher centrifugal forces lead to a stronger formed spout and thereby increasing the gas-liquid exchange area and accelerating the gas hydrate growth. This effect is restricted to the spout depth as with higher rotation frequencies the spout reaches the agitator. Another conclusion is gained from the gravity. On earth it is difficult to influence this parameter, but in space it could be possible to promote gas hydrate formation, which would potentially be interesting for aerospace research.

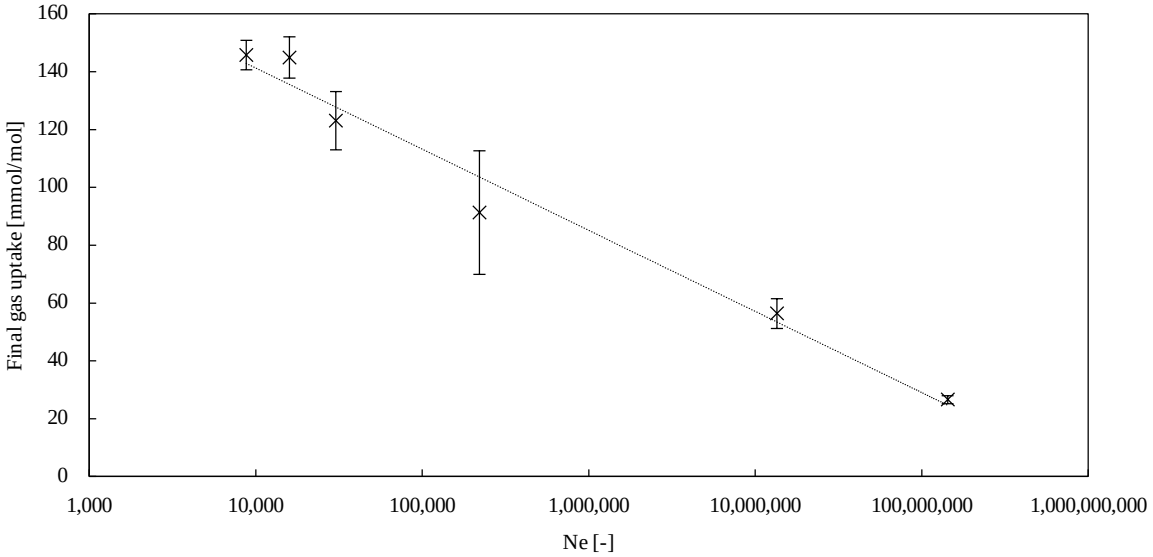

Figure 7-12 Average final gas uptake [mmol/mol] with standard deviation for methane hydrate formation vs. Newton number

Figure 7-12 describes the correlation of the Newton number and the final gas uptake. It is recognizable that with a higher Newton number the final gas uptake decreases. The Newton

number represents the relation between the affiliated motor power and the de facto into the fluid transferred power. Hence, a small Newton number designates an optimal power transmission into the fluid and promotes the hydrate formation. The increased power input facilitates molecular transposition and enhances the mobility of molecules, promoting the formation of hydrate cage structures.

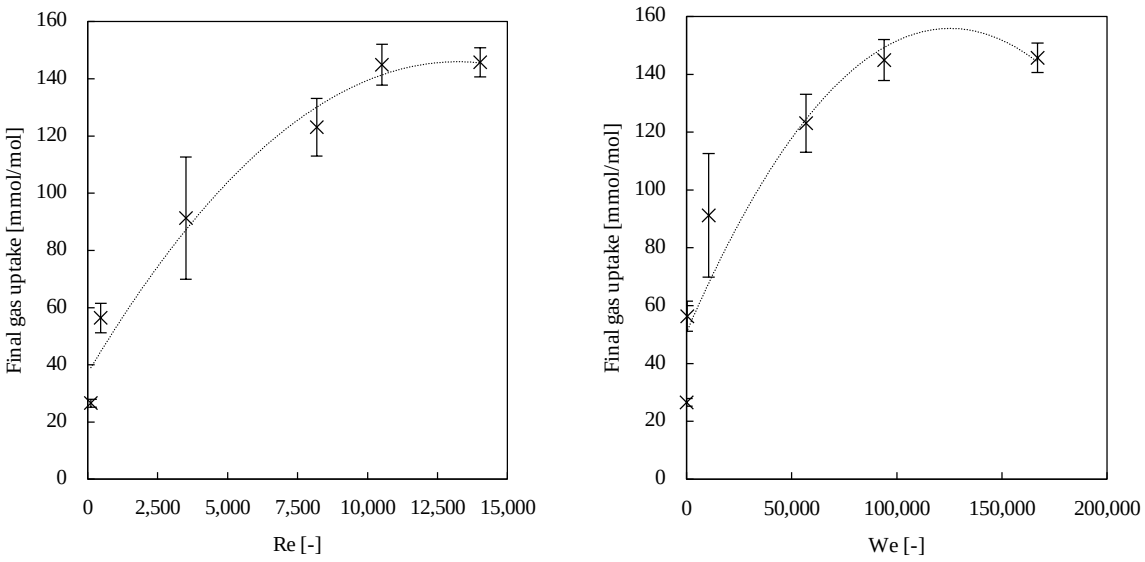

Figure 7-13 Average final gas uptake [mmol/mol] with standard deviation for methane hydrate formation vs. Reynolds number and Weber number

Outlining the final gas uptake versus the Reynolds number and the Weber number shows a similar trend (see Figure 7-13). The final gas uptake increases with higher values of the dimensionless numbers reaching a limitation at the end of the contemplated experimental range. With higher Reynolds numbers, a higher turbulence in the reaction vessel can be achieved. As hydrate formation is a mass transport phenomenon, it is sped up by providing small diffusional boundary layers at the phase exchange areas via turbulence flow conditions.

A higher Weber number characterizes a higher deformation and better suspension of gas bubbles which are supplied by the gas entry stirrer. This means an increase in the phase exchange area and thus in the mass transport velocity. Furthermore, the Weber number exhibits that a decrease in the surface tension accelerates the hydrate formation. This was already an object of several works dealing with the influences of surfactants on gas hydrate formation. The promoting effect of surfactants can be traced back on the lowering of the surface tension and improvement of the methane solubility in the liquid phase [28].

In addition, the final gas uptake was drawn against the gas flow (see Figure 7-14). Only three rates were tested, due to the necessarily high rotation frequencies to achieve gas entry by the stirrer. Therefore, the trend outlines that there could be a limitation or a maximum for the optimal gas flow. However, further investigations are required. Furthermore, it was observed that with the gas entry occurring at a rotation frequency of approx. 610 rpm, the induction of the hydrate

formation appeared immediately. Hence, gas hydrate formation can be induced and controlled by choosing the right agitation setup.

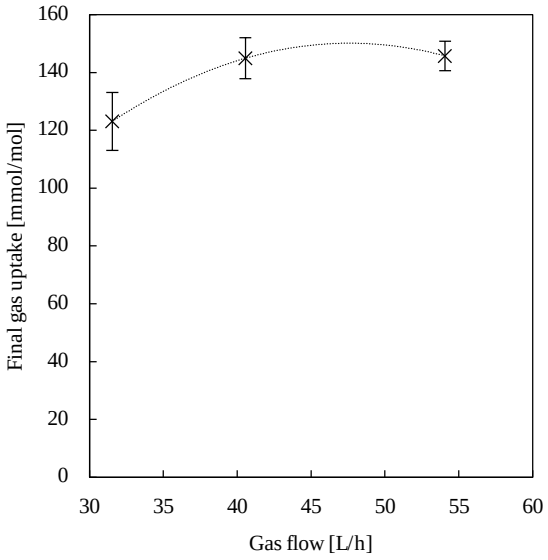

Figure 7-14 Average final gas uptake [mmol/mol] with standard deviation for methane hydrate formation vs. gas flow [L/h]

All investigations lead to the fact, that the hydrate formation process is a mass transport limited process, which can be modeled based on the diffusional boundary theory, e.g. by Eq. 7-2. Hence, gas hydrate formation can be kinetically promoted by either influencing the mass transport coefficient k_L or the volumetric phase exchange area A. The limitations of promoting effects achieved by agitation are apparatus dependent.

This chapter investigated the influences of different rotation frequencies, power inputs and gas entry rates on the gas hydrate formation. It was proved that the promoting effects are explainable by using a model based on the diffusional boundary theory. The found complex influences of the stirrer setup showed that a suitable stirring system to maximize the mass and heat transport plays an essential factor to enable the gas hydrate storage technology. Therefore it is insufficient to only investigate and mathematically model the hydrate formation process with experiments performed with magnetic stirrer bar setups. The key findings gained from the correlation between the final gas uptake and dimensionless numbers are summarized as follows:

- A waterspout increases the phase exchange area and therefore in line with that the gas hydrate formation. It is characterized by the Froude number with an optimum value around 1.0. The effect is limited by the spout depth. Gas hydrate formation in lower gravitation could be faster compared to earth conditions.
- An increased power input into the fluid facilitates molecular diffusion processes and promotes the formation of gas hydrate cage structures. Optimal power transmission is achieved by a Newton number in a magnitude of 10^8.

- Higher turbulences lower the diffusional boundary layer thickness and enhance the mass transfer coefficient. The gas hydrate formation is optimized at Reynolds number dimensions around 10^4.
- Form and size of bubbles can be influenced by deformation through stirring and lowering the surface tension of the liquid. This leads to a higher volumetric exchange area and acceleration of gas hydrate formation. These phenomena can be described by the Weber number. Optimal conditions can be found in a magnitude of 10^5.
- Gas entry under turbulent stirring conditions is capable of inducing gas hydrate formation immediately. There could be an optimum or limiting value concerning the gas flow rate.

Overall, this chapter provides a guideline for the optimization of experimental setups in gas hydrate research. In addition, dimensionless numbers were determined which can be used to do scale-up considerations up to an industrial size.

7.3 Gas hydrate formation in a spray reactor

Spray reactors were already the subject of various studies. Mori et al. performed studies to form structure sH hydrates by spraying water and a promoter into different hydrocarbon atmospheres achieving a high rate gas hydrate production [165,166]. Furthermore, gas hydrate formation via spraying was investigated in a 15L-cell showing a successful rapid methane hydrate production with a maximum uptake larger than 80% in a pilot scale [161]. The effect which accelerates the gas hydrate formation is an increased gas–liquid interfacial area, where gas is dissolved into the liquid phase [150]. As gas hydrate formation by spraying seems to be such a promising approach, the aim of this experimental series was to compare this process with gas entry stirring. Furthermore, a working hydrate spraying process enables the possibility of a new and innovative process of a hydrate absorption, where gas components are separated by absorption and simultaneous enclathration in gas hydrates.

Experimental procedure

The experimental series were performed in the Büchi reactor system (see chapter 4.2). In addition, a recycle for the injection was implemented, consisting of a Bete MicroWhirl MW85 nozzle, an electromagnetic vibration pump Ulka EX5 and a cooling bath. To agitate the liquid bulk phase and secure turbulent flow conditions, a pitched blade stirrer was used. The experimental setup is shown in Figure 7-15.

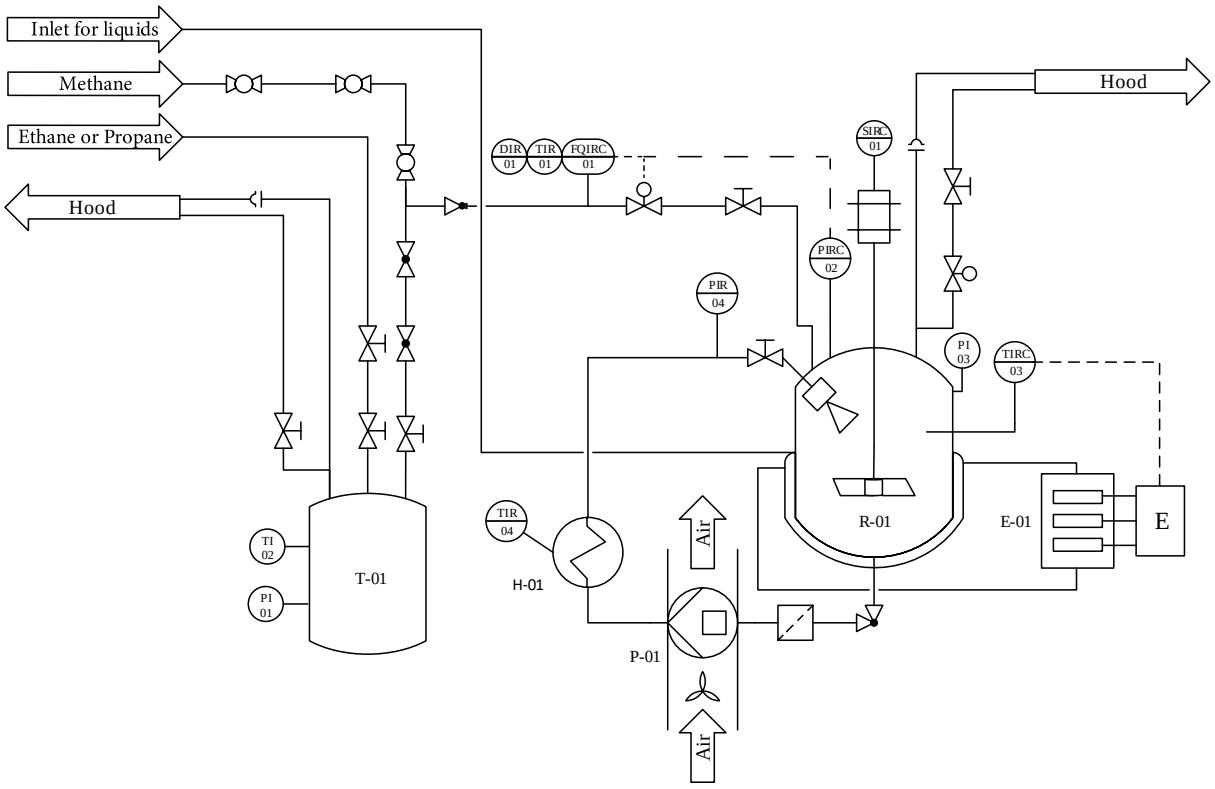

Short sign	E-01	H-01	P-01	R-01	T-01
Name	Thermostat	Cooling bath	Vibration pump	Autoclave	Deposit
Technical data	2.7 kW	10 L	39 L/h	0.5 L	0.7 L
Permitted pressure [bar(g)]	1.7		15	12	100
Permitted temperature [°C]	250			150	250
Material	316L	Glass	Brass	Glass	316L

Figure 7-15 Experimental setup for gas hydrate formation by spraying

Test procedures had the following course of actions. The autoclave was filled with 370 mL of the hydrate forming mixture consisting of distilled water and 5.6 mol% THF. Thereby, 270 mL remain in and are necessary to operate the recycle, not taking part in the gas hydrate formation process. Afterwards, the hydrate forming autoclave was purged 3 times with the gas mixture up to a pressure of 5 bar(g) each time. After purging, the reactor was cooled down to 6 °C, thereafter a pressure of 8 bar(g) was adjusted and the pump for recycle injection via the nozzle and optional the stirrer (900 rpm, Reynoldsnumber ≈ 25483) were started. The injection pressure difference was 11 bar. The external cooling coil temperature is held at 6 °C. The experiments ended after 120 minutes. Gas entry stirring, injection and injection plus stirring are compared and each experiment was repeated three times.

Results and discussion

In sum, the experimental results are presented in Figure 7-16.

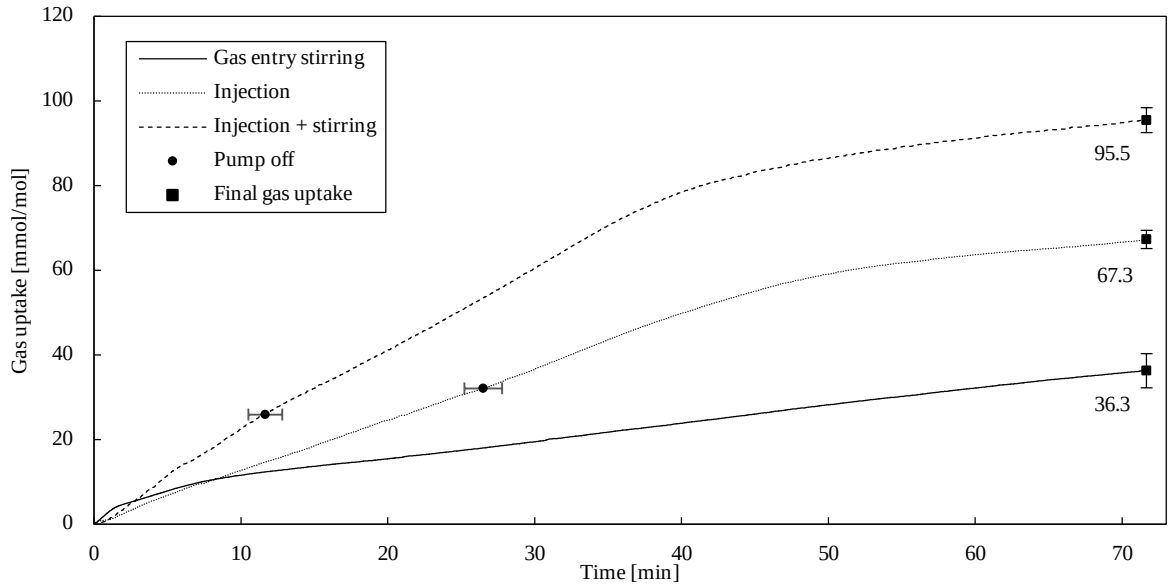

Figure 7-16 Average gas uptake trends with final gas uptake [mmol/mol] and standard deviation for the comparison of methane-THF hydrate formation via gas entry stirring, injection and injection+ stirring

From the experimental trends it can be concluded that spraying plus stirring features the highest and fastest gas uptake, followed by solely injection and finally gas entry stirring being the worst process. The effect which accelerates the hydrate formation is the increased gas–liquid interfacial area caused by the injection. The stirring process is only better in the first minutes due to the sudden gas entry which is accompanied by the start of the stirrer.

In case of the injection, the pump for the recycle must be turned off at a water consumption of approximately 30 mmol/mol water. Afterwards, the pump ran dry and was not able to keep the recycle in operation. Contrary to our expectations, the rate of gas uptake did not slow down subsequently. It is visible that switching off the pump has no effect. It is assumed that fine dispersed water droplets remain as fog in the gas phase, which enable the formation of gas hydrates with an unrestricted growth rate. Once these droplets form gas hydrates and fall into the bulk phase, the growth rate slows down passing over into a diffusion-limited process. Furthermore, in contrast to the stirring process, the injection process enables the possibility to form gas hydrates above the liquid phase as water droplets partly condensate on the reactor walls. The additional stirrer secures turbulent flow conditions promoting hydrate formation due to the same phenomena which are described in chapter 7.1 and 7.2. Considering all effects, the spraying process under turbulent flow conditions is advantageous in comparison to the gas entry stirring.

7.4 Gas hydrate formation in a packed bed reactor

This chapter examines methane hydrate formation in a packed bed reactor system made of silica particles with an average size of 1.15 mm under transient conditions. As natural gas hydrate deposits can be found in deep sea and permafrost areas or rather rock strata or sand sediments, the idea to form gas hydrates in packed bed systems is obvious. However, only a few works dealt with such systems with regard to an industrial application. Back in 2009, rapid growth rates and high water to hydrate conversions were achieved in different silica beds, following a three-state formation mechanism. Thereby smaller particle bed diameters had a stronger promoting effect [167]. Magnetic resonance imaging measurements showed that the gas hydrate formation was enhanced with low water contents and smaller particle diameters [168]. It was also shown that a packed bed reactor system has a superior performance in terms of a fast and complete gas hydrate formation in comparison to a stirred tank reactor [149]. In packed bed reactor systems, gas hydrates form above the particle bed, which requires an upward transport of water. Therefore, capillary forces should play an important role in this reactor design [169].
The influences of the dimensional parameters were already analyzed while the impact of the particles surface properties along with the capillary forces has not been investigated yet. To investigate these effects, silica particles were modified via silanization and sodium dodecyl sulfate was used. The capillary pressure was calculated in each bed configuration by using Eq. 7-6 and set into relation with the final gas uptake. The capillary pressure p_C depends on the porosity ϵ, the volume specific surface area S, the surface tension σ and the contact angle Θ [170].

$$p_C = \frac{(1-\epsilon) * S * \sigma * \cos\Theta}{\epsilon} \qquad \text{Eq. 7-6}$$

Experimental procedure

Modified glass particles and contact angle measurements were made in analogy to chapter 6.1. In addition to contact angle measurements with deionized water, a SDS solution in the CMC was used. The hydrate formation tests were performed in the Parr reactor system (see chapter 4.1) with the pitched blade stirrer in the gas phase. The experimental procedure had the following course of actions. The autoclave was filled with 100 mL of a hydrate forming mixture consisting of degased milli-Q water or a SDS solution in the CMC. The packed bed was created with 495 g of glass spheres and the dimensions are displayed in Figure 7-17. The reactor was purged three times with methane to a pressure of 5 bar(g). Afterwards the reactor was cooled down to 4 °C and filled to an experimental pressure of 150 bar(g). The stirrer was turned on for 10 min to achieve

an immediate induction, turned off thereafter and the measurements lasted for approximately 19 hours. Each experiment was repeated three times.

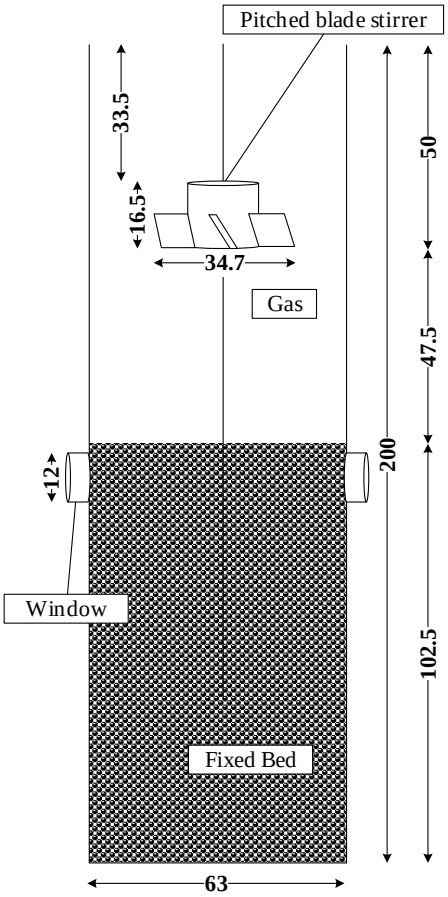

Figure 7-17 Dimensions of the packed bed reactor system

Results and discussion

The aim of this experimental series was to investigate the methane hydrate formation in a packed bed of modified silica particles with an average diameter of 1.15 mm. The results for the contact angle measurements are shown in Figure 7-18.

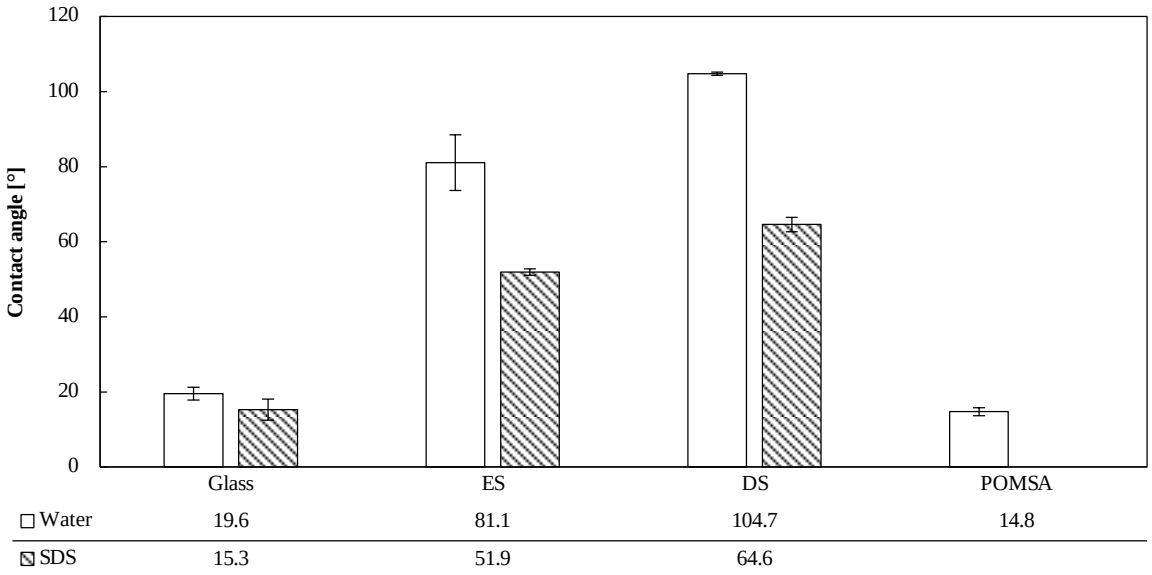

Figure 7-18 Average contact angle of water and SDS-solution (CMC) on glass slides without and after treatment with ES, DS and POMSA with standard deviation

In comparison to the untreated glass, the ES and DS treated surfaces show an increased hydrophobicity for both liquids, water and SDS-solution. The POMSA treated surface is more hydrophilic as the contact angle has a value of 14.8 ° for pure water. As the surface tension of a SDS solution is quite low, no measurements could be performed on the POMSA treated surface as the applied drops dissolved immediately. The differences in the contact angles vary less during measurements with the SDS-solution.

Due to the high driving forces (starting pressure 150 bar(g)) and turbulences caused by the pitched blade stirrer in the gas phase, a nearly immediate induction occurred. Therefore, hydrate induction times cannot be considered in this discussion of the results. However, in view of technical applications, an immediate induction is favorable and the experimental setup secures exactly this. Figure 7-19 shows the averaged gas uptake trends from three experimental series without SDS added. Additionally, the trend for the gas uptake of the rotation frequency optimized system equipped with a gas entry stirrer + gas phase stirrer was added to allow a comparison.

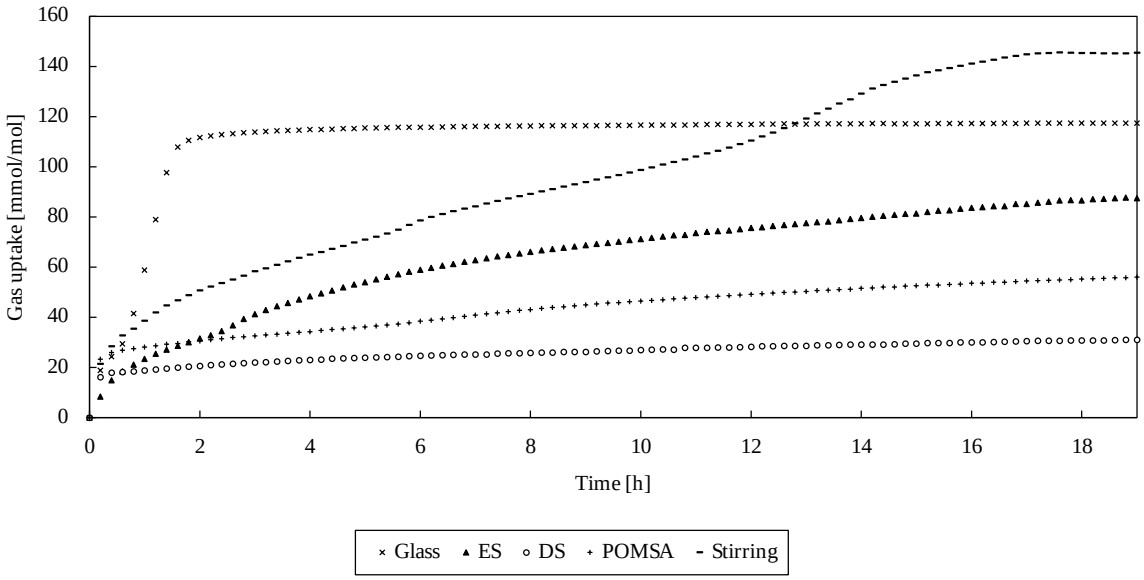

Figure 7-19 Average gas uptake [mmol/mol] without SDS in a fixed bed reactor system. Stirring trend obtained from chapter 6.2

All trends are optically similar to graphs of an earlier study [149]. Within the first two hours all trends have a fast gas uptake and slow down afterwards. Thereby the untreated glass packed bed achieves the highest final gas uptake. The final gas uptake of the other packed beds declines in the order ES, POMSA and DS. In comparison to the stirred tank reactor, all packed beds reach a lower final gas uptake comparable to previous works [149,167]. However, the untreated glass bed shows a rapid gas hydrate growth ending in a certain plateau, where the gas hydrate formation is completed due to mass transport restrictions. According to Bagherzadeh et al. the fast gas hydrate growth is due to an improved gas transport and multiple nucleation events within the packed bed [168]. Additionally, an enhanced water flow due to capillary forces should be mentioned here and will be discussed in detail later.

By comparing both designs, the conclusion is that gas hydrate formation in a packed bed should be cheaper, as a stirred tank reactor consumes more energy and causes higher maintenance costs. Nevertheless, a packed bed reactor design has the disadvantage that the packing occupies a large space reducing the reactor volume and therefore increasing the investment costs of an exemplary application like a gas hydrate storage. Linga et al. already compared both reactor designs and came to a different conclusion. However, their study was not conducted with an optimized stirred tank reactor but rather in a magnetic stirrer bar agitated reactor representing an insufficient technical system [149]. Figure 7-20 shows the average trends from the experimental series with SDS added.

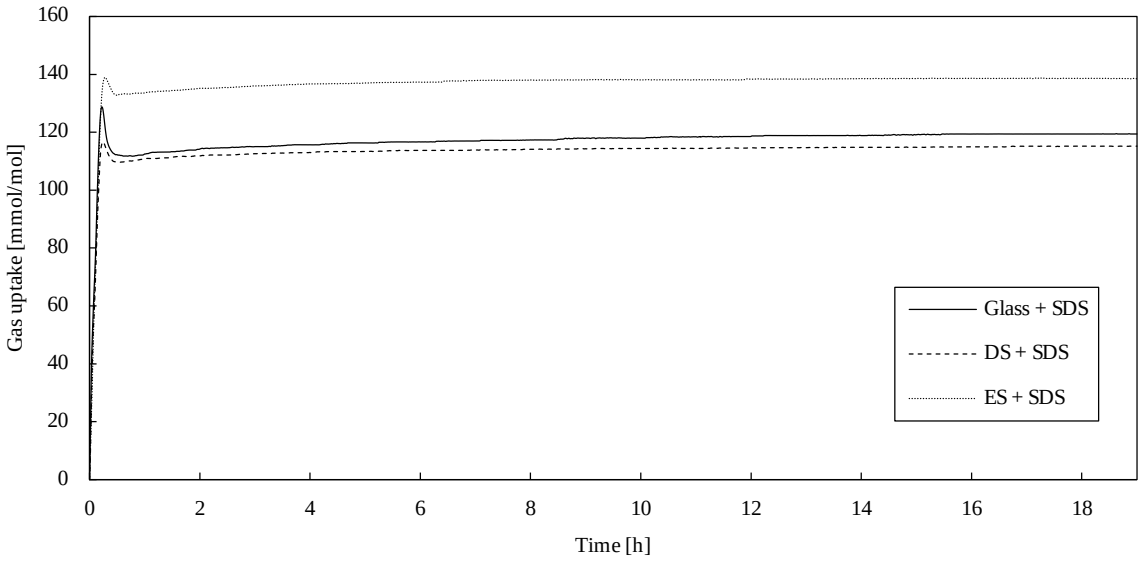

Figure 7-20 Average gas uptake [mmol/mol] for methane hydrate formation with SDS added in a packed bed reactor system

All systems have a similar trend and the final gas uptake declines in the order ES, glass and DS. In each system, the gas hydrate formation is completed within the first 30 minutes due to the use of SDS known from previous studies to be an outstanding kinetic promoter for methane hydrate formation [171–173]. Once more, the kinetic promoting effect is ascribed to a surface tension reduction and increased solubility of methane into the liquid phase although no micelles are formed under gas hydrate formation conditions [28,98,99,174]. A detailed look onto the first 100 minutes can be obtained from Figure 7-21.

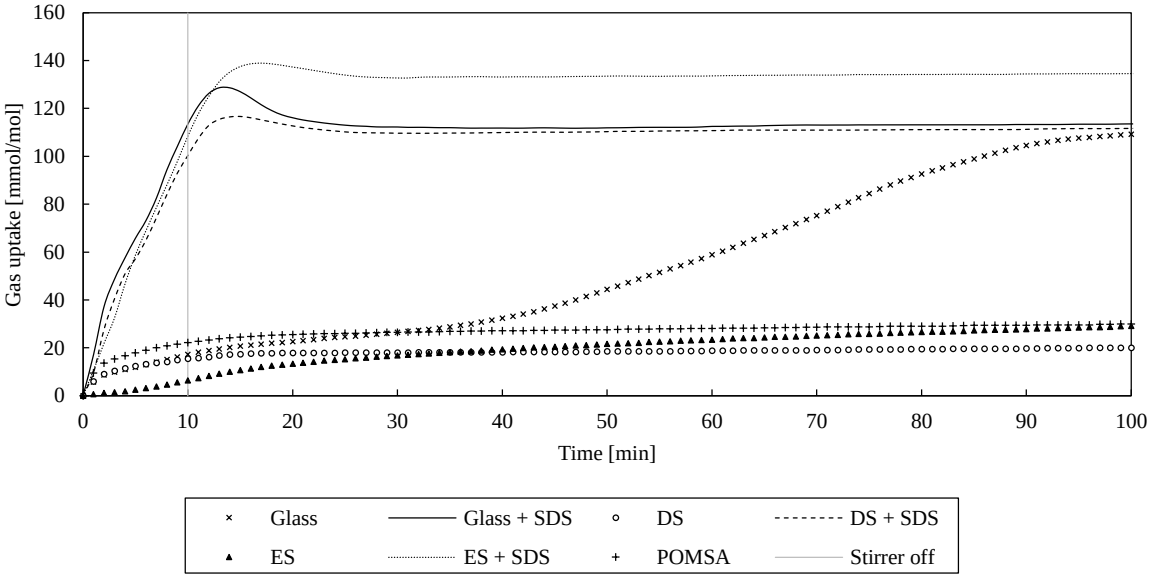

Figure 7-21 Average gas uptake [mmol water/mol gas] of methane hydrate formation fixed bed reactor systems within the first 100 minutes

With the help of Figure 7-21 the graphs can be divided into three groups. ES, DS and POMSA have the slowest gas hydrate growth, followed by the untreated glass bed with a medium formation

rate, ending with SDS systems coming along with a rapid methane hydrate formation. The system with added SDS, shows a surprising trend as their gas uptake passes a maximum at 15 minutes, decreasing thereafter. According to Schicks and Ripmeester in a pressure range of 3.0 MPa to 9.0 MPa and a temperature range of 1.5 °C to 12 °C, due to fast kinetics, the formation of a thermodynamic unstable structure sII can be observed. However, the formation of structure sII as well as of structure sH can be excluded as both maximum gas uptakes account to approx. 176.5 mmol/mol whereas sI has a maximum gas uptake of 173.9 mmol/mol which equals to maximum difference of 1.47 %. Here, a larger decrease is observed, eliminating the formation of a thermodynamic unstable gas hydrate structure. As a conclusion, during the rapid gas hydrate growth, methane molecules are presumably entrapped into intercrystalline spaces and consequently diffuse to the grain boundaries later, leading to a pressure increase or rather gas uptake decrease. Last, the effects of the capillary forces can be discussed with the help of Figure 7-22 providing the final gas uptake plotted against the capillary pressure.

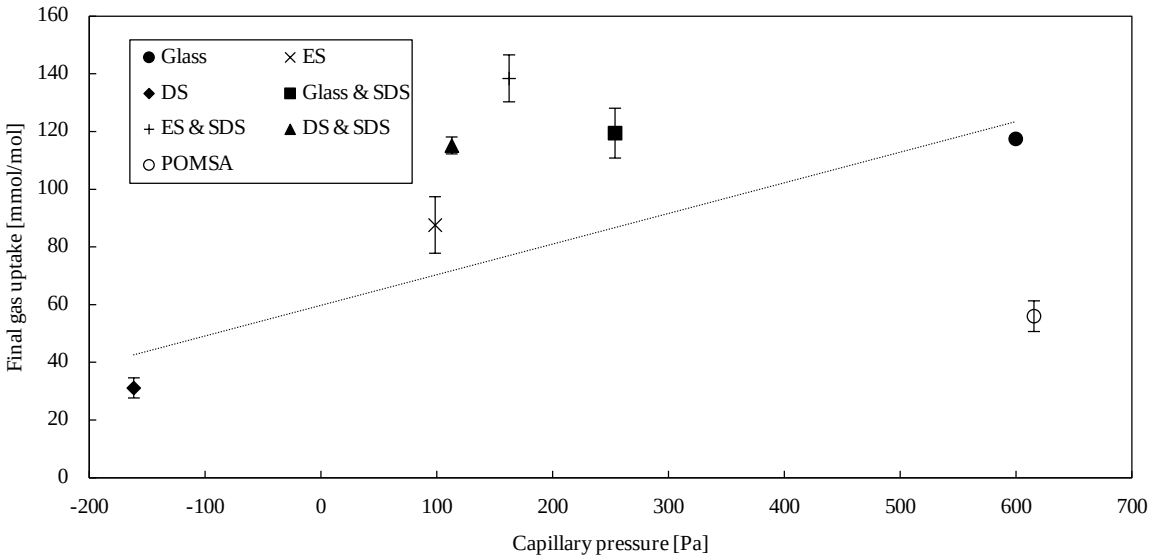

Figure 7-22 Average final gas uptake [mmol/mol] with standard deviation vs. capillary pressure [Pa] for methane hydrate formation in a packed bed reactor. Linear trend sketched between data points for glass, ES and DS

All necessary calculation parameters for the capillary pressure are presented in Table 7-5. The surface tension of a SDS-solution in the CMC was obtained from Watanbe et al. [175] and the measured contact angle (see Figure 7-18). The capillary pressure was calculated by using the equation mentioned by White (Eq. 7-6).

Table 7-5 Calculation parameters for the capillary pressure in the fixed bed systems

System	Surface tension σ [N/m²]	Porosity ε [-]	Volume specific surface area S [m²/m³]	Contact angle θ [°]	Capillary pressure P_C [Pa]
Glass				19.6	599.7
ES	0.075			81.1	98.5
DS				104.7	-161.5
Glass+ SDS		0.38	5202	15.3	253.8
ES + SDS	0.031			51.9	162.3
DS + SDS				64.6	112.9
POMSA	0.075			14.8	615.4

The untreated systems (glass, ES and DS) show a raising trend concerning the final gas uptake with raising capillary pressure. Due to a negative capillary pressure and therefore a holdback of the water at the reactor bottom, the DS-system shows the worst performance. Like in the work of Babu et al. a hydrate plug formed above the particle bed (see Figure 7-23) [169].

Figure 7-23 Hydrate plug above the particle bed

This leads to the conclusion that, driven by capillary forces, a steady water flow to the top is developed in the particle bed and essential to achieve a fast and almost complete gas hydrate formation. The systems without a kinetic promoter are clearly dominated by the capillary forces. The particle bed treated with POMSA has a hydrophilic surface with activated hydroxyl groups attached to it. Similar to the usage of alcohols in the field of flow assurance, the POMSA particle bed has an inhibiting effect as well [27,176]. The OH-groups interact with water molecules and prevent the formation of gas hydrate cage structures [177]. Wang et al. observed similar

kinetically inhibiting effects on methane hydrate formation during experiments with hydrophilic silica nanoparticles [178]. In presence of SDS the ES packed bed achieved the highest final gas uptake, however no correlation between the capillary pressure and the final gas uptake can be identified here, as the kinetically promoting effect of SDS completely negates the impact of the capillary effects.

All fixed bed systems have the same volumetric surface area and the impact of an increased surface area was not investigated. Therefore, Adeyemo et al. should be referenced here who stated that a larger particle size is less important than a large pore diameter facilitating the diffusion of gas into the bulk phase [179]. Furthermore, Kumar et al. achieved an enhanced gas hydrate formation and final gas uptake with higher surface areas [104]. This is consistent with the statement that in presence of hydrophobic particles an interfacial gas enrichment and increased local ordering tendency of the water close to the surface can be found [142].

The measured contact angles allow the ranking of the packed beds without SDS with a decreasing hydrophobicity: DS (104.7 °) > ES (81.1 °) > Glass (19.6 °) > POMSA (14.8 °). Nguyen et al. stated that in presence of a hydrophobic surface an interfacial gas enrichment and increased local ordering tendency of the water close to the surface can be observed leading to a promoted gas hydrate nucleation and growth [142]. However, hydrophobicity is not the prevailing factor as the following decreasing order was found with regard to the strength of the promoting effect: Glass > ES > POMSA > DS. Therefore, with the aim to maximize the gas hydrate growth and gas uptake in a packed bed reactor system, the capillary forces should be as high as possible and particles less but still hydrophobic. An increased hydrophobicity is less important than high capillary forces in a packed bed system.

8 Biogas conditioning

Facing the shrinking amount of fossil fuels, biogas from biodegradable waste as a renewable energy resource seems to be a promising replacement for natural gas. The problem is that biogas cleaning and conditioning requires high and costly efforts [44,180]. Typical upgrading technologies are water scrubbing, chemical and physical adsorption, cryogenic separation and membrane processes. As a result, there is an increased interest in finding alternatives, which reduce the energy and resource consumption in comparison to the existing methods. Gas hydrate separation is one possibility [181,182]. As 1 m^3 of methane hydrate contains up to 170 m^3 of gas, storing of methane in gas hydrates and simultaneously separating of carbon dioxide from a gas feed promises significant improvements in terms of safety and costs [55,172,183,184].

This chapter follows the approach to separate methane and carbon dioxide as a simulated biogas by gas hydrate formation. First, the combination of the thermodynamic promoter THF and the kinetic promoter SDS is tested in presence and absence of additives which are expected to enhance the selectivity. Additionally, a feasibility study was conducted, delivering a first-time proof-of-concept for an integrated process chain combining a fermentation and gas hydrate separation unit. A preceding experimental series deals with the usage of three different semiclathrate formers to improve the separation efficiency.

8.1 Gas hydrate separation with THF

This section examines the purification of biogas, namely a gas mixture consisting of carbon dioxide and methane, by using a THF promoted gas hydrate system and parts of this chapter havve been published in [185].

In the last decades, due to the slow hydrate formation kinetics, several works dealt with promoter systems which uses the synergetic effects of kinetic and thermodynamic promoters to separate carbon dioxide from methane. For example, Ricaurte et al. used THF and SDS as a promoter combination observing that low driving forces and high THF concentrations increase the selectivity. However, the SDS concentration did not affect the separation efficiency. The conclusion was that combining THF and SDS seems to be a promising approach but further additives have to be tested to enhance the selectivity [186].

The fundamental challenge is that the separation efficiency of methane and carbon dioxide via gas hydrate separation is low due to the similar competitiveness for the occupation of gas hydrate cages [187]. Under the usage of four organic compounds (tetrahydrofuran, 1,3-dioxolane, 2-methyl-tetrahydrofuran and cyclopentane) and three surfactants (sodiumdodecylsulfate, sodium dodecyl benzene sulfonate, dodecyl trimethyl ammonium chloride) it was observed that the combination of THF and SDS is the best combination regarding the selectivity [171]. Another study

performed by Di Profio et al. tested several surface active substances for the separation of methane and carbon dioxide via gas hydrate formation and found a decreasing selectivity when kinetic promoters, overpressurization, stirring and other means and increased process driving forces were used [188].

Like in the mentioned studies, this chapter focuses on the separation of biogas by forming a structure sII hydrate in presence of different additives. First, a preliminary study is performed to test different gas hydrate forming systems pragmatically regarding their separation efficiency. Following this experimental series, two gas hydrate forming mixtures are chosen to create adapted McCabe-Thiele diagrams and determine a necessary stage number for a hypothetical biogas treatment process.

Finally, a complete process chain, starting with biogas production via fermentation followed by compression and subsequent gas hydrate separation is operated for the first time, to deliver a proof-of-concept.

8.1.1 Preliminary studies

The experimental series had the intention to find an optimal promoter system with a maximized separation factor. Moderate operating conditions and a fast hydrate formation were guaranteed by using the known combination of the thermodynamic promoter THF and the kinetic promoter SDS. To obtain a higher selectivity, further substances were tested. One promising approach to increase the selectivity might be the usage of additional surfactants with varying hydrophilic-lipophilic balance (HLB) numbers. Another attempt tries to take advantage of the characteristics of physical absorbents. Through the combination of thermodynamic and kinetic promoters and a physical absorbent, an increased selectivity is expected. Several systems were tested with the aim to find an optimal gas hydrate forming separation system.

In the following experimental series, SDS was used in the critical micelle concentration of $0.0082\,\frac{mol}{L}$ and THF with the stoichiometric optimum of 5.56 mol% to secure a filling of all large cavities. Experimental challenges caused by the high volatility of THF, especially in the gas composition measurements, were found to be negligible as no THF was detected during gas chromatography analysis. Although, the separation efficiency of pure water is better than the mixture with both promoters added, the combination of water, THF and SDS is the basis for the experimental series [171,186,189]. Moreover, considering an industrial application, moderate operating conditions and fast gas hydrate kinetics would be economically beneficial. To enhance selectivity the following three additives were tested: Tween 80, Triton X-100 and propylene carbonate (PC).

Ueno et al. suggested that the gas solubility has a significant influence on the mixed gas hydrates formation [190]. Furthermore, García-Aguilar et al. delivered the correlation that nonionic surfactants with high HLB numbers increase the methane solubility [100]. Therefore, Tween 80 (HLB = 15) and Triton X-100 (HLB = 13.5) were used in the critical micelle concentration of $1.2 * 10^{-5} \frac{mol}{L}$ and $2.4 * 10^{-4} \frac{mol}{L}$, respectively.

Another approach focuses on the usage of aprotic solvents like dimethyl sulfoxide, which increases the storage capacity and selectivity towards carbon dioxide [119]. Therefore, the even more aprotic solvent propylene carbonate was used in a concentration of 2 mol%.

Experimental procedure

The experimental series was performed in the Büchi reactor system (See Chapter 4.2). First, the deposit reactor was purged three times and filled afterwards with a mixture of 50 mol% methane and carbon dioxide each. Thereafter the autoclave for the gas hydrate separation was filled with 250 mL of the hydrate forming mixture consisting of distilled water, SDS, THF and one of the mentioned additives in dependency of the experimental series. An overview is given in Table 8-1.

Table 8-1 Overview of the experimental series performed with varying additives

Exp.	Tween 80	Triton X-100	Propylene carbonate
V1	No	No	No
V2	No	No	Yes
V3	Yes	No	No
V4	Yes	No	Yes
V5	No	Yes	No
V6	No	Yes	Yes

The reactor was purged three times with the gas mixture to a pressure of 5 bar(g) each time. Afterwards an operating pressure of 8 bar(g) was adjusted, the reactor was cooled down until hydrate induction occurred. Since temperature controls had a slow response time, the gas hydrate formation heat accumulated and a constant equilibrium temperature for the given pressure was achieved. Due to this heat transfer limitation, from this point in time pressure and temperature were held constant during the experiment. The stirrer speed was constantly set to 1500 rpm resulting in turbulent stirring conditions at Re ≈ 57421. When the gas flow tend to zero, the gas hydrate formation was assumed to be complete and a gas sample was taken for analysis by using a gas chromatography system - Agilent type “6890 Series”. Thereafter, the pressure was drained as fast as possible to ambient conditions and the temperature raised to a temperature of 20°C to dissociate the former gas hydrates. The decomposed gas hydrates released the stored gas, raising the reactor pressure and leading to a gas phase that had the composition of the former gas

hydrates. Another gas sample was taken and analyzed. To determine the initial gas composition a gas sample from the deposit was taken as well. It is stated here that during this experimental procedure gas, especially carbon dioxide, is absorbed in the residual liquid which cannot be considered by this experimental procedure. Therefore, the obtained results represent a worst case scenario but simulate a technical process realistically in which a possible small contamination of absorbed CO_2 in the liquid phase is likely to occur. The residual gas at atmospheric pressure after the first reactor venting was computationally respected. Each gas sample which was examined in this experimental series was measured five times. An exemplary measurement until the drainage is shown in Figure 8-1.

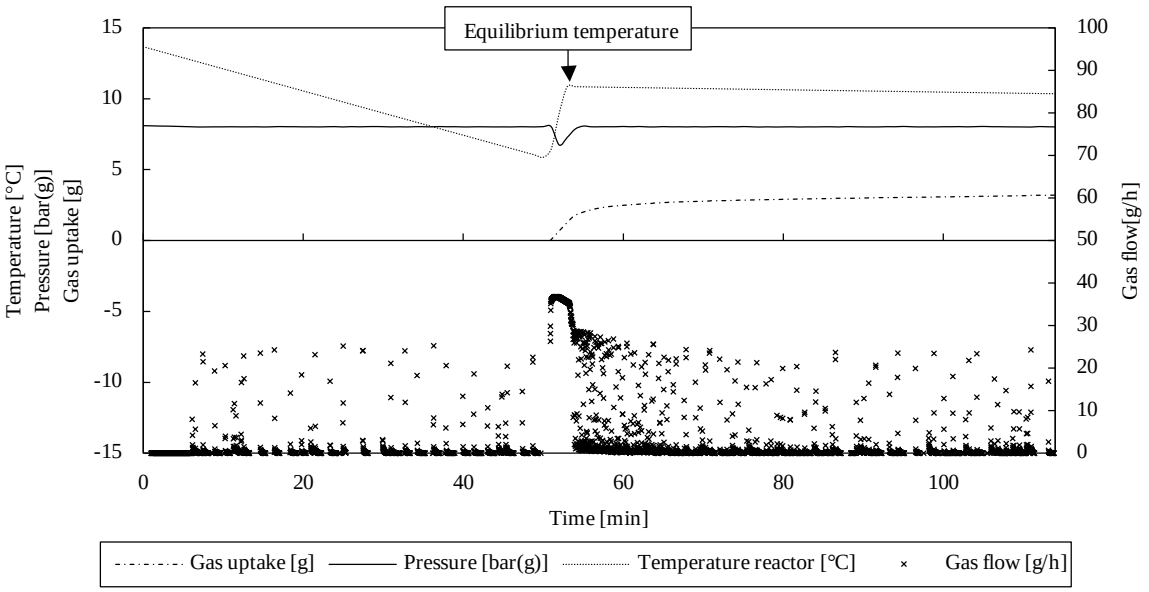

Figure 8-1 Representative measurement for the experimental series of chapter 8.1.1

Results and discussion

The gas composition measurements are displayed with their average and standard deviation in Table 8-2.

Table 8-2 Results for experimental series of chapter 8.1.1 with deviation

Exp.	Mole Fraction CH_4 feed [-]	Mole Fraction CH_4 gas [-]	Mole Fraction CH_4 hydrate [-]
V1	0.48 ± 0.00	0.45 ± 0.00	0.53 ± 0.01
V2	0.45 ± 0.00	0.49 ± 0.00	0.47 ± 0.01
V3	0.52 ± 0.02	0.43 ± 0.02	0.57 ± 0.00
V4	0.51 ± 0.00	0.45 ± 0.01	0.57 ± 0.05
V5	0.49 ± 0.03	0.45 ± 0.01	0.50 ± 0.00
V6	0.48 ± 0.01	0.43 ± 0.02	0.54 ± 0.02

By using equation Eq. 8-1, two ideal separation factors α can be calculated for each pair of data point [87].

$$\alpha_1 = \frac{y_{CH_4}^{Hyd} * \left(1 - x_{CH_4}^{Initial}\right)}{\left(1 - y_{CH_4}^{Hyd}\right) * x_{CH_4}^{Initial}} \qquad \alpha_2 = \frac{y_{CH_4}^{Initial} * \left(1 - x_{CH_4}^{Gas}\right)}{\left(1 - y_{CH_4}^{Inital}\right) * x_{CH_4}^{Gas}} \qquad \textbf{Eq. 8-1}$$

Eq. 8-1 describes the ratio in the equilibrium state between the molar fraction of methane in the hydrate $y_{CH_4}^{Hyd}$ and in the initial gas $x_{CH_4}^{Initial}$ and the ratio between the molar fraction in the initial gas $y_{CH_4}^{Inital}$ and in the gas phase $x_{CH_4}^{Gas}$. An ideal separation process would be described if this factor becomes infinite, hence the higher the value the better the separation efficiency. The separation factors were calculated to describe the selectivity of each gas hydrate forming mixture and to identify the best composition for further biogas separation experiments. The results are shown in Figure 8-2.

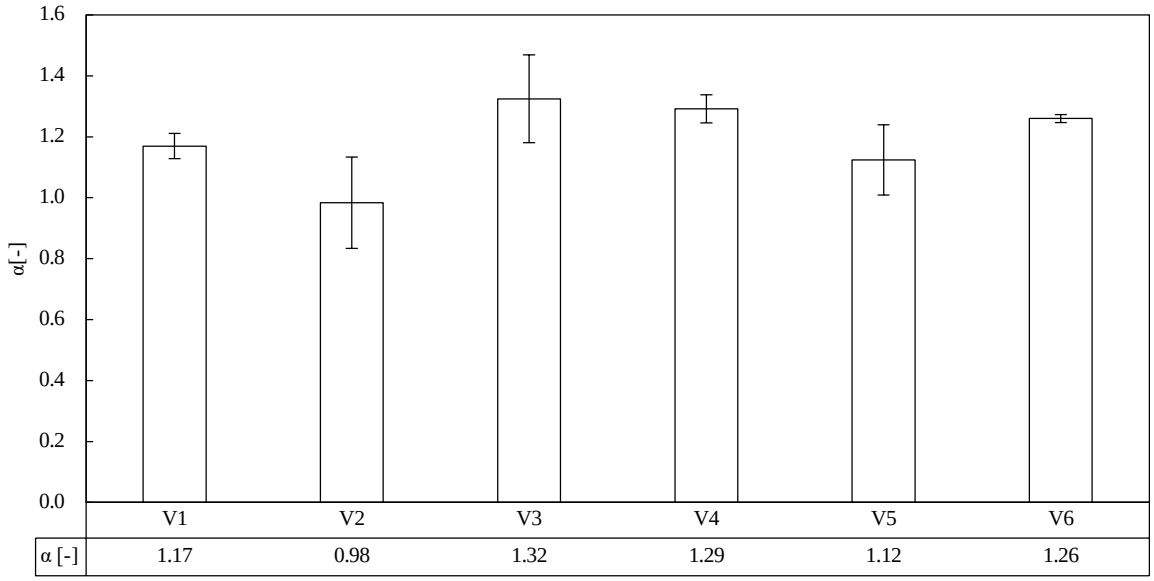

Figure 8-2 Average ideal separation factor of the preliminary tests

The experiments were performed only once as the aim of this preliminary study was to find an optimized promoter system with the least afford and the values represent the average of five gas composition measurements with standard deviation. The experiment V2 with no nonionic surfactant and PC added had the smallest separation efficiency, followed by V1, V5 and V6 with Triton X-100. The best performance showed Tween 80 (V3 and V4). Therefore, it is proven that a non-ionic surfactant with a high HLB number (Tween 80 HLB = 15; Triton X-100 HLB = 13.4) increases the selectivity towards methane hydrate formation due to an increased methane solubility. This is in agreement with the results of García-Aguilar et al. [100,100]. Investigations with Tween 80 and SDS showed faster gas hydrate formation kinetics in comparison to pure water. However, no enhanced gas uptake was observed during carbon dioxide hydrate formation [104]. Hence, the addition of Tween 80 should not influence the solubility of carbon dioxide.

During methane hydrate formation, cationic and nonionic surfactants lead to higher conversion rates [173]. All these studies support the conclusion that nonionic surfactants have a positive influence on the solubility of methane and therefore increase the selectivity.
By comparing each pair of experimental series with and without PC, a tendency towards decreasing the selectivity for methane was observed. The experimental series V2 resulted in an enrichment in both phases. Possibly an absorption of carbon dioxide in the liquid phase by the added PC occurred, which cannot be registered by solely analyzing the gas phase composition. Since V3 and V4 showed a significantly better performance than the other mixtures, V3 was chosen as a benchmark to perform the biogas separation feasibility study (see chapter 8.1.3) since the effect of PC could not be clarified.

8.1.2 Construction of an adapted McCabe-Thiele diagram

The preliminary tests showed that it is unavoidable to perform an applicable gas hydrate separation in a multistage process. As a result, it is impossible with the evaluated gas hydrate forming mixtures to purify biogas to an applicable specification of at least 93 mol% in a single step. [191–193]. However, for designing such a process it is necessary to evaluate a minimal stage number for a given separation task. Therefore, the following experimental series was conducted to enable the construction of adapted McCabe-Thiele diagrams to investigate the necessary stage numbers to reach a purity within industrial specifications. Therefore, Eq. 8-1 is converted to:

$$y_{CH_4}^{Hyd} = \frac{\alpha * x_{CH_4}^{Gas}}{1 + x_{CH_4}^{Gas} + (\alpha - 1)} \qquad \textbf{Eq. 8-2}$$

Experimental procedure

The experimental setup is identical to chapter 8.1.1. The test procedure was similar as well using an operating pressure of 8 bar(g). The hydrate forming mixture consisted of V3, distilled water, SDS, THF and Tween 80. To investigate the effects of propylene carbonate, additional experiments were performed with a hydrate forming mixture in a composition of V4. The composition of the experimental gas mixture was varied in steps of approximately 10 mol%. For each experiment, six parameters were determined: the equilibrium temperature [°C], the gas uptake [mmol/mol], the separation factors by using Eq. 8-1, the composition of the gas at the start, in the equilibrium and in the gas hydrates.

Results and discussion

The results from this experimental series are summarized in Table 8-3. Two measurements, V4-1 and V4-4, are standing out as the mole fraction in the gas and the hydrate phase decreased in comparison to the start concentration. Due to the difficult to measure merely small changes in the molar fraction, these are considered as inaccurately. However, the experiments were not repeated as enough data points were available because of the decision to measure in 10 mol% steps

Table 8-3 Experimental data for the construction of a McCabe-Thiele diagram

Nr.	x_{CH_4} start [-]	x_{CH_4} gas [-]	x_{CH_4} hydrate [-]	T_{eq} [°C]	Gas uptake $\left[\frac{mmol}{mol}\right]$	α [-]
V3–1	0.89 ± 0.01	0.86 ± 0.01	0.89 ± 0.01	14.1	16.67	1.00/1.32
V3–2	0.82 ± 0.01	0.82 ± 0.00	0.83 ± 0.00	13.9	16.81	1.07/1.00
V3–3	0.68 ± 0.02	0.66 ± 0.00	0.71 ± 0.00	13.3	20.47	1.15/1.09
V3–4	0.58 ± 0.00	0.56 ± 0.01	0.59 ± 0.00	12.8	15.66	1.04/1.09
V3–5	0.52 ± 0.02	0.44 ± 0.01	0.57 ± 0.00	12.3	15.82	1.22/1.38
V3–6	0.38 ± 0.00	0.37 ± 0.01	0.41 ± 0.01	12.3	17.79	1.13/1.04
V3–7	0.27 ± 0.00	0.26 ± 0.00	0.29 ± 0.01	12.2	16.04	1.10/1.05
V3–8	0.18 ± 0.01	0.17 ± 0.00	0.20 ± 0.01	12.1	16.52	1.14/1.07
V3–9	0.09 ± 0.01	0.09 ± 0.01	0.08 ± 0.01	12.1	17.15	0.88/1.00
V4–1	0.97 ± 0.03	0.92 ± 0.01	0.95 ± 0.01	11.9	21.73	0.59/2.81
V4–2	0.82 ± 0.03	0.80 ± 0.00	0.84 ± 0.00	11.7	22.43	1.15/1.14
V4–3	0.73 ± 0.01	0.71 ± 0.01	0.75 ± 0.00	11.4	21.73	1.11/1.10
V4–4	0.63 ± 0.02	0.59 ± 0.01	0.59 ± 0.00	11.2	22.23	0.85/1.18
V4–5	0.51 ± 0.00	0.45 ± 0.01	0.57 ± 0.05	10.8	15.34	1.27/1.27
V4–6	0.38 ± 0.01	0.36 ± 0.01	0.41 ± 0.01	11.0	22.75	1.13/1.09
V4–7	0.27 ± 0.01	0.27 ± 0.01	0.31 ± 0.01	10.3	22.30	1.21/1.00
V4–8	0.17 ± 0.01	0.18 ± 0.01	0.19 ± 0.01	10.2	20.56	1.15/0.93

The results were used to construct the adapted McCabe-Thiele-diagrams. Figure 8-3 allows the comparison of the trends at 8 bar(g) with and without PC added.

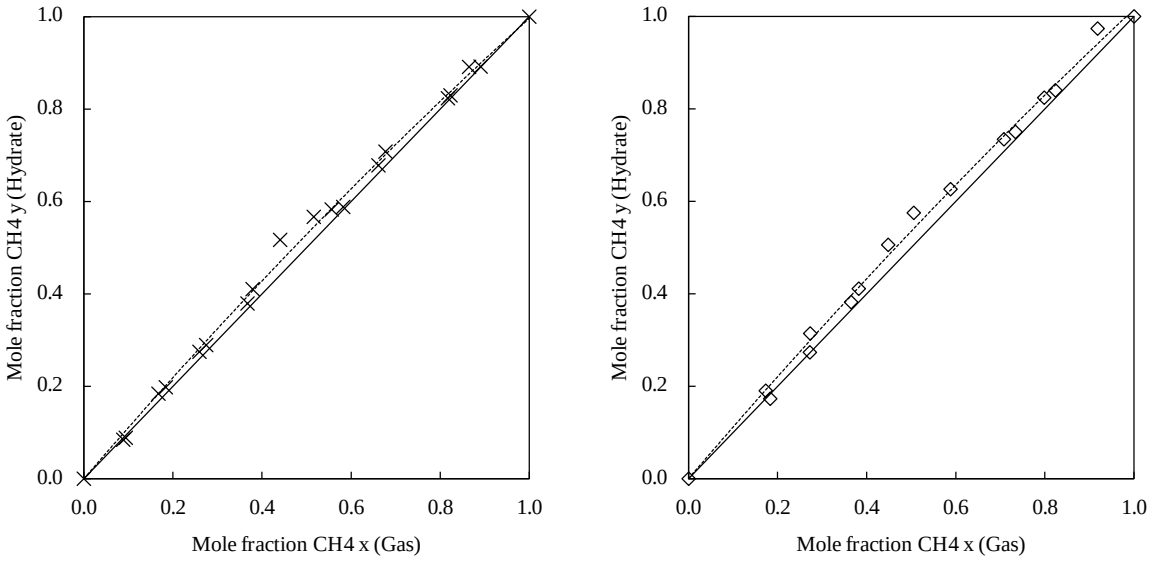

Figure 8-3 Mole fraction of methane in the hydrate vs. mole fraction in the gas for the experimental series w/o (left) and w/ (right) propylene carbonate

Both trends are very flat which proves that the selectivity is rather unsatisfactory. PC does not seem to affect the separation efficiency as both trends are nearly identical. The average ideal separation factor α of the experimental series without PC is 1.10 ± 0.12 and with PC 1.11 ± 0.12, which underlines the qualitative findings.

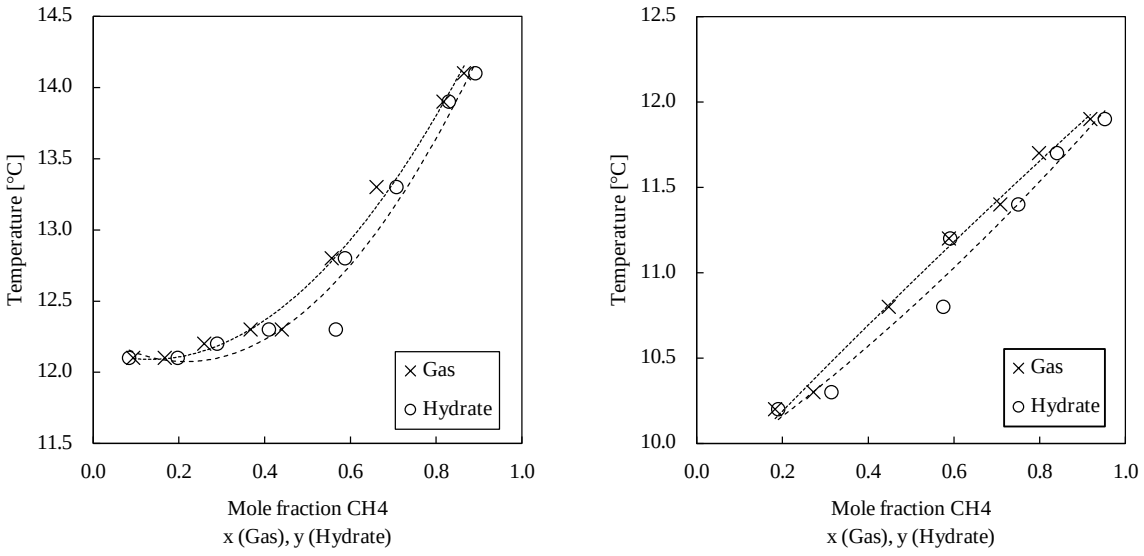

Figure 8-4 Equilibrium temperature vs. mole fraction of methane in the gas and the hydrate for the experimental series w/o (left) and w/ (right) propylene carbonate

Figure 8-4 shows the equilibrium temperature [°C] against the mole fraction of methane in the gas and the hydrate phase for both experimental series. With PC, the equilibrium temperature seems to be 2 K lower than with PC. Hence, PC shows an inhibiting effect. Similar effects were observed in presence of ethylene carbonate. The oxygen atoms in this molecule shifts the hydrate phase boundary to an inhibiting region [194]. Visually both trends intersect at a mole fraction of

approximately 20 mol%. Therefore, an "azeotropic" point can be expected. As THF occupies all the large cages, methane and carbon dioxide compete for the occupation of the small cavities. Therefore, the tendency to fill these cavities under the given condition is assumed to be equal for both gases at this point and it would be impossible to get pure methane and carbon dioxide from a multistage process operated at 8 bar(g). The measured corresponding temperature of approximately 11.8 °C at the azeotropic point in absence of PC is also in agreement with the work of Lee et al. who investigated the equilibrium of mixed THF hydrates with methane and carbon dioxide. In this work, at 10 °C, the dissociation pressure of gas hydrates formed by 5.56 mol% THF and carbon dioxide is equal to that of 5.56 mol% THF and CH_4. Below that temperature, mixed hydrates from THF and carbon dioxide are thermodynamically favorable whereas at higher temperatures mixed gas hydrate from THF and methane are more stable. The effect was assigned to the different stabilization effects of the corresponding gas molecules located in the small cages [37]. Therefore, the selectivity of gas hydrate separation processes depends significantly on the stability and occupancy of the hydrate cages if the solubility is disregarded. Figure 8-5 shows the influence of the propylene carbonate on the gas uptake [mmol/mol].

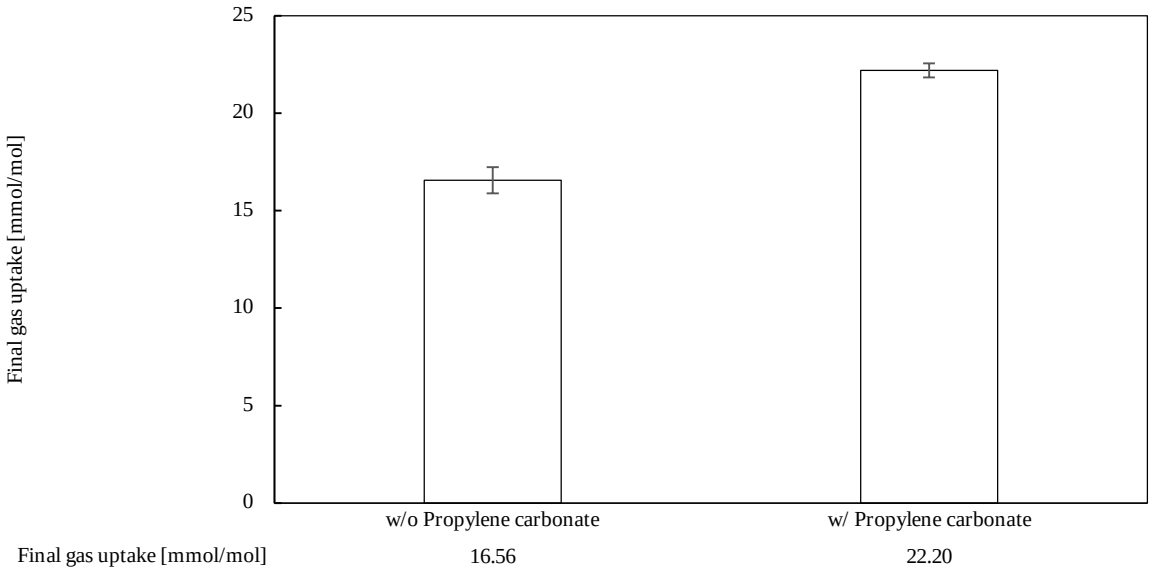

Figure 8-5 Final average gas uptake [mmol/mol] with standard deviation for the experimental series w/ and w/o propylene carbonate

In presence of PC the final gas uptake increased from 16.56 [mmol/mol] to 22.20 [mmol/mol]. These values are similar in comparison to Mech et al. or Veluswamy et al., who measured the gas consumption in synergetic promoter systems as well. However, higher values were obtained with higher driving forces [172,195]. It is stated here that it cannot be ruled out, that gas is stored in gas hydrates and additionally absorbed by PC.

Altogether, it has been shown that the solubility of methane and carbon dioxide in the liquid phase significantly affects the gas hydrate formation and selectivity. These findings are in agreement with the work from Xu et al. who found a dependency of the gas uptake on the dissolution behavior

while using methane and carbon dioxide and THF as thermodynamic promoter [196]. As the final gas uptake is quite low, throughout the experiments water remained partially liquid and was able to absorb gas. However, this is of lower importance as in an industrial multi-stage process like a crystallization column, a flowable hydrate slurry would be desirable as well. Therefore, the residual liquid simulates an application case appropriately. Since carbon dioxide is particularly dissolved in water, future works should focus on improving the carbon dioxide solubility with additives with subsequent CO_2 capturing in gas hydrates as Xia et al. suggested [197,198]. Figure 8-6 displays the results of the determination of the necessary stage number to purify biogas to a specification of at least 93 mol%.

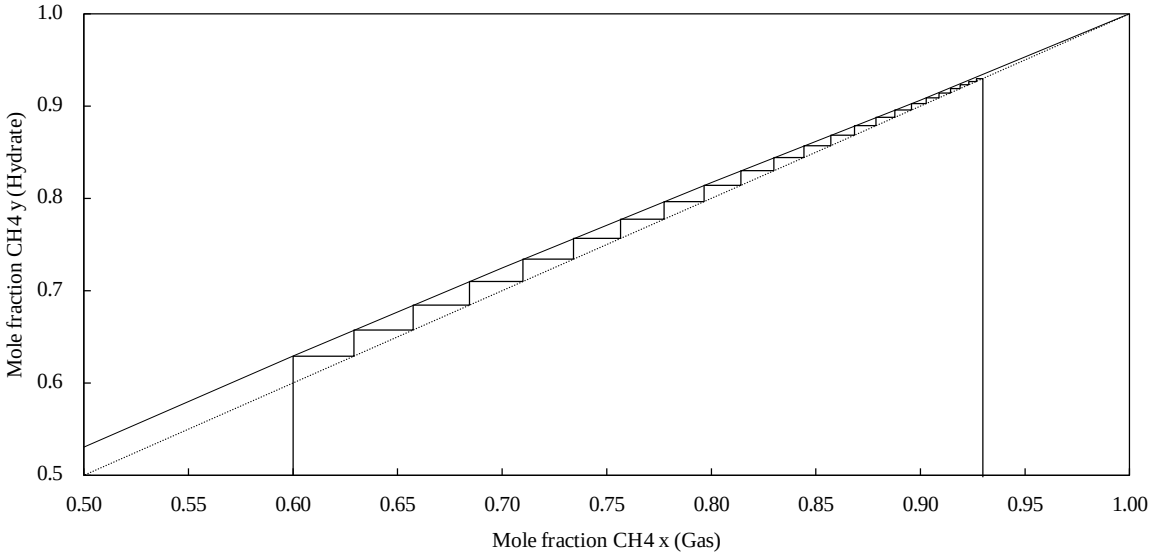

Figure 8-6 Determination of the necessary stage number to purify biogas to a specification of > 93 mol% with THF

The trend from Figure 8-3 without propylene carbonate was used based on a gas mixture of 60 mol% methane. By drawing each equilibrium stage into the graph, the minimum stage number is evaluated as 22.

8.1.3 Biogas production and purification – feasibility study

The aim of this chapter is to deliver a proof-of-concept for an integrated process chain, which combines a continuous biogas production via fermentation and the pioneering gas hydrate separation technology. First, biogas was produced in an optimized fermentation reactor. Thereby, a mixed culture from sewage sludge obtained from a local clarification plant was cultivated by insertion of a nutritious saccharose solution. The biogas was scrubbed and a molar fraction of approximately 60 mol% methane was achieved whereas the rest mainly consisted of carbon dioxide. Afterwards, the biogas was compressed into an autoclave and separated by promoted gas hydrate formation. Finally, the selectivity was evaluated to prove the successful operation of this combined test facility. The process flow diagram is pictured in Figure 8-7.

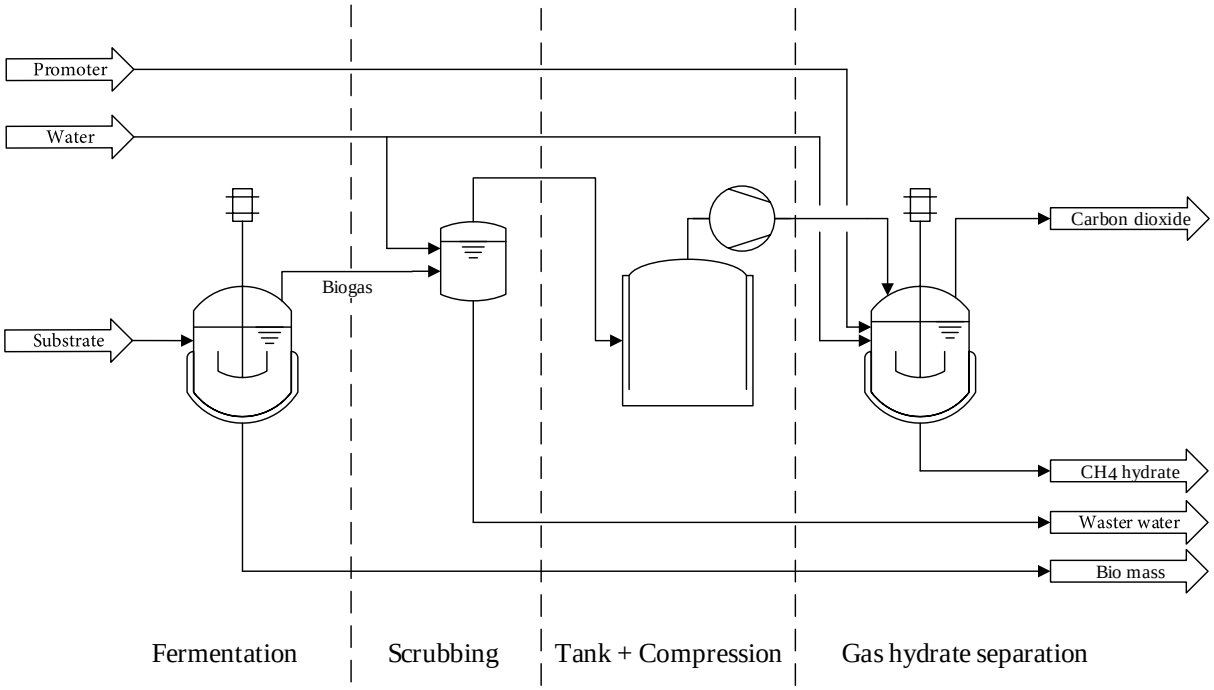

Figure 8-7 Process flow diagram for the feasibility study

Launch of a biogas production unit

The technical process for biogas production via fermentation is nowadays an established and largely optimized process. Instructions for setting-up a fermentation unit can be found in several sources and will not be described in detail here [199–202]. In this case an anaerobic mesophilic mixed culture from sewage sludge was used and fed with a substrate based on saccharose with 0.062 L/h resulting in a gas flow of 0.35 L/h at lab conditions. The used reactor was manufactured by MBR Bioreaktor AG and has a volume of 20 L. Agitation was secured with a 3-stage disk stirrer at 25 rpm. Temperature was kept constantly at 37 °C using a warm water heating jacket.

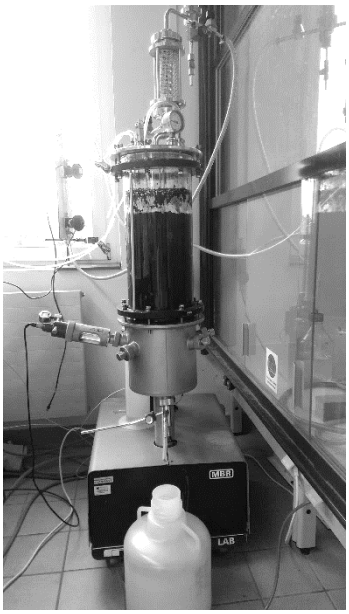

Figure 8-8 Photo of the fermentation reactor [185]

The pH-value was adjusted to a range of 6.7 to 7.5 and gas detection performed with Bluesens IR-sensors. The results were additionally checked via gas chromatography. After scrubbing and storing, the biogas composition was approximately 60 mol% methane and 40 mol% carbon dioxide.

Combination of the biogas production with a hydrate separation unit

The experimental series was performed in the Parr reactor system (see chapter 4.1). The reactor was filled with 250 mL of a hydrate forming mixture consisting of distilled water, SDS, THF and Tween 80 referring to the experimental series V3 of chapter 8.1.1. Thereafter, the produced biogas was compressed and stored in a reservoir. After purging the reactor 3 times with biogas to a pressure of 5 bar(g) the reactor was pressurized to a maximum pressure of 35 bar(g). Then the stirrer was turned on and the rotation frequency was set to 900 rpm. Like in the preceding separation experiments the reactor was cooled down until hydrate formation eventuated. According to Lee et al. the equilibrium trends for THF plus methane and THF plus carbon dioxide hydrates diverge with higher pressure and temperature and a higher selectivity was expected as the temperature was held at 20 °C for approximately 17 hours resulting in an equilibrium pressure of 25 bar(g). A gas sample was taken and analyzed via a gas chromatography system by Agilent type “6890 Series”. All gas was released quickly until the pressure dropped to ambient conditions and the hydrates were dissociated by raising the temperature to 40 °C. While gas was released by hydrate decomposition, the reactor pressure increased, and the gas phase composition was nearly equal to the hydrates. Another gas sample was taken from both, the reactor and the reservoir, and analyzed subsequently. The results are shown in Figure 8-9 which proves a successful purification of the produced biogas by storing methane in gas hydrates.

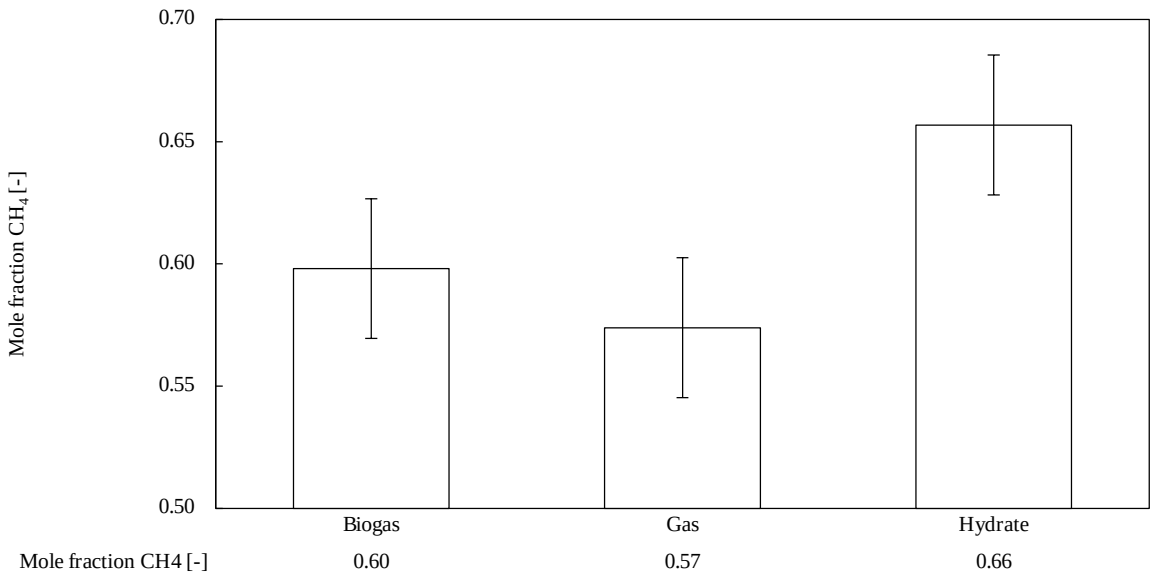

Figure 8-9 Results of the biogas separation

The ideal separation factor α was 1.21 ± 0.11, showing that higher pressures and temperatures only slightly improved the separation efficiency compared to chapter 8.1.2. A possible explanation is that carbon dioxide is more soluble at higher pressures. Although the selectivity must be improved to allow an industrial usage of this technology, the possibility to startup an integrating process chain in a lab scale - starting with the production, followed by scrubbing and closing with the purification and storing of biogas in form of gas hydrates - was proven for the first time in this work. According to Xia et al. much higher separation efficiencies are possible by using a synergizing combination of a semiclathrate promoter like tetra-n-butyl ammonium bromide and gas solvents like tetramethylene sulfone or dimethyl sulfoxide [197,198]. This idea will be followed up in chapter 8.2 to optimize the biogas purification via gas hydrate separation.

8.2 Gas hydrate separation with semiclathrates

In 1940, Fowler et al. found "unusual" hydrates of quaternary ammonium salts, namely tetra-n-butylammonium and tetraisoamylammonium salts [203]. Later this was extended to peralkylonium salts and analogues (Alk_3X^+, with X=Nitrogen, Phospor, Arsenic). The so-called semi-clathrates differ from gas hydrates as they act as host and guest at the same time. Anions replace some water molecules in the hydrate framework and broken cages occur to enclose the large cations [204,205]. Lately, semi-clathrates came into focus as they are stable at atmospheric conditions, offer the possibility to entrap gas molecules and therefore show a vast potential with regard to gas separation [206], refrigeration [207] and gas storage [208].

This work focuses on the separation of carbon dioxide and methane from biogas. Xia et al. observed, originating from a simulated biogas (45 mol% carbon dioxide and 55 mol% methane), the preferred capture of carbon dioxide while using THF and tetra-n-butylammonium bromide (TBAB). In addition, they tested the synergic additive dimethyl sulfoxide (DMSO). As a result, gas uptake and selectivity were best in case of a mixture of DMSO and TBAB [197]. However, it seems to be contradictory to the results from chapter 8.1 as carbon dioxide was enriched in the gas hydrate phase in the case of THF as thermodynamic promoter in a concentration of 5.56 mol%. Furthermore, separation factors ranging from 6.89 up to 14.16 were achieved, which seems quite high in comparison to other works. Zang et al. measured separation factors ranging from 1.48 to 3.95, using a binary mixture of methane and carbon dioxide and TBAB in a concentration of 0.29 mol% [209]. Yue et al. used THF (1 mol%) and TBAB (0.3 mol%) in combination with 1-octyl-3-methylimidazolium tetrafluoroborate to separate a simulated biogas with a composition of 37 mol% carbon dioxide and 67 mol% methane. As only phase compositions were given, separation factors were calculated to be 1.58 and 1.40 for TBAB and THF respectively. Adding 1-octyl-3-methylimidazolium tetrafluoroborate to the TBAB solution lowered the separation efficiency to 1.44 [210]. Another study performed by Li et al. investigated the separation of a carbon dioxide/methane mixture (40 mol%/60 mol%) while using tetra-n-butyl phosphonium bromide as semiclathrate former. Separation factors ranged from 7.3 for 0.6 mol% to 34.2 for 2.6 mol% of TBPB [211].

Although the potential of using TBAB and TBPB for biogas separation seems to be very promising preceding works came to divergent results, hence both substances are tested here again. In addition, the semiclathrate former tetra-n-butyl ammonium chloride was used to investigate the effect of the anion of the semiclathrate former. Furthermore, all experiments were repeated in presence of sulfolane (TMSO), as the idea of a synergetic additive seems to bear the possibility to enhance the separation efficiency. Figure 8-10 shows the structures of the used semiclathrate former.

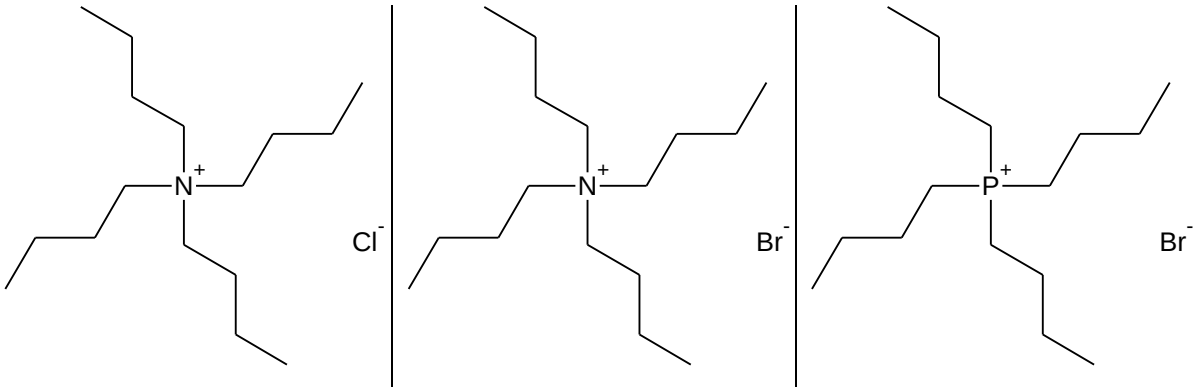

Figure 8-10 From left to right, structure of TBACl, TBAB and TBPB

Both tetra-n-butyl ammonium semiclathrate formers build the tetragonal structure TS-I in which the unit cell consists of $10(5^{12}) \cdot 16(5^{12}6^2) \cdot 4(5^{12}6^3) \cdot 172\ H_2O$. In this structure, the large cages $5^{12}6^2$ and $5^{12}6^3$ are occupied by the cations, the anions substitute water molecules in the cage structure and the small 5^{12} cages can be filled with gas molecules. The thermodynamically most stable ratios between the semiclathrate former and water are 29.7 for TBACl and 38.1 for TBAB respectively [38,212–214]. TBPB in a stoichiometry of 36.6 is the most stable version of a TBPB semiclathrate and corresponds to an orthorhombic structure RS with a unit cell of $3(5^{12}) \cdot 2(5^{12}6^2) \cdot 2(5^{12}6^3) \cdot 38\ H_2O$. Once again, large cages are occupied by the tetra-n-butyl phosphonium cation, the anions replaces water molecules and gas can fill the small 5^{12} cages [215,216]. At this point it is evident that the orthorhombic structure RS has a superior gas uptake the ratio between empty 5^{12} cages and occupied cages amounts to

$$RS = \frac{3\ (5^{12})}{2(5^{12}6^2) + 2(5^{12}6^3)} = \frac{3}{4} = 0.75 \qquad \text{Eq. 8-3}$$

compared to

$$TS - I = \frac{10\ (5^{12})}{16(5^{12}6^2) + 4(5^{12}6^3)} = \frac{10}{20} = 0.5 \qquad \text{Eq. 8-4}$$

The semiclathrate structure of TBAB in presence of carbon dioxide is sketched in Figure 8-11.

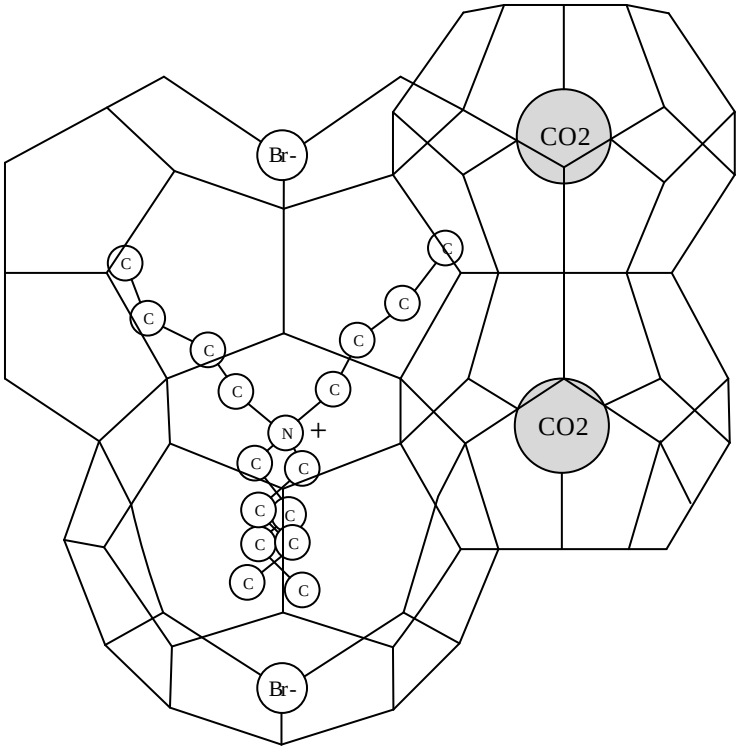

Figure 8-11 Schematic semiclathrate structure of TBAB in presence of carbon dioxide

Sulfolane is a polar aprotic solvent and soluble in water. In industry it is used for aromatic extraction in the sulfolane process or for the removal of acid gases like carbon dioxide and sulfur from natural gas in the sulfinol process [217,218]. Therefore, it also seems to be a promising candidate for a synergetic additive to enhance the selectivity of a semiclathrate separation process.

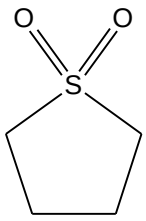

Figure 8-12 Structure of sulfolane

Experimental procedure

The experimental design has in mind that experiments are conducted with a semiclathrate forming mixture based on 100 g of water. As the aim is to operate at moderate conditions, an amount of the corresponding semiclathrate former, to create the most stable stoichiometric ratio, is added. For TBAB, TBACl and TBPB it is 32 wt%, 34 wt% and 34 wt% respectively [38,212,219]. The gas mixture was varied from 10 mol% to 90 mol% of carbon dioxide in steps of 10 mol%. In addition, all experiments were repeated with 5 mol% TMS added. For each experiment three carbon dioxide mole fractions (initial mixture, gas phase & hydrate phase), equilibrium

temperature T_{eq} [°C], gas uptake [mmol/mol], two separation factors $\alpha_{1,2}$ and induction time t_{ind} [min] were recorded. Separation factors were calculated to evaluate the separation efficiency, determine the best semiclathrate forming mixture and enable the construction of adapted McCabe-Thiele diagrams. The experiments were conducted analogously to chapter 8.1.2.

Results and discussion

Table 8-4 and Table 8-5 show the results of the experimental series conducted here.

Table 8-4 Experimental results for the separation of methane and carbon dioxide by semiclathrates without sulfolane added

Des.	x_{CO_2} start [-]	x_{CO_2} gas [-]	x_{CO_2} hydrate [-]	T_{eq} [K]	Gas uptake $\left[\frac{mmol}{mol}\right]$	α [-]	t_{ind} [min]
TBAB 90/10	0.10 ± 0.01	0.09 ± 0.00	0.16 ± 0.00	12.26	20.10	1.16/1.66	33.25
TBAB 80/20	0.19 ± 0.01	0.17 ± 0.00	0.31 ± 0.00	11.97	5.64	1.14/2.00	35.95
TBAB 70/30	0.29 ± 0.00	0.24 ± 0.00	0.45 ± 0.00	12.04	8.32	1.28/1.96	42.32
TBAB 60/40	0.40 ± 0.01	0.35 ± 0.01	0.57 ± 0.00	12.21	5.91	1.23/1.99	50.15
TBAB 50/50	0.49 ± 0.01	0.44 ± 0.00	0.67 ± 0.00	12.51	5.52	1.22/2.10	42.57
TBAB 40/60	0.60 ± 0.00	0.55 ± 0.00	0.78 ± 0.00	12.59	8.08	1.22/2.45	54.48
TBAB 30/70	0.70 ± 0.01	0.64 ± 0.00	0.85 ± 0.00	12.31	8.87	1.32/2.39	51.23
TBAB 20/80	0.80 ± 0.00	0.76 ± 0.00	0.91 ± 0.00	12.68	8.78	1.23/2.75	54.52
TBAB 10/90	0.89 ± 0.00	0.88 ± 0.00	0.95 ± 0.00	13.35	7.95	1.21/2.18	44.33
TBACl 90/10	0.11 ± 0.01	0.11 ± 0.01	0.20 ± 0.03	14.67	8.80	1.01/2.07	30.28
TBACl 80/20	0.20 ± 0.02	0.19 ± 0.01	0.32 ± 0.01	14.33	5.65	1.11/1.82	36.02
TBACl 70/30	0.29 ± 0.01	0.27 ± 0.01	0.42 ± 0.01	15.86	7.03	1.08/1.78	39.47
TBACl 60/40	0.39 ± 0.01	0.35 ± 0.01	0.51 ± 0.00	15.00	7.84	1.18/1.63	29.40
TBACl 50/50	0.45 ± 0.02	0.40 ± 0.01	0.75 ± 0.00	15.27	9.46	1.25/3.68	44.08
TBACl 40/60	0.60 ± 0.01	0.54 ± 0.01	0.68 ± 0.01	15.41	9.85	1.24/1.46	33.32
TBACl 30/70	0.70 ± 0.01	0.64 ± 0.01	0.83 ± 0.00	15.90	9.55	1.26/2.10	32.40
TBACl 20/80	0.81 ± 0.01	0.77 ± 0.00	0.88 ± 0.00	15.84	12.21	1.25/1.71	27.07
TBACl 10/90	0.92 ± 0.00	0.90 ± 0.00	0.95 ± 0.00	15.89	9.40	1.28/1.63	32.55
TBPB 90/10	0.11 ± 0.01	0.08 ± 0.00	0.19 ± 0.01	10.32	16.94	1.32/1.96	55.08
TBPB 80/20	0.20 ± 0.01	0.14 ± 0.01	0.31 ± 0.00	10.69	17.86	1.47/1.79	46.32
TBPB 70/30	0.30 ± 0.01	0.24 ± 0.01	0.41 ± 0.01	10.21	15.92	1.32/167	69.62
TBPB 60/40	0.40 ± 0.01	0.33 ± 0.02	0.56 ± 0.00	10.28	16.93	1.37/1.89	59.28
TBPB 50/50	0.50 ± 0.01	0.43 ± 0.01	0.64 ± 0.01	11.10	20.32	1.31/1.75	66.23
TBPB 40/60	0.60 ± 0.01	0.52 ± 0.01	0.76 ± 0.00	11.27	20.50	1.37/2.12	47.10
TBPB 30/70	0.70 ± 0.00	0.62 ± 0.01	0.82 ± 0.00	11.86	23.49	1.39/1.99	52.05
TBPB 20/80	0.80 ± 0.01	0.73 ± 0.00	0.89 ± 0.00	12.04	23.55	1.43/2.14	42.95
TBPB 10/90	0.89 ± 0.00	0.85 ± 0.00	0.95 ± 0.00	12.34	26.06	1.38/2.27	48.37

Table 8-5 Experimental results for the separation of methane and carbon dioxide by semiclathrates with sulfolane added

Des.	x_{CO_2} start [-]	x_{CO_2} gas [-]	x_{CO_2} hydrate [-]	T_{eq} [K]	Gas uptake $\left[\frac{mmol}{mol}\right]$	α [-]	t_{ind} [min]
TBAB+ 90/10	0.11 ± 0.00	0.09 ± 0.00	0.16 ± 0.00	8.40	20.12	1.26/1.53	88.42
TBAB+ 80/20	0.19 ± 0.00	0.15 ± 0.00	0.26 ± 0.00	7.28	20.40	1.29/1.55	73.52
TBAB+ 70/30	0.28 ± 0.00	0.23 ± 0.00	0.39 ± 0.00	7.59	19.21	1.30/1.61	74.78
TBAB+ 60/40	0.40 ± 0.01	0.33 ± 0.00	0.53 ± 0.00	7.79	19.15	1.34/1.71	59.78
TBAB+ 50/50	0.48 ± 0.01	0.42 ± 0.01	0.64 ± 0.00	8.33	23.36	1.28/1.92	68.90
TBAB+ 40/60	0.59 ± 0.00	0.51 ± 0.00	0.74 ± 0.00	7.69	20.65	1.39/2.01	55.77
TBAB+ 30/70	0.70 ± 0.00	0.64 ± 0.00	0.85 ± 0.00	8.14	22.26	1.29/2.43	57.88
TBAB+ 20/80	0.81 ± 0.00	0.76 ± 0.00	0.91 ± 0.00	8.43	20.85	1.37/2.37	51.82
TBAB+ 10/90	0.89 ± 0.00	0.88 ± 0.00	0.96 ± 0.00	8.81	25.54	1.15/2.71	50.08
TBACl+ 90/10	0.12 ± 0.01	0.09 ± 0.00	0.21 ± 0.01	9.72	12.83	1.26/2.07	38.88
TBACl+ 80/20	0.20 ± 0.01	0.15 ± 0.01	0.34 ± 0.01	9.62	7.80	1.44/2.04	41.08
TBACl+ 70/30	0.30 ± 0.01	0.24 ± 0.01	0.50 ± 0.02	9.74	10.40	1.38/2.33	41.88
TBACl+ 60/40	0.38 ± 0.00	0.32 ± 0.01	0.58 ± 0.01	9.83	14.33	1.30/2.29	44.30
TBACl+ 50/50	0.50 ± 0.01	0.42 ± 0.00	0.71 ± 0.01	10.11	12.75	1.39/2.38	41.55
TBACl+ 40/60	0.59 ± 0.01	0.50 ± 0.01	0.79 ± 0.00	10.26	14.26	1.48/2.54	42.62
TBACl+ 30/70	0.70 ± 0.01	0.63 ± 0.01	0.86 ± 0.00	10.49	14.08	1.35/2.68	41.82
TBACl+ 20/80	0.78 ± 0.00	0.72 ± 0.00	0.90 ± 0.00	10.67	14.01	1.41/2.61	42.12
TBACl+ 10/90	0.91 ± 0.00	0.88 ± 0.00	0.96 ± 0.00	11.79	13.03	1.35/2.89	29.83
TBPB+ 90/10	0.10 ± 0.00	0.08 ± 0.00	0.17 ± 0.00	6.13	45.42	1.35/1.70	53.60
TBPB+ 80/20	0.19 ± 0.01	0.16 ± 0.01	0.26 ± 0.02	6.46	47.18	1.22/1.51	69.88
TBPB+ 70/30	0.30 ± 0.01	0.24 ± 0.01	0.38 ± 0.01	7.59	28.34	1.31/1.45	51.73
TBPB+ 60/40	0.39 ± 0.01	0.31 ± 0.01	0.47 ± 0.01	6.87	49.87	1.48/1.36	43.63
TBPB+ 50/50	0.49 ± 0.01	0.40 ± 0.01	0.60 ± 0.00	7.24	50.63	1.43/1.54	60.48
TBPB+ 40/60	0.60 ± 0.01	0.52 ± 0.01	0.68 ± 0.00	7.64	47.07	1.39/1.42	45.17
TBPB+ 30/70	0.69 ± 0.01	0.63 ± 0.00	0.77 ± 0.00	7.77	44.79	1.30/1.55	43.37
TBPB+ 20/80	0.80 ± 0.00	0.73 ± 0.00	0.86 ± 0.00	7.88	42.61	1.47/1.53	45.05
TBPB+ 10/90	0.90 ± 0.00	0.89 ± 0.00	0.94 ± 0.00	8.24	42.02	1.12/1.65	44.18

The average induction times are illustrated in Figure 8-13 and in a range of 33.8 to 64.6 minutes depending on the semiclathrate system.

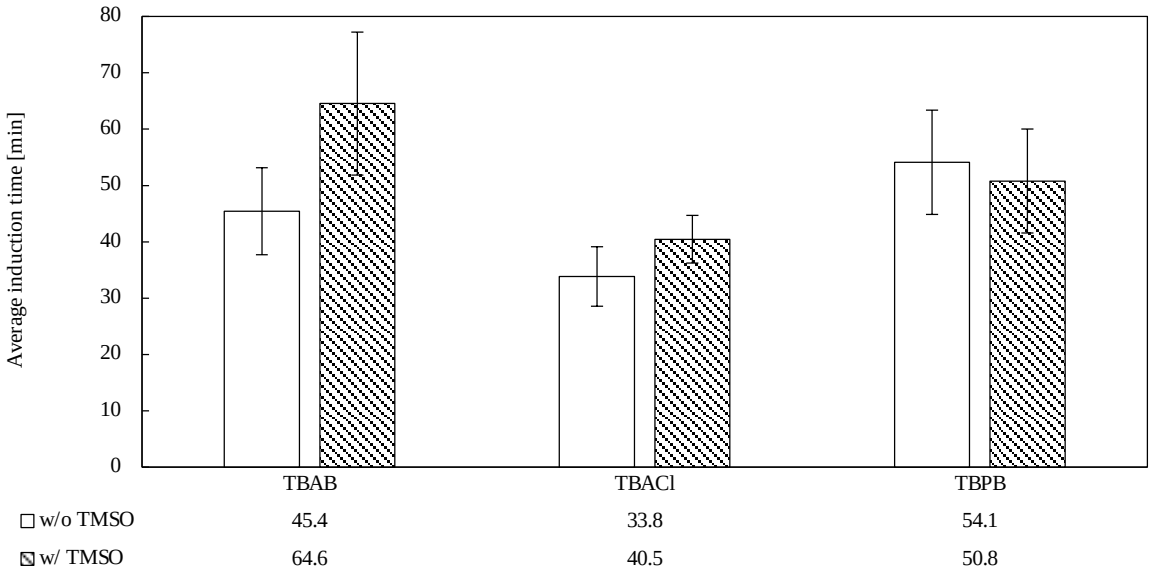

Figure 8-13 Average induction time [min] for biogas separation via semiclathrate formation w/o and w/ TMSO added

It is visibile that TBACl has the lowest induction times followed by TBPB and TBAB without added TMSO. By adding TMSO the induction times of TBACl and TBAB become longer whereas TBPB's are slightly shortened. Thereby, the order is changed to TBACl < TBPB < TBAB. The equilibrium temperature in dependence of the gas composition at the start is shown in Figure 8-14.

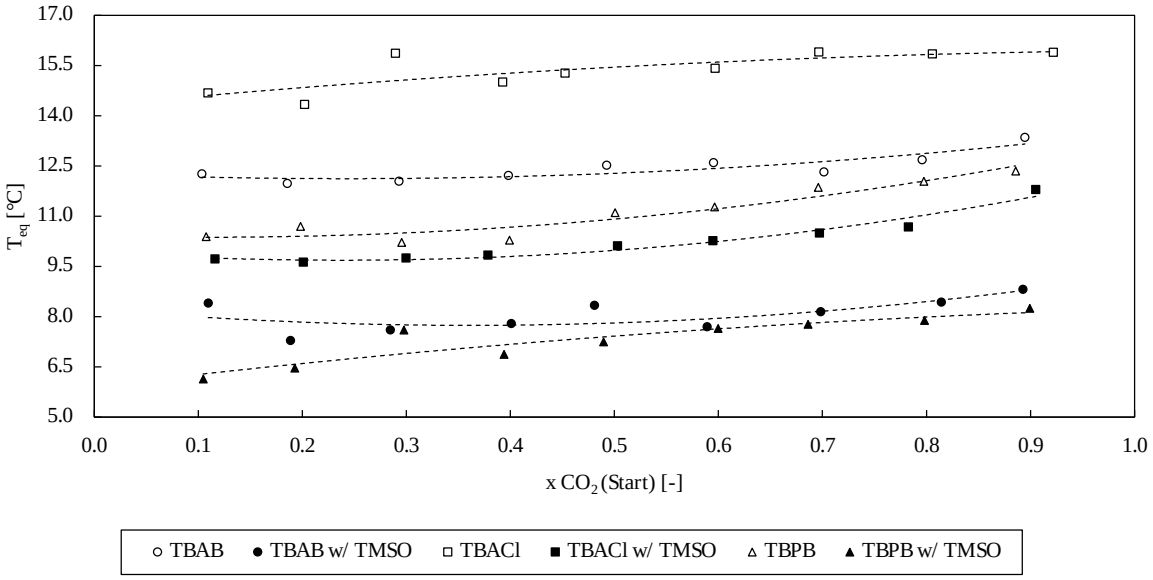

Figure 8-14 Equilibrium temperature [°C] vs. mole fraction of carbon dioxide [-] in the gas phase at the start

The equilibrium temperature shows that TBACl forms the most stable hydrate as temperatures are the highest with and without TMSO. TBACl is followed by TBAB and TBPB in both cases. The induction times and equilibrium temperature show that the thermodynamic stability depends on the combination of cation and anion. Smaller cations (ammonium smaller than phosphonium) form more stable semiclathrates which makes sense as the cavity structure becomes sturdier if

molecular interactions are narrower and nearer. TBPB distorts the semiclathrate framework stronger than TBAB [215]. Furthermore, as chloride and bromide are part of the semiclathrate structure, an increased electronegativity and smaller size should strengthen the hydrogen bonding. According to Manakov et al. chloride is substituting one water molecule or two hydrogen-bonded water molecules in the host structures which leads to "pressed in" 5^{12} cavities [220]. In case of bromide only the first variant is possible, the bromide anion replaces a water molecule in the framework [38].

Pure TBACl semiclathrate formed in a stoichiometry of 29.7 H_2O is supposed to melt at 15.1 °C which is consistent with the here obtained results in a temperature range of 14.33-15.90 °C [212]. The melting temperature of TBPB in a stoichiometry 36.6 H_2O is 9.25 °C according to Suginaka et al. [216]. Fukumoto et al. reported a melting temperature of 9.45 °C for pure TBAB and 27.75 for TBAF semiclathrates [221]. Here, the temperature found for TBAB and TBPB is higher as a range of 11.97-13.35 °C and 9.60-15.64 °C were obtained. Therefore, former literature confirms the superior stability of semiclathrates with a decreasing anion size but the similarity between TBPB and TBAB could not be validated as TBPB's equilibrium temperature was lower than TBAB's. Here, the effect of a guest molecule like methane or carbon dioxide and an increased pressure plays an important role as the filling of small 5^{12} cages stabilizes the semiclathrate structure leading to higher dissociation temperatures like it was found by Mayoufi et al. and Deschamps et al. [222,223].

The equilibrium temperature of each semiclathrate forming system shows an increasing trend with an increasing carbon dioxide concentration, which indicates a thermodynamically favored enclathration of carbon dioxide.

In presence of TMSO, a thermodynamic inhibiting effect is observed as all average equilibrium temperatures shift to lower values. The same effect was observed by Xia et al. while using a gas mixture of carbon dioxide and methane, 0.034 mol% TBAB and TMSO in different concentrations [198]. Figure 8-15 shows the average separation factors and average final gas uptake for all experimental series.

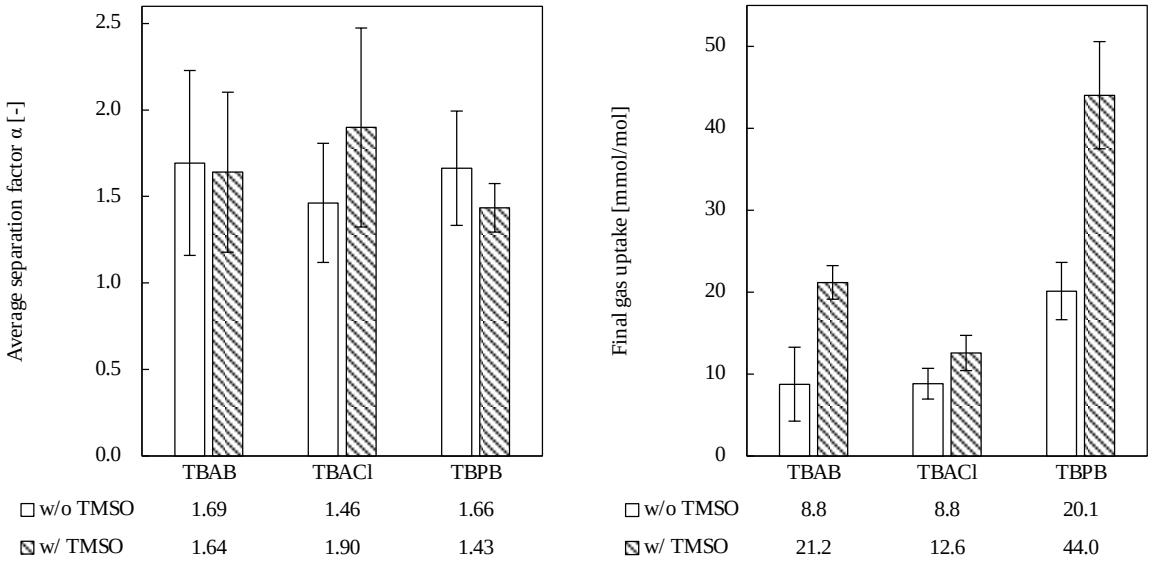

Figure 8-15 Average separation factors (left) and final gas uptake [mmol/mol] (right) for biogas separation via semiclathrate formation w/o and w/ TMSO added

Relating to the separation factors it is conceivable that without TMSO, TBAB and TBPB have a similar separation efficiency whereas the TBACl has a lower one. As chloride is integrated in the host framework in two ways. It either replaces one water molecule or two hydrogen-bonded water molecules and deforms the small 5^{12} cavities which become smaller [220]. Thereby, as carbon dioxide is a larger molecule, the small 5^{12} cages are preferably filled by methane and selectivity is lowered towards carbon dioxide. Therefore, selectivity of clathrate separation depends significantly on the competition of different molecules to occupy empty cages which was also a finding gained in chapter 8.1. Furthermore, the sort of anion influences the whole semiclathrate framework which has to be taken into account.

The average gas uptake w/o TMSO displays that TBAB and TBACl, forming the tetragonal structure TS-I, have an equal uptake with 8.8 mmol/mol each. TBPB, forming the orthorhombic structure RS, has a much higher uptake with 20.1 mmol/mol. This indicates that the storage capacity is related to the formed semiclathrate structure. In case of TBAB and TBACl, one cation corresponds to two 5^{12} cages, and therefore two gas molecules, whereas using TBPB, one cation equates to three 5^{12} cages. Furthermore, to form the structure TS-I for one gas molecule 17.2 water molecules are needed and regarding structure RS 12.7, which demonstrates the superior gas capacity of the latter structure.

By adding TMSO the selectivity decreases in the case of TBAB and TBPB whereas TBACl shows the opposite effect leading to the highest separation factor of 1.90 which is contrary to the work of Xia et al.. However, the experimental pressure used in their study ranged from 10 to 30 bar which could have an influence on the selectivity as well [198]. At the same time, the average gas uptake increases significantly for TBAB (8.8 → 21.2 mmol/mol ≡ 141 %) and TBPB (20.1 → 44.0

mmol/mol ≡ 119 %) except for TBACl (8.8 → 12.6 mmol/mol ≡ 43 %). The gas capture effect of sulfolane is based on interaction within carbon dioxide and the $-SO_2$ site and is less favored than between the rest of the molecule. In addition, cluster containing a large number of carbon dioxide molecules can arrange around a single $-SO_2$ site [224]. Therefore, the idea of the synergetic additive imposes itself as TMSO enhances the solubility and diffusivity of carbon dioxide, secures the full contact with surrounding water molecules and even increases the possibility of entrapment in the semiclathrate cavities like Xia et al. suggested [198]. In presence of TBACl and TMSO these effects seem to vanish. Due to the lack of literature up to this point, only assumptions can be given for this effect. It seems likely that this phenomenon is induced by interactions between the chloride and TMSO. Either the chloride prevents the capture of carbon dioxide by TMSO or, which is more likely, as a thermodynamic inhibiting effect is observed, TMSO influences the formation of the semiclathrate framework and the coordination of chloride within. However, it is stated here that these are assumptions and further fundamental research has to be conducted to gain more insights. Nevertheless, the separation factors α of 1.46 for the TBACl and 1.90 for the TBACl + TMSO system can now be used, in combination with Eq. 8-2, to construct adapted Mc-Cabe Thiele diagrams and determine the necessary stage number to purify biogas to a specification of at least 93 mol% outgoing from a mole fraction of 60 mol% methane. The results are shown in Figure 8-16.

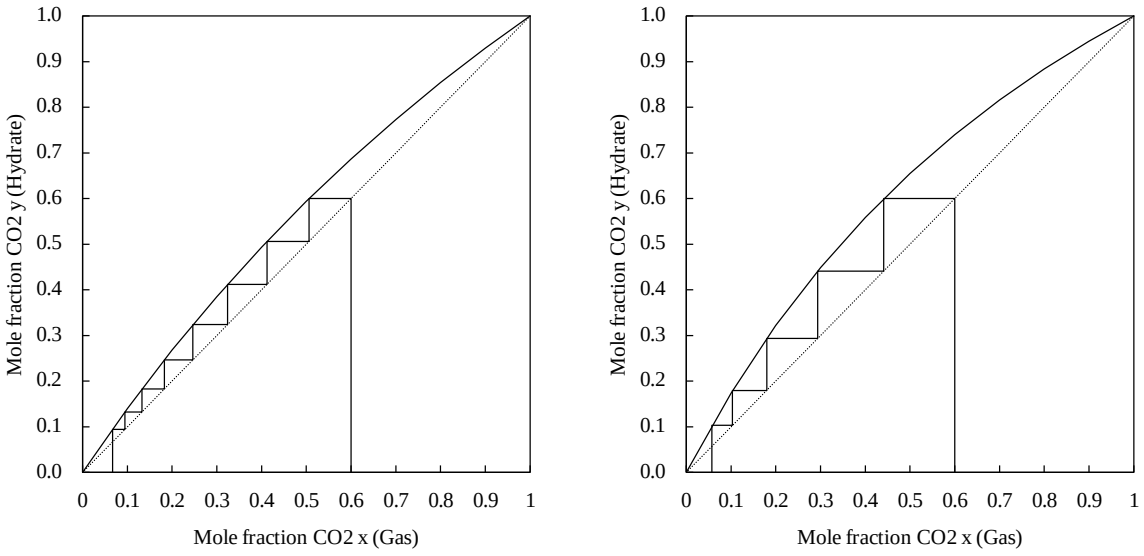

Figure 8-16 Determination of the necessary stage number to purify biogas to a specification of > 93 mol% via TBACl semiclathrate formation w/o (left) and w/ TMSO (right)

In comparison to the separation with THF (see chapter 8.1) it is visible that carbon dioxide is enriched in the semiclathrate and the necessary stage number is reduced from 22 to 5 to reach 93 mol% of methane. Thereby, as the experimental pressure was the same, the temperature should be around 10.2 °C which is slightly lower than in the case of THF (12.8 °C) but without TMSO, temperatures are around 15.4 °C and the necessary stage number is 8. Therefore, it is a

question of installation and operating costs if TMSO should be added or not. The only disadvantage in comparison to THF clearly indicated here is a lower gas uptake which results in a larger recycling stream to treat a given feed (12.6 mmol/mol TBACl+TMSO/16.56 mmol/mol THF).
Either way, this study extensively tested the potential of semiclathrates formed by three different substances and the effect of the synergetic additive TMSO for the application in biogas separation. As a result, biogas separation is achieved under moderate conditions with an appropriate efficiency but with a low amount of gas captured. In the case of TBAB and TBPB, TMSO enhanced the gas uptake significantly at the expense of a decreased separation efficiency. The effect of TMSO on the TBACl semiclathrate formation could not be clearly identified but an increased separation performance was observed. The effect of the anion of the semiclathrate former on the separation efficiency is significant and therefore future works are suggested to focus on further combinations of anion and cations, like tetra-n-butyl fluoride, iodide or nitrate for example.

9 Natural gas conditioning

The production of low-hydrocarbons via cryogenic distillation is a typical separation process in the petrochemical industry with the disadvantage of massive energy consumption [225]. However, several work showed that the gas hydrate separation technology is capable of separating gas mixtures of methane, ethane and propane. Kondo et al. observed a methane enrichment in the gas phase resulting from a feed mixture of methane, ethane, and propane in a 90:7:3 molar ratio during gas hydrate formation [226]. Thereby the separation of small hydrocarbons by gas hydrate formation should only be applicable for low and high methane concentrations [227]. Soltanimehr et al. described that ethane is preferably enriched in the gas hydrate phase and the selectivity is enhanced by an increasing pressure and decreasing temperature. While using THF, ethane and methane for gas hydrate formation it was found that ethane and THF compete for the large cages of structure sII enabling the separation of methane and ethane. Furthermore, a THF mole fraction of 0.06 allows the formation of a structure sII gas hydrate [228]. This is in accordance with findings from Ma et al. [229].
While using gas hydrate separation for the production of low-hydrocarbons seems to be quite promising, the here conducted study combines the rapid hydrate formation by spraying from chapter 7.3 and applies the gas separation experiments from chapter 8 on small hydrocarbons in a new, innovative process to absorb and store methane directly in form of a hydrate slurry in presence of THF as a thermodynamic promoter. Parts of this chapter have been published in [230].

Experimental procedure

Experiments were performed in the modified Büchi-reactor from chapter 7.3. GC-measurements were conducted via an Agilent type “6890 Series” gas chromatography system. Gas mixtures were prepared and stored from pure methane, ethane and propane in the 0.7 L Amar Equipments reactor. The test procedures had the following course of actions. The deposit reactor was purged and filled with a corresponding gas mixture. The reactor for the gas hydrate formation was filled with 370 mL of the hydrate forming mixture consisting of distilled water and 5.56 mol% THF. Thereafter, the gas hydrate forming reactor was purged three times with the gas mixture by pressurizing to 5 bar(g) each time. Afterwards, the experimental pressure was adjusted to 8 bar(g). The pump for the recycle injection over the nozzle and the stirrer (900 rpm, Reynoldsnumber ≈ 25483) were started before the reactor was cooled down until hydrate induction eventuated. The recycle flows through an external cooling coil which temperature was adjusted to 6 °C. Since temperature controls had a slow response time, a slight heat accumulation in the course of the exothermic gas hydrate formation was registered, finally leading to the equilibrium temperature for the given pressure of 8 bar(g) as gas hydrate decomposition and

formation are in equilibrium at this state. Thereupon, the thermostat temperature was set to the corresponding equilibrium temperature. The experiments lasted for 50 minutes with subsequent gas sampling for analysis. After taking the gas sample, the pressure was quickly drained to ambient conditions and the temperature was raised to 20 °C to dissociate the formed gas hydrates. Due to the gas hydrate decomposition, the reactor pressure rose again and the gas phase had nearly the composition of the former gas hydrates which was analyzed via GC-measurement as well. Additionally, the gas composition in the deposit was measured. All gas samples were measured five times. As gas could have been absorbed in the residual liquid during experiments, this cannot be taken into account by this experimental procedure. Residual gas at atmospheric pressure after the first reactor venting was mathematically taken into account.

Results and discussion

Table 9-1 shows the tested compositions, measured mole fractions in the gas and the hydrate phase at the end of the experiment, the gas uptake [mmol/mol], the equilibrium temperature [°C] and the ideal separation factors calculated by adapting Eq. 8-1.

Table 9-1 Experimental results for natural gas separation

	Initial composition [mol%]			Gas phase [mol%]			Hydrate phase [mol%]			Gas uptake $\left[\frac{mmol}{mol}\right]$	T_{eq} [°C]	α [-]
Nr.	CH_4	C_2H_6	C_3H_8	CH_4	C_2H_6	C_3H_8	CH_4	C_2H_6	C_3H_8			
1	92		8	90		10	96		4	44.97	14.2	2.09/1.28
2	90		10	88		12	95		5	38.01	14.2	2.11/1.23
3	83		17	79		21	92		8	40.04	13.6	2.36/1.30
4	78		22	72		28	89		11	33.34	14.1	2.28/1.38
5	72		28	64		36	85		15	35.26	13.7	2.20/1.45
6	70		30	63		37	84		16	34.58	13.5	2.25/1.37
7	92	8		88	12		98	2		42.50	13.5	4.26/1.57
8	81	19		67	33		92	8		19.44	13.2	2.70/2.10
9	70	30		56	44		92	8		22.17	12.8	4.93/1.83
10	56	44		40	60		87	13		20.58	10.9	5.26/1.91
11	44	56		30	70		78	22		27.96	10.3	4.51/1.83
12	33	67		26	74		74	26		19.28	9.8	5.78/1.21
13	26	74		18	82		57	43		12.44	8.7	3.77/1.60
14	88	7	5	84	11	5	96	2	2	42.92	13.3	3.55/1.44
15	88	7	5	81	13	6	94	3	3	40.43	13.5	2.18/1.73
16	89	6	5	81	13	6	94	3	3	55.81	13.3	1.99/1.87

First of all, the experimental data prove the successful gas separation via rapid hydrate absorption. Due to the occupation of large cavities by THF in the sII hydrate structure, methane is pushed to fill the small cages whereas other components remain in the gas phase. Using Eq. 8-1, separation factors were calculated for each data point. For the separation of methane + propane the separation factor α is 1.77 ± 0.47 and 3.09 ± 1.59 for methane + ethane which is nearly two times higher. Figure 9-1 shows the correlation between the gas uptake [mmol/mol] against the initial mole fraction of methane.

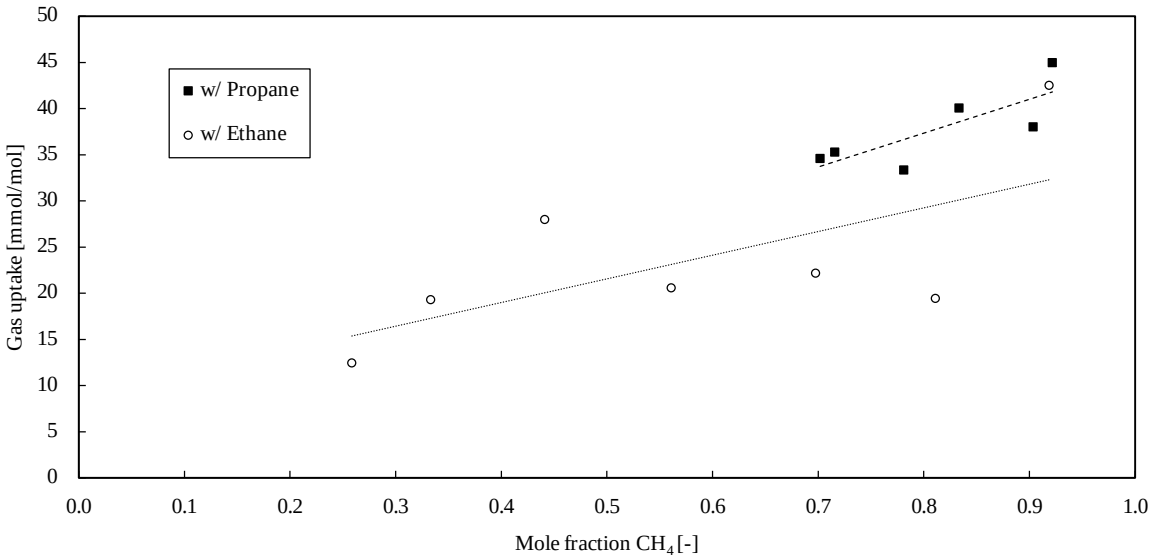

Figure 9-1 Gas uptake [mmol/mol] vs. mole fraction of methane for the natural gas separation experiments

The gas uptake decreases with a decrease in the mole fraction of methane for both gas mixtures. The methane-propane mixture shows a higher gas uptake. Considering the observed trend and the determined ideal separation factors allows the conclusion that the better selectivity, but worse gas uptake in case of a methane-ethane mixtures can be traced back to the fact that propane as a sII hydrate former is enclathrated in the same large cages like THF during gas hydrate formation. Ethane rather occupies the large cages of the sI gas hydrate structure. Morita et al. observed the occupancy of both gas hydrate cages of structure sI solely for high pressures of 3000 bar(a) [231]. By using THF in a stoichiometric concentration, structure sII is forced to form and the ethane is massively hindered to form gas hydrates as it is neither able to stabilize large cages of structure sI nor structure sII. By increasing the ethane amount, sI-sII mixed hydrates are formed. This is in accordance with Zhang et al. who observed exactly the same effects while forming gas hydrates from a methane-ethane gas mixture in presence of 6.0 mol% THF. By using their experimental data, ideal separation factors were calculated as $\alpha = 3.30 \pm 1.16$ for 21 bar(g) and $\alpha = 3.74 \pm 1.40$ for 31 bar(g) respectively which shows an increased separation efficiency at higher pressures [232].

All the gas uptakes are far away from total water to gas hydrate conversion which could reduce the selectivity of the process as some water remains in a liquid state with dissolved components in it. Nevertheless, the handling of a flowable hydrate slurry instead of solid gas hydrates at the outlet is expected to be favored in an industrial process. Therefore, complete water to hydrate conversion does not represent the application case appropriately.

The operating conditions are moderate with a pressure of 8 bar(g) and a temperature range of 14 to 9 °C. With a slightly higher pressure, ambient temperatures could be operated as well, which is an advantage in comparison to industrial demethanizers which are operated at 25 bar(g) and -83 °C [225]. The equilibrium temperatures in dependence of the initial methane mole fraction is visualized in Figure 9-2.

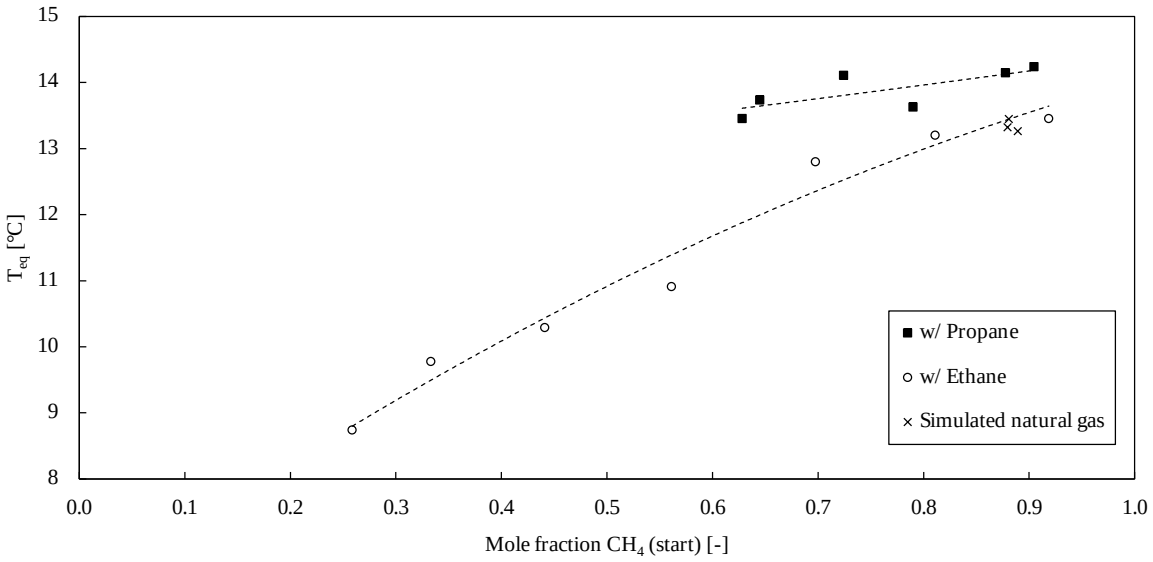

Figure 9-2 Equilibrium temperature [°C] vs. mole fraction of methane [-] in the gas phase at the start

Both curves, with ethane as well as with propane, show a decrease in the equilibrium temperature with a decreasing methane concentration. The equilibrium temperature of gas hydrates from simulated natural gas are in a magnitude of the CH_4-ethane-hydrate curve. Same effects and similar temperatures were found in an experimental series conducted by Sun et al. [228]. The phenomenon can be explained by a declining stability of the formed gas hydrates in the following order:

$$CH_4\text{-THF} > CH_4\text{-propane} > CH_4\text{-ethane}.$$

Figure 9-3 shows the mole fractions of methane in the gas hydrate and in the gas phase with corresponding adapted McCabe-Thiele trends. By using the McCabe-Thiele diagram, it is possible to estimate that for the purification of a methane-ethane mixture via gas hydrate separation, only eight theoretical stages would be necessary to get both components with a purity of 99 mol%. In comparison, the cryogenic distillation needs approximately 30 stages [225].

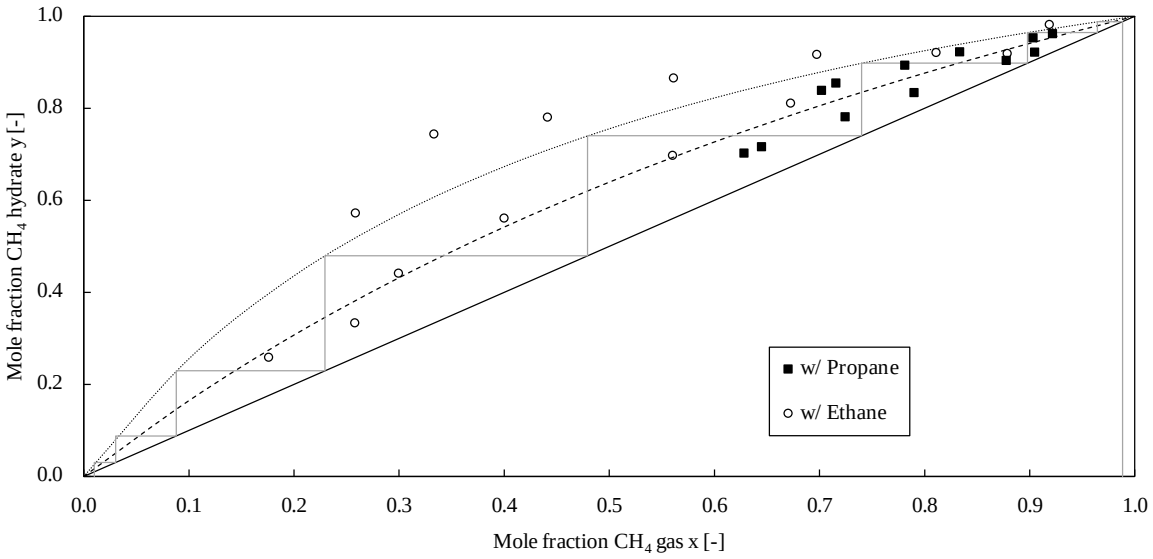

Figure 9-3 Mole fraction of methane in the hydrate phase vs. mole fraction of methane in the gas phase with adapted McCabe-Thiele-trends

In Figure 9-4 the averaged change in the mole fraction of a simulated natural gas, consisting of methane, ethane and propane, is visualized.

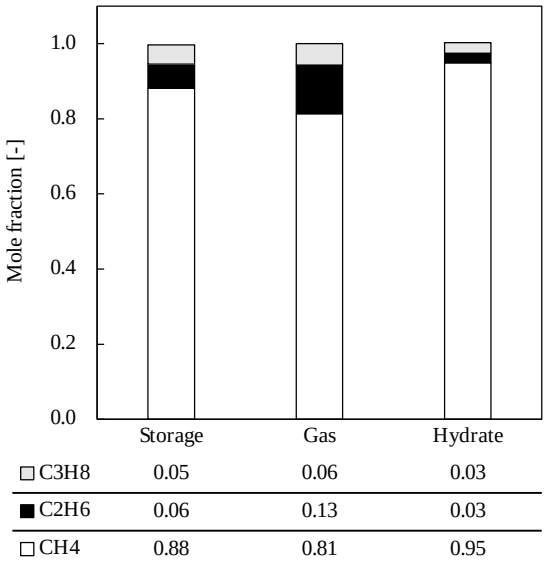

Figure 9-4 Averaged change in the mole fraction of a simulated natural gas

It was possible to achieve a typical gas specification for consumers with a high methane content of ≥ 95 mol% by using a one-stage hydrate absorption process. Thereby methane was stored in the form of gas hydrates which would subsequently enable the option for transportation in form of solidified natural gas. Nevertheless, high methane losses in the gas phase have to be taken into account. As a result, a multi-stage process would be recommended here as well.

10 Cost studies

The preceding chapters (chapter 8 and chapter 9) presented the possibility to separate methane from raw gas and biogas via gas hydrate separation with a separation factor α of 1.77 and 1.90, respectively. By constructing adapted Mc-Cabe-Thiele diagrams it was estimated that 12 stages are necessary to achieve appropriate qualities and produce saleable methane. As gas hydrate separation seems to be a promising alternative to existing methane separation processes, this chapter describes the cost estimation of gas hydrate separation processes which could replace the established ones. Therefore, simulations with the process simulation software CHEMCAD© were performed to calculate installation costs of the necessary process equipment for typical separation processes, obtained from literature and for a corresponding gas hydrate separation process. It is stated here, that the cost estimation performed by CHEMCAD© is based on several different references which are from the early 1980s, which is why the estimated costs cannot be assumed to be accurate but at least, as all calculations share the same basis, qualitatively comparable [233–242]. Furthermore, the costs for piping and instrumentation and control equipment remained unconsidered. Operating costs were calculated based on energy consumptions and typical energy costs. The used prices are listed in Table 10-1.

Table 10-1 Energy prices

Energy source	Price
Electricity	14.9 ct/kWh [243]
Condensate	1.16 €/t[1]
Cryogenic cooling	1.00 €/kWh[2]
Cooling (-20°C)	19.4 ct/kWh[3]

10.1 Biogas conditioning

With regard to chapter 2.6, the main technologies for carbon dioxide removal are amine and water absorption. As water scrubbing is the environmental favored alternative, this process will be focused on in this chapter. Water scrubbing has the advantage of simultaneously removing carbon dioxide and hydrogen sulfide, and is considered as a simple-to-maintain and economic process.

[1] Estimated value based on steam prices for 31 bara (20 €/t) and 6 bara (13 €/t) steam from personal experience

[2] Estimated value based on personal communication with employee at Messer Group GmbH

[3] Estimated value based on electricity price multiplied with the specific energy consumption of a vapor-compression refrigeration [244]

The process was simulated in a previous work by Cozma et al. and reconstructed in an own simulation for the cost study described here [245]. The results are shown in Figure 10-1.

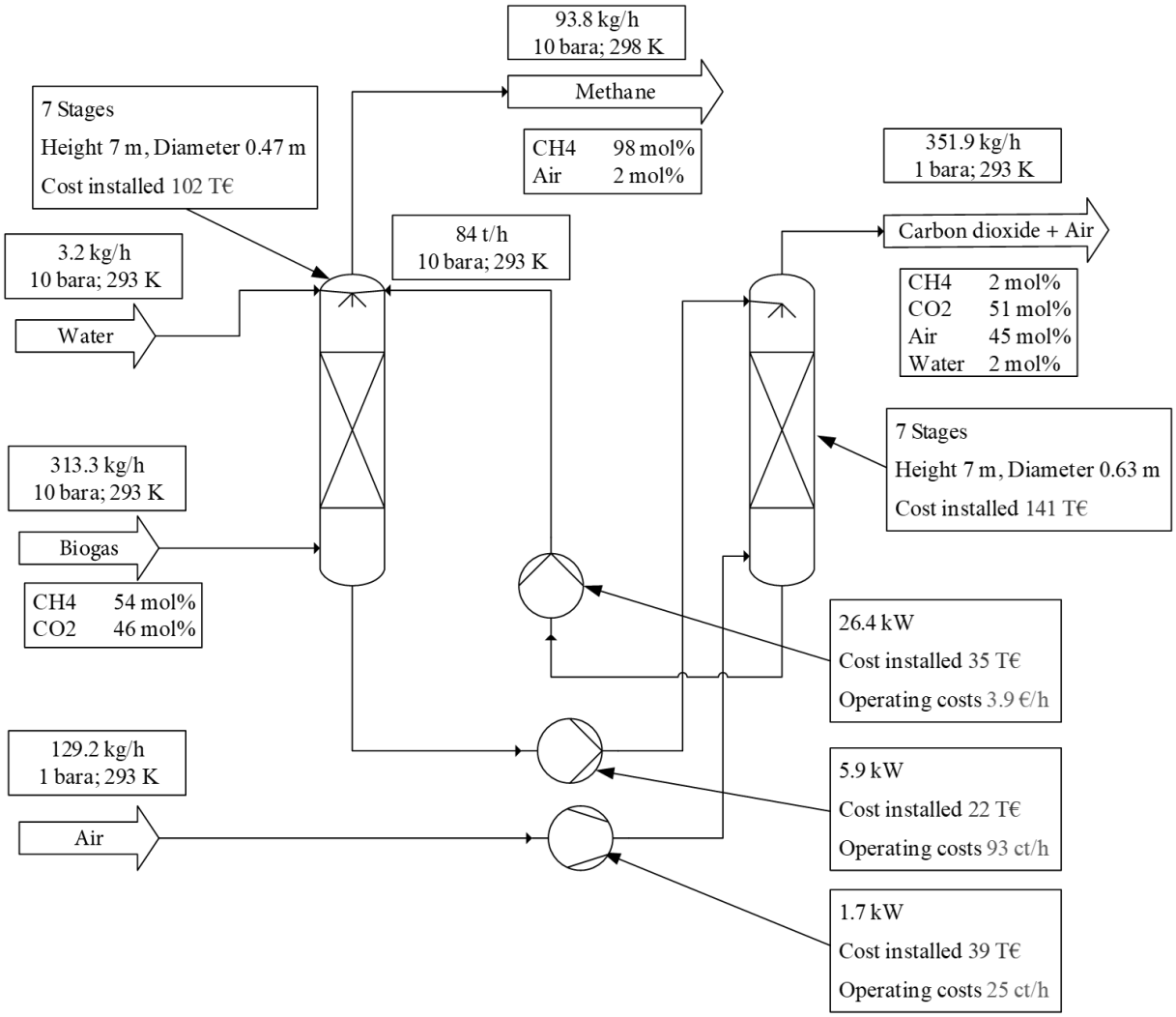

Figure 10-1 Simulation results - water scrubbing process

The process works as follows: Compressed and tempered biogas enters the first absorption column at the bottom in a concentration of 54 mol% methane and 46 mol% carbon dioxide. With a countercurrent flow, water runs down the column and carbon dioxide is absorbed at 10 bar(a). The carbon dioxide enriched water is pumped to the top of a second column (depressurized to 1 bar(a)) and treated with air in a countercurrent flow. Thereby, carbon dioxide is desorbed and exits the column at the top with humid air. As water exits the process through this stream, a small make up stream must be implemented in the former column. The regenerated water contains small amounts of air and is pumped back into the first column. In the first column, methane with small air impurities is obtained in a concentration of 98 mol%. The whole process consists of 2 columns (243 T€), 2 pumps (57 T€) and one compressor (39 T€). The summed up installation costs amount to approximately 339 T€ and operating costs to 5.08 €/h. The calculation results for a comparable gas hydrate separation process are shown in Figure 10-2.

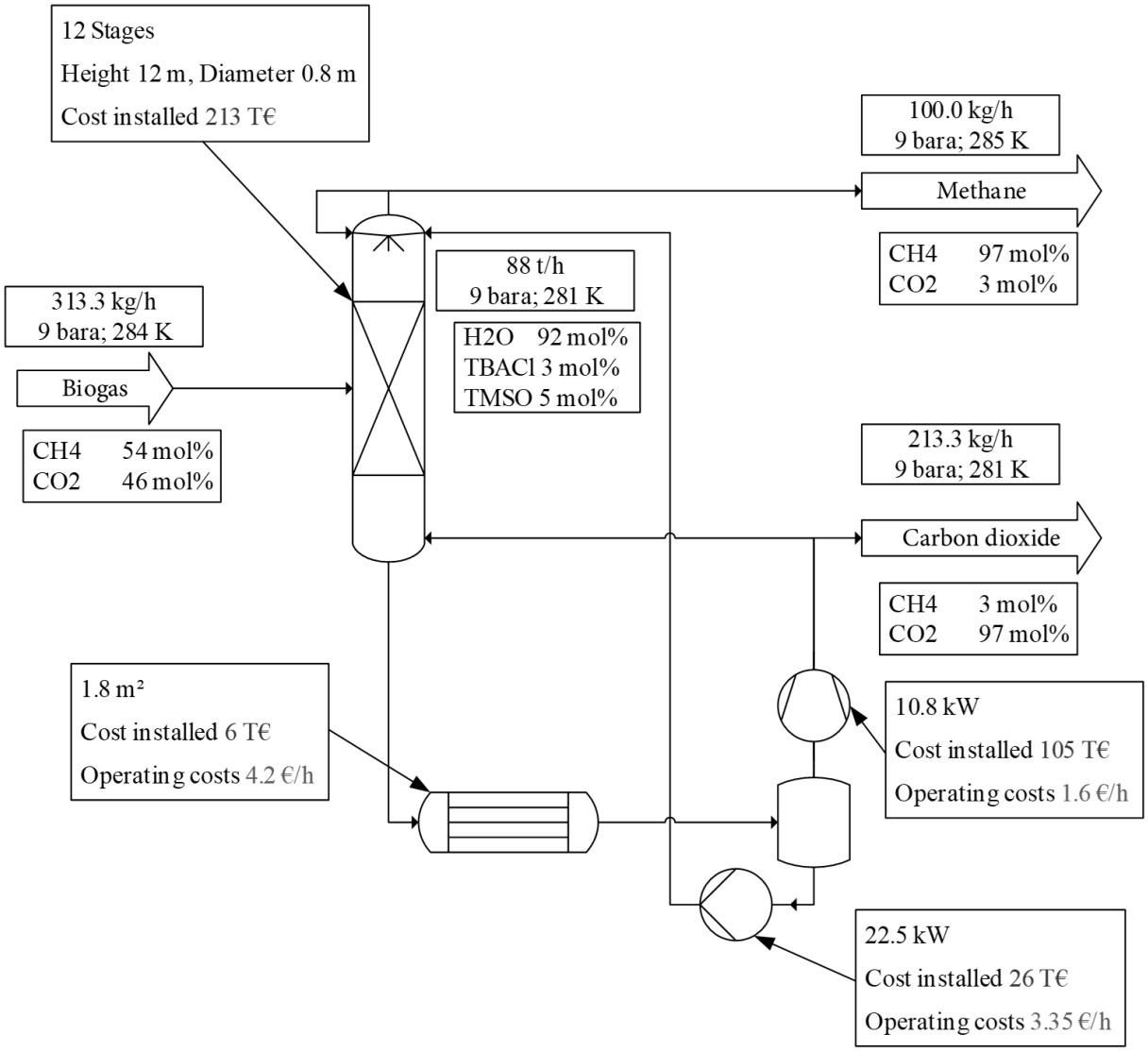

Figure 10-2 Simulation results – biogas hydrate separation process

In general, the gas hydrate separation process is based on the concept of a crystallization column. A cooled gas hydrate forming mixture is sprayed, by using a two-phase nozzle, into a pressurized column to secure an immediate hydrate nucleation and therefore continuous growth along the column. Simultaneously, the nozzle allows the implementation of a reflux ratio. Similar to a distillation column it is expected that, due to different gas phase compositions on every theoretical stage, the hydrate phase changes its composition as well and, because of varying hydrate formation enthalpies on each theoretical stage, the corresponding equilibrium temperature is prevailed. Therefore, from the bottom to the top, a decreasing temperature profile establishes and the favored gas component is enriched in the hydrate phase whereas other gas components remain in the gas phase. At the bottom, a hydrate slurry must be dissociated which can be done by using a heat exchanger and a subsequent depressurizing separator. The separator is connected to a pump which recycles the hydrate forming mixture, and to an optional compressor which transports the purified gas stream to the process outlet or either back into the column to allow the adjustment of a reflux ratio here as well. As hydrate decomposition is an endothermic process,

the temperature of the hydrate forming recycle stream can be set by controlling the energy consumption of the heat exchanger.

In this simulation, the inlet stream has the same specification as the water scrubbing process and flows into the crystallization column. Pressure and temperature are adjusted to the conditions on the equivalent entering stage. As a hydrate forming mixture of water, TBACl and TMSO had the highest separation factor, this mixture is used as a hydrate forming absorbent. With a separation factor α of 1.90 ± 0.58, 12 stages would be necessary to produce methane and carbon dioxide with a composition of 97 mol% each (chapter 8.2). The amount of hydrate forming mixture is calculated based on the fact that hydrate slurries which exceed a loading of 30 wt% of hydrate could cause problems like plugging or at least viscous flow properties [207,246]. Furthermore, as TBACl forms structure TS-I in a stoichiometric concentration of $TBACl \cdot 29.7\ H_2O$ the unit cell is described as f $10(5^{12}) \cdot 16(5^{12}6^2) \cdot 4(5^{12}6^3) \cdot 172\ H_2O$. TBA^+ is entrapped in four $5^{12}6^2$ cages and four times in $3(5^{12}6^2) \cdot (5^{12}6^3)$ cages, leaving ten 5^{12} cages empty, which can be filled by another guest. The Cl^- is included in the hydrate framework [212]. This means that the ideal carbon dioxide filled semiclathrate structure can be written as $TBACl \cdot 2\ CO_2 \cdot 29.7\ H_2O$ and this allows the calculation of the stream size. The carbon dioxide rich slurry flows into the heat exchanger at the bottom.

The transferred heat is given by the amount of formed semiclathrate from TBACl and carbon dioxide and a formation enthalpy of $346.6 \pm 3.5 \frac{kJ}{kg\ [H_2O]}$ [247]. The formation enthalpy of semiclathrate from TBACl and methane is assumed to be 339.8 $\frac{kJ}{kg\ [H_2O]}$ due to the lack of literature and calculations should be repeated as soon as experimental data are available[1]. By using this data, the heat exchanger can be designed, as energy consumption and heat transfer area can be calculated using an overall heat transfer coefficient of $600 \frac{W}{m^2K}$ [249]. The hydrodynamic calculation of the column and design of the pump and the compressor were simulated to estimate the installation and operating costs. The whole process consists of one crystallization column (213 T€), one heat exchanger (6 T€), one pump (26 T€) and one compressor (105 T€) which makes in sum 350 T€. The operating costs accumulate to 9.15 €/h. Figure 10-3 compares the cost trends for both processes. Thereby, 8000 hours of operation per year are assumed. In addition, an alternative without a compressor is shown as the exiting carbon dioxide in the water scrubbing process is also not compressed.

[1] It is assumed that $\Delta H_{mix\ CO_2} = \frac{1}{2}\Delta H_{TBACl} + \alpha\Delta H_{CO_2} \rightarrow \Delta H_{mix\ CH_4} = \frac{1}{2}\Delta H_{TBACl} + \alpha\Delta H_{CH_4}$ with $\Delta H_{mix\ CO_2} = 92.65 \frac{kJ}{mol}$, $\Delta H_{TBACl} = 156.9 \frac{kJ}{mol}$, $\Delta H_{CO_2} = 65.2 \frac{kJ}{mol}$, $\Delta H_{CH_4} = 56.8 \frac{kJ}{mol}$[212,247,248]. $\alpha = 0.218$ is a correction factor.

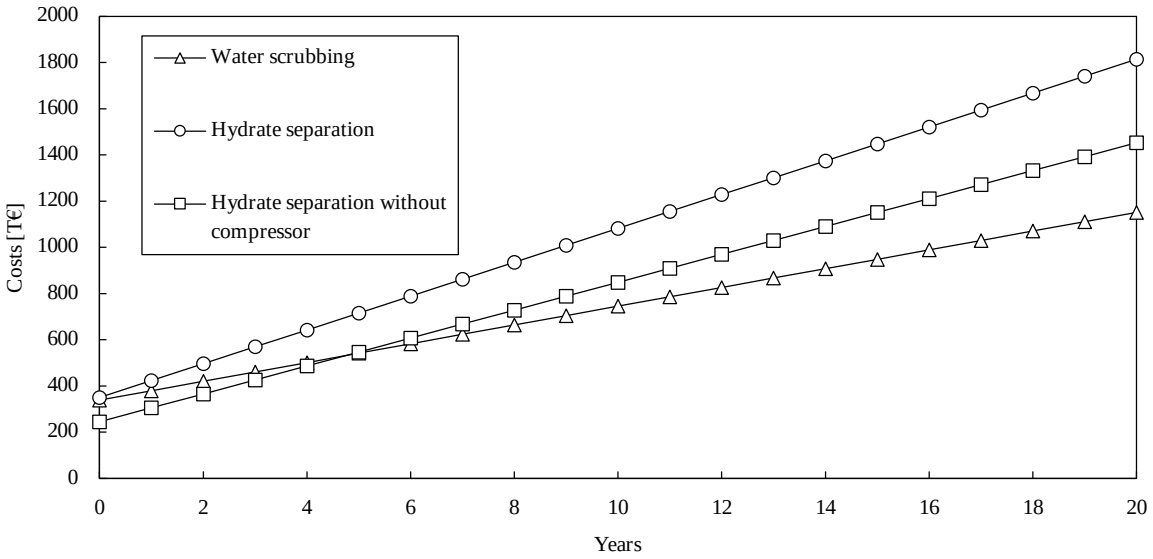

Figure 10-3 Comparison of cost trends over 20 years for biogas separation via water scrubbing and gas hydrate separation

The gas hydrate separation process has similar investment costs but a much higher energy consumption which is why this process would be much worse than the existing one. If the carbon dioxide is not compressed, which would also lead to methane losses as no reflux ratio could be adjusted, the process would be economically superior in the first 5 years. Afterwards, the process is more expensive as operating costs are still higher than in the case of water scrubbing and total costs would exceed the total costs of the water scrubbing process. The only possibility to make the gas hydrate separation process profitable would be if the produced carbon dioxide semiclathrate could be sold as a phase change material or rather refrigerant for air-conditioning systems for example as it is proposed in literature [207,250–252].

10.2 Natural gas conditioning

From chapter 9 it is known, that gas hydrate separation is assumed to be a promising alternative to the cost intensive cryogenic demethanization. Here the process described by Luyben et al. was reconstructed in a simulation and the results are shown in Figure 10-4 [225].

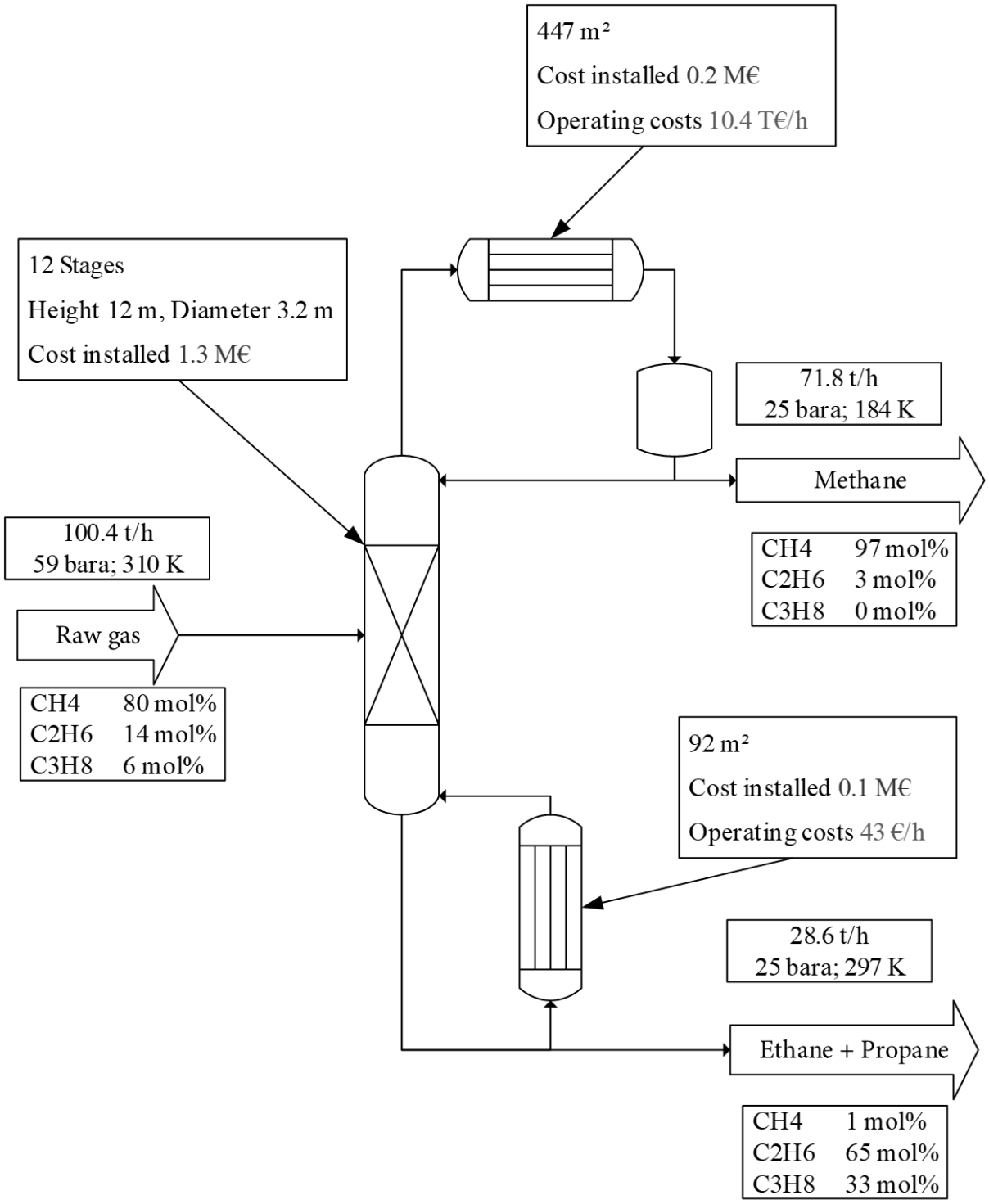

Figure 10-4 Simulation results - cryogenic demethanizer

The process consists of a distillation column operated with a cryogenic condenser and a reboiler fed with condensate. Compressed raw gas, consisting of methane, ethane and propane enters the

column and is separated by distillation. Methane leaves the column at the top in a concentration of 97 mol% and ethane and propane are produced as bottom product with less than 1 mol% methane. Therefore, the whole process consists of one distillation column (1.3 M€) and two heat exchangers (0.2 M€, 0.1 M€) which sum up to 1.6 M€. The operating costs amount to approximately 10.4 T€/h. The alternative gas hydrate process is shown in Figure 10-5.

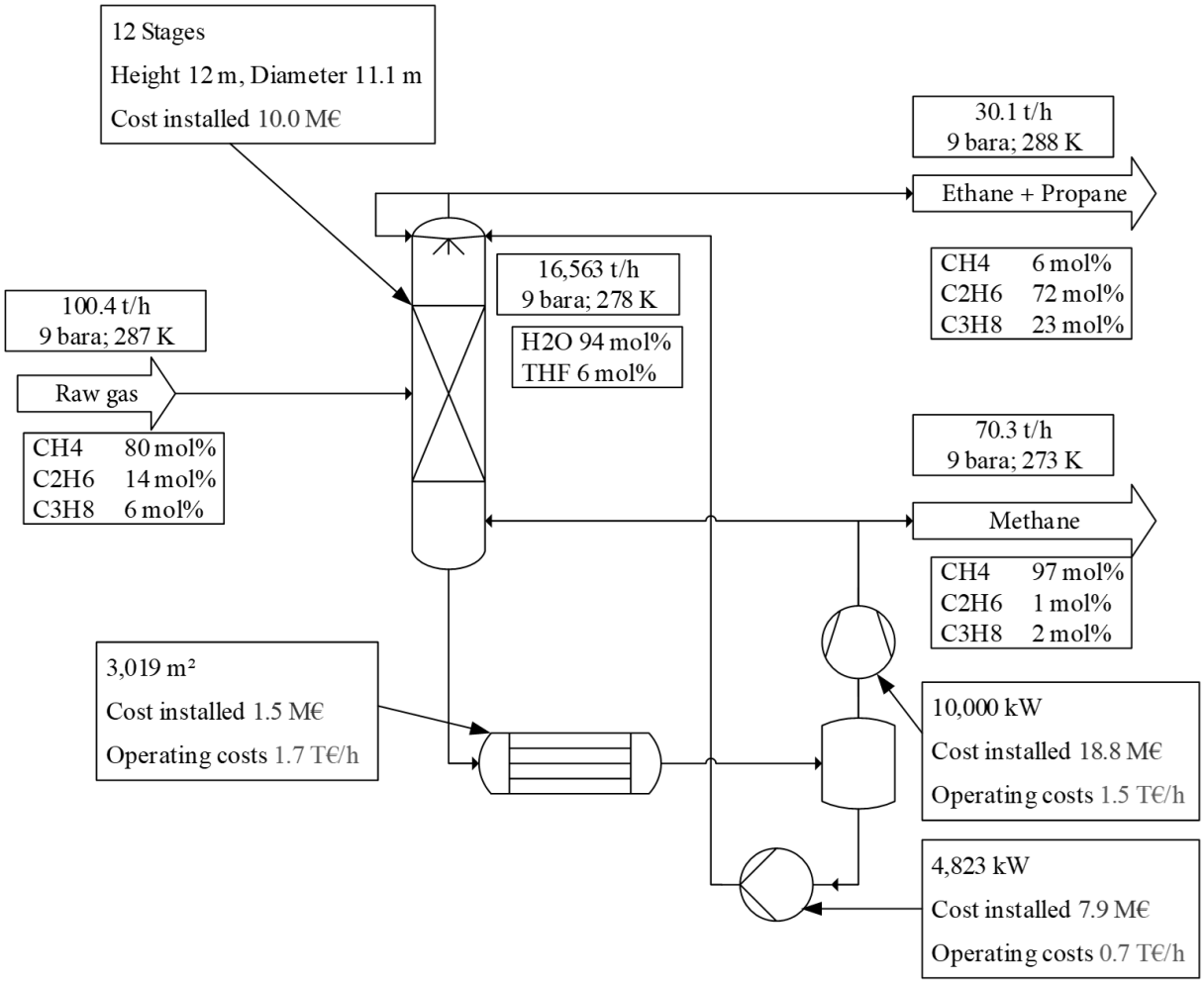

Figure 10-5 Simulation results – gas hydrate demethanizer

The underlying process works in the same way as described in chapter 10.1.

- A cooled hydrate forming mixture is sprayed by using a two-phase nozzle (reflux ratio possible) into a pressurized crystallization column.
- From the bottom to the top a decreasing temperature profile establishes itself and one gas component is enriched in a hydrate slurry whereas other components remain in the gas phase and leave at the top.
- The hydrate slurry is dissociated, hydrate forming mixture recycled and purified methane (97 mol%) compressed for exit or reflux.

The size of the hydrate forming stream results from two requirements:

- The hydrate slurry should not exceed a mass fraction of 30 wt% hydrate to secure flowability [207,246].

- THF is added in the stoichiometric concentration of 5.56 mol%, structure SII is formed where one mol gas binds 8.5 mol water.

The heat exchanger is designed based on the following considerations:

- Dissociation enthalpy of mixed hydrate from THF and methane is estimated as 138.4 kJ/mol[1].
- Propane and ethane are not assumed to form mixed hydrates with THF, therefore pure hydrate dissociation enthalpies were used → ethane 71.8 kJ/mol, propane 129.2 kJ/mol [6].
- Overall heat transfer coefficient of 600 $\frac{W}{m^2K}$ [249].
- It is stated here that calculations should be repeated as soon as experimental data are available.

Afterwards, the pump, compressor and column were simulated based on the size of the streams to estimate the installation costs and energy consumption. The installation costs amount to 38 M€ as one crystallization column (10 M€), one heat exchanger (1.5 M€), one pump (7.9 M€) and one compressor (18 M€) are necessary for the process. The operating costs total to 3.9 T€/h. Both results are compared in Figure 10-6. 8000 hours of operation per year were assumed.

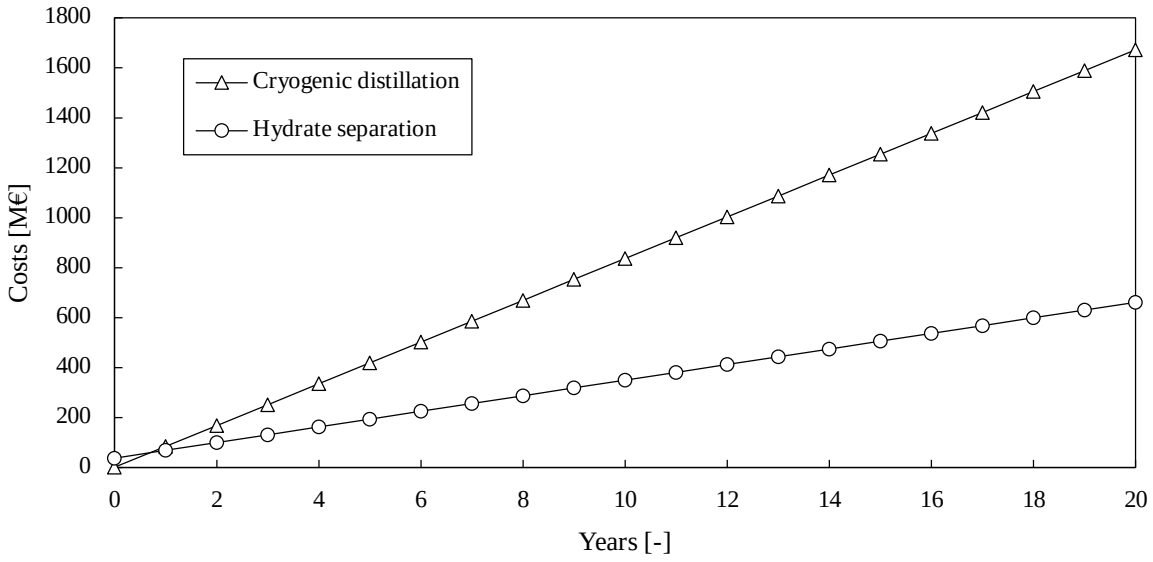

Figure 10-6 Comparison of cost trends over 20 years for demethanization via cryogenic distillation and gas hydrate separation

[1] It is assumed that $\Delta H_{mix\,CO_2} = \Delta H_{THF} + \alpha\Delta H_{CO_2} \rightarrow \Delta H_{mix\,CH_4} = \Delta H_{THF} + \alpha\Delta H_{CH_4}$ with $\Delta H_{mix\,co_2} = 142.0\,\frac{kJ}{mol}$, $\Delta H_{THF} = 110.0\,\frac{kJ}{mol}$, $\Delta H_{CO_2} = 65.2\,\frac{kJ}{mol}$, $\Delta H_{CH_4} = 56.8\,\frac{kJ}{mol}$ [6,253,254]. $\alpha = 0.5$ is a correction factor.

It can clearly be seen that the hydrate separation process has 24 times higher investment costs. However, as operating costs are 63 % less, already after 2 years the cryogenic distillation would be the more expensive option. Therefore, again it is shown that the gas hydrate separation process is a promising alternative to the cryogenic distillation with regard to demethanization.

11 Planning of a pilot plant

The preceding chapters contributed to the fundamental research of gas hydrate separation and additionally economic considerations were made. It was shown that it would make no sense to use gas hydrate separation for the purification of biogas. Nevertheless, the production of pure methane from natural gas via gas hydrate separation to replace the existing cryogenic process has a vast potential. Other gas mixtures were not in the scope of this thesis. However the current research shows, that there is also an interest in conditioning flue gas [255,256], acidic gases [198], fuel gas [206,257], greenhouse gases [258] etc. via gas hydrate formation. Moreover, gas separation via clathrate formation becomes relevant for the industry as the work of Coupan et al. proves. The mentioned paper describes the start-up of and research results from a pilot scale hydroquinone clathrate based gas separation process for the treatment of methane-carbon dioxide mixtures, which was supported by the Total E&P, "Gas Solutions" department [259]. Therefore, it would be of engineering scientific interest and, with regard to the registration of patents, necessary to build up a continuous operating pilot plant to take the next step to establish the gas hydrate separation as an industrial separation process. That is why this chapter describes the basic design of such a pilot plant. The here described pilot plant design focuses on the treatment of biogas via sII hydrate formation with THF in the stoichiometric concentration for an operating pressure of 20 bar(g) around temperatures of 20 °C [37]. Due to the low selectivity of this promoter system, this assumption represents a worst case scenario and is made to allow the necessary design calculations. The pilot plant can be used to investigate other systems as well.

In principle, the size of the pilot plant is limited by the size of the available fume cupboards, as otherwise EX-zones have to be declared, if explosive gases are used during experiments. The available space is: 3.7 m x 4.4 m x 0.85 m [height x width x length]. The concept is based on the gas hydrate separation performed in some kind of crystallization column as proposed in chapter 10 and used by Coupan et al. [259]. This column should be modifiable, which means, that the separation stage number can be varied, and in turn a random packed column is favored here as with the height of the packing the separation stage number can be easily adjusted. Raschig rings with a diameter of 8 mm are suggested and after consulting a manufacturer, a HETP value of 0.22 m^{-1} is estimated. According to Sattler, the column diameter should at least be 10 times higher than the packing diameter which results in a column diameter of 8 cm [260]. If one wants to create 10 separation stages, the column height H must be at least 2.2 m and if some additional spacing is added for the in- and outlets, the overall height will be estimated as 2.7 m. Therefore, 1 m of height is left to place equipment above and below the column. Following Mersmann et al. it is possible to determine the operating window for the column to prevent entrainment and flooding [261].

First, the particle diameter d_P is calculated in dependency of the packing material. The volumetric surface area S and porosity ϵ are tabulated as $S = 550\frac{m^2}{m^3}$ and $\epsilon = 0.63$ for 8 mm Raschig rings [262].

$$d_P = 6 * \frac{1-\epsilon}{S}\ [m] \qquad \text{Eq. 11-1}$$

Assuming an operating pressure of 20 bar(g), a temperature of 20°C and an inlet stream of 50 mol% methane and 50 mol% carbon dioxide, as a model fluid for the design, the Reynoldsnumber Re in dependency of the gas flow velocity w_g can be calculated which is necessary to evaluate the resistance coefficient ζ_0 of the packing. Under the assumed circumstances, the gas density ρ_g and viscosity η_g are $\rho_g = 26.4\frac{kg}{m^3}$ and $\eta_g = 1.405 * 10^{-5}\ Pa\ s$. The values b and c depend on the packing material and are tabulated for 8 mm Raschig rings as:

$$b = 34.6 \text{ and } c = -0.307 \text{ for } Re < 2100$$
$$b = 6.05 \text{ and } c = -0.079 \text{ for } Re \geq 2100 \text{ [262].}$$

$$Re = \frac{d_p * w_g * \rho_g}{\eta_g}\ [-] \qquad \text{Eq. 11-2}$$

$$\zeta_0 = b * Re_0^c\ [-] \qquad \text{Eq. 11-3}$$

Afterwards, the pressure-drop of the dry packing Δp_{dry} is calculated using the given formula which depends on the gas flow velocity w_g as well.

$$\Delta p_{dry} = \frac{3}{4} * \zeta_0 * \frac{1-\epsilon}{\epsilon^{4.65}} * \rho_g * \frac{w_g^2}{d_P} * H\ [Pa] \qquad \text{Eq. 11-4}$$

In the next step, the liquid hold-up h_L is calculated. In doing so, initially, the liquid hold-up below the flooding point h_{Lo}, which is independent from the gas load, must be determined. This liquid hold-up correlates with the liquid flow velocity w_L, the volumetric surface area a, the gravity g, the liquid density ρ_L, the liquid viscosity η_L and the liquid surface tension σ (here $\rho_L = 979.3\frac{\text{kg}}{\text{m}^3}$, $\eta_L = 1.63 * 10^{-3}\ Pa\ s$ and $\sigma = 0.063\frac{N}{m}$ for a hydrate forming mixture of 94 mol% water and 6 mol% THF).

$$h_{Lo} = 0.93 * \left(\frac{w_L^2 * a}{g}\right)^{\frac{1}{6}} * \left(\frac{\eta_L^2 * a^3}{\rho_L^2 * g}\right)^{\frac{1}{10}} * \left(\frac{\sigma * a^2}{\rho_L * g}\right)^{\frac{1}{8}} \qquad \text{Eq. 11-5}$$

The liquid hold-up h_L in the gas and liquid loaded packing can now be computed with Eq. 11-6.

$$h_L = h_{Lo}\left[1 + 20 * \left(\frac{\Delta p_{Sp}}{H * \rho_L * g}\right)^2\right] \quad \text{Eq. 11-6}$$

As the pressure loss of the sprinkled packing Δp_{Sp} is unknown, it must be calculated by using the next formula, which in turn depends on the liquid hold-up h_L.

$$\Delta p_{Sp} = \left[\frac{1 - \epsilon\left(1 - \frac{h_L}{\epsilon}\right)}{1 - \epsilon}\right]^{\frac{2+c}{3}} * \left(1 - \frac{h_L}{\epsilon}\right)^{-4.65} \quad \text{Eq. 11-7}$$

Here, iterative calculations are necessary until both terms converge, which are performed with Microsoft Excel©. While holding the liquid flow velocity w_L constant and varying the gas flow velocity w_g, characteristic curves to evaluate the flooding points can be created as shown in Figure 11-1.

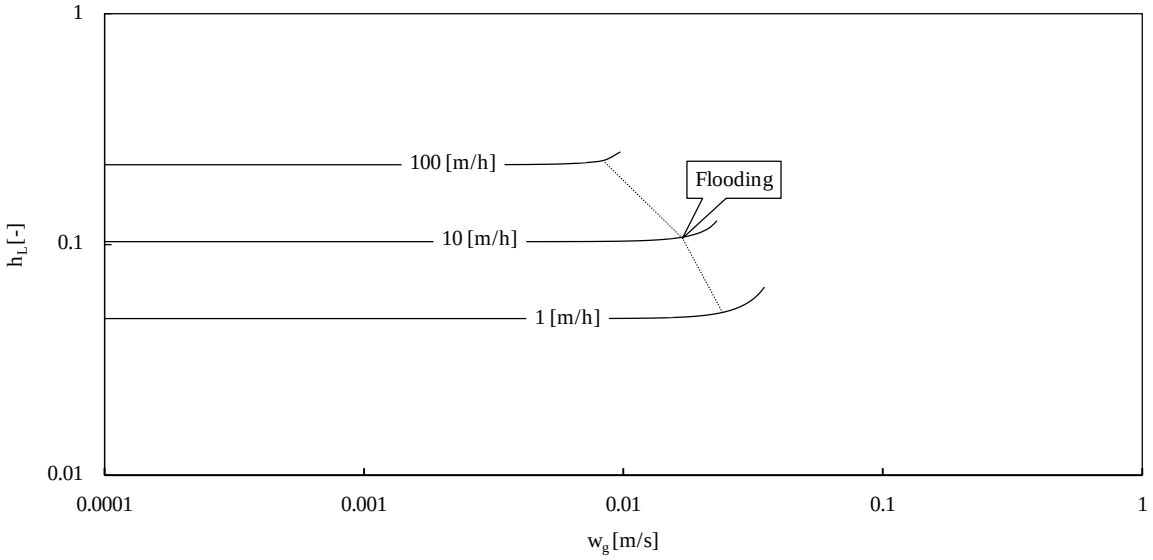

Figure 11-1 Liquid hold-up h_L [-] dependent on the gas flow velocity w_g [m/s] to determine the flooding point in dependency of the liquid load

Therefore, for each liquid flow velocity w_L a corresponding critical gas flow velocity w_g can be determined, which would result in flooding. Furthermore, the minimum liquid flow velocity $w_{L,min}$ to prevent entrainment can be calculated:

$$w_{L,min} = 7.7 * 10^{-6} * \left(\frac{\rho_L \sigma^3}{\eta_L^4 g}\right)^{\frac{2}{9}} * \left(\frac{g}{a}\right)^{\frac{1}{2}} \quad \text{Eq. 11-8}$$

Figure 11-2 shows the resulting operating window.

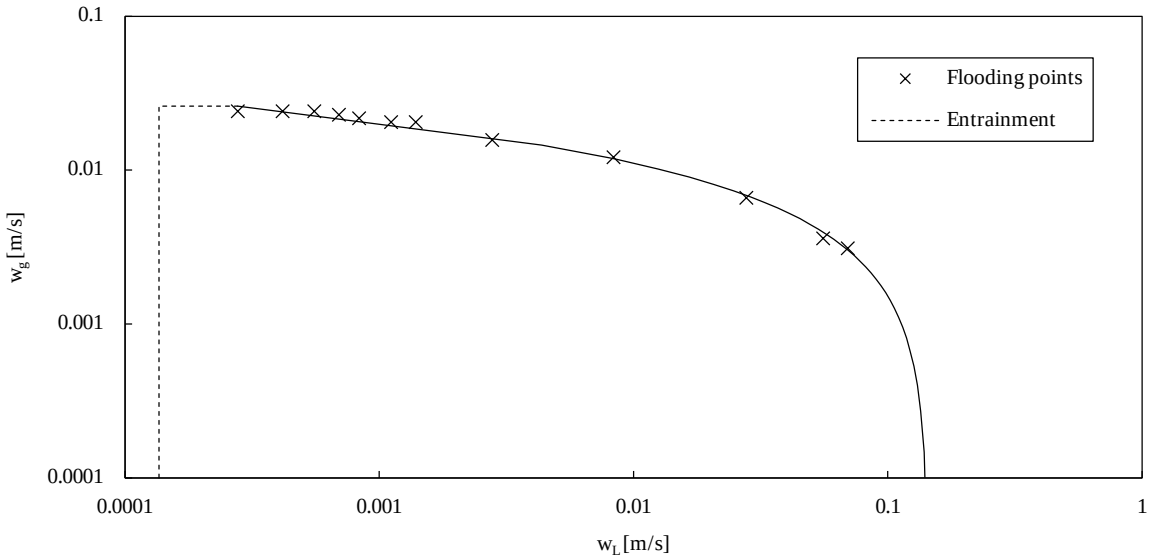

Figure 11-2 Operating window of the pilot plant hydrate absorption column

As the design of the hydrate absorption column is until this point adapted from the distillation case, in a further step, several operating points have to be evaluated to examine the possibility to operate the column with a hydrate forming mixture. The idea behind it is that in dependency of the gas feed the stream of hydrate forming liquid is defined. Assuming a ratio $x = \frac{\dot{n}_{Treated}}{\dot{n}_{Feed}}$ describing the molar amount of gas which is captured in the hydrate phase $\dot{n}_{Treated}$, rather representing the inlet specification, the reduced, operating gas flow velocity $w_{g,O}$ through the column can be calculated as the inlet gas stream is reduced by the amount of gas entrapped in gas hydrates.

$$w_{g,O} = x * w_g \qquad \text{Eq. 11-9}$$

The unit cell of sII hydrate can be written as $1(5^{12}) \cdot 0.5(5^{12}6^4) \cdot 8.5\ H_2O$ related to one occupied small cage. If the large $5^{12}6^4$ cage is filled with THF and the small one with either methane or carbon dioxide (mean value of 30 g/mol), the molar mass M_{Hyd} of one mole of gas hydrate is estimated as:

$$M_{Hyd} = 1 * 30\frac{g}{mol} + 0.5 * 72\frac{g}{mol} + 8.5 * 18\frac{g}{mol} = 219\frac{g}{mol} \qquad \text{Eq. 11-10}$$

In dependency of a desired hydrate loading $y = \frac{\dot{m}_{Hyd}}{\dot{m}_L}$ the total mass flow of the formed hydrate slurry can be calculated as the liquid stream velocity w_L is slightly reduced, due to the forming of a denser hydrate phase.

$$\dot{m}_{L,O} = \dot{n}_{Treated} * \frac{219 \frac{g}{mol}}{y} \quad \text{Eq. 11-11}$$

With the determined size of the gas and liquid stream during operation, different operating points with varying hydrate loading and partly treated gas can be plotted in the operating window which is shown in Figure 11-3.

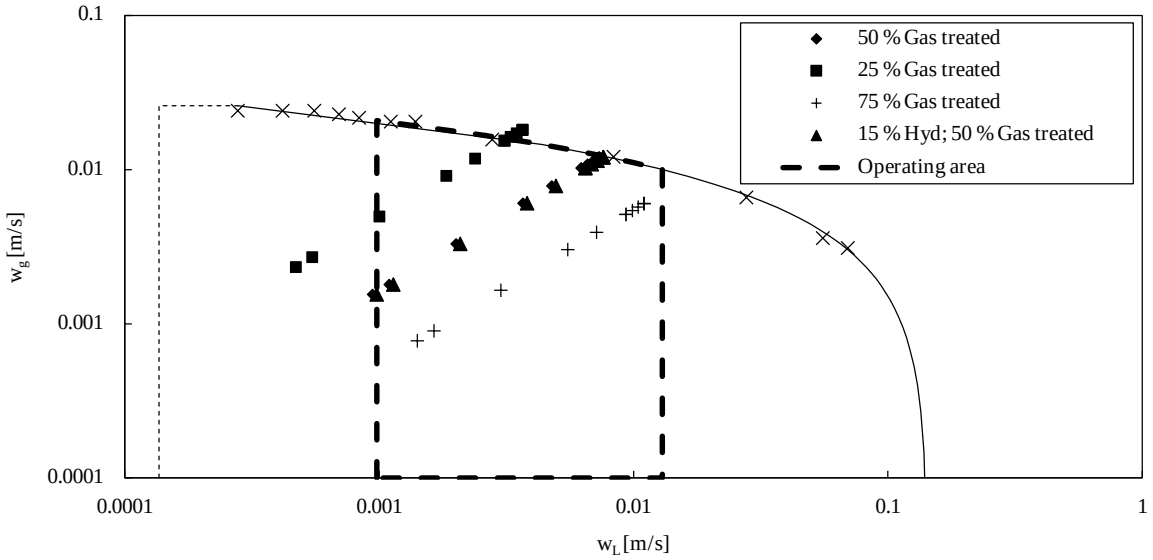

Figure 11-3 Operating window of the pilot plant hydrate absorption column with different operating points

In comparison to the underlying 50 mol% methane-50 mol% carbon dioxide case, it is visible, that if more gas molecules (here higher methane amount) have to be treated, the liquid loading has to be increased while the gas flow velocity declines as well, as more gas needs to be entrapped. The opposite applies to treating a lower amount of gas. If one wants to secure the flowability of the hydrate slurry only the liquid flow w_L increases, whereas gas flow velocity w_g remains nearly the same. Most of the points are located within the window which leads to the conclusion, that the operation of the column should be possible under hydrate forming circumstances. The rest of the pilot plant – pumps, compressor, tanks etc. - will be designed to allow the operation in the dashed framed operating area. Hence, the maximum mass flow of the hydrate forming liquid will be 145 kg/h and of the gas feed 6 kg/h. Next step is the design of a P&ID to explain the concept of the pilot plant, which is illustrated in Figure 11-4.

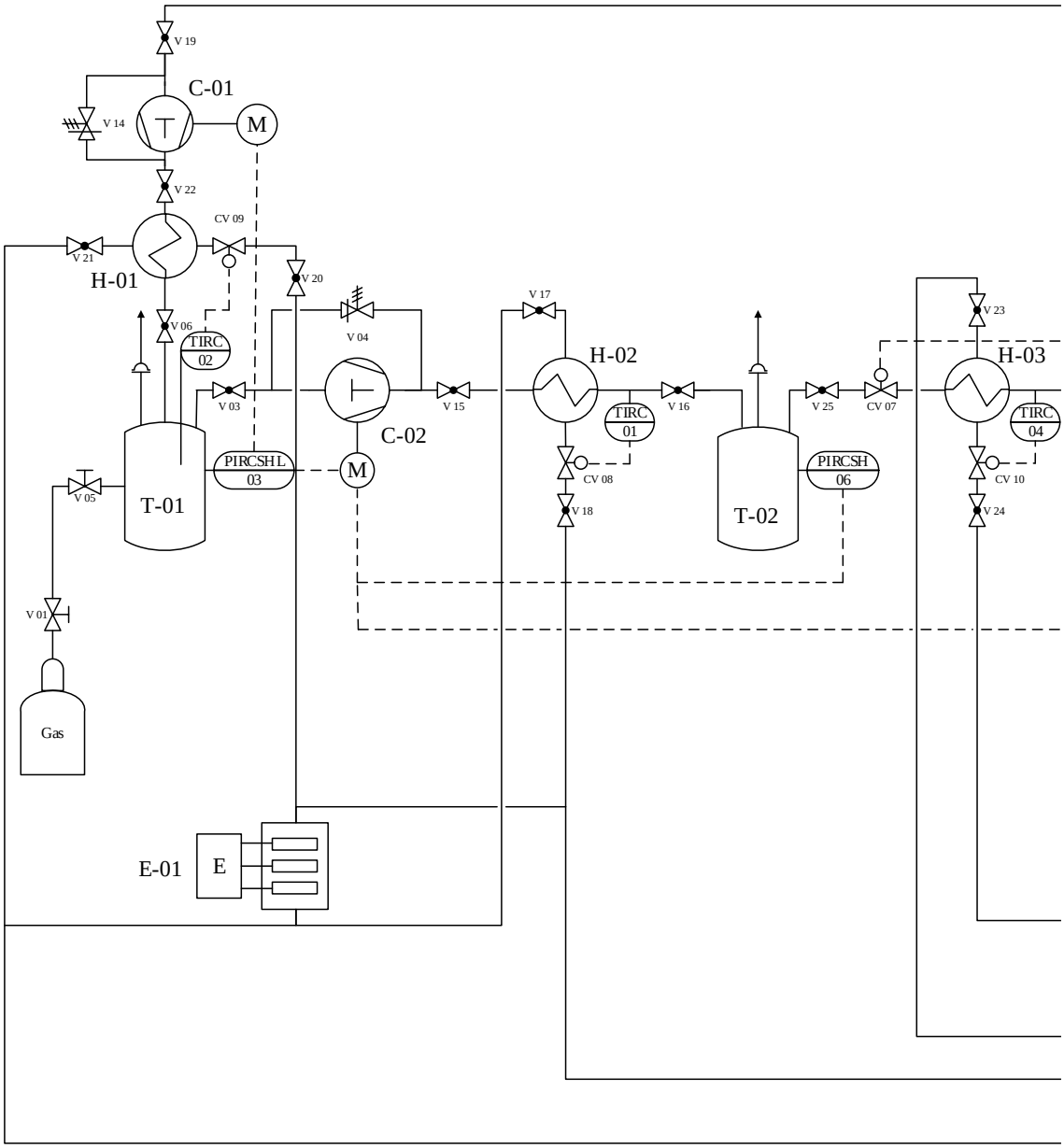

Figure 11-4 P&ID of a pilotplant

Short sign	C-01	C-02	E-01	E-02	G-01	H-01
Type	Compressor	Compressor	Cooling supply	Heating supply	Hydrate absorption	Heat exchanger
Technical data	0.5 kW	0.3 kW	1.0 kW	4.8 kW	H: 2 m D: 0.08 m HETP 0.22	0.5 kW 0.12 m^2
Permitted pressure [bar(g)]	100	200			100	100

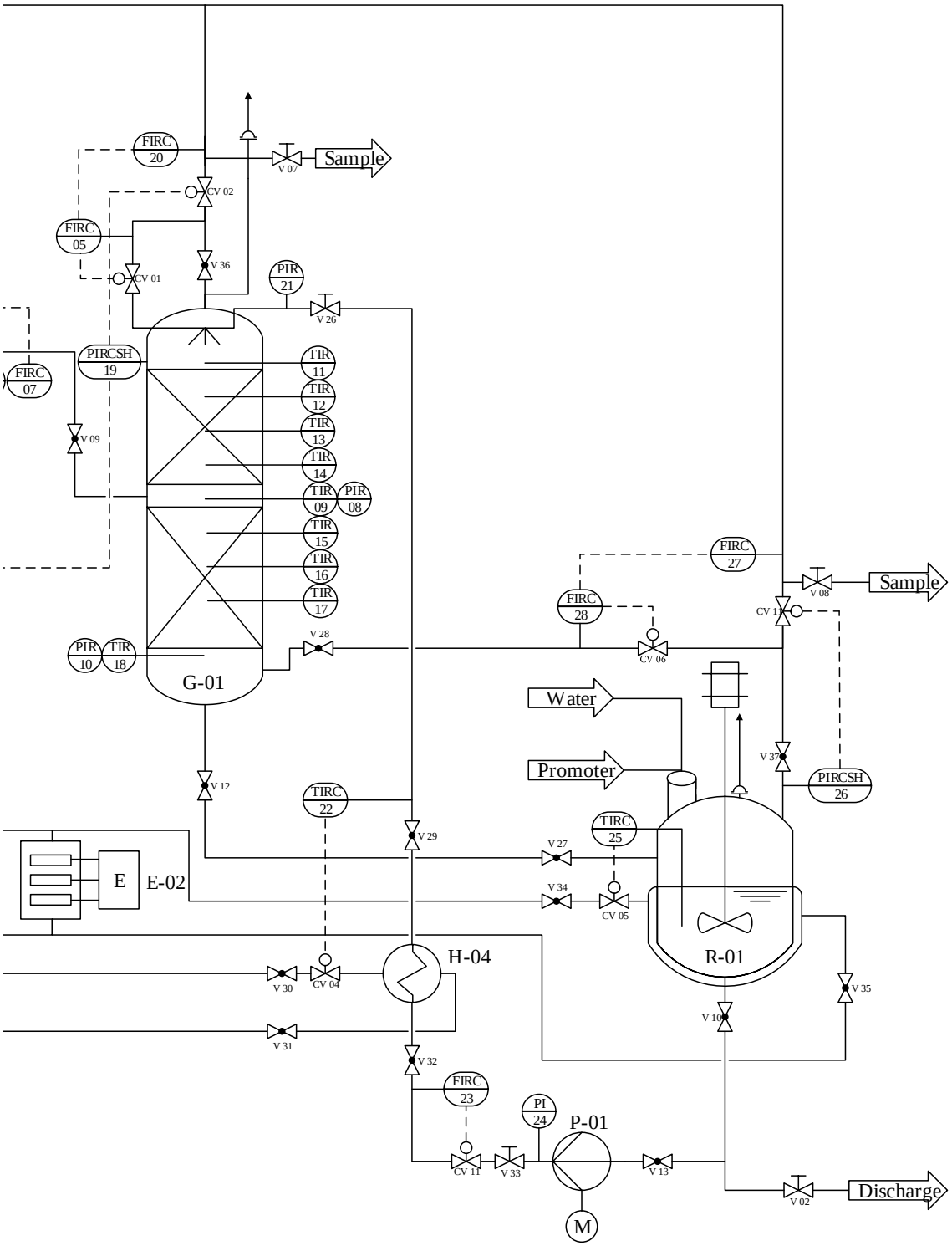

H-02	H-03	H-04	P-01	R-01	T-01	T-02
Heat exchanger	Heat exchanger	Heat exchanger	Pump	Separator	Gas storage	Gas storage
0.4 kW 0.09 m^2	0.1 kW 0.03 m^2	4.3 W 0.28 m^2	23 W	4.7 kW 12.6 L	5 L	7 L
200	200	100	100	100	100	200

Starting on the left side, tank T-01 is used as a buffer and mixing vessel to fill the system with different gases and simultaneously function as the first compression stage for the recycled gas stream coming from compressor C-01. A maximum pressure of 100 bar(g) and a volume of 5 L should be enough to fulfill this purpose. It is instrumented with a temperature sensor TIRC02, which is used to control the temperature of the gas recycle via the heat exchanger H-01 as the gas is heated up during compression. Additionally, a pressure sensor PIRCSHL03 is implemented to control the motor of compressor C-01, and therefore the pressure during operation and secure switch-off of the compressors C-01 and C-02 in case of exceeding a high or low limit, respectively. By using compressor C-02, the subsequent cooler H-02 and the temperature measurement TIRC01, gas is compressed and cooled a second time and stored in the buffer tank T-02. To start-up the pilot plant, the necessary total amount of gas for the operation should be stored in this tank. Therefore, its volume must be calculated, which is explained later. Tank T-02 is equipped with the pressure sensor PIRCSH06 to adjust and prevent surpassing of the pressure in the vessel by controlling the motor of compressor C-02.

The flow mass controller FIRC07 is used to control valve CV07 and consequently the feed stream into the gas hydrate absorption column G-01. In between, heat exchanger H-03 and temperature sensor TIRC04 adjust the temperature of the feed stream, as the gas is cooled down while expanding due to the Joule-Thompson-effect.

The gas hydrate absorption column G-01 is divided into two section- an up- and down comer section- and instrumented with sensors. Summarizing, several temperature sensors (TIR09, TIR11-18) allow the determination of the temperature profile over the column height. The pressure sensors PIR08, PIR10 and PIRCSH19 measure the pressure at the bottom, the top and in between of both packed sections to evaluate the pressure loss. The pressure sensor PIRCSH19 is additionally used to adjust the operating pressure by the controlling valve CV02. In case of exceeding the pressure limit, compressor C-02 is switched-off and pressure is released into the gas recycle pipeline by opening the control valve CV02. The purified gas leaves the column at the top and is expanded into the gas recycle pipeline which leads to compressor C-01. A reflux ratio can be set by controlling the valve CV01 as the mass flow sensors FIRC20 and FIRC05 measure the flow back into the column and to compressor C-01. The refluxed gas is mixed with the gas hydrate forming liquid and injected into the column by using a two-fluid nozzle. The gas hydrate slurry leaves the column at the bottom and flows into the separator R-01, where the gas hydrate slurry is dissociated in order to regain a liquid and purified gas phase.

The separator R-01 has a deck access to fill water and promoter into the pilot plant. Therefore, the size of the separator depends on the required hydrate forming liquid during operation and the underlying calculations are explained later. The separator is stirred and heated over a heating jacket and temperature is controlled by using the temperature sensor TIRC25. Pressure sensor PIRCSH26 controls the pressure in the separator by using the control valve CV11 which expands

the gas into the gas recycle pipeline leading to compressor C-01 as well. The mass flow sensors FIRC27 and FIRC28 allow the adjustment of a reflux ratio back into the column bottom.
The liquid without gas hydrate leaves the separator at the bottom and is pumped back – using pump P-01 - into two-fluid nozzle at the top of the column. In doing so, its flow rate can be controlled using the flow sensor FIRC23 and control valve CV03. The stream temperature can be adjusted using the temperature control TIRC22 and heat exchanger H-04. The injection pressure is measured with the sensor PIR21. Pressure sensor PI24 is only used for the start of centrifugal pump P-01.
Two sampling points are located in the gas recycle pipeline behind the expanding valves of the column and the separator. The gas hydrate forming liquid can be discharged through the pipeline at the bottom of the separator. The equipment E-01 and E-02 represent the cooling and heating supply units, respectively. Every apparatus is secured against overpressure by bursting disks.

To determine the required volume of the separator R-01 the assumption is that enough volume should be available to store enough hydrate forming liquid before the start-up of the pilot plant and to operate the facility. Therefore, the required volume of the separator is provided by the filled plant parts, mainly pipelines, during operation with the highest load of 145 kg/h. The pipelines are designed to meet the required guide values for the mean flow velocity in pipelines according to Decker et al. [263]. The design process is as follows.

- The mass flow $\dot{m}$ is transferred into a volume flow $\dot{V}$ using the density ρ.
- The volume flow $\dot{V}$ is divided by the required flow velocity $w_{Req.}$ to calculate the flow cross section A to gain the required pipe diameter $d_{Req.}$.
- The required pipe diameter $d_{Req.}$ is replaced by the DIN norm diameter DN.
- The volume V of the regarding pilot plant part accounts for the flow cross section A through the DIN norm pipe multiplied with an estimated pipe length.

The calculations are summarized in Table 11-1.

Table 11-1 Summarized calculations to determine the volume of separator R-01. Required flow velocity $w_{Req.}$ obtained from Decker et al. [263].

Flow…	$\dot{m}$ [kg/h]	ρ [kg/m^3]	$\dot{V}$ [m^3/h]	$w_{Req.}$ [m/s]	$d_{Req.}$ [mm]	DIN DN	Est. Length [m]	V [L]
from R-01 to P-01	145	979.3	0.15	1.00	7	8	1.0	0.05
from P-01 to G-01	145	979.3	0.15	2.25	5	6	2.5	0.07
from G-01 to R-01	145	979.3	0.15	1.00	7	8	0.5	0.03
through G-01	145	979.3	0.15	-	80	80	2.0	10.31
							Sum	10.46
							+20 %	12.55
							Final	≈12.6

The design of the gas storage tank T-02 requires a similar procedure. However, the pressure and temperature must be taken into account as they have a significant impact on the gas density and the aim is to calculate the amount of gas in the corresponding part of the pilot plant. Therefore, Table 11-2 contains additionally the assumed operating conditions in the corresponding pilot plant parts. The calculations are performed with support of CHEMCAD© to determine inter alia the gas density ρ.

Table 11-2 Summarized calculations to determine the volume of tank T-02. Required flow velocity $w_{Req.}$ obtained from Decker et al. [263]

Flow…	$\dot{m}$ [kg/h]	T [°C]	P [$bar(g)$]	ρ [kg/m^3]	$\dot{V}$ [m^3/h]	$w_{Req.}$ [m/s]	$d_{Req.}$ [mm]	DIN DN	Est. Length [m]	V [L]	m [g]
from T-01 to G-01	6	20	20	26.4	0.2	10	3	6	1.0	0.03	0.7
through G-01	6	20	20	26.4	0.2	0.2	80	80	2.0	10.31	272.1
through R-01	3	20	20	26.4			80% of volume of separator R-01←			10.00	264.0
from G-01 and R-01 to C-01	6	-93	0	2.0	3.0	10	10	10	6.5	0.51	1.0
from C-01 to T-01	6	20	10	12.7	0.5	10	4	6	0.5	0.01	0.2
through T-01	6	20	10	12.7				set to 5 L on page 144←		5.00	63.5
from T-01 to C-02	6	20	10	12.7	0.5	10	4	6	0.5	0.01	0.2
from C-02 to T-02	6	20	50	73.8	0.1	10	5	6	0.5	0.01	1.0
in T-02 during operation	6	20	50	73.8						5.49	405.1
in T-02 before start-up		20	100	183.6						5.49	1007.9
									+20 %	6.59	1209.4
									Final	≈7.0	1285.2

The energy consumption of the equipment is calculated by using CHEMCAD©. The energy consumption of separator R-01 to decompose the formed gas hydrates is determined by multiplying the molar gas flow $\dot{n}$ leaving the column bottom with a dissociation enthalpy of 140 kJ/mol gas [253]. By using tabulated overall heat transfer coefficients U taken from [249], the required heat exchange area is calculated as:

$$A = \frac{\dot{Q}}{U * \Delta T_{LM}} \; [m^2] \qquad \text{Eq. 11-12}$$

The specification of the heating and cooling supply units E-01 and E-02 is based on the sum of all energy consumptions. All specifications are already tabulated in Figure 11-4. Now that all equipment and a P&I diagram are designed, a rough cost estimation is performed in Table 11-3 and Table 11-4.

Table 11-3 Equipment costs of the pilot plant

Short sign	Type	Cost	Origin
C-01 + H-01	Compressor + Heat exchanger	10,000 €	From offer
C-02 + H-02	Compressor + Heat exchanger	10,000 €	From offer
E-01	Cooling supply	15,000 €	From offer
E-02	Heating supply	15,000 €	From offer
G-01	Absorption column	1,000 €	Estimated
H-03	Heat exchanger	1,000 €	From offer
H-03	Heat exchanger	1,000 €	Estimated
P-01	Pump	550 €	From offer
R-01	Separator	15,000 €	Estimated
T-01	Gas storage	100 €	Estimated
T-02	Gas storage	200 €	Estimated
	Sum	68,850 €	

Table 11-4 Instrument costs of the pilot plant

Type	Cost		Amount		Sum	Origin
Pressure sensor	500 €	X	7	=	3,500 €	From offer
Temperature sensor	100 €	X	14	=	1,400 €	Estimated
Flow sensor + control valve	14,000 €	X	6	=	84,000 €	From offer
					88,900 €	

The equipment costs accumulate to 68,850 € and the instrument costs to 88,900 € which sum up to 157,750 €. As pipes and hand armatures are not included, a percentage surcharge of 20 % on the sum is added. Finally the costs for the installed pilot plant add up to 189,300 €. Rounding up, the installation and start-up of the here designed pilot plant costs ≈200,000 €.

12 Summary, conclusion and outlook

This chapter summarizes the findings, recaps the conclusions and gives an outlook for future research works in the field of gas hydrates.

Summary

This thesis had the aim to investigate the possibilities and potential of the innovative and pioneering gas hydrate separation technology, especially applied to bio and natural gas conditioning. A multi-pronged approach was followed, which combined fundamental research on promoters and reactor designs, simulations and engineering science considerations. Different surfactants, crown and acyclic ethers, amino acids, aprotic solvents and fatty acids in different concentrations were investigated regarding their influences on the gas hydrate formation in presence of varying guest molecules, namely, methane, tetrahydrofuran and carbon dioxide. A rough, qualitative classification of all tested substances is presented in Figure 12-1.

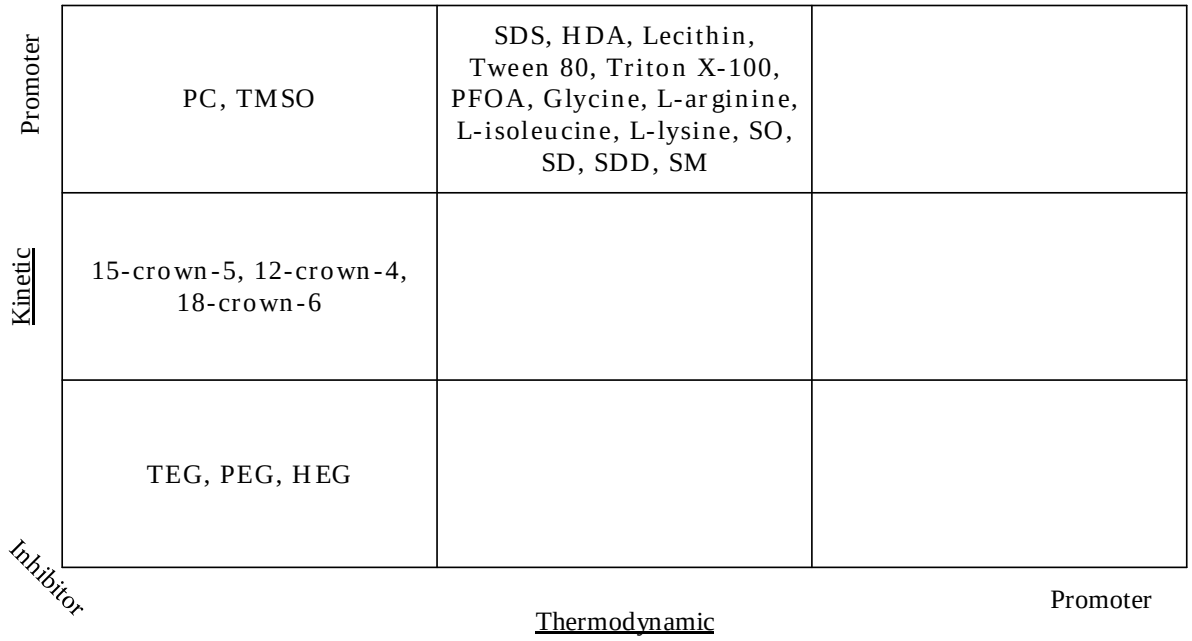

Figure 12-1 Qualitative classification of all tested substances regarding their influences on gas hydrate formation

Here it is conceivable that all substances divide into four groups. Surfactants, amino acids and fatty acids were tested in methane-THF mixed gas hydrate forming mixtures and showed mainly a promotion of the gas hydrate formation kinetic. Solvents like PC and TMSO were able to enhance the gas solubility in the system and thereby achieving a kinetic promotion, to the disadvantage of a thermodynamic inhibition. Acyclic ether or rather glycol ethers had a combined kinetic and thermodynamic inhibiting effect which was expected as glycol ethers are already used in the field of flow assurance. An unclear behavior was found in case of crown ethers, but overall a classification as thermodynamic inhibitor was undertaken.

While evaluating technical possibilities to promote gas hydrate formation, several findings were obtained. Primarily the reactor design has a significant influence on the gas hydrate formation. In an industrial process, two requirements must be fulfilled to enable pioneering gas hydrate technologies: Fast kinetics and moderate conditions. To overcome the first problem, Figure 12-2 compares the best results achieved with different reactor designs in this thesis.

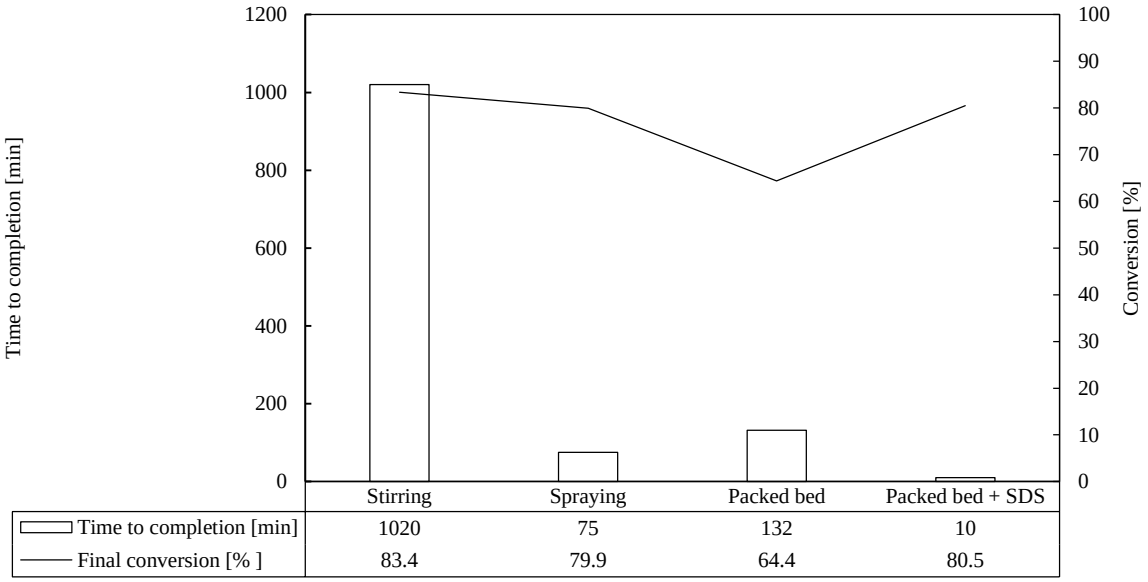

Figure 12-2 Comparison of different reactor designs regarding their time to complete gas hydrate formation [min] and their final water to hydrate conversion [%]

Figure 12-2 shows that gas hydrates formed in a stirred system are less favorable. Although the highest gas uptake is achieved, the process requires a long time, a continuous energy supply and high maintenance costs are expected. The spray and packed bed reactor are superior in the point of a fast kinetic. However, while spraying requires recycle and maintenance costs as well, the packed bed has the disadvantage of a reduced reactor volume and a random induction, if additional actions like gas phase stirring are not performed. The best results were achieved in case of a packed bed reactor with SDS in the hydrate forming mixture, though a foaming reactor system could cause problems in an application case. As the maximum final conversion was 83.4% in case of the stirred reactor, the successful developed promoting coating from chapter 6 could help to achieve a nearly complete gas hydrate formation. However, the apparatus and dimensional circumstances must be considered and longtime tests are still needed regarding the coating. Nevertheless, it was proven in this thesis that the reactor design and the surface characteristics of internals can influence the gas hydrate formation in a favored direction, promotion or inhibition.
With regard to the gas hydrate separation experiments, several systems were measured extensively and ideal separation factors determine to allow a rating of the selectivity. An overview is given in Figure 12-3 where the average ideal separation factors with standard deviation for gas hydrate separation of different gas mixtures in presence of different promoters is displayed. The first named component is enriched in the gas hydrate phase and the second one in the gas phase.

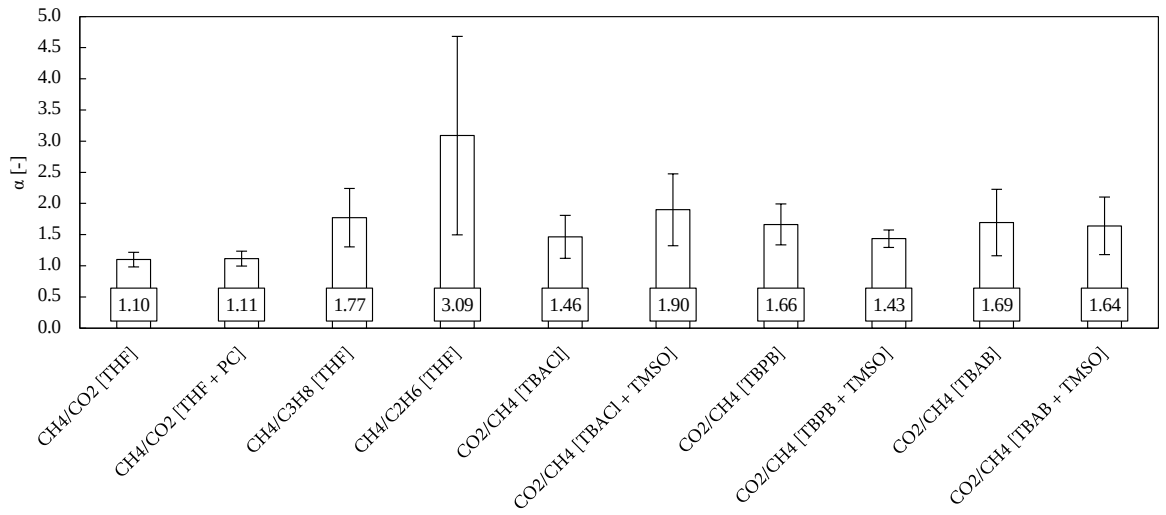

Figure 12-3 Average ideal separation factors [-] with standard deviation for gas hydrate separation of different gas mixtures in presence of different promoters. First named component is enriched in the hydrate phase and second named component in the gas phase

The separation of ethane and methane in a THF promoted system has an outstanding selectivity. Furthermore, a THF promoted system is capable of separating methane from propane quite fair as well. The first results with biogas were sobering as the separation efficiency was bad. However, by using the semiclathrate formers TBACl, TBAB and TBPB with the synergizing additive TMSO it was possible to achieve a separation factor of 1.90 which is even higher than that of methane-propane via THF promotion. These findings showed a vast potential for further economic considerations which were performed in chapter 10 since one aim of this thesis was to investigate the potential of replacing existing separation technologies by an energy saving gas separation process. Although, the potential for biogas is unfortunately low, impressive results were obtained with regard to low-hydrocarbon separation via gas hydrate separation since operating costs are 63 % less in comparison to the established cryogenic demethanization. As a result a pilot-plant which can operated in a laboratory was planned to allow the possibility to deliver a proof-of-concept of a working continuous gas hydrate separation to enable the transfer into an industrial scale and advance this innovative technology.

Finally, a low budget MS-Excel©-tool was developed to simulate gas hydrate equilibria. Until now, it is only possible to simulate the gas hydrate equilibrium for a few systems with a competitive accuracy, but further improvements could allow a reliable prediction of separation efficiencies.

Conclusion

As many experiments were conducted in this thesis, the following conclusions are obtained: First of all, the gas hydrate formation process is dividable into two steps the nucleation and the growth phase. The growth phase can be divided into two mass transfer limited phases with an ambiguous transition where gas is dissolved initially into a liquid and later diffuses into a gas hydrate plug. In addition, the gas hydrate formation is influenced by its exothermic crystallization characteristic which makes heat transfer processes the second limitation process. However, heat transfer limitations can be easily overcome by delivering enough cooling supply to the gas hydrate forming system and is therefore manageable. The largest challenge with regard to industrial processes is to enhance and control the kinetics of gas hydrate formation. The mass transfer process can be described by Eq. 2-1 which at the same time provides a solution for that problem. This equation describes the gas hydrate growth rate in dependency of a mass transfer coefficient k_L and the volume specific gas-liquid exchange area $A_{(g-l)}$. This means that gas hydrate formation can be accelerated by enlarging the volume specific gas-liquid exchange area $A_{(g-l)}$, for example by spraying liquid into the gas phase or gas injection right into the liquid phase with a preferably fine bubble/drop diameter or enhancing the mass transfer coefficient $k_L = \frac{D}{\delta}$ which describes the ratio between a diffusion coefficient D and film thickness δ. The diffusion coefficient D is assumed to be constant in dependency of the medium in which gas molecules diffuse. In dependency of the additives in the gas hydrate forming mixture, the diffusion velocity can be influenced. Furthermore, the film thickness δ can be lowered by turbulences and/or modified surface characteristics. Therefore, substances which enhance the gas transport into the liquid – in this thesis surfactants, amino acids, fatty acids and aprotic solvents – and hydrophobic surfaces which enrich the gas density at the phase boundary act as kinetic promoters. With proceeding gas hydrate formation, the liquid phase transforms from a slurry into a gas hydrate plug which lowers the diffusion rate significantly, as the gas diffusion in a liquid with low viscosity is higher in comparison to that in a solid plug. However, the diffusion rate in the gas hydrate plug state is influenced by its morphology as well, which is why some promoters are able to improve or impair the growth rate and final gas uptake at this point.

Although promising kinetic promoting substances were found in this thesis, from an engineering and industrial point of view, the usage of kinetic promoters does not make sense, as multi component streams are difficult to handle and a foaming gas hydrate storage or separation column which contaminates a product gas stream are not desirable. Therefore, the search for *kinetic* promoters is, in difference to the optimization of reactor designs, barely expedient. On the other hand, the usage of *thermodynamic* promoters is unavoidable to operate gas hydrate processes at moderate and economic conditions.

Thermodynamic effects during gas hydrate formation can be traced back to interactions between water molecules and other substances. To form gas hydrate structures, water molecules have to arrange in a certain order around suitable guest molecules. Afterwards, the gas hydrate framework is stabilized by continuous attracting and repulsing van der Waals forces between guest and host molecules. If a substance can fulfill the purpose of a guest molecule better than another component, it is possible to act as thermodynamic promoter. If an additive interacts with its functional groups with water molecules on its own thereby preventing the structured arrangement of water molecules, it acts as a thermodynamic inhibitor.

Gas hydrate separation is based on the effect, that large cages are filled by thermodynamic promoters while small cages of the corresponding clathrate structure can be occupied by other guest molecules like small gases. This represents a selective process as not all guest molecules can stabilize the small cages of a certain structure in the same manner. This conversely means that the selectivity of gas hydrate separation depends significantly on the used promoters, as kinetic promoters have an impact on the solubility of different gas species in the clathrate forming mixture, which boosts the chance for this guest to be entrapped in clathrate cavities, while thermodynamic promoters determine the formed clathrate structure and shape of the vacant cages. Furthermore, as the gas solubility and clathrate stability depends on the thermodynamic conditions, pressure and temperature affect the selectivity as well.

The economic considerations showed that there is a vast potential of the gas hydrate separation technology regarding the described application cases. Even though, in view of biogas separation no added value was observed, low-hydrocarbon separation seems to be a promising application area. In the course of this thesis an attempt to declare a corresponding patent was made, but was rejected. Experimental data were not sufficient to achieve this aim which is why a pilot-plant was planned. A successful operation could prove the feasibility of a continuous working gas hydrate separation unit for the industrial use, allowing the transfer into a large scale and opening the opportunity for the commercial use of this technology. This is of great interest as not only bio- and natural gas can be treated by gas hydrate separation but also fuel and flue gas as well as air.

Outlook

As shown in this thesis, the interest in gas hydrate research grows rapidly, as several application possibilities are thinkable. However, there is a great need in conducting further research to enable not only the pioneering gas hydrate separation technology but other gas hydrate technologies as well. By combining fundamental research, simulations and engineering science, a comprehensive overview with a clear orientation towards an industrial use was given. The promising results proof the applicability of gas hydrate separation in established process chains leading to economical and sustainable advantages due to energy savings. In the future, the construction of a pilot plant should be planned to do the next step to transfer the valuable research results and enable gas hydrate technologies for industry.

In addition, further thermodynamic promoters and new semiclathrate formers should be tested with regard to their separation efficiency in view of different gas mixtures. As air fractioning is, like demethanization, performed under cryogenic conditions though largely unexplored, a vast potential could be found here as well. As it was shown, the anion of the semiclathrate former has a significant impact on the selectivity, new combinations, like for example tetra butylammonium formate or lactate, should be tested here. The neutralization of a tetra butylammonium hydroxide solution is easily performed and offers therefore a variety of combination possibilities.

With regard to further reactor designs, a bubble column or gas injection into the packed bed could be interesting options as well. Furthermore, room for improvement is expected within the use of the spray reactor design as only one nozzle type and one injection pressure were measured at a certain reactor pressure of 8 bar(g). The used nozzle was a “Fine Atomization Fog Misting Spray Nozzle”, which would create a fine, heavy fog at higher differential pressures ($\Delta p \approx 100$ bar(a)) resulting in smaller liquid droplets creating an even a larger volumetric surface area. Another option would be the usage of a two-substance nozzle which mixes the gas and the liquid phase during the spray process. In doing so, the hydrate forming liquid would be supersaturated with gas components on injection into the reactor which could lead to an enhanced gas hydrate formation as well.

One point which remained largely unconsidered in this thesis is the measurement of gas hydrate slurry flow characteristics. Especially if new promoters are used, viscosities of the clathrate slurries could vary. Nonetheless an appropriate knowledge is required to secure the flowability through continuous operated gas hydrate processes, no matter if it is a separation, desalination or cooling process. This problem was taken into account by considering a surplus of the hydrate forming mixture. However, a plugging of the column is not excluded but tests with the pilot plant are necessary to investigate and potentially solve this problem. Furthermore, it is also thinkable that the column design is not the optimal and some kind of counter-flow flow-loop with a number of separation chambers could also be an option.

The MS-Excel©-tool for the prediction of gas hydrate equilibra is still in an early stage of development, although the simulation results had a competitive accuracy in comparison to existing algorithms. Further improvements could expand the functionality of this tool and enable the possibility to feature more guest molecules and/or semichlathrate formers and predict McCabe-Thiele trends reducing the experimental afford.

At the end it needs to be said that this thesis gives a holistic view of the potential of gas hydrate separation in presence of promoters with regard to biogas and natural gas. Many aspects were examined and the fundamental knowledge of gas hydrate research from an engineering standpoint extended. However, further research and development has to be done to enable energy saving and environmental friendly gas hydrate technologies for the industrial use, although this thesis created significant progress into this direction.

13 References

[1] J. Priestley, Versuche und Beobachtungen über verschiedene Gattungen der Luft, bey Rudolph Gräffer, 1780.

[2] H. Davy, I. The Bakerian Lecture. On some of the combinations of oxymuriatic gas and oxygene, and on the chemical relations of these principles, to inflammable bodies, Phil. Trans. R. Soc. Lon 101 (1811) 1–35. https://doi.org/10.1098/rstl.1811.0001.

[3] J. Grace, Energy from gas hydrates: Assessing the opportunities & challenges for Canada, Council of Canadian Academies = Conseil des académies canadiennes, Ottawa, 2008.

[4] L.R. Raymond (Ed.), Hard Truths. Facing the Hard Truths About Energy. A Comprehensive View to 2030 of Global Oil and Natural Gas., 2007.

[5] M. Nič, J. Jirát, B. Košata, A. Jenkins, A. McNaught (Eds.), IUPAC Compendium of Chemical Terminology, IUPAC, Research Triagle Park, NC, 2009.

[6] E.D. Sloan, C.A. Koh, Clathrate hydrates of natural gases, 3rd ed., CRC Press Taylor & Francis, Boca Raton, FL, 2008.

[7] A. Demirbas, Methane Gas Hydrate, Springer London, London, 2010.

[8] Y.F. Makogon, Hydrates of natural gas, PennWell, Tulsa, Okla., 1981.

[9] H.J. Schultz, Zum Gashydratabbau mittels Mammut-Pumpen-Prinzip, Fraunhofer IRB Verl., Stuttgart, 2004.

[10] H.J. Schultz, H. Fahlenkamp, G. Deerberg, Simulation des Abbaus ozeanischer Gashydrate, Chemie Ingenieur Technik 76 (6) (2004) 751–754. https://doi.org/10.1002/cite.200403330.

[11] H.J. Schultz, G. Deerberg, H. Fahlenkamp, New perspectives for the extraction of oceanic gas hydrates, GEOTECHNOLOGIEN - Science Report (7) (2006) 138–151.

[12] H.J. Schultz, Deerberg G., Fallenkamp H., Neue Perspektive zum Abbau von Gashydraten, VGB Powertech (84) (2004) 130–137.

[13] A. Falenty, T.C. Hansen, W.F. Kuhs, Formation and properties of ice XVI obtained by emptying a type sII clathrate hydrate, Nature 516 (7530) (2014) 231–233. https://doi.org/10.1038/nature14014.

[14] R.L. Christiansen, E.D. Sloan, Mechanisms and Kinetics of Hydrate Formation, Ann NY Acad Sci 715 (1 Natural Gas H) (1994) 283–305. https://doi.org/10.1111/j.1749-6632.1994.tb38841.x.

[15] J. Long, Gas Hydrate Formation Mechanism and Its Kinetic Inhibition: Ph.D. Thesis, Colorado School of Mines, Golden, 1994.

[16] B. Kvamme (Ed.), Proc. Second International Conference on Gas Hydrates, 1996.

[17] C. Moon, P.C. Taylor, P.M. Rodger, Molecular dynamics study of gas hydrate formation, J. Am. Chem. Soc. 125 (16) (2003) 4706–4707. https://doi.org/10.1021/ja028537v.

[18] R. Radhakrishnan, B.L. Trout, A new approach for studying nucleation phenomena using molecular simulations: Application to CO2 hydrate clathrates, J. Chem. Phys. 117 (4) (2002) 1786–1796. https://doi.org/10.1063/1.1485962.

[19] L.C. Jacobson, W. Hujo, V. Molinero, Amorphous precursors in the nucleation of clathrate hydrates, J. Am. Chem. Soc. 132 (33) (2010) 11806–11811. https://doi.org/10.1021/ja1051445.

[20] Y. Bi, A. Porras, T. Li, Free energy landscape and molecular pathways of gas hydrate nucleation, J. Chem. Phys. 145 (21) (2016) 211909. https://doi.org/10.1063/1.4961241.

[21] Z. Yin, M. Khurana, H.K. Tan, P. Linga, A review of gas hydrate growth kinetic models, Chemical Engineering Journal 342 (2018) 9–29. https://doi.org/10.1016/j.cej.2018.01.120.

[22] A. Vysniauskas, P.R. Bishnoi, A kinetic study of methane hydrate formation, Chemical Engineering Science 38 (7) (1983) 1061–1072. https://doi.org/10.1016/0009-2509(83)80027-X.

[23] P. Englezos, N. Kalogerakis, P.D. Dholabhai, P.R. Bishnoi, Kinetics of formation of methane and ethane gas hydrates, Chemical Engineering Science 42 (11) (1987) 2647–2658. https://doi.org/10.1016/0009-2509(87)87015-X.

[24] P. Skovborg, P. Rasmussen, A mass transport limited model for the growth of methane and ethane gas hydrates, Chemical Engineering Science 49 (8) (1994) 1131–1143. https://doi.org/10.1016/0009-2509(94)85085-2.

[25] C.A. Tulk, J.A. Ripmeester, D.D. Klug, The Application of Raman Spectroscopy to the Study of Gas Hydrates, Ann NY Acad Sci 912 (1) (2000) 859–872. https://doi.org/10.1111/j.1749-6632.2000.tb06840.x.

[26] R. Kumar, P. Englezos, I. Moudrakovski, J.A. Ripmeester, Structure and composition of CO 2 /H 2 and CO 2 /H 2 /C 3 H 8 hydrate in relation to simultaneous CO 2 capture and H 2 production, AIChE J. 55 (6) (2009) 1584–1594. https://doi.org/10.1002/aic.11844.

[27] M.A. Kelland, Production Chemicals for the Oil and Gas Industry, Second Edition, 2nd ed., Taylor and Francis, Hoboken, 2014.

[28] A. Kumar, G. Bhattacharjee, B.D. Kulkarni, R. Kumar, Role of Surfactants in Promoting Gas Hydrate Formation, Ind. Eng. Chem. Res. 54 (49) (2015) 12217–12232. https://doi.org/10.1021/acs.iecr.5b03476.

[29] P. Linga, M.A. Clarke, A Review of Reactor Designs and Materials Employed for Increasing the Rate of Gas Hydrate Formation, Energy Fuels 31 (1) (2017) 1–13. https://doi.org/10.1021/acs.energyfuels.6b02304.

[30] H.P. Veluswamy, P.Y. Lee, K. Premasinghe, P. Linga, Effect of Biofriendly Amino Acids on the Kinetics of Methane Hydrate Formation and Dissociation, Ind. Eng. Chem. Res. 56 (21) (2017) 6145–6154. https://doi.org/10.1021/acs.iecr.7b00427.

[31] M. Mohammad-Taheri, A.Z. Moghaddam, K. Nazari, N.G. Zanjani, Methane hydrate stability in the presence of water-soluble hydroxyalkyl cellulose, Journal of Natural Gas Chemistry 21 (2) (2012) 119–125. https://doi.org/10.1016/S1003-9953(11)60343-5.

[32] A. Kumar, T. Sakpal, R. Kumar, Influence of Low-Dosage Hydrate Inhibitors on Methane Clathrate Hydrate Formation and Dissociation Kinetics, Energy Technology 3 (7) (2015) 717–725. https://doi.org/10.1002/ente.201500004.

[33] U. Karaaslan, M. Parlaktuna, Promotion Effect of Polymers and Surfactants on Hydrate Formation Rate, Energy Fuels 16 (6) (2002) 1413–1416. https://doi.org/10.1021/ef020023u.

[34] H. Fakharian, H. Ganji, A. Naderi Far, M. Kameli, Potato starch as methane hydrate promoter, Fuel 94 (2012) 356–360. https://doi.org/10.1016/j.fuel.2011.10.029.

[35] Q. Sun, B. Chen, X. Li, X. Guo, L. Yang, The investigation of phase equilibria and kinetics of CH 4 hydrate in the presence of bio-additives, Fluid Phase Equilibria 452 (2017) 143–147. https://doi.org/10.1016/j.fluid.2017.09.002.

[36] S. Maghsoodloo Babakhani, A. Alamdari, Effect of maize starch on methane hydrate formation/dissociation rates and stability, Journal of Natural Gas Science and Engineering 26 (2015) 1–5. https://doi.org/10.1016/j.jngse.2015.05.026.

[37] Y.-J. Lee, T. Kawamura, Y. Yamamoto, J.-H. Yoon, Phase Equilibrium Studies of Tetrahydrofuran (THF) + CH 4 THF + CO 2 CH 4 + CO 2 and THF + CO 2 + CH 4 Hydrates, J. Chem. Eng. Data 57 (12) (2012) 3543–3548. https://doi.org/10.1021/je300850q.

[38] S. Muromachi, K.A. Udachin, S. Alavi, R. Ohmura, J.A. Ripmeester, Selective occupancy of methane by cage symmetry in TBAB ionic clathrate hydrate, Chem. Commun. (Camb) 52 (32) (2016) 5621–5624. https://doi.org/10.1039/c6cc00264a.

[39] C. Giavarini, K. Hester, Gas Hydrates, Springer London, London, 2011.

[40] A. Bahadori, Natural gas processing: Technology and engineering design, Elsevier Science, Amsterdam, 2014.

[41] U.S. Energy Information Administration, Annual Energy Outlook 2017, Annual Energy Outlook 2017 (2017).

[42] Basic data on biogas, 2nd ed., Svenskt gastekniskt center, Malmö, 2012.

[43] T.E. Rufford, S. Smart, G.C.Y. Watson, B.F. Graham, J. Boxall, J.C. Diniz da Costa, E.F. May, The removal of CO2 and N2 from natural gas: A review of conventional and emerging process technologies, Journal of Petroleum Science and Engineering 94-95 (2012) 123–154. https://doi.org/10.1016/j.petrol.2012.06.016.

[44] O.W. Awe, Y. Zhao, A. Nzihou, D.P. Minh, N. Lyczko, A Review of Biogas Utilisation, Purification and Upgrading Technologies, Waste Biomass Valor 8 (2) (2017) 267–283. https://doi.org/10.1007/s12649-016-9826-4.

[45] R. Muñoz, L. Meier, I. Diaz, D. Jeison, A review on the state-of-the-art of physical/chemical and biological technologies for biogas upgrading, Rev Environ Sci Biotechnol 14 (4) (2015) 727–759. https://doi.org/10.1007/s11157-015-9379-1.

[46] M. Prytz, B.A. Nikitin, Das Radonhydrat, Z. Anorg. Allg. Chem. 227 (1) (1936) 81–93. https://doi.org/10.1002/zaac.19362270111.

[47] K. Ohgaki, K. Takano, H. Sangawa, T. Matsubara, S. Nakano, Methane exploitation by carbon dioxide from gas hydrates. Phase equilibria for CO2-CH4 mixed hydrate system, J. Chem. Eng. Japan / JCEJ 29 (3) (1996) 478–483. https://doi.org/10.1252/jcej.29.478.

[48] H. Bruusgaard, J.G. Beltrán, P. Servio, Solubility measurements for the CH4 + CO2 + H2O system under hydrate–liquid–vapor equilibrium, Fluid Phase Equilibria 296 (2) (2010) 106–109. https://doi.org/10.1016/j.fluid.2010.02.042.

[49] S. Adisasmito, R.J. Frank, E.D. Sloan, Hydrates of carbon dioxide and methane mixtures, J. Chem. Eng. Data 36 (1) (1991) 68–71. https://doi.org/10.1021/je00001a020.

[50] V. Belandria, A.H. Mohammadi, D. Richon, Phase equilibria of clathrate hydrates of methane+carbon dioxide: New experimental data and predictions, Fluid Phase Equilibria 296 (1) (2010) 60–65. https://doi.org/10.1016/j.fluid.2010.03.038.

[51] V. Belandria, A. Eslamimanesh, A.H. Mohammadi, P. Théveneau, H. Legendre, D. Richon, Compositional Analysis and Hydrate Dissociation Conditions Measurements for Carbon Dioxide + Methane + Water System, Ind. Eng. Chem. Res. 50 (9) (2011) 5783–5794. https://doi.org/10.1021/ie101959t.

[52] Y.-T. Seo, S.-P. Kang, H. Lee, C.-S. Lee, W.-M. Sung, Hydrate phase equilibria for gas mixtures containing carbon dioxide: A proof-of-concept to carbon dioxide recovery from multicomponent gas stream, Korean J. Chem. Eng. 17 (6) (2000) 659–667. https://doi.org/10.1007/BF02699114.

[53] A. Eslamimanesh, A.H. Mohammadi, D. Richon, P. Naidoo, D. Ramjugernath, Application of gas hydrate formation in separation processes: A review of experimental studies, The Journal of Chemical Thermodynamics 46 (2012) 62–71. https://doi.org/10.1016/j.jct.2011.10.006.

[54] M.E. Benesh US 2270016 A, 1942.

[55] R. Boswell, T.S. Collett, Current perspectives on gas hydrate resources, Energy Environ. Sci. 4 (4) (2011) 1206–1215. https://doi.org/10.1039/C0EE00203H.

[56] H.P. Veluswamy, A. Kumar, Y. Seo, J.D. Lee, P. Linga, A review of solidified natural gas (SNG) technology for gas storage via clathrate hydrates, Applied Energy 216 (2018) 262–285. https://doi.org/10.1016/j.apenergy.2018.02.059.

[57] J.-S. Gudmundsson, Mahmut Parlaktuna, A. A. Khokhar, Storing Natural Gas as Frozen Hydrate.

[58] J.S. Gudmundson US005,536,893A, 1996.

[59] A.A. Khokhar, J.S. Gudmundsson, E.D. Sloan, Gas storage in structure H hydrates, Fluid Phase Equilibria 150-151 (1998) 383–392. https://doi.org/10.1016/S0378-3812(98)00338-0.

[60] Y. Nakajima, T. Takaoki, K. Ohgaki, S. Ota, Use of Hydrate Pellets for Transportation of Natural Gas - II - Proposition of Natural Gas Transportation in form of Hydrate Pellets, Proc. 4th Int. Conf. Gas Hydrates (2002).

[61] H. Shirota, I. Aya, S. Namie, P. Bollavaram, D. Turner, E.D. Sloan, Measurement of methane hydrate dissociation for application to natural gas storage and transportation, Proc. 4th Int. Conf. Gas Hydrates (2002).

[62] H. Kanda, Economic study on natural gas transport with natural gas hydrate (NGH) pellets, 23rd World Gas Conference (2006).

[63] J.S. Gudmundsson, A. Borrehaug, Natural gas hydrate-an alternative to liquefied natural gas? Petroleum Review 50 (592) (1996) 232–235.

[64] J. Javanmardi, K. Nasrifar, S.H. Najibi, M. Moshfeghian, Economic evaluation of natural gas hydrate as an alternative for natural gas transportation, Applied Thermal Engineering 25 (11-12) (2005) 1708–1723. https://doi.org/10.1016/j.applthermaleng.2004.10.009.

[65] Z. Taheri, M.R. Shabani, K. Nazari, A. Mehdizaheh, Natural gas transportation and storage by hydrate technology: Iran case study, Journal of Natural Gas Science and Engineering 21 (2014) 846–849. https://doi.org/10.1016/j.jngse.2014.09.026.

[66] H. Najibi, R. Rezaei, J. Javanmardi, K. Nasrifar, M. Moshfeghian, Economic evaluation of natural gas transportation from Iran's South-Pars gas field to market, Applied Thermal Engineering 29 (10) (2009) 2009–2015. https://doi.org/10.1016/j.applthermaleng.2008.10.008.

[67] R. Khalilpour, I.A. Karimi, Evaluation of LNG, CNG, GTL and NGH for Monetization of Stranded Associated Gas with the Incentive of Carbon Credit, in: International Petroleum Technology Conference, Doha, Qatar, International Petroleum Technology Conference, 2013.

[68] G. Rehder, R. Eckl, M. Elfgen, A. Falenty, R. Hamann, N. Kähler, W.F. Kuhs, H. Osterkamp, C. Windmeier, Methane Hydrate Pellet Transport Using the Self-Preservation Effect: A Techno-Economic Analysis, Energies 5 (12) (2012) 2499–2523. https://doi.org/10.3390/en5072499.

[69] A. Kumar, H.P. Veluswamy, R. Kumar, P. Linga, Direct use of seawater for rapid methane storage via clathrate (sII) hydrates, Applied Energy 235 (2019) 21–30. https://doi.org/10.1016/j.apenergy.2018.10.085.

[70] W.I. Wilcox, D.B. Carson, D.L. Katz, Natural Gas Hydrates, Ind. Eng. Chem. 33 (5) (1941) 662–665. https://doi.org/10.1021/ie50377a027.

[71] D.L. Katz, Prediction of conditions for hydrate formation in natural gases, Transactions of the AIME 160 (01) (1945) 140–149.

[72] W.R. Parrish, J.M. Prausnitz, Dissociation Pressures of Gas Hydrates Formed by Gas Mixtures, Ind. Eng. Chem. Proc. Des. Dev. 11 (1) (1972) 26–35. https://doi.org/10.1021/i260041a006.

[73] S. Maghsoodloo Babakhani, B. Bouillot, J. Douzet, S. Ho-Van, J.M. Herri, A new approach of studying mixed gas hydrates involving propane at non-equilibrium conditions and final state: An experimental study and modeling, Chemical Engineering Science 179 (2018) 150–160. https://doi.org/10.1016/j.ces.2018.01.017.

[74] A.L. Ballard, C.S.o.M.D.o.C.a.P.-R. Engineering, A Non-ideal Hydrate Solid Solution Model for a Multi-phase Equilibria Program, 2002.

[75] A.A. Bandyopadhyay, J.B. Klauda, Gas Hydrate Structure and Pressure Predictions Based on an Updated Fugacity-Based Model with the PSRK Equation of State, Ind. Eng. Chem. Res. 50 (1) (2011) 148–157. https://doi.org/10.1021/ie100440s.

[76] A. Martín, C.J. Peters, New Thermodynamic Model of Equilibrium States of Gas Hydrates Considering Lattice Distortion, J. Phys. Chem. C 113 (1) (2008) 422–430. https://doi.org/10.1021/jp8074546.

[77] Schultz H.J., Deerberg G., Schlüter S., Fahlenkamp H., Program for the simulation of gas hydrate equilibrium, GEOTECHNOLOGIEN - Science Report (1) (2002) 116–118.

[78] Schultz H.J., Deerberg G., Schlüter S., Fahlenkamp H., Simulation of the oceanic gas hydrate removal using the mammoth-pump-principle, GEOTECHNOLOGIEN - Science Report (1) (2002) 113–115.

[79] M. Ghavipour, M. Ghavipour, M. Chitsazan, S.H. Najibi, S.S. Ghidary, Experimental study of natural gas hydrates and a novel use of neural network to predict hydrate formation conditions, Chemical Engineering Research and Design 91 (2) (2013) 264–273. https://doi.org/10.1016/j.cherd.2012.08.010.

[80] S.M. Babakhani, M. Bahmani, J. Shariati, K. Badr, Y. Balouchi, Comparing the capability of artificial neural network (ANN) and CSMHYD program for predicting of hydrate formation pressure in binary mixtures, Journal of Petroleum Science and Engineering 136 (2015) 78–87. https://doi.org/10.1016/j.petrol.2015.11.002.

[81] J. Gmehling, B. Kolbe, M. Kleiber, J.R. Rarey, Chemical thermodynamics for process simulation, Wiley-VCH-Verl., Weinheim, 2012.

[82] R. Stryjek, J.H. Vera, PRSV: An improved peng-Robinson equation of state for pure compounds and mixtures, Can. J. Chem. Eng. 64 (2) (1986) 323–333. https://doi.org/10.1002/cjce.5450640224.

[83] P. Stephan, F. Mayinger, K. Schaber, K. Stephan, Thermodynamik: Grundlagen und technische Anwendungen; Band 1: Einstoffsysteme, 18th ed., Springer Berlin Heidelberg, Berlin, Heidelberg, 2009.

[84] A.H.S. Dehaghani, B. Karami, A new predictive thermodynamic framework for phase behavior of gas hydrate, Fuel 216 (2018) 796–809. https://doi.org/10.1016/j.fuel.2017.11.128.

[85] J.B. Klauda, S.I. Sandler, A Fugacity Model for Gas Hydrate Phase Equilibria, Ind. Eng. Chem. Res. 39 (9) (2000) 3377–3386. https://doi.org/10.1021/ie000322b.

[86] K. Růržička, V. Majer, Simple and controlled extrapolation of vapor pressures toward the triple point, AIChE J. 42 (6) (1996) 1723–1740. https://doi.org/10.1002/aic.690420624.

[87] U. Feuerriegel, Verfahrenstechnik mit EXCEL, Springer Fachmedien Wiesbaden, Wiesbaden, 2016.

[88] J. Munck, S. Skjold-Jørgensen, P. Rasmussen, Computations of the formation of gas hydrates, Chemical Engineering Science 43 (10) (1988) 2661–2672. https://doi.org/10.1016/0009-2509(88)80010-1.

[89] T.A. Strobel, C.A. Koh, E.D. Sloan, Thermodynamic predictions of various tetrahydrofuran and hydrogen clathrate hydrates, Fluid Phase Equilibria 280 (1-2) (2009) 61–67. https://doi.org/10.1016/j.fluid.2009.02.012.

[90] S.-P. Kang, H. Lee, C.-S. Lee, W.-M. Sung, Hydrate phase equilibria of the guest mixtures containing CO2, N2 and tetrahydrofuran, Fluid Phase Equilibria 185 (1-2) (2001) 101–109. https://doi.org/10.1016/S0378-3812(01)00460-5.

[91] D. Scholz, Numerik interaktiv: Grundlagen verstehen, Modelle erforschen und Verfahren anwenden mit taramath, Springer Spektrum, Berlin, Heidelberg, 2016.

[92] National Institute of Standards and Technology. https://gashydrates.nist.gov/ (accessed 2018).

[93] E.D. Sloan, Clathrate hydrates of natural gases, 2nd ed., Marcel Dekker, New York, 1998.

[94] Y. Zhang, P.G. Debenedetti, R.K. Prud'homme, B.A. Pethica, Accurate prediction of clathrate hydrate phase equilibria below 300 K from a simple model, Journal of Petroleum Science and Engineering 51 (1-2) (2006) 45–53. https://doi.org/10.1016/j.petrol.2005.11.008.

[95] M.-K. Hsieh, Y.-T. Yeh, Y.-P. Chen, P.-C. Chen, S.-T. Lin, L.-J. Chen, Predictive Method for the Change in Equilibrium Conditions of Gas Hydrates with Addition of Inhibitors and Electrolytes, Ind. Eng. Chem. Res. 51 (5) (2012) 2456–2469. https://doi.org/10.1021/ie202103a.

[96] S.-P. Kang, J.-W. Lee, Kinetic behaviors of CO2 hydrates in porous media and effect of kinetic promoter on the formation kinetics, Chemical Engineering Science 65 (5) (2010) 1840–1845. https://doi.org/10.1016/j.ces.2009.11.027.

[97] M. K. Moraveji, A. Sadeghi, A. Fazlali, R. Davarnejad, Effect of an Anionic Surfactant on the Methane Hydrate Formation: Induction Time and Stability, World Applied Sciences Journal (9 (10)) (2010) 1121–1128.

[98] P. Di Profio, S. Arca, R. Germani, G. Savelli, Surfactant promoting effects on clathrate hydrate formation: Are micelles really involved? Chemical Engineering Science 60 (15) (2005) 4141–4145. https://doi.org/10.1016/j.ces.2005.02.051.

[99] M. Albertí, A. Costantini, A. Laganá, F. Pirani, Are micelles needed to form methane hydrates in sodium dodecyl sulfate solutions? J. Phys. Chem. B 116 (14) (2012) 4220–4227. https://doi.org/10.1021/jp301124z.

[100] B. García-Aguilar, A. Ramirez, J. Jones, M. Heitz, Solubility of methane in pure non-ionic surfactants and pure and mixtures of linear alcohols at 298 K and 101.3 kPa, Chemical Papers 65 (3) (2011). https://doi.org/10.2478/s11696-011-0008-3.

[101] W.C. Griffin, Classification of surface-active agents by" HLB", J. Soc. Cosmet. Chem. 1 (1949) 311–326.

[102] D.K. Chou, R. Krishnamurthy, T.W. Randolph, J.F. Carpenter, M.C. Manning, Effects of Tween 20 and Tween 80 on the stability of Albutropin during agitation, J. Pharm. Sci. 94 (6) (2005) 1368–1381. https://doi.org/10.1002/jps.20365.

[103] S. Li, S. Fan, J. Wang, X. Lang, Y. Wang, Clathrate Hydrate Capture of CO2 from Simulated Flue Gas with Cyclopentane/Water Emulsion, Chinese Journal of Chemical Engineering 18 (2) (2010) 202–206. https://doi.org/10.1016/S1004-9541(08)60343-2.

[104] A. Kumar, T. Sakpal, P. Linga, R. Kumar, Influence of contact medium and surfactants on carbon dioxide clathrate hydrate kinetics, Fuel 105 (2013) 664–671. https://doi.org/10.1016/j.fuel.2012.10.031.

[105] C. Dicharry, C. Duchateau, H. Asbaï, D. Broseta, J.-P. Torré, Carbon dioxide gas hydrate crystallization in porous silica gel particles partially saturated with a surfactant solution, Chemical Engineering Science 98 (2013) 88–97. https://doi.org/10.1016/j.ces.2013.05.015.

[106] G.E. Tiller, T.J. Mueller, M.E. Dockter, W.G. Struve, Hydrogenation of Triton X-100 eliminates its fluorescence and ultraviolet light absorption while preserving its detergent properties, Analytical Biochemistry 141 (1) (1984) 262–266. https://doi.org/10.1016/0003-2697(84)90455-X.

[107] R. Karimi, F. Varaminian, A.A. Izadpanah, A.H. Mohammadi, Effects of Different Surfactants on the Kinetics of Ethane-Hydrate Formation: Experimental and Modeling Studies, Energy Technology 1 (9) (2013) 530–536. https://doi.org/10.1002/ente.201300064.

[108] Q. Yu, R. Zhang, S. Deng, J. Huang, G. Yu, Sorption of perfluorooctane sulfonate and perfluorooctanoate on activated carbons and resin: Kinetic and isotherm study, Water Res. 43 (4) (2009) 1150–1158. https://doi.org/10.1016/j.watres.2008.12.001.

[109] N.M. Kovalchuk, A. Trybala, V. Starov, O. Matar, N. Ivanova, Fluoro- vs hydrocarbon surfactants: why do they differ in wetting performance? Adv. Colloid Interface Sci. 210 (2014) 65–71. https://doi.org/10.1016/j.cis.2014.04.003.

[110] N. Choudhary, V.R. Hande, S. Roy, S. Chakrabarty, R. Kumar, Effect of Sodium Dodecyl Sulfate Surfactant on Methane Hydrate Formation: A Molecular Dynamics Study, J. Phys. Chem. B 122 (25) (2018) 6536–6542. https://doi.org/10.1021/acs.jpcb.8b02285.

[111] Crown Ethers and Phase Transfer Catalysis in Polymer Science, Springer US, Boston, MA, s.l., 1984.

[112] Handbook of Phase Transfer Catalysis, Springer Netherlands, Dordrecht, 1997.

[113] C.M. Starks, Phase-Transfer Catalysis: Fundamentals, Applications, and Industrial Perspectives, Springer Netherlands, Dordrecht, 1994.

[114] S.D. Naik, L.K. Doraiswamy, Phase transfer catalysis: Chemistry and engineering, AIChE J. 44 (3) (1998) 612–646. https://doi.org/10.1002/aic.690440312.

[115] K.P.C. Vollhardt, N.E. Schore, H. Butenschön, B. Elvers (Eds.), Organische Chemie, 4th ed., Wiley-VCH, Weinheim, 2009.

[116] P.Y. Bruice, T. Lazar, O. Reiser, Organische Chemie: Studieren kompakt, 5th ed., Pearson Studium, München, 2011.

[117] Ullmann's Encyclopedia of Industrial Chemistry, Wiley-VCH Verlag GmbH & Co. KGaA, Weinheim, Germany, 2000.

[118] R.W. Bucklin, R.L. Schendel, Comparison of Fluor Solvent and Selexol processes, Energy Prog. 4 (3) (1984) 137–142.

[119] Z.-M. Xia, X.-S. Li, Z.-Y. Chen, Q.-N. Lv, C.-G. Xu, C. Chen, Hydrate-based Capture CO2 and Purification CH4 from Simulated Landfill Gas with Synergic Additives Based on Gas Solvent, Energy Procedia 61 (2014) 450–454. https://doi.org/10.1016/j.egypro.2014.11.1146.

[120] F.S. Merkel, Research on inhibition of gas hydrate formation in pipelines and armatures using surface active substances. Dissertation, Universitätsbibliothek Duisburg-Essen, Duisburg, Essen, 2016.

[121] Z.S. Nickolov, K. Ohno, H. Matsuura, FTIR-ATR Studies of the Hydration of 15-Crown-5 and 18-Crown-6 in Aqueous Solutions, J. Phys. Chem. A 103 (37) (1999) 7544–7551. https://doi.org/10.1021/jp991258i.

[122] J.-H. Sa, B.R. Lee, D.-H. Park, K. Han, H.D. Chun, K.-H. Lee, Amino acids as natural inhibitors for hydrate formation in CO2 sequestration, Environ. Sci. Technol. 45 (13) (2011) 5885–5891. https://doi.org/10.1021/es200552c.

[123] P. Naeiji, A. Arjomandi, F. Varaminian, Amino acids as kinetic inhibitors for tetrahydrofuran hydrate formation: Experimental study and kinetic modeling, Journal of

Natural Gas Science and Engineering 21 (2014) 64–70. https://doi.org/10.1016/j.jngse.2014.07.029.

[124] G. Bhattacharjee, N. Choudhary, A. Kumar, S. Chakrabarty, R. Kumar, Effect of the amino acid l-histidine on methane hydrate growth kinetics, Journal of Natural Gas Science and Engineering 35 (2016) 1453–1462. https://doi.org/10.1016/j.jngse.2016.05.052.

[125] H.P. Veluswamy, A. Kumar, R. Kumar, P. Linga, An innovative approach to enhance methane hydrate formation kinetics with leucine for energy storage application, Applied Energy 188 (2017) 190–199. https://doi.org/10.1016/j.apenergy.2016.12.002.

[126] G.M. Cooper, R.E. Hausman, The cell: A molecular approach, 3rd ed., ASM Press, Washington, DC, 2004.

[127] J. Kyte, R.F. Doolittle, A simple method for displaying the hydropathic character of a protein, Journal of Molecular Biology 157 (1) (1982) 105–132. https://doi.org/10.1016/0022-2836(82)90515-0.

[128] David J. Anneken, Sabine Both, Ralf Christoph, Georg Fieg, Udo Steinberner, Alfred Westfechtel, Ullmann's Encyclopedia of Industrial Chemistry (2000). https://doi.org/10.1002/14356007.

[129] F.E. Stanley, A.M. Warner, E. Schneiderman, A.M. Stalcup, Rapid determination of surfactant critical micelle concentrations using pressure-driven flow with capillary electrophoresis instrumentation, J. Chromatogr. A 1216 (47) (2009) 8431–8434. https://doi.org/10.1016/j.chroma.2009.09.026.

[130] Wen, Franses, Effect of Protonation on the Solution and Phase Behavior of Aqueous Sodium Myristate, J. Colloid Interface Sci. 231 (1) (2000) 42–51. https://doi.org/10.1006/jcis.2000.7156.

[131] A.N. Campbell, G.R. Lakshminarayanan, Conductances and surface tensions of aqueous solutions of sodium decanoate, sodium laurate, and sodium myristate, at 25° and 35°, Can. J. Chem. 43 (6) (1965) 1729–1737. https://doi.org/10.1139/v65-228.

[132] K. Okutani, Y. Kuwabara, Y.H. Mori, Surfactant effects on hydrate formation in an unstirred gas/liquid system: An experimental study using methane and sodium alkyl sulfates, Chemical Engineering Science 63 (1) (2008) 183–194. https://doi.org/10.1016/j.ces.2007.09.012.

[133] J. Yoslim, P. Linga, P. Englezos, Enhanced growth of methane–propane clathrate hydrate crystals with sodium dodecyl sulfate, sodium tetradecyl sulfate, and sodium hexadecyl sulfate surfactants, Journal of Crystal Growth 313 (1) (2010) 68–80. https://doi.org/10.1016/j.jcrysgro.2010.10.009.

[134] C. Dicharry, J. Diaz, J.-P. Torré, M. Ricaurte, Influence of the carbon chain length of a sulfate-based surfactant on the formation of CO 2 CH 4 and CO 2 –CH 4 gas hydrates,

Chemical Engineering Science 152 (2016) 736–745. https://doi.org/10.1016/j.ces.2016.06.034.

[135] Siegfried Rebsdat, Dieter Mayer, Ullmann's Encyclopedia of Industrial Chemistry (2000). https://doi.org/10.1002/14356007.

[136] F. Filarsky, C. Schmuck, H.J. Schultz, Development of a Surface-Active Coating for Promoted Gas Hydrate Formation, Chemie Ingenieur Technik 30 (11) (2018) 9141. https://doi.org/10.1002/cite.201800002.

[137] F.S. Merkel, C. Schmuck, H.J. Schultz, T.A. Scholz, S. Wolinski, Research on Gas Hydrate Plug Formation under Pipeline-Like Conditions, International Journal of Chemical Engineering 2015 (12) (2015) 1–5. https://doi.org/10.1155/2015/214638.

[138] H.J. Schultz, F.S. Merkel, Feasibility study concerning gas hydrate inhibition in pipelines via permanent functional coating, 9th International Conference on Gas Hydrates Denver, Colorado USA (2017).

[139] H. Zhang, S. Fan, Y. Wang, X. Lang, Investigation into relationship between hydrate particles and hydrophobic surface, 9th International Conference on Gas Hydrates Denver, Colorado USA (2017).

[140] H. Li, L. Wang, Hydrophobized particles can accelerate nucleation of clathrate hydrates, Fuel 140 (2015) 440–445. https://doi.org/10.1016/j.fuel.2014.10.005.

[141] J. Park, K. Shin, J. Kim, H. Lee, Y. Seo, N. Maeda, W. Tian, C.D. Wood, Effect of Hydrate Shell Formation on the Stability of Dry Water, J. Phys. Chem. C 119 (4) (2015) 1690–1699. https://doi.org/10.1021/jp510603q.

[142] N.N. Nguyen, A.V. Nguyen, K.M. Steel, L.X. Dang, M. Galib, Interfacial Gas Enrichment at Hydrophobic Surfaces and the Origin of Promotion of Gas Hydrate Formation by Hydrophobic Solid Particles, J. Phys. Chem. C 121 (7) (2017) 3830–3840. https://doi.org/10.1021/acs.jpcc.6b07136.

[143] Z. Kutelova, H. Mainka, K. Mader, W. Hintz, J. Tomas, Glass Spheres: Functionalization, Surface Modification and Mechanical Properties, Surface Effects in Solid Mechanics. Advanced Structured Materials 30 (2013) 95–104. https://doi.org/10.1007/978-3-642-35783-1_8.

[144] K. Jradi, C. Daneault, B. Chabot, Chemical surface modification of glass beads for the treatment of paper machine process waters, Thin Solid Films 519 (13) (2011) 4239–4245. https://doi.org/10.1016/j.tsf.2011.02.080.

[145] S.-H. Chang, Y.-C. Hsiao, Surface and Protein Adsorption Properties of 316L Stainless Steel Modified with Polycaprolactone Film, Polymers 9 (10) (2017) 545. https://doi.org/10.3390/polym9100545.

[146] P.S. Noonan, A. Shavit, B.R. Acharya, D.K. Schwartz, Mixed alkylsilane functionalized surfaces for simultaneous wetting and homeotropic anchoring of liquid crystals, ACS Appl. Mater. Interfaces 3 (11) (2011) 4374–4380. https://doi.org/10.1021/am201026r.

[147] B. Arkles, Hydrophobicity, Hydrophilicity and Silanes, Paint and Coatings Industry 22 (114) (2006).

[148] B. Arkles, Tailoring surfaces with silanes, Chemtech 12 (7) (1977) 766–778.

[149] P. Linga, N. Daraboina, J.A. Ripmeester, P. Englezos, Enhanced rate of gas hydrate formation in a fixed bed column filled with sand compared to a stirred vessel, Chemical Engineering Science 68 (1) (2012) 617–623. https://doi.org/10.1016/j.ces.2011.10.030.

[150] Y. Mori, On the Scale-up of Gas-Hydrate-Forming Reactors: The Case of Gas-Dispersion-Type Reactors, Energies 8 (2) (2015) 1317–1335. https://doi.org/10.3390/en8021317.

[151] Wilson, Haymet, The effect of stirring on the heterogeneous nucleation of water and of clathrates of tetrahydrofuran/water mixtures, Condens. Matter Phys. 19 (2) (2016) 23602. https://doi.org/10.5488/CMP.19.23602.

[152] M.F. Qureshi, M. Atilhan, T. Altamash, S. Aparicio, M. Aminnaji, B. Tohidi, High-pressure gas hydrate autoclave hydraulic experiments and scale-up modeling on the effect of stirring RPM effect, Journal of Natural Gas Science and Engineering 38 (2017) 50–58. https://doi.org/10.1016/j.jngse.2016.12.023.

[153] R.-E. Meindinyo, T. Svartaas, Gas Hydrate Growth Kinetics: A Parametric Study, Energies 9 (12) (2016) 1021. https://doi.org/10.3390/en9121021.

[154] J. S. Parent, P.R. Bishnoi, Investigations into the nucleation behaviour of methane gas hydrates, Chemical Engineering Communications 144 (1) (1996) 51–64. https://doi.org/10.1080/00986449608936444.

[155] W. Ke, T.M. Svartaas, Effects of stirring and cooling on methane hydrate formation in a high-pressure isochoric cell, Proceedings of the 7th International Conference on Gas Hydrates (ICGH 2011) (2011).

[156] C.P. Ribeiro, P.L.C. Lage, Modelling of hydrate formation kinetics: State-of-the-art and future directions, Chemical Engineering Science 63 (8) (2008) 2007–2034. https://doi.org/10.1016/j.ces.2008.01.014.

[157] A.J.L. Hutchinson US2356407 A, 1944.

[158] R.E. Rogers, C.Y. Yevi, M. Swalm, Hydrates for storage of natural gas, Proceedings of the 2nd International Conference on Natural Gas Hydrates (ICGH1996) (1996).

[159] R. Ohmura, S. Kashiwazaki, S. Shiota, H. Tsuji, Y.H. Mori, Structure-I and Structure-H Hydrate Formation Using Water Spraying, Energy Fuels 16 (5) (2002) 1141–1147. https://doi.org/10.1021/ef0200727.

[160] K. Yoshikawa, Y. Kondo, T. Kimura, T. Fujimoto US6653516 B1, 2003.

[161] T.D. Brown, C.E. Taylor, M.P. Bernardo, Rapid Gas Hydrate Formation Processes: Will They Work? Energies 3 (6) (2010) 1154–1175. https://doi.org/10.3390/en3061154.

[162] J.M. Herri, J.S. Pic, F. Gruy, M. Cournil, Methane hydrate crystallization mechanism fromin-situ particle sizing, AIChE J. 45 (3) (1999) 590–602. https://doi.org/10.1002/aic.690450316.

[163] B. Lucia, B. Castellani, F. Rossi, F. Cotana, E. Morini, A. Nicolini, M. Filipponi, Experimental investigations on scaled-up methane hydrate production with surfactant promotion: Energy considerations, Journal of Petroleum Science and Engineering 120 (2014) 187–193. https://doi.org/10.1016/j.petrol.2014.06.015.

[164] M. Zlokarnik, Scale-up in Chemical Engineering, Wiley-VCH, Hoboken, 2006.

[165] T. Murakami, H. Kuritsuka, H. Fujii, Y.H. Mori, Forming a Structure-H Hydrate Using Water and Methylcyclohexane Jets Impinging on Each Other in a Methane Atmosphere, Energy Fuels 23 (3) (2009) 1619–1625. https://doi.org/10.1021/ef800880f.

[166] T. Kobayashi, N. Imura, R. Ohmura, Y.H. Mori, Clathrate Hydrate Formation by Water Spraying in a Methane + Ethane + Propane Gas Mixture: Search for the Rate-Controlling Mechanism of Hydrate Formation in the Presence of Methylcyclohexane, Energy Fuels 21 (2) (2007) 545–553. https://doi.org/10.1021/ef060461r.

[167] P. Linga, C. Haligva, S.C. Nam, J.A. Ripmeester, P. Englezos, Gas Hydrate Formation in a Variable Volume Bed of Silica Sand Particles, Energy Fuels 23 (11) (2009) 5496–5507. https://doi.org/10.1021/ef900542m.

[168] S.A. Bagherzadeh, I.L. Moudrakovski, J.A. Ripmeester, P. Englezos, Magnetic Resonance Imaging of Gas Hydrate Formation in a Bed of Silica Sand Particles, Energy Fuels 25 (7) (2011) 3083–3092. https://doi.org/10.1021/ef200399a.

[169] P. Babu, R. Kumar, P. Linga, Unusual behavior of propane as a co-guest during hydrate formation in silica sand: Potential application to seawater desalination and carbon dioxide capture, Chemical Engineering Science 117 (2014) 342–351. https://doi.org/10.1016/j.ces.2014.06.044.

[170] L.R. White, Capillary rise in powders, J. Colloid Interface Sci. 90 (2) (1982) 536–538. https://doi.org/10.1016/0021-9797(82)90319-8.

[171] M. Ricaurte, C. Dicharry, X. Renaud, J.-P. Torré, Combination of surfactants and organic compounds for boosting CO2 separation from natural gas by clathrate hydrate formation, Fuel 122 (2014) 206–217. https://doi.org/10.1016/j.fuel.2014.01.025.

[172] H.P. Veluswamy, S. Kumar, R. Kumar, P. Rangsunvigit, P. Linga, Enhanced clathrate hydrate formation kinetics at near ambient temperatures and moderate pressures: Application to natural gas storage, Fuel 182 (2016) 907–919. https://doi.org/10.1016/j.fuel.2016.05.068.

[173] H. Ganji, M. Manteghian, K. Sadaghiani zadeh, M.R. Omidkhah, H. Rahimi Mofrad, Effect of different surfactants on methane hydrate formation rate, stability and storage capacity, Fuel 86 (3) (2007) 434–441. https://doi.org/10.1016/j.fuel.2006.07.032.

[174] D. Daniel-David, F. Guerton, C. Dicharry, J.-P. Torré, D. Broseta, Hydrate growth at the interface between water and pure or mixed CO2/CH4 gases: Influence of pressure, temperature, gas composition and water-soluble surfactants, Chemical Engineering Science 132 (2015) 118–127. https://doi.org/10.1016/j.ces.2015.04.015.

[175] K. Watanabe, S. Niwa, Y.H. Mori, Surface Tensions of Aqueous Solutions of Sodium Alkyl Sulfates in Contact with Methane under Hydrate-Forming Conditions, J. Chem. Eng. Data 50 (5) (2005) 1672–1676. https://doi.org/10.1021/je050139v.

[176] F.S. Merkel, C. Schmuck, H.J. Schultz, Investigation of the Influence of Hydroxyl Groups on Gas Hydrate Formation at Pipeline-Like Conditions, Energy Fuels 30 (11) (2016) 9141–9149. https://doi.org/10.1021/acs.energyfuels.6b01795.

[177] S. Alavi, S. Takeya, R. Ohmura, T.K. Woo, J.A. Ripmeester, Hydrogen-bonding alcohol-water interactions in binary ethanol, 1-propanol, and 2-propanol+methane structure II clathrate hydrates, J. Chem. Phys. 133 (7) (2010) 74505. https://doi.org/10.1063/1.3469776.

[178] R. Wang, T. Liu, F. Ning, W. Ou, L. Zhang, Z. Wang, L. Peng, J. Sun, Z. Liu, T. Li, H. Sun, G. Jiang, Effect of hydrophilic silica nanoparticles on hydrate formation: Insight from the experimental study, Journal of Energy Chemistry (2018). https://doi.org/10.1016/j.jechem.2018.02.021.

[179] A. Adeyemo, R. Kumar, P. Linga, J. Ripmeester, P. Englezos, Capture of carbon dioxide from flue or fuel gas mixtures by clathrate crystallization in a silica gel column, International Journal of Greenhouse Gas Control 4 (3) (2010) 478–485. https://doi.org/10.1016/j.ijggc.2009.11.011.

[180] Q. Sun, H. Li, J. Yan, L. Liu, Z. Yu, X. Yu, Selection of appropriate biogas upgrading technology-a review of biogas cleaning, upgrading and utilisation, Renewable and Sustainable Energy Reviews 51 (2015) 521–532. https://doi.org/10.1016/j.rser.2015.06.029.

[181] M.K. Mondal, H.K. Balsora, P. Varshney, Progress and trends in CO2 capture/separation technologies: A review, Energy 46 (1) (2012) 431–441. https://doi.org/10.1016/j.energy.2012.08.006.

[182] L. Yang, X. Ge, C. Wan, F. Yu, Y. Li, Progress and perspectives in converting biogas to transportation fuels, Renewable and Sustainable Energy Reviews 40 (2014) 1133–1152. https://doi.org/10.1016/j.rser.2014.08.008.

[183] H.P. Veluswamy, A.J.H. Wong, P. Babu, R. Kumar, S. Kulprathipanja, P. Rangsunvigit, P. Linga, Rapid methane hydrate formation to develop a cost effective large scale energy

storage system, Chemical Engineering Journal 290 (2016) 161–173. https://doi.org/10.1016/j.cej.2016.01.026.

[184] F.S. Merkel, H.J. Schultz, Methane Extraction from Natural Gas Hydrate Reservoirs with Simultaneous Storage of Carbon Dioxide, Chemie Ingenieur Technik 87 (4) (2015) 475–483. https://doi.org/10.1002/cite.201300164.

[185] F. Filarsky, C. Schmuck, H.J. Schultz, Development of a biogas production and purification process using promoted gas hydrate formation — A feasibility study, Chemical Engineering Research and Design 134 (2018) 257–267. https://doi.org/10.1016/j.cherd.2018.04.009.

[186] M. Ricaurte, C. Dicharry, D. Broseta, X. Renaud, J.-P. Torré, CO_2 Removal from a CO_2–CH_4 Gas Mixture by Clathrate Hydrate Formation Using THF and SDS as Water-Soluble Hydrate Promoters, Ind. Eng. Chem. Res. 52 (2) (2013) 899–910. https://doi.org/10.1021/ie3025888.

[187] J. Tang, D. Zeng, C. Wang, Y. Chen, L. He, N. Cai, Study on the influence of SDS and THF on hydrate-based gas separation performance, Chemical Engineering Research and Design 91 (9) (2013) 1777–1782. https://doi.org/10.1016/j.cherd.2013.03.013.

[188] P. Di Profio, V. Canale, N. D'Alessandro, R. Germani, A. Di Crescenzo, A. Fontana, Separation of CO 2 and CH 4 from Biogas by Formation of Clathrate Hydrates: Importance of the Driving Force and Kinetic Promoters, ACS Sustainable Chem. Eng. 5 (2) (2017) 1990–1997. https://doi.org/10.1021/acssuschemeng.6b02832.

[189] D.-L. Zhong, Z. Li, Y.-Y. Lu, J.-L. Wang, J. Yan, Evaluation of CO 2 removal from a CO 2 + CH 4 gas mixture using gas hydrate formation in liquid water and THF solutions, Applied Energy 158 (2015) 133–141. https://doi.org/10.1016/j.apenergy.2015.08.058.

[190] H. Ueno, H. Akiba, S. Akatsu, R. Ohmura, Crystal growth of clathrate hydrates formed with methane + carbon dioxide mixed gas at the gas/liquid interface and in liquid water, New J. Chem. 39 (11) (2015) 8254–8262. https://doi.org/10.1039/C5NJ01080B.

[191] S.-P. Kang, H. Lee, Recovery of CO 2 from Flue Gas Using Gas Hydrate: Thermodynamic Verification through Phase Equilibrium Measurements, Environ. Sci. Technol. 34 (20) (2000) 4397–4400. https://doi.org/10.1021/es001148l.

[192] N.H. Duc, F. Chauvy, J.-M. Herri, CO2 capture by hydrate crystallization – A potential solution for gas emission of steelmaking industry, Energy Conversion and Management 48 (4) (2007) 1313–1322. https://doi.org/10.1016/j.enconman.2006.09.024.

[193] N. Dabrowski, C. Windmeier, L.R. Oellrich, Purification of Natural Gases with High CO 2 Content Using Gas Hydrates, Energy Fuels 23 (11) (2009) 5603–5610. https://doi.org/10.1021/ef9005669.

[194] A.P. Semenov, V.I. Medvedev, P.A. Gushchin, M.S. Kotelev, V.S. Yakushev, A.S. Stoporev, A.A. Sizikov, A.G. Ogienko, V.A. Vinokurov, Phase equilibrium for clathrate hydrate formed in

methane + water + ethylene carbonate system, Fluid Phase Equilibria 432 (2017) 1–9. https://doi.org/10.1016/j.fluid.2016.10.015.

[195] D. Mech, P. Gupta, J.S. Sangwai, Kinetics of methane hydrate formation in an aqueous solution of thermodynamic promoters (THF and TBAB) with and without kinetic promoter (SDS), Journal of Natural Gas Science and Engineering 35 (2016) 1519–1534. https://doi.org/10.1016/j.jngse.2016.06.013.

[196] C.-G. Xu, Y.-S. Yu, Y.-L. Ding, J. Cai, X.-S. Li, The effect of hydrate promoters on gas uptake, Phys. Chem. Chem. Phys. 19 (32) (2017) 21769–21776. https://doi.org/10.1039/c7cp02173a.

[197] Z.-M. Xia, X.-S. Li, Z.-Y. Chen, G. Li, K.-F. Yan, C.-G. Xu, Q.-N. Lv, J. Cai, Hydrate-based CO 2 capture and CH 4 purification from simulated biogas with synergic additives based on gas solvent, Applied Energy 162 (2016) 1153–1159. https://doi.org/10.1016/j.apenergy.2015.02.016.

[198] Z.-M. Xia, X.-S. Li, Z.-Y. Chen, G. Li, J. Cai, Y. Wang, K.-F. Yan, C.-G. Xu, Hydrate-based acidic gases capture for clean methane with new synergic additives, Applied Energy 207 (2017) 584–593. https://doi.org/10.1016/j.apenergy.2017.06.017.

[199] R. Font, J.M. López Cabanes, Fermentation in fed-batch reactors—Application to the sewage sludge anaerobic digestion, Chemical Engineering Science 50 (13) (1995) 2117–2126. https://doi.org/10.1016/0009-2509(95)00058-D.

[200] C.C. Chen, C.Y. Lin, Start-up of Anaerobic Hydrogen Producing Reactors Seeded with Sewage Sludge, Acta Biotechnol. 21 (4) (2001) 371–379. https://doi.org/10.1002/1521-3846(200111)21:4<371:AID-ABIO371>3.0.CO;2-Z.

[201] H. Carrère, C. Dumas, A. Battimelli, D.J. Batstone, J.P. Delgenès, J.P. Steyer, I. Ferrer, Pretreatment methods to improve sludge anaerobic degradability: A review, J. Hazard. Mater. 183 (1-3) (2010) 1–15. https://doi.org/10.1016/j.jhazmat.2010.06.129.

[202] M. Kaltschmitt, H. Hartmann, H. Hofbauer, Energie aus Biomasse, Springer Berlin Heidelberg, Berlin, Heidelberg, 2016.

[203] D. L. Fowler, W. V. Loebenstein, D. B. Pall, and Charles A. Kraus, Some Unusual Hydrates of Quaternary Ammonium Salts.

[204] Y.A. Dyadin, K.A. Udachin, Clathrate polyhydrates of peralkylonium salts and their analogs, J Struct Chem 28 (3) (1987) 394–432. https://doi.org/10.1007/BF00753818.

[205] Y.A. Dyadin, K.A. Udachin, Clathrate Formation in Wateer-Peralkylonium Salts Systems, in: J.L. Atwood, J.E.D. Davies, T. Osa (Eds.), Clathrate Compounds, Molecular Inclusion Phenomena, and Cyclodextrins, Springer Netherlands, Dordrecht, 1985, pp. 61–72.

[206] J. Zheng, K. Bhatnagar, M. Khurana, P. Zhang, B.-Y. Zhang, P. Linga, Semiclathrate based CO 2 capture from fuel gas mixture at ambient temperature: Effect of concentrations of tetra-

n-butylammonium fluoride (TBAF) and kinetic additives, Applied Energy 217 (2018) 377–389. https://doi.org/10.1016/j.apenergy.2018.02.133.

[207] J. Douzet, M. Kwaterski, A. Lallemand, F. Chauvy, D. Flick, J.-M. Herri, Prototyping of a real size air-conditioning system using a tetra-n-butylammonium bromide semiclathrate hydrate slurry as secondary two-phase refrigerant – Experimental investigations and modelling, International Journal of Refrigeration 36 (6) (2013) 1616–1631. https://doi.org/10.1016/j.ijrefrig.2013.04.015.

[208] J. Deschamps, D. Dalmazzone, Hydrogen Storage in Semiclathrate Hydrates of Tetrabutyl Ammonium Chloride and Tetrabutyl Phosphonium Bromide, J. Chem. Eng. Data 55 (9) (2010) 3395–3399. https://doi.org/10.1021/je100146b.

[209] X. Zang, D. Liang, Phase Equilibrium Data for Semiclathrate Hydrate of Synthesized Binary CO 2 /CH 4 Gas Mixture in Tetra- n -butylammonium Bromide Aqueous Solution, J. Chem. Eng. Data 62 (2) (2017) 851–856. https://doi.org/10.1021/acs.jced.6b00876.

[210] G. Yue, A. Liu, Q. Sun, X. Li, W. Lan, L. Yang, X. Guo, The Combination of 1-octyl-3-methylimidazolium tetrafluorborate with TBAB or THF on CO 2 hydrate formation and CH 4 separation from biogas, Chinese Journal of Chemical Engineering (2018). https://doi.org/10.1016/j.cjche.2018.03.014.

[211] Z. Li, D.-L. Zhong, Y.-Y. Lu, J. Yan, Z.-L. Zou, Preferential enclathration of CO 2 into tetra- n -butyl phosphonium bromide semiclathrate hydrate in moderate operating conditions: Application for CO 2 capture from shale gas, Applied Energy 199 (2017) 370–381. https://doi.org/10.1016/j.apenergy.2017.05.043.

[212] T. Rodionova, V. Komarov, G. Villevald, L. Aladko, T. Karpova, A. Manakov, Calorimetric and structural studies of tetrabutylammonium chloride ionic clathrate hydrates, J. Phys. Chem. B 114 (36) (2010) 11838–11846. https://doi.org/10.1021/jp103939q.

[213] M. Oshima, M. Kida, J. Nagao, Hydration numbers and thermal properties of tetra- n -butyl ammonium bromide semiclathrate hydrates determined by ion chromatography and differential scanning calorimetry, The Journal of Chemical Thermodynamics 123 (2018) 32–37. https://doi.org/10.1016/j.jct.2018.03.018.

[214] Y.A. Dyadin, I.V. Bondaryuk, L.S. Aladko, Stoichiometry of clathrates, J Struct Chem 36 (6) (1995) 995–1045. https://doi.org/10.1007/BF02578558.

[215] S. Muromachi, S. Takeya, Y. Yamamoto, R. Ohmura, Characterization of tetra-n-butylphosphonium bromide semiclathrate hydrate by crystal structure analysis, CrystEngComm 16 (10) (2014) 2056. https://doi.org/10.1039/c3ce41942h.

[216] T. Suginaka, H. Sakamoto, K. Iino, S. Takeya, M. Nakajima, R. Ohmura, Thermodynamic properties of ionic semiclathrate hydrate formed with tetrabutylphosphonium bromide, Fluid Phase Equilibria 317 (2012) 25–28. https://doi.org/10.1016/j.fluid.2011.12.010.

[217] H.O. Folkins, Ullmann's Encyclopedia of Industrial Chemistry (2000). https://doi.org/10.1002/14356007.

[218] Georg Hammer, Torsten Lübcke, Roland Kettner, Mark R. Pillarella, Herta Recknagel, Axel Commichau, et al., Ullmann's Encyclopedia of Industrial Chemistry (2000). https://doi.org/10.1002/14356007.

[219] T.V. Rodionova, V.Y. Komarov, G.V. Villevald, T.D. Karpova, N.V. Kuratieva, A.Y. Manakov, Calorimetric and structural studies of tetrabutylammonium bromide ionic clathrate hydrates, J. Phys. Chem. B 117 (36) (2013) 10677–10685. https://doi.org/10.1021/jp406082z.

[220] A. Manakov, T. Rodionova, I. Terekhova, V. Komarov, A. Burdin, A. Sizikov (Eds.), Structural and physico-chemical studies of ionic clathrate hydrates of tetrabutyl-and tetraisoamylammonium salts, 2011.

[221] A. Fukumoto, P. Paricaud, D. Dalmazzone, W. Bouchafaa, T.T.-S. Ho, W. Fürst, Modeling the Dissociation Conditions of Carbon Dioxide + TBAB, TBAC, TBAF, and TBPB Semiclathrate Hydrates, J. Chem. Eng. Data 59 (10) (2014) 3193–3204. https://doi.org/10.1021/je500243k.

[222] N. Mayoufi, D. Dalmazzone, A. Delahaye, P. Clain, L. Fournaison, W. Fürst, Experimental Data on Phase Behavior of Simple Tetrabutylphosphonium Bromide (TBPB) and Mixed CO 2 + TBPB Semiclathrate Hydrates, J. Chem. Eng. Data 56 (6) (2011) 2987–2993. https://doi.org/10.1021/je2003918.

[223] J. Deschamps, D. Dalmazzone, Dissociation enthalpies and phase equilibrium for TBAB semi-clathrate hydrates of N2, CO2, N2 + CO2 and CH4 + CO2, J Therm Anal Calorim 98 (1) (2009) 113–118. https://doi.org/10.1007/s10973-009-0399-3.

[224] A. Gutiérrez, M. Atilhan, S. Aparicio, Microscopic Characterization of CO 2 and H 2 S Removal by Sulfolane, Energy Fuels 31 (9) (2017) 9800–9813. https://doi.org/10.1021/acs.energyfuels.7b01577.

[225] W.L. Luyben, NGL Demethanizer Control, Ind. Eng. Chem. Res. 52 (33) (2013) 11626–11638. https://doi.org/10.1021/ie400454y.

[226] W. Kondo, H. Ogawa, R. Ohmura, Y.H. Mori, Clathrate Hydrate Formation from a Hydrocarbon Gas Mixture: Evolution of Gas-Phase Composition in a Hydrate-Forming Reactor, Energy Fuels 24 (12) (2010) 6375–6383. https://doi.org/10.1021/ef100950p.

[227] P. Naeiji, M. Mottahedin, F. Varaminian, Separation of methane–ethane gas mixtures via gas hydrate formation, Separation and Purification Technology 123 (2014) 139–144. https://doi.org/10.1016/j.seppur.2013.12.028.

[228] C.-Y. Sun, G.-J. Chen, L.-W. Zhang, Hydrate phase equilibrium and structure for (methane+ethane+tetrahydrofuran+water) system, The Journal of Chemical Thermodynamics 42 (9) (2010) 1173–1179. https://doi.org/10.1016/j.jct.2010.04.021.

[229] Q. Ma, G. Chen, L. Zhang, Vapor-hydrate phases equilibrium of (CH4+C2H6) and (CH4+C2H4) systems, Pet. Sci. 5 (4) (2008) 359–366. https://doi.org/10.1007/s12182-008-0042-0.

[230] F. Filarsky, C. Schmuck, H.J. Schultz, Development of a Gas Hydrate Absorption for Energy storage and Gas separation – Proof of Concept based on Natural Gas, Energy Procedia 158 (2019) 5367–5373. https://doi.org/10.1016/j.egypro.2019.01.628.

[231] K. Morita, S. Nakano, K. Ohgaki, Structure and stability of ethane hydrate crystal, Fluid Phase Equilibria 169 (2) (2000) 167–175. https://doi.org/10.1016/S0378-3812(00)00320-4.

[232] L.-W. Zhang, G.-J. Chen, X.-Q. Guo, C.-Y. Sun, L.-Y. Yang, The partition coefficients of ethane between vapor and hydrate phase for methane + ethane + water and methane + ethane + THF + water systems, Fluid Phase Equilibria 225 (2004) 141–144. https://doi.org/10.1016/j.fluid.2004.08.032.

[233] B.G. Liptak, Costs of process instruments, Chemical Engineering 77 (19) (1970) 60-&.

[234] G.P. Purohit, Estimating costs of shell-and-tube heat exchangers, Chemical Engineering 90 (17) (1983) 56–67.

[235] R.S. Hall, J. Matley, K.J. McNaughton, Current Costs of Process Equipment, Chemical Engineer 89 (7) (1982) 80–83.

[236] J. Cran, Improved factored method gives better preliminary cost estimates, Chem. Eng 74 (1981) 65–79.

[237] L.B. Evans, A. Mulet, A.B. Corripio, K.S. Chretien, Costs of pressure vessels, storage tanks, centrifugal pumps, motors, distillation and absorption towers, Chemical Engineering Magazine, Modern Cost Engineering II (1984) 140–146.

[238] A. Chauvel, Manual of economic analysis of chemical processes: Feasibility studies in refinery and petrochemical processes, McGraw-Hill Companies, 1981.

[239] R.H. Perry, D.W. Green, J.O. Maloney, Perry's Chemical Engineer's Handbook Chemical Engineer's Handbook, McGraw-Hill, 1984.

[240] A. Pikulik, H.E. Diaz, Costs of process equipment and other items, Chem. Eng 84 (1977) 106.

[241] W.M. Vatavuk, Estimating costs of air pollution control, CRC Press, 1990.

[242] G.D. Ulrich, A guide to chemical engineering process design and economics, Wiley New York, 1984.

[243] Bundesnetzagentur, Bundeskartellamt, Strompreise für Gewerbe- und Industriekunden in Deutschland in den Jahren 2007 bis 2017 (in Euro-Cent pro Kilowattstunde). quote from Statista - Das Statistik-Portal, 2017. https://de.statista.com/statistik/daten/studie/154902/umfrage/strompreise-fuer-industrie-und-gewerbe-seit-2006/ (accessed 3 August 2018).

[244] F. Wosnitza, H.G. Hilgers, Energieeffizienz und Energiemanagement: Ein Überblick heutiger Möglichkeiten und Notwendigkeiten, Vieweg+Teubner Verlag, Wiesbaden, 2012.

[245] P. Cozma, W. Wukovits, I. Mămăligă, A. Friedl, M. Gavrilescu, Modeling and simulation of high pressure water scrubbing technology applied for biogas upgrading, Clean Techn Environ Policy 17 (2) (2015) 373–391. https://doi.org/10.1007/s10098-014-0787-7.

[246] E.B. Webb, P.J. Rensing, C.A. Koh, E.D. Sloan, A.K. Sum, M.W. Liberatore, High-Pressure Rheology of Hydrate Slurries Formed from Water-in-Oil Emulsions, Energy Fuels 26 (6) (2012) 3504–3509. https://doi.org/10.1021/ef300163y.

[247] N. Mayoufi, D. Dalmazzone, W. Fürst, A. Delahaye, L. Fournaison, CO 2 Enclathration in Hydrates of Peralkyl-(Ammonium/Phosphonium) Salts: Stability Conditions and Dissociation Enthalpies, J. Chem. Eng. Data 55 (3) (2010) 1271–1275. https://doi.org/10.1021/je9006212.

[248] S.-P. Kang, H. Lee, B.-J. Ryu, Enthalpies of dissociation of clathrate hydrates of carbon dioxide, nitrogen, (carbon dioxide+ nitrogen), and (carbon dioxide + nitrogen+ tetrahydrofuran), The Journal of Chemical Thermodynamics 33 (5) (2001) 513–521. https://doi.org/10.1006/jcht.2000.0765.

[249] Springer-Verlag GmbH, VDI-Wärmeatlas: Mit 320 Tabellen, 11th ed., Springer Vieweg, Berlin, 2013.

[250] B. Castellani, E. Morini, M. Filipponi, A. Nicolini, M. Palombo, F. Cotana, F. Rossi, Clathrate Hydrates for Thermal Energy Storage in Buildings: Overview of Proper Hydrate-Forming Compounds, Sustainability 6 (10) (2014) 6815–6829. https://doi.org/10.3390/su6106815.

[251] Q. Sun, Y.T. Kang, Review on CO2 hydrate formation/dissociation and its cold energy application, Renewable and Sustainable Energy Reviews 62 (2016) 478–494. https://doi.org/10.1016/j.rser.2016.04.062.

[252] U. Neupert, Energiespeicher: Technische Grundlagen und energiewirtschaftliches Potenzial, Fraunhofer-IRB-Verl., Stuttgart, 2009.

[253] A. Delahaye, L. Fournaison, S. Marinhas, I. Chatti, J.-P. Petitet, D. Dalmazzone, W. Fürst, Effect of THF on Equilibrium Pressure and Dissociation Enthalpy of CO_2 Hydrates Applied to Secondary Refrigeration, Ind. Eng. Chem. Res. 45 (1) (2006) 391–397. https://doi.org/10.1021/ie050356p.

[254] D.G. Leaist, J.J. Murray, M.L. Post, D.W. Davidson, Enthalpies of decomposition and heat capacities of ethylene oxide and tetrahydrofuran hydrates, J. Phys. Chem. 86 (21) (1982) 4175–4178. https://doi.org/10.1021/j100218a017.

[255] C. Giavarini, F. Maccioni, M.L. Santarelli, CO2 sequestration from coal fired power plants, Fuel 89 (3) (2010) 623–628. https://doi.org/10.1016/j.fuel.2009.09.035.

[256] S. Kim, S.-P. Kang, Y. Seo, Semiclathrate-based CO2 capture from flue gas in the presence of tetra-n-butyl ammonium chloride (TBAC), Chemical Engineering Journal 276 (2015) 205–212. https://doi.org/10.1016/j.cej.2015.04.083.

[257] J. Cai, Y. Zhang, C.-G. Xu, Z.-M. Xia, Z.-Y. Chen, X.-S. Li, Raman spectroscopic studies on carbon dioxide separation from fuel gas via clathrate hydrate in the presence of tetrahydrofuran, Applied Energy 214 (2018) 92–102. https://doi.org/10.1016/j.apenergy.2018.01.055.

[258] E. Kim, G. Ko, Y. Seo, Greenhouse Gas (CHF 3) Separation by Gas Hydrate Formation, ACS Sustainable Chem. Eng. 5 (6) (2017) 5485–5492. https://doi.org/10.1021/acssuschemeng.7b00821.

[259] R. Coupan, C. Dicharry, J.-P. Torré, Hydroquinone clathrate based gas separation (HCBGS): Application to the CO 2 /CH 4 gas mixture, Fuel 226 (2018) 137–147. https://doi.org/10.1016/j.fuel.2018.03.170.

[260] K. Sattler, Thermische Trennverfahren: Grundlagen, Auslegung, Apparate, 3rd ed., Wiley-VCH, Weinheim, 2012.

[261] A. Mersmann, M. Kind, J. Stichlmair, Thermische Verfahrenstechnik: Grundlagen und Methoden, 2nd ed., Springer, Berlin, 2005.

[262] J. Mackowiak, Fluid Dynamics of Packed Columns: Principles of the Fluid Dynamic Design of Columns for Gas/Liquid and Liquid/Liquid Systems, Springer-Verlag Berlin Heidelberg, Berlin, Heidelberg, 2010.

[263] K.-H. Decker, K. Kabus, Maschinenelemente, 20th ed., Hanser, München, 2018.

[264] International Organization for Standardization, Graphical symbols for diagrams — Part 6: Measurement and control functions, 01th ed. 01.080.30, 25.040.40, 2002.

[265] T. Hatami, M. Rahimi, H. Daraei, E. Heidaryan, A.A. Alsairafi, PRSV equation of state parameter modeling through artificial neural network and adaptive network-based fuzzy inference system, Korean J. Chem. Eng. 29 (5) (2012) 657–667. https://doi.org/10.1007/s11814-011-0235-x.

[266] Dortmund Data Bank, 2018. www.ddbst.com (accessed 2018).

[267] M. Frost, E. Karakatsani, N. von Solms, D. Richon, G.M. Kontogeorgis, Vapor–Liquid Equilibrium of Methane with Water and Methanol. Measurements and Modeling, J. Chem. Eng. Data 59 (4) (2014) 961–967. https://doi.org/10.1021/je400684k.

[268] E.U. Franck, Walter Hayduk (Eds.): Ethane, Vol. 9 aus: Solubility Data Series. Pergamon Press, Oxford, New York, Toronto, Sydney, Paris, Frankfurt 1982. 263 Seiten, Preis: $ 100.-, Berichte der Bunsengesellschaft für physikalische Chemie 87 (7) (1983) 618. https://doi.org/10.1002/bbpc.19830870718.

[269] A. Chapoy, S. Mokraoui, A. Valtz, D. Richon, A.H. Mohammadi, B. Tohidi, Solubility measurement and modeling for the system propane–water from 277.62 to 368.16K, Fluid Phase Equilibria 226 (2004) 213–220. https://doi.org/10.1016/j.fluid.2004.08.040.

[270] S.-X. Hou, G.C. Maitland, J.M. Trusler, Measurement and modeling of the phase behavior of the (carbon dioxide+water) mixture at temperatures from 298.15K to 448.15K, The Journal of Supercritical Fluids 73 (2013) 87–96. https://doi.org/10.1016/j.supflu.2012.11.011.

[271] J.N. Nayak, M.I. Aralaguppi, B.V. Kumar Naidu, T.M. Aminabhavi, Thermodynamic Properties of Water + Tetrahydrofuran and Water + 1,4-Dioxane Mixtures at (303.15, 313.15, and 323.15) K †, J. Chem. Eng. Data 49 (3) (2004) 468–474. https://doi.org/10.1021/je030196t.

14 Appendix

14.1 Abbreviations & symbols

Abbreviations

Abbreviation	Description
% AAD	Percent absolute average pressure deviation
AA	Anti-agglomerant
ANG	Adsorbed natural gas
C_2H_6	Ethane
C_3H_8	Propane
CH_4	Methane
CHF_3	Fluoroform
CMC	Critical micelle concentration
CNG	Compressed natural gas
CO_2	Carbon dioxide
Des.	Description
DMSO	Dimethyl sulfoxide
DS	n-Dodecyltriethoxysilane
EoS	Equation of State
ES	Ethyltriethoxysilane
Exp.	Experiment
GHS	Gas hydrate storage
H_2	Hydrogen
H_2O	Water
H_2O_2	Hydrogen peroxide
H_2S	Hydrogen sulfide
H_2SO_4	Sulfuric acid
HDA	Hexadecylamine
HEG	Hexatehylene glycol
HLB	Hydrophilic-lipophilic balance
IGE	Interfacial gas enrichment
KHI	Kinetic hydrate inhibitor
LDHI	Low-dosage hydrate inhibitor
Lec	Lecithin
LNG	Liquified natural gas
MD	Molecular dynamics
N_2	Nitrogen
Nr.	Number
OS	n-Octyltriethoxysilane
PC	Propylene carbonate
PEG	Pentaethylene glycol
PFOA	Perfluorooctanic acid
POMSA	Peroxymonosulfuric acid
PS	1H, 1H, 2H, 2H Perrfluorooctyltriethoxysilane
PTC	Phase transfer catalyst
SD	Sodium decanoate
SDD	Sodium dodecanoate

Abbreviation	Description
SDS	Sodium dodecyl sulfate
Sim.	Simulation
SM	Sodium myristate
SO	Sodium octanoate
SO_2	Sulfur dioxide
TBAB	Tetrabutylammonium bromide
TBACl	Tetrabutylammonium chloride
TBPB	Tetrabutylphosphonium bromide
TEG	Tetraethylene glycol
THF	Tetrahydrofruan
TMSO	Sulfolane
U.S.	United states

Latin symbols

Symbol	Description	Unit
A	Exchange Area or cross section area	$\frac{1}{m}$ or m^2
C	Conversion	-
C	Langmuir absorption constant	-
Fr	Froude number	-
H	Height	m
ΔH	Formation enthalpy	$\frac{kJ}{mol}$
$HETP$	Height equivalent to a theoretical plate	$\frac{1}{m}$
M	Torque	Ncm
M	Molar mass	$\frac{g}{mol}$
N	Stirring frequency	$\frac{1}{min}$
N_A	Avogadro's number	$\frac{1}{mol}$
Ne	Newton number	-
P	Power	W
P_C	Capillary pressure	Pa
R	Universal gas constant	$\frac{bar\ L}{K\ mol}$
R	Radius	m
Re	Reynolds number	-
S	Volumetric surface area	$\frac{m^2}{m^3}$
T	Temperature	$°C$ or K
U	Overall heat transfer coefficients	$\frac{W}{m^2K}$
V	Volume	L
$\dot{V}$	Volume flow	$\frac{L}{h}$
We	Weber number	-
Z	Real gas factor	-
a	Internal pressure	-
a	Radius	m
b	Intrinsic volume	-
d	Diameter	mm or cm or m

Symbol	Description	Unit
f	Fugacity	Pa
g	Gravity	$\frac{m}{s}$
g^E	Free Gibbs energy	$\frac{kJ}{mol}$
h_L	Liquid hold-up	-
k	Boltzmann constant	$\frac{J}{K}$
k_L	Mass transfer coefficient	$\frac{m}{s}$
m	Mass	$g\ or\ kg$
$\dot{m}$	Mass flow	$\frac{g}{h}$
n	Molar amount	mol
p	Pressure	$bar(g)\ or\ bar(a)$
$\dot{q}$	Gas flow	$\frac{L}{h}$
t	Time	$s\ or\ \min\ or\ h$
v	Molar volume	$\frac{m^3}{mol}$
w	Velocity	$\frac{m}{s}$
x, y, z	Molar fraction	-
z	Cage type specific coordination number	-

Greek symbols

Symbol	Description	Unit
ζ_0	Resistance coefficient	-
α	Ideal separation factor	-
γ	Activity coefficient	-
η	Kinematic viscosity	$mPa\ s$
θ	Angle or cage occupancy	°
κ	Constant	$-$
μ	Activity	$\frac{bar\ L}{mol}$
π	Pi	-
ρ	Density	$\frac{kg}{m^3}$
σ	Surface tension	$\frac{mN}{m}\ or\ \frac{N}{m^2}$
σ	Distance between the cores at zero potential energy	m
φ	Fugacity coefficient	-
ω	Acentric factor	-
ω	Cell potential	J
ϵ	Porosity	-
ϵ	Energy parameter	-
ϑ	Temperature	°C

ISO 14617-6 was used for the description and identification of instruments in all P&ID, namely Figure 4-1, Figure 4-2, Figure 7-15 and Figure 11-4 [264].

14.2 Tables

14.3 Figures

named component is enriched in the hydrate phase and second named component in the gas phase 152

14.4 Simulation parameter for chapter 3

Table 14-1 Parameter for vapor-liquid-equilibrium modelling [265,266]

Component	T_c [K]	P_c [bar]	ω [-]	κ_1 [-]
Methane	190.6	46.00155	0.008	-0.00159
Ethane	305.4	48.83865	0.098	0.02669
Propane	369.8	42.455175	0.152	0.03136
Carbon dioxide	304.2	73.7646	0.225	0.04285
THF	540.2	51.8784	0.22535	0.03961
Water	647.3	220.4832	0.344	-0.06635

Table 14-2 NRTL-parameter for vapor-liquid-equilibrium modelling

Components	α	g'_{ij}	g''_{ij}	g'''_{ij}	g''''_{ij}	Fitted to data from
H_2O-CH_4	0.200812	-0.066822	0.00484	-0.041980	0.000111	[267]
CH_4-H_2O		0.256139	0.00039	-0.308662	0.001827	
H_2O-C_2H_6	0.040023	-0.084999	0	1.226781	0	[268]
C_2H_6-H_2O		0.521155	0	6.087316	0	
H_2O-C_3H_8	0.42873	-0.081444	0	-0.002527	0.018505	[269]
C_3H_8-H_2O		0.348760	0	0.000459	0.137759	
H_2O-CO_2	0.145636	-0.012973	0.000194	-0.082989	-0.000045	[270]
CO_2-H_2O		0.171577	0.001161	-0.769349	-0.000453	
H_2O-THF	0.475479	0.000008	0	24.701944	0	[271]
THF-H_2O		0	0	14.746786	0	

Table 14-3 Parameter to calculate the vapor pressure of a hypothetical empty hydrate shell fitted to data from [92]

	Structure SI				Structure SII			
Guest	A_i^β	B_i^β	C_i^β	D_i^β	A_i^β	B_i^β	C_i^β	D_i^β
Methane	0.1514	-2428.9	2.7891	0.0448	4.2177	-5033.4	2.7891	-0.0044
Ethane	4.6966	-5385.1	2.7891	-0.0090	3.8900	-4289.2	2.7891	-0.0078
Propane	-	-	-	-	4.5793	-5362.3	2.7891	-0.0075
Carbon dioxide	4.6201	-5379.8	2.7891	-0.0075	4.5652	-5283.9	2.7891	-0.0082
THF	-	-	-	-	3.8719	-4510.1	2.7891	-0.0045

Table 14-4 Constants for calculation of Langmuir-constants [88,253]

	Structure SI				Structure SII			
Cage	Small 5^{12}		Large $5^{12}6^2$		Small 5^{12}		Large $5^{12}6^4$	
Guest	$A\left[\frac{K}{Pa}\right]$	$B[K]$	$A\left[\frac{K}{Pa}\right]$	$B[K]$	$A\left[\frac{K}{Pa}\right]$	$B[K]$	$A\left[\frac{K}{Pa}\right]$	$B[K]$
Methane	7.133E-09	3187	2.304E-07	2653	2.178E-09	3453	9.869E-07	1916
Ethane	-	-	2.999E-08	3861	-	-	2.369E-06	2967
Propane	-	-	-	-	-	-	5.384E-08	4638
Carbon dioxide	2.442E-09	3414	4.190E-07	2813	8.340E-10	3615	8.399E-06	2025
THF	-	-	-	-	-	-	2.129E-09	6282

14.5 Chemicals

This section shows all used substances with their purities and their manufacturer in tabularized presentation. (See Table 14-5)

Table 14-5 Tabularized listing of the used chemicals with their purity

Name	Abbreviation	Purity	Manufacturer
Acetone		≥ 97 %	Sigma Aldrich/Merck
Carbon dioxide	CO_2	99.5 %	Messer Industriegase GmbH
Deionized water		Conductivity 17 µS /cm	In-Lab purification system
Ethanol	EtOH	96 – 97.2 %	Sigma Aldrich/Merck
Hexadecylamine	HDA	98 %	Sigma Aldrich/Merck
Hydrogen	H_2	99.999 %	Messer Industriegase GmbH
Lecithin	Lec	unknown	dm-drogerie markt GmbH + Co. KG
Methane	CH_4	≥ 99.5 %	Messer Industriegase GmbH
Milli-Q-water		Conductivity 1-3 µS /cm	Millipore purification system
Nitrogen	N_2	99.999 %	Messer Industriegase GmbH
Propane	C_3H_8	99,95 %	Messer Industriegase GmbH
Propylene carbonate	PC	99.7 %	Sigma Aldrich/Merck
Sodium dodecyl sulfate	SDS	98.5 %	Sigma Aldrich/Merck
Synthetic air		20.5 % Oxygen, 79.5 % Nitrogen	Messer Industriegase GmbH
Tetrabutylphosphonium bromide	TBPB	98 %	Sigma Aldrich/Merck
Tetrahydrofuran	THF	≥ 99.9 %	Sigma Aldrich/Merck
Triton X-100	TX-100	laboratory grade	Sigma Aldrich/Merck
Tween 80	T80	viscous liquid	Sigma Aldrich/Merck
15-crown-5		98 %	Sigma Aldrich/Merck
Ethane	C_2H_6	≥ 99.95 %	Messer Industriegase GmbH

Name	Abbreviation	Purity	Manufacturer
12-crown-4		98 %	Sigma Aldrich/Merck
18-crown-6		99 %	Sigma Aldrich/Merck
Sodiumdecanoate	SD	≥ 98 %	Sigma Aldrich/Merck
Sodiumoctanoate	SO	≥ 99%	Sigma Aldrich/Merck
Sodiumdodeanoate	SDD	99-100%	Sigma Aldrich/Merck
Sodiummyristate	SM	≥ 99%	Sigma Aldrich/Merck
Tetrabutylammonium bromide	TBAB	98.0+%	Alfa Aesar
Tetrabutylammonium chloride	TBACl	≥ 95%	Sigma Aldrich/Merck
Sulfolane	TMS	99%	Sigma Aldrich/Merck
Tetraethylene glycol	TEG	99%	Sigma Aldrich/Merck
Pentaethylene glycol	PEG	98%	Sigma Aldrich/Merck
Hexaethylene glycol	HEG	97%	Sigma Aldrich/Merck
Perfluorooctanic acid	PFOA	96%	Sigma Aldrich/Merck
Glycine		≥ 99%	Sigma Aldrich/Merck
L-Arginine		≥ 98%	Sigma Aldrich/Merck
L-Isoleucine		≥ 98%	Sigma Aldrich/Merck
L-Lysine		≥ 98%	Sigma Aldrich/Merck

14.6 List of publications

The following section contains all publications emerged from this PhD-project.

Peer-reviewed publications

1. Filarsky, F.; Schmuck, C.; Schultz, H.J. (2019): Impact of Modified Silica Beads on Methane Hydrate Formation in a Fixed-Bed Reactor. In: Ind. Eng. Chem. Res. DOI: 10.1021/acs.iecr.9b01952.
2. Filarsky, F.; Schmuck, C.; Schultz, H.J. (2019): Development of a Gas Hydrate Absorption for Energy storage and Gas separation – Proof of Concept based on Natural Gas. In: Energy Procedia 158, S. 5367–5373. DOI: 10.1016/j.egypro.2019.01.628.
3. Filarsky, F.; Schmuck, C.; Schultz, H.J. (2018): Development of a Surface-Active Coating for Promoted Gas Hydrate Formation. In: Chemie Ingenieur Technik 30 (11), S. 9141. DOI: 10.1002/cite.201800002.
4. Filarsky, F.; Schmuck, C.; Schultz, H.J. (2018): Development of a Biogas Production and Purification Process using promoted Gas Hydrate Formation – A Feasibility Study. In: Chemical Engineering Research and Design 134, S. 257–267. DOI: 10.1016/j.cherd.2018.04.009.

Publications

1. Filarsky, F.; Schmuck, C.; Schultz, H.J. (2018): Innovative Konzepte zur Biogaskonditionierung und Speicherung mittels Gashydratbildung. In: Chemie Ingenieur Technik 90 (9), S. 1174. DOI: 10.1002/cite.201855094.

Presentations

1. Filarsky, F.; Schmuck, C.; Schultz, H.J. „Development of a Gas Hydrate Absorption for Energy storage and Gas separation – Proof of Concept based on Natural Gas", 10th International Conference on Applied Energy (ICAE2018), Hong Kong, China, 25.08.2018
2. Filarsky, F.; Schmuck, C.; Schultz, H.J. „Untersuchungen zu verschiedenen Reaktordesigns zur Entwicklung zukunftsorientierter Gashydratspeicher", Jahrestreffen der ProcessNet-Fachgruppe Hochdruckverfahrenstechnik, Erlangen, Germany, 21.02.2018
3. Filarsky, F.; Schmuck, C.; Schultz, H.J. „Einfluss turbulenter Strömungsverhältnisse auf die Gashydratbildung in gerührten Druckautoklaven und Pipelines", Jahrestreffen der ProcessNet-Fachgruppe Hochdruckverfahrenstechnik, Erlangen, Germany, 21.02.2018
4. Filarsky, F.; Schmuck, C.; Schultz, H.J. „Untersuchungen zum Einfluss turbulenter Strömungsverhältnisse auf die Gashydratbildung in gerührten Druckautoklaven und Pipelines", Jahrestreffen der ProcessNet-Fachgruppen Mehrphasenströmungen, Partikelmesstechnik, Zerkleinern und Klassieren, Computational Fluid Dynamics und Mischvorgänge, Dresden, Germany, 17.03.2017

5. Filarsky, F.; Schmuck, C.; Schultz, H.J. „Bedeutung der Bio- und Erdgasaufbereitung mittels promotierter Gashydratbildung im Zuge des Klimawandels“, Promovendentag #4, Krefeld, Germany, 18.01.2017

Five additional presentations were performed during internal events at the University Duisburg-Essen and University of Applied Sciences Niederrhein.

Poster presentations

1. Filarsky, F.; Schmuck, C.; Schultz, H.J. „Gashydratabsorption – Innovativer Prozess zur Bio- und Erdgaskonditionierung“, Promovendentag #6, Krefeld, Germany, 07.03.2019
2. Filarsky, F.; Schmuck, C.; Schultz, H.J. „Innovative Konzepte zur Biogaskonditionierung und Speicherung mittels Gashydratbildung“, ProcessNet-Jahrestagung und 33. DECHEMA-Jahrestagung der Biotechnologen 2018, Aachen, Germany, 11.09.2018
3. Filarsky, F.; Schmuck, C.; Schultz, H.J. „Entwicklung einer promotierenden Oberflächenbeschichtung zur Intensivierung innovativer Gashydratspeichertechniken“, Jahrestreffen der ProcessNet-Fachgruppe Hochdruckverfahrenstechnik, Erlangen, Germany, 21.02.2018
4. Filarsky, F.; Schmuck, C.; Schultz, H.J. “Development of a Biogas Production and Upgrading Process under the use of Promoted Gas Hydrate Formation – Part 1”, 9th International conference on gas hydrates, Denver, USA, 26.06.2017
5. Filarsky, F.; Schmuck, C.; Schultz, H.J. “Development of a Biogas Production and Upgrading Process under the use of Promoted Gas Hydrate Formation – Part 2”, 9th International conference on gas hydrates, Denver, USA, 26.06.2017
6. Filarsky, F.; Schultz, H.J. „Biogaskonditionierung über Gashydratbildung in Gegenwart von Promotoren“, ProcessNet-Jahrestagung und 32. DECHEMA-Jahrestagung der Biotechnologen 2016, Aachen, Germany, 13.09.2016

Three additional poster presentations were performed during internal events at the University of Applied Sciences Niederrhein.

14.7 Curriculum vitae

"Der Lebenslauf ist in der Online-Version aus Gründen des Datenschutzes nicht enthalten"